STUDY ON CRYSTALLINITY, PROPERTIES AND DEGRADABILITY OF POLY-4-HYDROXYBUTYRATE AND RELATED POLYESTERS

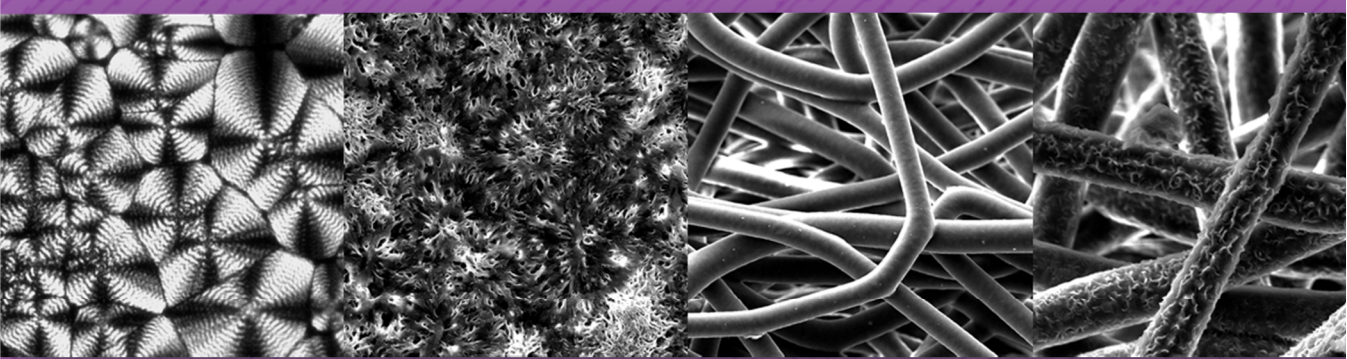

INA KERIDOU

UNIVERSITAT POLITÈCNICA DE CATALUNYA BARCELONATECH

STUDY ON CRYSTALLINITY, PROPERTIES AND DEGRADABILITY OF POLY-4-HYDROXYBUTYRATE AND RELATED POLYESTERS

Ina Keridou

Directors: Dr. Jordi Puiggalí Dr. Mª Lourdes Franco

Department of Chemical Engineering
Polytechnic University of Catalonia

Barcelona, 2021

ACKNOWLEDGEMENTS

I would like to express my deepest appreciation to my supervisor, Prof. Dr. Jordi Puiggalí Bellalta for giving me the unique opportunity of being a part of his research team. Without his valuable guidance and constant feedback, the planning and development of this research work would not have been successful.

I cannot begin to express my thanks to my supervisor Dr. M. Lourdes Franco Garcia, who has been a great help in concluding this thesis, which would be impossible without her endless support, useful critiques, and profound belief in my abilities.

I would also like to extend my gratitude to Dr. Luis Javier del Valle for the patience that cannot be underestimated and his willingness to share his time and immense knowledge on any occasion. Many thanks to Dr. M. Teresa Casas who provided me with moral support and useful suggestions throughout these times.

I gratefully acknowledge the assistance of Dr. Trifon Trifonov for teaching me the use of scanning electron microscopy and his unceasing disposition to assist me at any time. The assistance and invaluable experience of Juan Carlos Martinez and Ibraheem Yousef of ALBA synchrotron, has been very much appreciated.

I would also like to express my gratitude to B. Braun Surgical S.A.U., and particularly to Dr. Pau Turon for the financial support received through the collaborative work.

I would also like to extend my gratitude to all and each of my colleges and friends from PSEP and IMEM research groups with whom not only I shared lab time, but also a lot of lunchtimes, coffees, celebrations, fiestas, and even home and always with a lot of laughter and only good energy. I am grateful and blessed to have in my life Angy, Brenda, Soni, and Ludka, who all helped me in numerous ways during various stages not only of my Ph.D. but also of my life in Spain. Special thanks to Hamidreza and Max for being the best team ever. A big thank you to Maricruz and Kattya for always offering a warm hug when I

needed it the most. A sincere thank you to Fran for all the all-nighters spend at synchrotron and encouraging messages left on my desk by him and Kattya. Many thanks to Filip for the infinite good energy and the amazing figure of sutures who drew for this thesis. Thank you to Rosalia for all the years of just listening to me. A very special thank you to Vitor for just being there and for unparalleled support and patient throughout this stressful period. Many thanks to Neudys, Omid, Jordi, Hamidreza, Guillem, Georgina, Maricarmen, Cinthia, Anna, Helena, Matteo, Amir, and Reza, for always providing me encouragement and supportive words.

I would also like to say a heartfelt thank you to my Dad, Mum, Inga, and Dima for being the best family that anyone can ask for and giving me immeasurable support in all aspects of my life. I'm extremely grateful to Anna, Katerina, Christina, Kikh, and Anastasia for being the best friends by helping in whatever way they could during this challenging period. Last but not least, to the "Greek Ghetto Gracia" that opened their homes and offered me their priceless friendship during all these years away from my family and friends.

ABSTRACT

In the last decades, polymeric biomaterials, due to their advanced physical and mechanical properties, have been used in a vast variety of surgical and pharmaceutical applications. In this thesis, a study on crystallinity, properties, and degradability of poly-4-hydroxybutyrate (P4HB), commercially marketed as MonoMax® by B. Braun Surgical S.A.U. as an absorbable monofilament suture, and related polyesters is presented.

Part of this work has been executed under the collaborative research project established between PSEP (Polímeros Sintéticos. Estructura y Propiedades) research group of Universitat Politècnica de Catalunya and B. Braun Surgical S.A.U. (Center of Excellence for Closure Technologies) with the principal purpose of evolving and investigating polymeric systems with specific biomedical applications.

This study covers different topics related to P4HB such as (a) the physical, chemical, thermal and mechanical characterization; (b) the study of the crystallization kinetics; (c) the study of the degradation behavior of P4HB; and (d) the production of nanofibers by the electrospinning technique. Moreover, the work includes a study on blends of two different polyesters: PGA/PCL blends also produced employing the electrospinning technique and biphasic PLA/PA blends.

Crystallization was studied under both isothermal and non-isothermal conditions using optical microscopy and differential scanning calorimetry. Furthermore, supplementary experiments performed in a synchrotron radiation facility provided us with further information about the lamellae morphology, crystal structure, and molecular orientation.

Hydrolytic and enzymatic degradation of different matrices of P4HB was carried out in different buffered media. The hydrolytic degradation has been studied considering media of different pH values and temperatures. Enzymatic degradation has also been evaluated at physiological conditions using two

different lipases. The hydrolytic degradation mechanism differs from the enzymatic, where bulk degradation and a random chain scission are characteristic of samples exposed to hydrolytic media, whereas surface erosion and successive removal of monomer units are characteristic of samples exposed to enzymatic media. For annealed fibers, small-angle X-ray diffraction studies revealed a supramolecular structure with two different types of lamellar stacks. The spherulitic morphology of the enzymatically degraded films was highlighted by the elimination of the amorphous regions.

Nanofibers of PGA/PCL and P4HB were prepared using the electrospinning technique. The PGA/PCL nanofibers were also loaded with pharmacological drugs and used as a reinforcing agent of biodegradable polymer matrices. On the other hand, the biological performance of P4HB nanofibers was achieved with the incorporation of fibroblast growth factors. For this purpose, wound healing assay for two different cell lines (e.g., epithelial and fibroblast) were studied.

Finally, a study on the blends of PLA and Polyamide 6,10 was carried out to investigate the confinement effect of neighboring polymer domains on the phase separation and the structure and the influence of the disperse phase of polyamide in promoting PLA crystallization.

SCIENTIFIC PUBLICATIONS

- Keridou, I.; Franco, L.; Turon, P.; del Valle, L. J.; Puiggalí, J. Scaffolds with Tunable Properties Constituted by Electrospun Nanofibers of Polyglycolide and Poly(ε-Caprolactone). *Macromol. Mater. Eng.* 2018, *303* (7), 1–14. https://doi.org/10.1002/mame.201800100.
- Keridou, I.; del Valle, L. J.; Funk, L.; Turon, P.; Yousef, I.; Franco, L.; Puiggalí, J. Isothermal Crystallization Kinetics of Poly(4-Hydroxybutyrate) Biopolymer. *Polym. Morphol. Princ. Charact. Process.* 2019, *12* (2488), 1–20. https://doi.org/10.3390/ma12152488.
- Keridou, I.; del Valle, L. J.; Funk, L.; Turon, P.; Franco, L.; Puiggalí, J. Non-Isothermal Crystallization Kinetics of Poly(4-Hydroxybutyrate) Biopolymer. *Molecules* 2019, *24* (2840), 1–24. https://doi.org/10.3390/molecules24152840.
- Keridou, I.; Cailloux, J.; Martínez, J. C.; Santana, O.; Maspoch, M. L.; Puiggalí, J.; Franco, L. Biphasic Polylactide/Polyamide 6,10 Blends: Influence of Composition on Polyamide Structure and Polyester Crystallization. *Polymer (Guildf).* **2020**, *202*. https://doi.org/10.1016/j.polymer.2020.122676
- Keridou, I.; Franco, L.; del Valle, L. J.; Martínez, J. C.; Funk, L.; Turon, P.; Puiggalí, J. Microstructural Changes during Degradation of Biobased Poly(4-Hydroxybutyrate) Sutures. Polymers (Basel). 2020, 12 (9), 1–18. https://doi.org/10.3390/POLYM12092024.
- Keridou, I.; Franco, L.; del Valle, L. J.; Martínez, J. C.; Funk, L.; Turon, P.; Puiggalí, J. Hydrolytic and Enzymatic Degradation of Biobased Poly(4-Hydroxybutyrate) Films. Selective Etching of Spherulites. *Polymer Degrad. Stab.* **2021**, *183*, 1–11. https://doi.org/10.1016/j.polymdegradstab.2020.109451
- Keridou, I.; Franco, L.; del Valle, L. J.; Martínez, J. C.; Turon, P.; Puiggalí, J. Electrospun scaffolds for wound healing applications from poly-4-hydroxybutyrate: A bio-based and biodegradable linear polymer with elastomeric properties. *Pending*

ABBREVIATIONS

ATR	Attenuated Total Reflection
CA	Contact Angle
CAD	Computer-Aided Design
CFU	Colony Forming Units
CUR	Curcumin
DSC	Differential Scanning Calorimetry
E. coli	Escherichia coli
ECM	Extracellular Matrix
ELISA	Enzyme-linked Immunosorbent Assay
EtOH	Ethanol
FDA	Food and Drug Administration
FT-IR	Fourier transform infrared spectroscopy
GFs	Growth factors
GPC	Gel Permeation Chromatography
HA	Hydroxyalkanoate
HFIP	1,1,1,3,3,3-hexafluoroisopropanol
LH	Lauritzen-Hoffman
NMR	Nuclear magnetic resonance
P3HB	Poly-3-hydroxybutyrate
P4HB	Poly-4-hydroxybutyrate
P. cepacia	*Pseudomonas cepacia*
PA	Polyamide
PA-6	Polyamide- 6
PA-6,6	Polyamide- 6,6
PA-6,10	Polyamide- 6,10
PAA	Poly(acrylic acid)
PAN	Polyacrylonitrile
PANI	Polyaniline
PBS	Phosphate Buffer Saline
PC	Polycarbonate
PCL	Poly-ε-caprolactone
PES	Polyester
PEG	Polyethylene glycol
PET	Polyethylene terephthalate
PGA	Polyglycolide
PHA	Polyhydroxyalkanoates
PHB	Polyhydoxybutyrate
PHMB	Poly(hexamethylene biguanide)
PHV	Polyhydroxyvalerate
PLA	Polylactide
PLA_{REx}	Modified polylactide
POM	Polarizing Optical Microscopy

PP	Polypropylene
PTFE	Polytetrafluoroethylene
PS	Polystyrene
PVA	Polyvinyl alcohol
RCS	Refrigerated Cooling System
R. oryzae	*Rhizopus oryzae*
S. aureus	*Staphylococcus aureus*
SAXS	Small-angle X-ray Scattering
SEM	Scanning Electron Microscopy
TGA	Thermogravimetric Analysis
UV–vis	Ultraviolet-visible spectroscopy
USP	United Pharmacopeia States
WAXD	Wide-angle X-ray Diffraction
XRD	X-Ray Diffraction

TABLE OF CONTENTS

1. Introduction

1. INTRODUCTION

Nowadays, millions of tons of synthetic polymers are produced worldwide every year. Total global production of plastics topped 359 million metric tons in 2018, continuing a slow but steady increase since 2008, according to Statista.com (**Figure 1.1**). Production in Europe, meanwhile, kept constant in the last ten years with 61.8 million metric tons in 2018, showing a peak of 64.4 million metric tons in 2017. According to this source, 30% of all plastic produced in 2018 came from China, compared to 17% from Europe. Materials made from synthetic polymers are not biodegradable and are often improperly discarded. Therefore, waste plastics and water-soluble synthetic polymers in wastewater have led to serious environmental issues.[1,2]

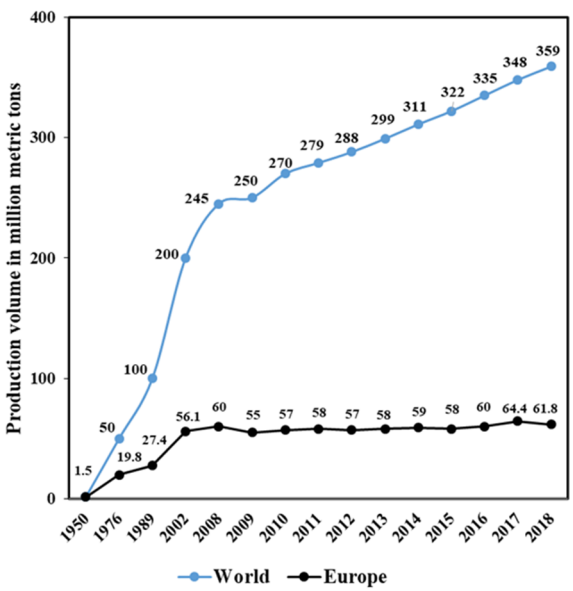

Figure 1.1. Global plastic production from 1950 to 2018 (in million metric tons). Includes thermoplastics, polyurethanes, thermosets, elastomers, adhesives, coatings and sealants, and polypropylene-fibers. Does not include the following fibers: PET, PA, PP, and polyacryl-fibers (Source: Statista.com).

As polymers are an integrated part of our daily existence a lot of steps were done to overcome this problem and develop novel materials

labeled as "environmentally-friendly", i.e., materials from renewable and sustainable resources, with lower energy consumption, biodegradable, and non-toxic to the environment.[3,4]

The polymer degradation process, regarding the degradation mechanism, can generally be classified into mechanical-, chemical-, photo-, thermal- and bio-degradation.[5] Nevertheless, the most environmentally benign method of degradable polymeric materials is biodegradation.

Biodegradation is a natural process by which organic materials are converted to simple molecules found in the environment, such as carbon dioxide, water, or methane, mainly by the enzymatic action of microorganisms. This leads to an important change in the material chemical structure.[4,6,7]

As biodegradable polymers are growing in importance, current research is focused on producing novel biopolymers. Biopolymers are polymers formed in nature during the growth cycles of all organisms; hence, they are also referred to as natural polymers and are available for material applications. Their synthesis generally involves enzyme-catalyzed, chain-growth polymerization reactions of activated monomers, which are typically formed within cells by complex metabolic processes.[6,8]

For material applications, natural polymers derived from agricultural products (e.g., starch, proteins, cellulose, and plant oils) are the most interesting alternative route to replace petrochemicals in many short-life range applications (packaging, agriculture, etc.).[9–11] Nevertheless, there is increasing attention in more complex hydrocarbon polymers produced by bacteria and fungi, particularly polysaccharides, i.e., xanthan, curdlan, pullulan, chitin, chitosan, and hyaluronic acid.[12]

Nonetheless, as compared to conventional thermoplastic synthetic polymers, most biopolymers are more expensive and sometimes lack of mechanical properties for practical use.[3,4,13] Either way, due to the necessity to decrease the emission of CO_2 and develop bio-based methods to produce chemicals, polymers, and fuels that in the long term can replace costly petroleum-based materials, there has been an important pursuit for the

improvement of these biopolymers to make them fully competitive with common thermoplastics.[14]

1.1 BIOMATERIAL

A biomaterial is defined as any natural or synthetic substance engineered to interact with biological systems to direct medical treatment.[15] The most important attribute of biomaterials is biocompatibility, namely, they perform their function with an appropriate host response.

Depending on their source the polymeric biomaterials can be divided into two main categories: non-synthetic polymers, which include natural and microbial, or synthetic polymers (**Figure 1.1.1**).[16] In the present work we are mainly focusing on the study of poly-4-hydroxybutyrate (P4HB) that belongs to the non-synthetic polyester group of polyhydroxyalkanoates (PHA), as well as related polyesters, such as polylactide (PLA), polyglycolide (PGA), and poly-ε-caprolactone (PCL).

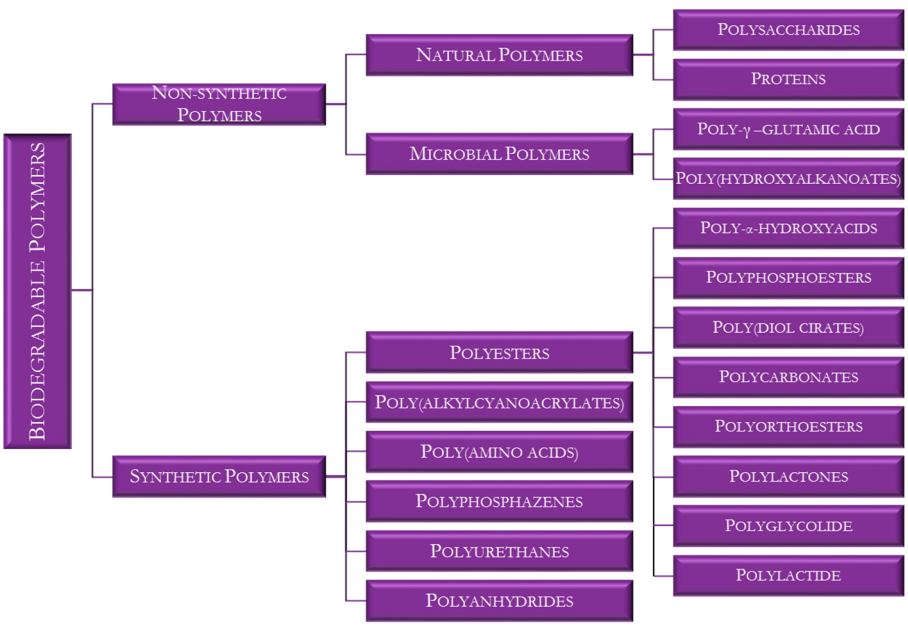

Figure 1.1.1. Classification of biodegradable polymers.

In recent years, the use of polymer biomaterials in a wide variety of surgical and pharmaceutical applications has increased due to their physical and mechanical properties, and their relatively simple feasibility. Medical applications of polymers can be divided into three main categories:

- Extracorporeal uses (e.g., catheters, tubing, dialysis membranes, ocular devices, wound dressing, and artificial skin).
- Permanently implanted devices (e.g., sensory, cardiovascular, orthopedic, and dental devices).
- Temporary implants (e.g., wound closure devices, implantable drug delivery systems, polymeric scaffolds, temporary vascular grafts and arterial stent, and temporary bone fixation devices).

Figure 1.1.2 shows some examples of applications of polymeric biomaterials:

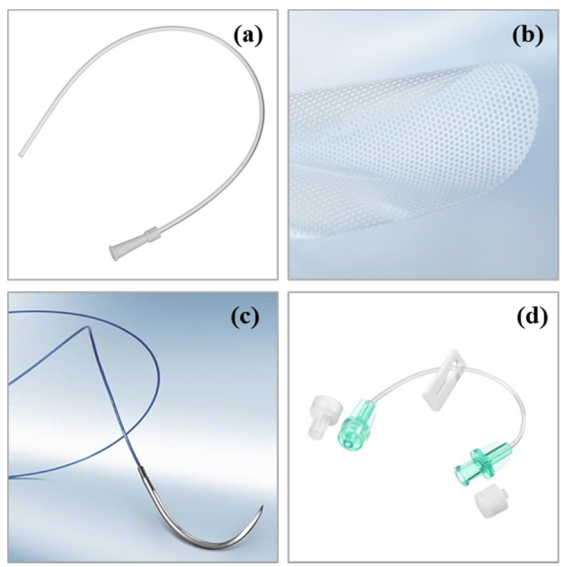

Figure 1.1.2. Examples of applications of polymeric biomaterials: (**a**) suction catheter, (**b**) Omyra® mesh TX engineered for thoracic reconstruction, (**c**) Dafilon® surgical suture, and (**d**) small bore connection tubing.

1.2 BIOMEDICAL APPLICATIONS

Newly, advanced materials have been constantly developed to meet new challenges. There is a wide range of degradable polymers that hold potential as

biomaterials, however, polymers require many parameters to be used for biomedical applications, such as definite structure and composition, polymer properties (mechanical, thermodynamic, etc.), biocompatibility (toxicity, immunogenicity, biodegradability, etc.), interaction with cells/tissues, and biodistribution.[16]

The biomedical applications are classified into several areas:

- **Medical devices** include a huge variety of elements, from temporary vascular grafts and arterial stents, commonly used in cardiovascular diseases or orthopedic devices,[17] to disposable devices such as syringes, catheters, surgical gloves, amongst others.
- **Wound dressing**,[18] is an important group for developing surgical practice. Sutures are the most well-known example of a wound closure device.
- **Tissue engineering**,[19] is also called regenerative medicine. It develops biological substitutes or reconstructs tissues to restore, maintain, or improve tissue functions.
- **Drug delivery systems** focused on controlling drug release and developing smart polymers that lead to a more accurate and programmable drug delivery.[20]
- **In control release and gene delivery**, synthetic polymer vectors in gene therapy provide improved safety, greater flexibility, and more facile manufacturing for treating various humans diseases, avoiding the use of viral vectors.[21]
- **Patterned biomaterials for diagnostics**, able to amplify and transmit signals. They must be sensitive to screening in a reduced size. Patterning has enabled researchers to create diagnostic tools by miniaturizing and combining laboratory procedures onto a single device.[22]

1.3 BIODEGRADATION

A core issue when choosing materials for biomedical applications is biodegradation because the performance of medical devices depends essentially on the stability of the material. As biodegradable polymers are materials with the capability to function for a temporary period and then degrade, biodegradability not only eliminates the risk of complications associated with the long-term presence of foreign material and the need for a second surgery for implant removal but also allows improved healing, as viable tissue interacts and grows into the degrading construct.

Drug delivery applications also require the use of degradable polymeric materials under physiological conditions that can gradually release the encapsulated drug and should demonstrate a continuous mass loss profile to enable repeated dosing and ensure the successful effect of the treatments.

Thus, choosing and designing materials for specific applications is essential to understand the degradation mechanisms of biomaterials since the degradation process may affect various events such as cell growth, tissue regeneration, drug release, host response, and material function.

Although biodegradable polymers can undergo different types of degradation (i.e., mechanical, thermal, photo), only hydrolytic and enzymatic degradation will be discussed in more detail.

Hydrolytic polymer degradation is defined as the cleavage of chemical bonds in the polymer backbone by reaction with water to form oligomers and lastly monomers. There are several natural (i.e., protein, cellulose) and synthetic polymers (i.e., polylactide, polycaprolactone) that undergo hydrolytic bond scission to form water-soluble fragments, resulting in polymer erosion. The physical erosion that accompanies the hydrolytic degradation of polymers is classified as bulk or surface erosion.[23]

During bulk erosion, the material is initially completely soaked with a certain amount of water and then diffusion into the amorphous parts occurs. Subsequently, hydrolysis starts, and gradually the crystalline regions are

penetrated and degraded by moisture. On the other hand, surface erosion occurs at the interfacial areas between polymeric specimens and the aqueous environment, where the erosion rate is constant. **Figure 1.3.1** is illustrating the two basic mechanisms of hydrolytic degradation.

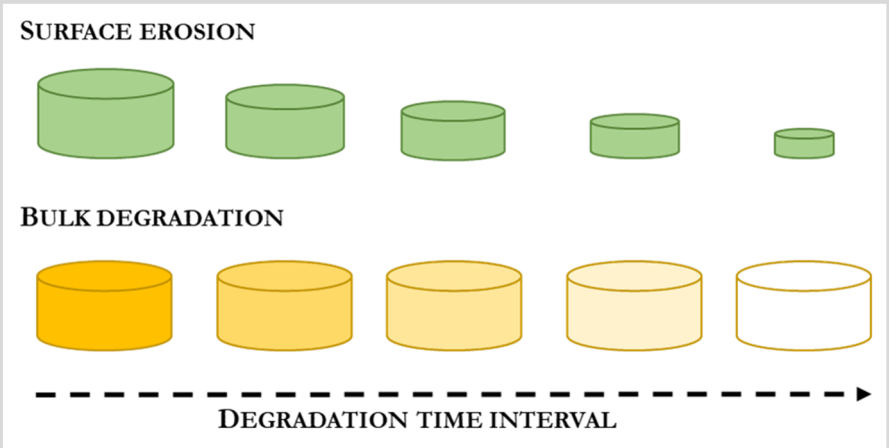

Figure 1.3.1. Schematic illustration of surface erosion and bulk degradation mechanisms.

The hydrolytic stability of polymers depends on various factors such as pH, temperature, hydrophobicity, morphology, degree of crystallinity, and porosity. Almost all these factors affect the amount of water that penetrates the material and thus the bulk erosion rate. The degradation rate is greatly dependent on the pH because an acid or a base acts as a catalyst, and may accelerate the degradation process. Hydrophobic polymers are less susceptible to hydrolysis and subsequent hydrolytic degradation in comparison to hydrophilic polymers. The water diffusion rate within the polymer plays also a critical role. The degradation rate is higher when the diffusion rate and permeability are higher. For instance, polymers with crystalline domains prevent the diffusion of water, limiting in this way the access to hydrolytically labile bonds. Finally, the rate of degradation can be greatly increased in porous materials where the surface area to volume ratio is high.[24]

Hydrolysis reactions can be catalyzed by enzymes known as hydrolases (e.g., phosphatases, esterases, proteases, glycosidases). These biologic catalysts are capable of accelerating the reaction rate in living organisms without undergoing any permanent change. Enzymatic degradation of synthetic polymers can be either surface erosion or bulk degradation and is mainly dependent on the location and stability of the acting enzyme. Nevertheless, most hydrophobic polymers undergo surface erosion due to the limited water accessibility. Still, for hydrophilic polymers that permit the diffusion of the enzyme to the interior of the polymer, the degradation also occurs by surface erosion mechanism if the scission of bonds is faster than the rate of enzyme diffusion. To occur bulk degradation of synthetic polymers during enzymatic activity, the enzyme should be able to infiltrate and distribute uniformly throughout the bulk of the polymer, and the diffusion of the enzyme should be faster than the rate of the enzymatic bond cleavage.[25]

Generally, during the enzymatic degradation, the enzyme first diffuses from the solution to the solid surface of the polymeric material. Then the enzyme gets adsorbed on the substrate, resulting in the enzyme-substrate complex formation, followed by the catalysis of the degradation reaction. Finally, soluble degradation products are diffused from the solid substrate to the solution.

The enzymatic degradation of polymeric materials is affected by both the polymer physicochemical properties (i.e., molecular weight, crosslinking, chemical composition, surface area, porosity, crystallinity) and the properties of the enzyme (i.e., activity, solubility, stability). It is also essential to take into account the pH and temperature of the medium.

Synthetic polymers mostly vulnerable to enzyme, acid, or base-catalyzed hydrolysis include polyesters with short midblocks (e.g., PLA, PGA, PCL, PHB). The aforementioned biodegradable materials are used in many pharmaceutical and medical applications such as resorbable surgical sutures, resorbable orthopedic devices, and controlled-release coatings for drug delivery systems.

As mentioned above, both hydrolytic and enzymatic degradation is mostly affected by the degree of crystallinity. Various researchers have demonstrated that the degradation rate increases when the polymer crystallinity decreases. However, the properties of the polymers, such as hardness, density, transparency, and diffusion, are also significantly influenced by the degree of crystallinity. Polymers have superior properties when the crystallinity and the glass transition temperature (T_g) are higher.

1.4 POLYMER CRYSTALLIZATION

Crystallinity is defined as the degree of structural order of a solid. The degree of crystallinity of a polymer is a critical parameter that controls a variety of polymer properties. A high or low degree of crystallinity can be required depending on the specific application. The capability of polymers to crystallize is associated with the partial alignment of the molecular chains. Crystalline polymers are attributed with regularly aligned chains in contrast to amorphous polymers that are not highly organized. Because of the polydispersity of the molecular weight of polymers, the majority of the polymers are semicrystalline, meaning that they form superstructures containing both crystalline and amorphous regions.

Crystallization of polymers from dilute solutions can lead to forming lamellar-shaped single crystals. Lamellae are the basic crystalline structures where the polymer chains are organized according to the "folded chain model" suggested by Keller[26] (**Figure 1.4.1**). Polymers can also arrange into regular crystalline structures by slowly cooling or quenching from the melt or during heating below the T_g (cold crystallization). Based on lamellar crystals spherulites[27] are formed, which are crystals that grow radially outwards from the center in the absence of thermal gradient. These spherulites are large enough to be seen in the optical microscopy as birefringent areas presenting a dark Maltese cross pattern (**Figure 1.4.2**).

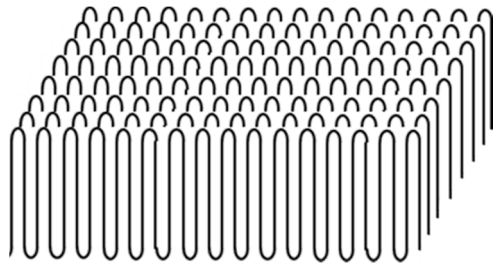

Figure 1.4.1. Schematic representation of the folded chain model.

The type and the structure of the polymers, as well as the growth conditions, affect the type and the structure of the crystals and the degree of crystallinity. Crystallinity depends on several factors such as crystallization temperature, cooling rate, and tacticity. In the case of strain-induced crystallization, it is affected by the stretch ratio, strain rate, and the forming process of the polymer film or fiber. Furthermore, crystallinity increases in polymers with narrow molecular weight distribution, linear polymer chains, and high molecular weight.[28]

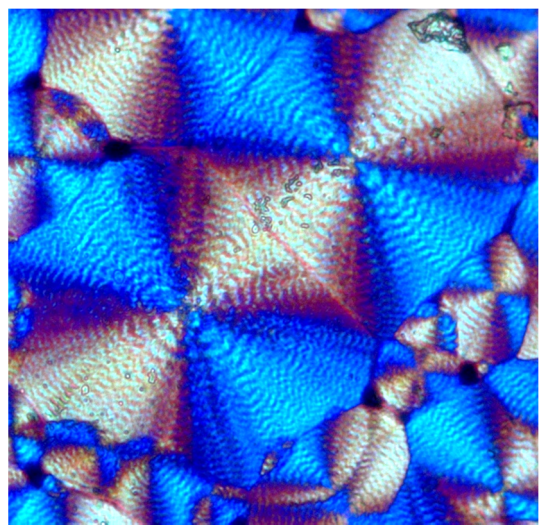

Figure 1.4.2. Optical micrograph of banded spherulites.

In various cases, polymers are demonstrating the phenomenon of polymorphism, where the same kind of molecules forms different crystals depending on the intermolecular arrangements.[29] The physical properties of polymers depend on their crystal structures, hence, controlling the

crystallization conditions is essential, even more, when they adopt different polymorphic structures.

The crystallinity degree and superstructural morphology greatly influence thermal and mechanical properties. One important aspect to take into account in polymer crystallization is the crystallization under confinement. A confined polymer system consists of a bulk polymer with a series of domains of reduced dimensions and independent from one another. These isolated crystallizable domains, referred to as microdomains, can have different dimensions ranging from the micro to the nanometer scale and can have different morphologies such as droplets, cylinders, lamellae, etc.

These microdomains affect the nucleation and crystallization of the polymer. Thus, if the number of microdomains is higher than the number of heterogeneities present in the bulk polymer the crystallization occurs at a lower temperature. On the contrary, when the number of heterogeneities is similar to the number of microdomains then a phenomenon called fractionated crystallization is produced with a crystallization process in several steps.[30]

Several techniques have been applied to identify the degree of crystallinity: Nuclear Magnetic Resonance (NMR), Differential Scanning Calorimetry (DSC), Infrared spectrophotometry (IR spectroscopy), X-Ray Diffraction (XRD). However, depending on the applied technique, differences in values of the degree of crystallinity are observed due to various physical features and the different use of the crystalline order definition.[31]

More specifically, DSC is applied for a fast determination of the degree of crystallinity by measuring the enthalpy of fusion and normalizing it according to the enthalpy of fusion of 100 % crystalline polymer.[32] Deconvolution of CH_3, CH_2, and CH lines in quantitative ^{13}C NMR spectra within crystalline domains, can be used for the estimation of the degree of crystallinity, due to the different magnetic fields experience that undergoes the nuclei of the same functional group within crystalline and amorphous domains.[33] Regarding the XRD technique, there are two different X-ray diffraction methods to determine the degree of crystallinity of polymer melts, blends, and solutions, the wide-angle

(WAXD) and small-angle (SAXS) scattering. WAXD gives information about the atomic structure of the crystals in contrast to SAXS that focuses mainly on the large-scale structures and the determination of important parameters such as long period (L), crystal lamellar thickness (l_c), and amorphous layer thickness (l_a) of semi-crystalline polymer from melts and blends.[34]

SAXS and WAXD measurements are enhanced with the combination of modern synchrotron radiation facilities with advanced instrumentation and computational methods that enable the fast acquisition and monitoring of high spatial resolution results.[35] Crystallization of polymers can then also be analyzed by simultaneous WAXD and SAXS synchrotron radiation experiments to determine the evolution of the degree of crystallinity and morphological parameters on the crystallization process. Moreover, these types of experiments are very useful to gain insight into the structural transitions induced by temperature.

1.5 Polymer Blends

Polymer blending is a relatively easy way to obtain new polymers with enhanced properties than those of the individual polymers. Polymer blends are a mixture of two or more homopolymers that can be used for the production of materials with different properties. Some of the benefits of blending, if successful, are the obtainment of materials with improved and desirable properties, adjustment of the composition to suit the costumers' requirements at the cheapest price, and recycling industrial/municipal plastics scrap.

Most polymer blends are immiscible, meaning that they are not formed spontaneously and exhibit more than two phases. There are several methods for producing polymer blends such as melt mixing, solution blending, latex mixing, partial block or graft polymerization, and interpenetrating polymer networks. From all above melt mixing and solution blending are the most used:

- **Melt mixing** is the environmentally friendly and cost-effective most widely used method in which the polymers are mixed in the molten state in extruders or batch mixers. To avoid thermal degradation,

undesirable chemical reactions, and non-uniform morphologies, novel methods have been developed such as solid-state shear pulverization[36] and cryogenic mechanical alloying.[37]

- **Solution blending** is a fast mixing, without a large energy consumption method where polymers are dissolved in a common solvent and intensively stirred. Separation of the blend occurs by precipitation or solvent evaporation, however, environmental issues arise due to the solvent removal and disposal.

Over the last decades, the interest in bio-based polymeric blends has increased due to extensive potential applications in several fields, such as packaging, electronics, tissue engineering, and household appliances. Thus, one of the essential areas of study in macromolecular science is the polymer blend's structures and properties.

The most common biodegradable polyesters blends that have been extensively studied for tissue engineering,[38] drug delivery systems,[39] and packaging applications[40] are PGA, PCL, PLA, and PHB.

PLA is an interesting bio-based polymer due to its overall properties together with a combination of processability and cost which makes it very appropriate to blend not only with polyesters but also with other polymers such as polyamides (PA) that improve the mechanical properties of PLA. One of the ongoing challenges remains in the manufacturing of PLA/PA bioblends with a high content of PLA in order to take advantage of the renewable resource-based origin and low price of PLA. On the other hand, aliphatic polyamides are the preferred material due to their useful properties such as good thermal stability, toughness, stiffness, and resistance to fatigue and abrasion.

For instance, the structure and the properties of PLA/PA6/PA66/PA610 blends were studied to improve the tensile properties of blends and the roughness of PLA.[36] Furthermore, Quiles-Carrillo L. et al.[42] used blends of PA1010/PLA to produce environmentally friendly films for packaging by the addition of four compatibilizers, while García-Masabet et al. studied the morphological properties of the blends by taking into account the rheological

criteria that have to do with the phases' viscosity, elasticity, and its capability to be regulated by extrusion variables.

In the case of immiscible polymer blends, a confined environment is obtained when the amount of dispersed phase is small (around 20%) since droplets with micrometric size are commonly formed and a fractionated crystallization can exist if the dispersed component can crystallize.[41] It has been reported that blend composition is one of the major factors governing the final morphology as well as the rheological and interfacial properties between the melted disperse and continuous phases. Specifically, it has been demonstrated that the modification of the properties of PLA before blending with PA leads to a shift in the onset of co-continuity towards lower PA content in PLA/ PA610 blends.

1.6 TISSUE ENGINEERING

Tissue engineering aims at the therapeutic reconstruction, maintenance, and improvement of the function of the human tissues and organs, by using biological substitutes based on the principles of engineering and life sciences.[43,44] In general, tissue engineering techniques require the use of scaffolds that can mimic the natural extracellular matrix (ECM) until the seeded cells can produce a new natural matrix and regenerate the desired tissue structure.[45] Tissue regeneration can be accelerated by providing growth factors (i.e., epidermal, fibroblast, transforming) that will facilitate cell differentiation and proliferation (**Table 1.6.1**).[46] Additionally, scaffolds may be used as drug or biomolecule carriers to alleviate some stages during tissue replacement and regeneration.[47]

Different categories of biomaterials are commonly used as scaffolds for cell and drug delivery. Biomaterials used for the fabrication of scaffolds can be bioceramics (e.g., hydroxyapatite, tricalcium phosphate),[55–58] natural polymers (e.g., alginate, proteins, collagens, gelatin, fibrins, and albumin)[59–64] or synthetic polymers (e.g., PVA, PCL, PLA, PGA, and PHA).[65–69] **Figure 1.6.1** depicts different available forms of polymeric scaffolds for cell/drug delivery: (a) a

highly 3D porous matrix, (b) a self-assembly or electrospun nanofibrous matrix (c) a thermosensitive sol-gel transition hydrogel, and (d) a porous microsphere.

Table 1.6.1. Most common growth factors used in tissue engineering.

Growth Factor	Acronym	Effects	Applications
Bone morphogenetic proteins	BMPs	Bone-forming cell differentiation migration	Bone regeneration for fracture healing and bone allograft integration[48]
Transforming growth factor beta	TGF-βs	Proliferation and differentiation of bone-forming cells Chemoattraction of fibroblasts Synthesis of ECM	Cartilage regeneration[49] Periodontal tissue engineering[50]
Fibroblast growth factors	FGFs	Wide range cell proliferation, survival, migration, and differentiation	Soft tissue regeneration[51]
Epidermal growth factor	EGF	Proliferation of epithelial, mesenchymal, and fibroblast cells	Wound healing[52]
Vascular endothelial growth factor	VEGF	Migration, proliferation, and survival of endothelial cells	Vascular engineering[53]
Platelet-derived growth factors	PDGFs	Proliferation and chemoattraction of smooth muscle cells Synthesis of ECM and deposition	Periodontal[54]

Generally, the mainstream research groups have been focused on the development and design of biomaterial scaffolds as three-dimensional porous solid biomaterials with a unique combination of essential properties.[47] A biomaterial designed for scaffolds should provide biocompatibility, biodegradability, mechanical stability for supporting the organ during tissue regeneration[65] and specific surface topography,[70] as well as chemical and physical properties for cell adhesion and proliferation.[71,72]

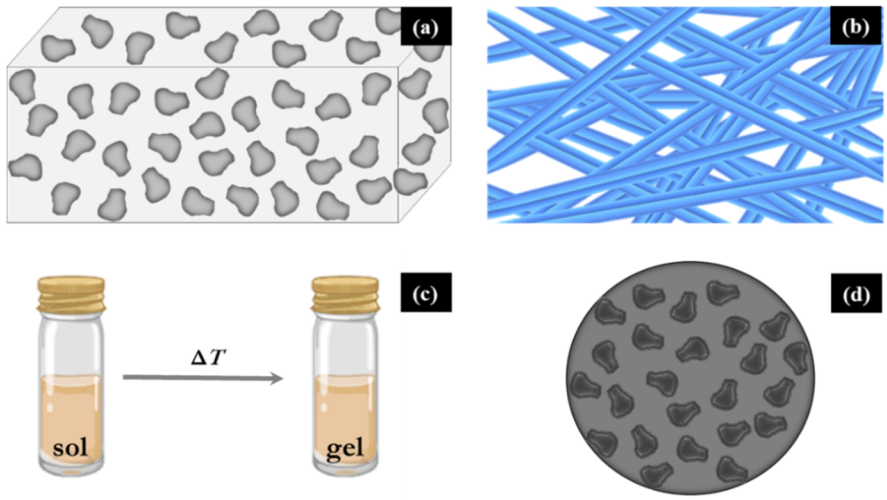

Figure 1.6.1. Different forms of polymeric scaffolds for cell/drug delivery: (**a**) 3D porous matrix, (**b**) nanofibre matrix (**c**) hydrogel, and (**d**) microsphere.

Several biodegradable and non-degradable polymeric biomaterials have been analyzed and tested for tissue engineering applications. Several polymeric scaffolds have been developed and used successfully in the regeneration and development of hard tissues (e.g., bone and cartilage),[65,67,69,71,73] as well as the repair and replacement of soft tissues (e.g., vascular and skin grafts).[74–77]

Table 1.6.2. Several polymeric biomaterials are used as scaffolds in tissue engineering applications.

Polymer	Applications
PCL	Suture coating, dental orthopedic implants
PGA	Suture anchors, meniscus repair, medical devices, drug delivery
PGCL	Smooth muscle
PLA	Fracture fixation, interference screws, suture anchors, meniscus repair
PLGA	Artificial skin, wound healing, suture
P3HB	Orthopedic, plastic surgeries
P4HB	Sutures, tendon and hernia repair, plastic and reconstructive surgeries

The most commonly used synthetic polymers in tissue engineering are polyesters such as PCL, PGA, PLA, PHB, and their copolymers (**Table 1.6.2**).[78] These materials have adequate biodegradable properties and enable the fabrication of scaffolds with excellent mechanical properties.[79]

There are various techniques to prepare polymeric scaffolds for tissue engineering applications, such as:

- **Emulsification freeze-drying**, fabrication of porous scaffolds by pouring in a mold a polymer dissolved in a suitable solvent solution followed by emulsification with a water phase, and then removing the solvents by freezing with liquid nitrogen and lyophilization.[80]
- **Solvent casting**, obtaining a porous structure by casting into the desired shape mode a biodegradable polymer solution mixed with a water-soluble salt (e.g. sodium chloride, sodium citrate), and then leaching out the salt particles by removing the solvent by evaporation or lyophilization.[81]
- **Melt molding**, acquiring a porous scaffold by casting into a mold the polymer embedded with the solid porogen and after applying heat and pressure, leaching away the porogen by washing the resulting product with water.[82]
- **Thermally-induced phase separation**, getting micro-porous structural scaffold by first dissolving the polymer in a solvent where liquid-liquid or solid-liquid phase separation is induced by quenching the solution at a certain temperature. A polymer rich and a polymer poor phases are formed. Afterward, the solvent should be removed from the phase-separated solutions either by freeze-drying or solvent extraction.[83,84]
- **Gas foaming**, highly interconnected porous polymer foams, free of organic solvents are fabricated. Solid disc-shaped structures made of the desired polymer by compression molding are produced. Afterward, the discs are exposed to high pressure of carbon dioxide inside a chamber. The porous microstructure is formed due to the escaping of carbon dioxide from the polymer.[85,86]
- **Electrospinning**, facile and effective fabrication of nonwoven ultrafine fiber matrices by applying a high voltage between the polymer

solution and a conductive target, towards which the polymer is projected, followed by solvent evaporation.[87]

- **Self-assembly**, creating biomaterials with a resemblance of the physiological environment by organizing the components into patterns or structures autonomously without human intervention.[88]
- **Rapid prototyping**, producing rapidly 3D scaffolds with desirable physical, chemical, and mechanical properties, from a computer-aided design (CAD) model (e.g., 3D printing).[89]

Some applications, as well as the advantages and drawbacks of these fabrication methods, are presented in **Table 1.6.3**.[47] Depending on the exact required scaffold properties the above-discussed techniques can be combined. However, electrospinning is considered one of the simplest processes to obtain porous matrices constituted by micro- and nano-fibers. Moreover, electrospinning provides the most promising results for tissue engineering, tissue regeneration, and drug delivery applications, since fibers can be easily loaded with drugs during their preparation.[90,91] Thus, in the present work, among the techniques presented in **Table 1.6.3**, the electrospinning technique is preferred for the production of scaffolds.

Table 1.6.3. Summary of scaffold fabrication methods and their recent applications.

Fabrication Technique	Pros	Cons	Porous size (µm)	Application
Emulsification freeze-drying	Requires low temperature. Does not require a separate leaching step.	Small pore size Long processing time	10-300	Tendon Bone Skin
Solvent casting	Simple setup Reproducible	Optimization is needed for high porosity without loss of mechanical properties. Difficulty in leaching out particles. Probable residuals	100-500	Coronary arteries Bone

Melt molding	No solvents	Nonporous layer on the surface. Residual porogen in the scaffold. Requires high operating temperatures.	30-450	Bone
Thermally-induced phase separation	Good control of pore size and structure	Difficult to obtain pore size >200	35-200	Cardiovascular Bone
Gas foaming	No solvent	Difficult to control the pore size	50-2,000	Bone
Electrospinning	Easy control of fiber morphology and geometry. Drug delivery	Small pore sizes Small thickness	0.0007-1.5	Vascular Bone Neural Ligament Wound dressing
Self-assembly	The resemblance of the physiological environment	Difficult to control the pore size. Limitation to form mechanically stable 3D geometry.	0.005-0.3	Cartilage
Rapid prototyping	Rapid production of complex products	Difficult to design and fabricate scaffolds with fine microstructures	50-300	Skin Bone

1.6.1 ELECTROSPINNING

In the early 1900s, an apparatus was patented by J.F. Cooly, and it permitted the development of the electrospinning technique.[92] Electrospinning is a simple and cost-effective method to fabricate tissue-engineered scaffolds by using an electric field to format and deposit the polymer fibers onto a target substrate, with diameters ranging from sub-micron to nanometers. Although there are several techniques of producing fibers such as phase-separation and self-assembly, electrospinning is favored due to its versatility, flexibility, and easy fiber fabrication.

A typical electrospinning set-up consists of a polymer solution (or melt), a syringe, a flat tip needle, a high voltage source, and a conducting collector[93] (**Figure 1.6.2**). In this technique, the polymer solution is charged with a high voltage source that results in the stretching of the liquid followed by the forming

of the Taylor cone.[94] Eventually, the buildup of the electrostatic repulsion within the liquid, causes it to eject a thin fibrous stream that later travels towards a charged collector. After the evaporation of the solvent, the dried polymers are collected onto a flat plate collector with a random orientation[95,96] or an electrically grounded rotating drum when the preferred orientation is desired.[97,98]

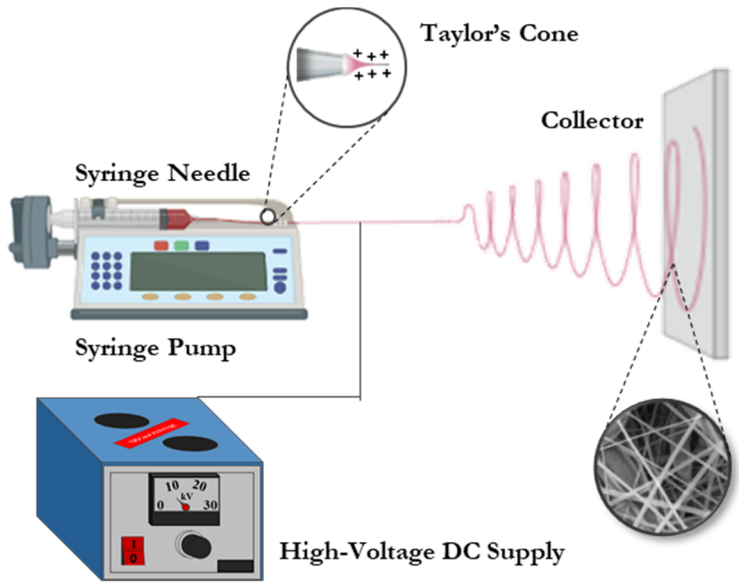

Figure 1.6.2. Schematic illustration of the electrospinning process.

There are several advantages in using electrospinning over other methods not only due to its simplicity, high efficiency, and ease of variation, but also its capability to produce scaffolds with an appropriate structure that mimics the ECM structure and facilitates the cell attachment, proliferation, and differentiation.[99,100] Furthermore, it provides a high aspect ratio and molecular orientation, porosity, large surface area, as well as excellent mechanical properties. However, with the electrospinning technique are mainly fabricated two-dimensional scaffolds with nanoscale pore size, which hinders cell seeding and infiltration.[101] Thus, essential challenges still exist in producing complex 3D scaffold shapes or in generating designed internal pore structures by this method.

The overall architecture of the scaffolds depends on several factors that are classified as electrospinning parameters, applied electric field solution, and environmental parameters (**Table 1.6.4**). It is well known that there is a critical voltage at which the Taylor cone is formed and ultrafine fibers are produced. However, beads or bead fibers with increased diameters are formed if the applied voltage is higher than the critical voltage due to deformation of the Taylor cone and an increase in the jet velocity for the same flow rate. Likewise, the flow of the polymeric solution determines the production of uniform, free of bead electrospun fibers, hence a minimum flow rate to maintain a balance between the leaving polymeric solution and replacement of that solution with a new one during jet formation is preferred. Equally, the determination of the critical concentration/viscosity of the charged jet is essential to obtain beadless nanofibers. When a voltage is applied on a low concentrated polymeric solution, a break of the entangled polymer chains before reaching the collector is caused. On the other hand, when the concentration is higher than the critical then the flow of the solution through the needle hinders and forms defective fibers. In the same way, a critical conductivity value of the solution is crucial to form the Taylor cone and obtain smaller diameter fibers. If the solution conductivity is lower or higher than the critical value then no electrospinning can take place or is hindered. One of the additional key factors to obtain fibers with desirable properties is adequate solvent selection. In general, volatile, with a moderate boiling point solvents are preferred, because of the easy evaporation of the solvent from the nanofibers during their flight from the needle tip to a collector.[102] It is crucial to take into consideration all these parameters to produce smooth and bead-free electrospun fibers.

Table 1.6.4. Parameters that affect the morphology of the electrospun fibers.

Electrospinning parameters	Solution	Environmental
Electric field	Solvent	Humidity
Flow rate	Polymer concentration	Temperature
Distance between the needle and collector	Viscosity	
Needle diameter	Solution conductivity	

Numerous natural macromolecules (i.e., collagen, gelatin, chitosan, hydroxyapatite, silk fibroin)[103–106] and synthetic polymers (i.e., PLA, PGA, PCL, PGLA, and P4HB)[39,107–109] have been processed into nanofibers by electrospinning for use in almost every field (**Table 1.6.5**) and paved the way for advancements in the biomedical field, emphasizing its importance.

Table 1.6.5. Examples of electrospun nanofiber scaffolds used in different fields.

Materials	Application
PVA, PLA, PEG, PS	Food packaging[110]
PA-6, PA-6,6, PAN,PU, PAA	Sensors[111]
PU, PP, PES, glass, aramid fibers	Air filtration[112]
PAN, PET, PVA, PS, PU, PC, PCL, PGA, PHB, chitosan, chitin, collagen, gelatin, silk	Liquid filtration[113]
PAN, PVA	Oil spill cleanup[114]
PAN, PU	Protective clothing[115]
PLA, PCL, PLGA	Drug delivery[116]

Tissue engineering and drug delivery are closely related areas in the biomedical field where once again electrospinning is favored in comparison to other methods because it enables the use of various materials and drugs for drug delivery applications. Drug delivery aims to transport therapeutic compounds into the body at a specific time and rate[46] using electrospun polymer nanofibers which have high loading capacity and encapsulation efficiency. For instance, such fibers are used in the development of wound dressing materials for infection treatments and wound healing by incorporating bactericide agents and growth factors.[117] In general, depending on their final purpose the electrospun nanofiber scaffolds can be tailored accordingly. PGA and PHB have a limited degree of employment in comparison to PCL, which is used extensively for the fabrication of electrospun tissues.

1.7 Wound Healing

Wound healing is a complex biological process where highly integrated cellular and molecular events take place leading to tissue repair. Wound healing consists of several distinct but overlapping phases: hemostasis, inflammation, proliferation, and remodeling (**Figure 1.7.1**).[118]

- **Hemostasis** initiates right after the injury when platelets or thrombocytes aggregation near the wound plays a critical role in clot formation. The resulting clot provides an extracellular matrix (ECM) for cell migration.
- **Inflammation** starts once the bleeding is controlled under the presence of a diverse array of cells, including neutrophils, macrophages, and lymphocytes that begin to remove bacteria, debris, and dead cells formed at the injured area. These cells release a mixture of pro-inflammatory cytokines and growth factors that allow the wound healing process to continue.
- **Proliferation** follows and overlaps with the inflammatory phase, during which the formation of granulation tissue occurs. Granulation tissue formation is attributed to three main key events; re-epithelialization, fibroplasia, and angiogenesis. During epithelialization, epithelial cells proliferate and migrate across the injury site. In fibroplasia, fibroblasts and endothelial cells form and organize collagen and other ECM molecules to form new tissue. Concurrent with these events is the angiogenesis process, whereby new blood vessels are formed.
- **Remodeling** is the final process of tissue repair which can take place over months to years and involves the gradual organization of collagen fibril. The main feature of this phase is the reconstruction of the ECM that utmost resembles that of the normal tissue.

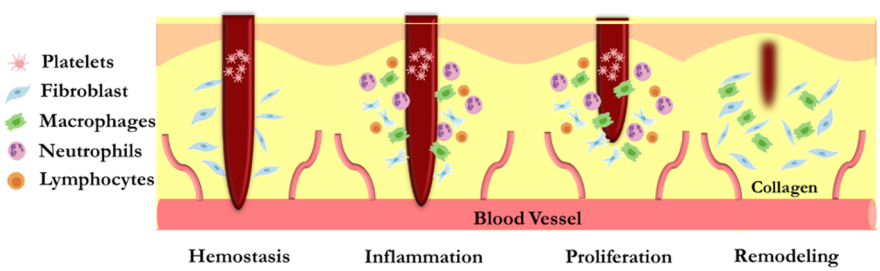

Figure 1.7.1. The main phases of the wound healing.

The progress of these phases should occur with no interruption, aberrancies, or prolongation because it can lead to delayed wound healing or a non-healing chronic wound. Several factors affect the proper repair of the wound and are classified as local, which influence directly the attributes of the wound itself and systemic, that depends on the health condition of the patient (**Figure 1.7.2**).[119]

The agents that play a critical role in the augmentation of several aspects of tissue repair in normal and impaired healing processes are growth factors. Growth factors (GFs) are defined as peptides that are responsible for regulating various cellular processes involved in granulation tissue formation and wound healing. Normally are produced by healthy cells, nonetheless, there are some cases in that GFs should be provided exogenously to cause tissue regeneration, because tissue regeneration cannot occur normally. Each GF can be produced by several, related or not related cell lines and can have different effects on different cell types. Typically they are named after their tissue of origin (e.g., platelet-derived growth factors), their biologic action (e.g., transforming growth factor), or the cell on which they act (e.g., epidermal growth factor).[120]

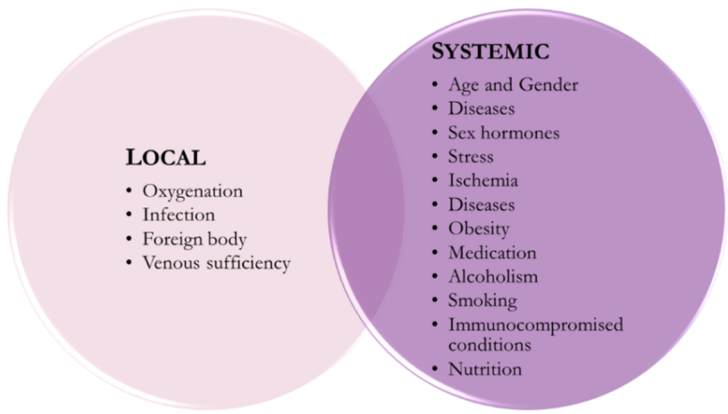

Figure 1.7.2. Factors affecting wound healing.

1.8 WOUND DRESSING

Nowadays, surgeons can choose among a wide variety of closure materials. The decision of which material to use depends on the nature and location of the wound, age of the patient, infection risk, rapidity, and cost. There are several equally efficient methods of wound closure and the definitive decision lies with the knowledgeable surgeon.[18]

Generally, wound closure biomaterials and devices can be categorized as:

- **Sutures**, natural or synthetic materials, are used to ligate blood vessels and to approximate tissues together. Therefore, bringing and holding tissues together after an injury or trauma are their major functions,[121](e.g., Novosyn®,[122]).
- **Tissue adhesives**, an alternative wound closure method that is painless, rapid and does not require removal. The tissue adhesive is applied on approximated wound edges where they undergo an exothermic reaction that forms a strong tissue bond,[123] (e.g., Histoacryl[124]).
- **Adhesive strips**, porous nonwoven materials that can be used for closure of wound edges after buried sutures are placed or with superficial wounds,[125] (e.g., Askina).
- **Staples/Ligating clips**, a reluctantly wound closure method when a rapid and not cosmetic closure is essential.
- **Surgical meshes**, woven or non-woven sheets which are used as either a permanent or temporary support for organs or other tissues during surgery.[126] The most popular types of surgical mesh are made from polypropylene, (e.g., Premilene®,[127]).

Some examples of wound closure materials and devices are depicted in **Figure 1.8.1**.

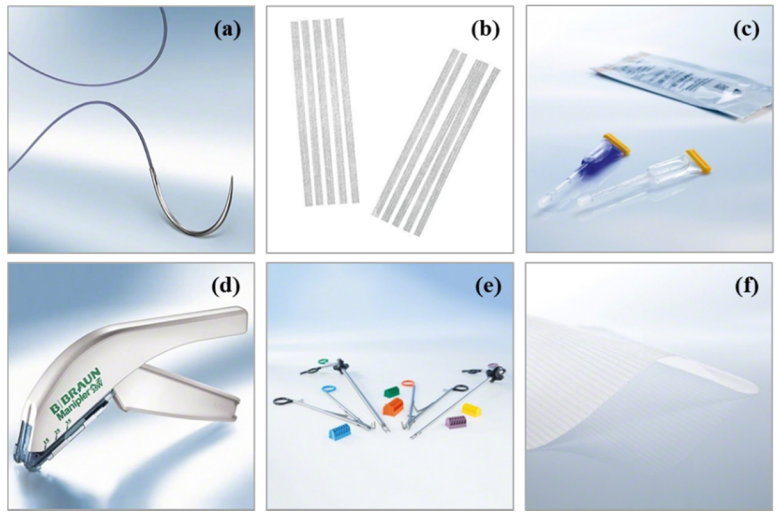

Figure 1.8.1. Examples of wound closure materials and devices used from B. Braun Surgical S.A.U. (**a**) Monosyn® sterile synthetic absorbable monofilament surgical suture, (**b**) Sterile skin closure strip Askina®, (**c**) Histoacryl® tissue adhesive, (**d**) DS Titanium Ligation Clips, (**e**) Manipler AZ sterile single-use skin stapler, (**f**) Premilene® Mesh implant for reinforcement of connective tissue structures.

The former mentioned, sutures, have received the most attention since they have been the most widely used in wound closure for many centuries.[128]

1.8.1 SUTURES

As previously mentioned, surgical sutures are used to hold apposing tissues together. The objectives of wound closure comprise obliteration of dead space, distribution of tension along deep suture lines, maintenance of tensile strength across the wound until tissue tensile strength is adequate, as well as an approximation of the epithelial portion of the closure.[129]

Historically, sutures have been used for millennia and it is well recognized that they have been an effective and critical part of the purpose of wound healing and its management. As far back as 2,000 B.C., it has been found that physicians have been using a vast variety of natural materials such as silk, cotton, linen, animal intestines, tendons, and hair, while some of them are still in use today.[121,129] In the 1940s the use of various synthetic biomaterials such as polydioxanone,[130] poly (lactic-co-glycolic acid) has been introduced as suture

materials. Lately, there have been important advancements in refining suture material; including antibiotic-coated and knotless sutures.[18] Although the availability of a wide range of suture materials, there is no single ideal suture material that would be adequate for all kinds of surgical and medical requirements.[131] Therefore, it is essential to understand the fundamental properties of suture materials to choose the most appropriate suture for each specific wound closure.

The characterization of suture materials involves physical and mechanical properties, handling characteristics, and biological and biodegradation behavior. The ideal suture should be non-electrolytic, noncapillary, nonallergenic, and noncarcinogenic, easy to tie, forming secure knots to prevent unraveling, ensure appropriate tensile strength to resist breakage, have optimal pliability and workability for ease of handling (suture memory, elasticity, and plasticity), and require minimal tissue reactivity, ability to resist to bacteria contamination/infection and be easily visible in the surgical intervention. Furthermore, the ideal suture would be easily sterilized, readily available, and have a consistent uniform diameter at a reasonable cost.[129,132]

1.8.1.1 Classification of Suture Materials

Sutures are categorized according to the type of material (natural or synthetic), the lifetime of the material in the body (absorbable or nonabsorbable), diameter, type of coated materials used to facilitate handling properties, and physical configuration (multifilament and monofilament).[128]

Generally, natural sutures are made of catgut, cotton, silk, or linen. On the other hand, synthetic nonabsorbable sutures are usually made of polypropylene (PP), poly(ethylene terephthalate)(PET), poly(butylene terephthalate) (PBT), polyamide (PA). It has been observed that natural sutures cause a more intense inflammatory reaction than synthetic materials.[121]

Absorbable sutures are often defined as sutures that lose their tensile strength within 2 to 3 months after implantation and later removal is not compulsory.[133] By this definition, synthetic polyesters polyglycolide (PGA),

poly(glycolide-lactide) (Vicryl®), and polydioxanone (PDS®), as well as natural products like catgut, are all classified as absorbable sutures. Silk, nylon, polybutester (Novafil™)[134], and propylene (Prolene ™)[135] are commonly used as non-absorbable sutures that are resistant to absorption and maintain their tensile strength although they can be slowly absorbed over a longer time. In contrast with the absorbable sutures that are usually used for buried sutures, the nonabsorbable sutures require eventual removal, thus are most commonly placed superficially.

Sutures can be divided into monofilament and multifilament, twisted or braided sutures in terms of the physical configuration (**Figure 1.8.2**). A monofilament suture confirmation contains a single brand of material and usually is uncoated. Monofilament sutures have low tissue drag, less inflammatory effect, and exhibit less resistance to passage through tissue than multifilament sutures do. However, they are less flexible than multifilament sutures, meaning that they have poorer handling characteristics and require more knots to ensure secure placement. Moreover, most monofilament constructions also have a memory effect, a bad trait, because they hold the shape they had in the package, becoming more difficult to work with.

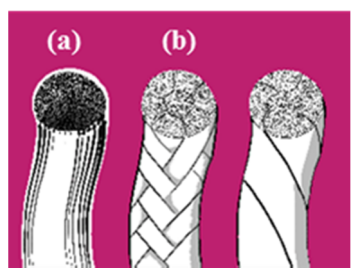

Figure 1.8.2. Physical configuration of fibers (**a**) monofilament and (**b**) multifilament (braided or twisted).

A multifilament configuration consists of numerous filaments or strands being braided or twisted together, resulting in a strong, flexible, and easy to handle suture. Normally, multifilament sutures are known as braided sutures because it is the common configuration for multifilament threads As a consequence of their physical structure they tend to promote tissue infection

and reactivity. The increase in tissue infection is a result of capillary penetration by bacteria and other foreign materials. However, both problems are significantly reduced by coating the braided material.[136]

An additional classification according to their size refers to the diameter (caliber or gauge) of the suture strand and is determined in millimeters and expressed in multiples of zeroes. The United States Pharmacopeia (USP) standard is more commonly used and the size is represented by a combination of two Arabic numerals: a 0 and any number other than 0, (e.g., 2-0 or 2/0). The higher the first number, the smaller the caliber of the suture; the lesser the tensile strength of the strand. The suture diameter can vary from 11 to 1. According to the USP, the tensile strength of any given suture material depends on its diameter. Hence, depending on the tensile strength required for each repair, a selection of an adequate suture size is recommended. This practice minimizes trauma as the suture is passed through the tissue to effect closure. It also ensures that the minimum mass of foreign material is left in the body. Finally, it should be pointed out that not all USP sizes correspond to the same diameters for all sutures materials.[137] For instance, 4-0 catgut is larger than 4-0 nylon.

Typically, the addition of a coating material to a suture aims to facilitate its handling properties and to ensure consistent performance. Especially, braided or twisted sutures are coated to improve passage through tissue and to reduce the surface area available for infection. The tendency is to develop coating materials that have a similar chemical property to the coated suture, thus absorbable or nonabsorbable sutures require different types of coating.[128] Common coating materials used are wax, silicone, poly(tetrafluoroethylene) (PTFE), etc.

1.8.2 MATERIALS

The necessity to develop methods to produce biodegradable polymers with all the necessary features for biomedical applications has been increasing gradually. Therefore, scientists have been studying a source that could meet the

various requirements of chemical and material industries and focused on a family of biopolyesters.[138]

1.8.2.1 Biodegradable Polyesters

Polyesters are thermoplastic polymers with hydrolytically labile aliphatic ester linkages in their backbone. Generally, all polyesters are theoretically degradable, but only aliphatic polyesters with reasonably short aliphatic chains between ester bonds can degrade over the time frame required for the majority of biomedical applications. The singularity of this group of polymers lies in the relative ease and versatile synthesis, via ring-opening or condensation polymerization, depending on the monomeric units.[16] Among polyesters, some of the most widely researched biodegradable are poly(α-ester)s (e.g., PGA, PCL, PLA) and the microbial poly(hydroxyalkanoate)s (PHA), e.g., (poly-3-hydroxybutyrate (P3HB), poly-4-hydroxybutyrate (P4HB), poly(hydroxy-butyrate-co-hydroxyvalerate) (PHBV)). **Figure 1.8.3** shows the chemical structures of various biodegradable polyesters.

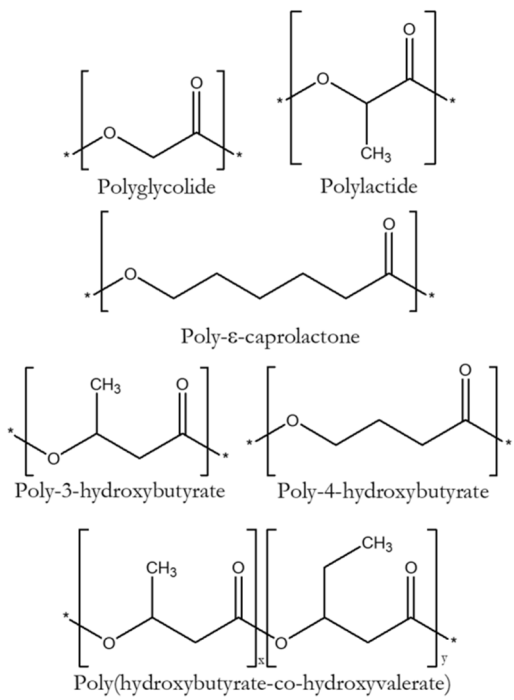

Figure 1.8.3. Chemical structures of different biodegradable polyesters.

1.8.2.1.1 Polyglycolide

Polyglycolide (PGA) is the simplest linear, aliphatic polyester and is produced by ring-opening polymerization of glycolide. It has approximately 45-55% crystallinity and therefore is not soluble in many organic solvents, but degrades comparatively quickly into acidic products. It has a high melting point (T_m ~220 °C) and very high tensile strength (12.8 GPa) in comparison with other polyesters and a glass transition temperature of T_g ~35 °C.[139,140,141]

These attributes favored PGA as one of the very first degradable polymers ever investigated for biomedical use, being often copolymerized with caprolactone[142], lactide[143], or trimethylene carbonate.[144] In 1970 the first synthetic absorbable suture from PGA was developed by Devis and Geck under the commercial name Dexon[145] and because of its good biocompatibility in tissues, sutures from PGA are now widely used (i.e., Petcryl ®,[146], Safil ®,[147]). They are multifilament-type sutures, which can be easily handled. Nevertheless, for continuous suturing, braided sutures with non-smooth surfaces are not suitable. Monofilament sutures are adequate for continuous suturing due to their smooth surfaces, but PGA is too stiff and inflexible for such applications.[6]

1.8.2.1.2 Polycaprolactone

Polycaprolactone (PCL) is a semicrystalline polyester that is produced by ring-opening polymerization of caprolactone. It has a melting temperature of T_m ~55-60 ºC and a glass transition temperature (T_g ~-54 ºC).[148,149] Furthermore, PCL has a moderately low tensile strength (23 MPa) but very high elongation at breakage (>700%).[150]

PCL has been thoroughly studied for biomedical applications due to its high solubility in organic solvents, degradation rate, and high drug permeability. However, it has some restrictions and cannot be used in some applications. Hence, PCL is generally blended with other polymers to improve crack resistance, dyeability, and adhesion (i.e., PLLA[151,152], PGA[149,153], and PBS[154]) or copolymerized (i.e., Monosyn ®,[155], Monocryl®,[156]). Several synthetic absorbable sutures are made from aliphatic absorbable polyesters and contain

one or more of the five basic building blocks: glycolide, L-lactide, p-dioxanone, ε-caprolactone, and trimethylene carbonate.[157] Practically all commercial synthetic absorbable sutures have at least one 'hard' segment (glycolide or L-lactide) and one 'soft' segment (ε-caprolactone, p-dioxanone, and trimethylene carbonate). The addition of the soft building blocks provides more flexibility to the sutures (i.e., Caprosyn™[158]).

1.8.2.1.3 Polylactide

Polylactide (PLA) is a thermoplastic polyester polymer and is synthesized by the lactide ring-opening polymerization. There are four forms of PLA polymers: poly(L-lactic acid) (PLLA), poly(D-lactic acid) (PDLA), poly(D, L-lactic acid) (PDLLA)—a racemic mixture of PLLA and PDLA, and meso-poly(lactic acid). However, mainly PLLA and PDLA have been extensively studied for biomedical applications due to their biodegradability, high tensile strength, and modulus.

Their degree of crystallinity is around 37%, the glass transition temperature between 50-80 ºC, the melting temperature around 173-178 ºC, and mechanical strength of 4.8 GPa. Thus, PLA polymers are among the most commonly used biomaterials having applications in biomedical and pharmaceutical industries as resorbable implant materials,[159] wound closure,[160] bone fixation devices, and drug delivery systems. However, due to the additional methyl group in PLA, the polymer is more hydrophobic and stable against hydrolysis than PGA, a reason that affects their clinical applications. Hence, blending PLA with other polymers is used to modify and improve the properties of PLA and to control its degradation behavior to be suitable for any desired application.[161]

1.8.2.1.4 Polyhydroxyalkanoates

Polyhydroxyalkanoates (PHAs) are thermoplastic linear polyesters that are synthesized and accumulated intracellularly during unbalanced growth by a large variety of bacteria (**Figure 1.8.4**). Thus far, over 150 different types have been reported. Several monomers consisting of carbon chain lengths from 3 to 14 can be used to synthesize PHA, depending on the bacteria types, their PHA

synthases, and the PHA synthesis processes. On several occasions, part of the monomer structures can be functional groups, namely unsaturated bonds, benzene, halogens, epoxides, and cyclic chemicals.[14,162] Depending on the length of the carbon chains of monomers, PHA consisting of 3–5 and 6–14 carbon atoms have been categorized into short-chain (scl) and medium-chain length (mcl), respectively.[163]

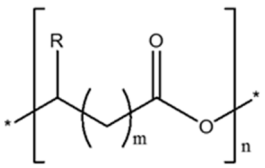

Figure 1.8.4. Chemical structure of a generic polyhydroxybutyrate, (m= 1, 2, 3, 4, n=100-30000 and R is variable. (P4HB: R=H and m=3, P3HB: R=CH_3 and m=2).

PHAs demonstrate various physicochemical properties adequate for several applications, such as tissue engineering scaffolds[164,165], drug delivery systems (implants, tablets)[166], therapeutic reasons[167], and medical devices (sutures, wound dressing, conduits).[168] The most common studied PHAs are poly-3-hydroxybutyrate (P3HB)[169], poly(3-hydroxybutyrate-co-3-hydroxyvale rate) (PHBV)[170], poly-4-hydroxybutyrate (P4HB)[171], poly(3- hydroxybutyrate-co-3-hydroxyhexanoate) (PHBHHx)[67], and poly-3-hydroxyoctanoate (PHO).[172] The most promising PHA is P4HB and it is the only one cleared to be used clinically in a medical device by the Food and Drug Administration-(FDA) and the Conformité Européene-(CE) marked it for use in Europe, due to its biodegradability, biocompatibility, and mechanical properties.

Poly-4-hydroxybutyrate (P4HB), is a thermoplastic, linear semicrystalline polyester which is used for the manufacture of a wide range of systems for medical applications, such as cardiovascular, wound healing, orthopedic, drug delivery, and tissue engineering.[173]

P4HB, in contrast to other absorbable polyesters, such as PGA and PCL, is not manufactured through ring-opening polymerization but is produced through a fermentation process with a similar chemical structure, however

without containing the residual metal catalysts that are used in chemical production. Despite the attempts to produce P4HB chemically, the results were not satisfying for most applications due to its lower molecular weight.[173]

Table 1.8.1. P4HB properties in comparison with other thermoplastic polyesters.[174]

Polymer	T_m (ºC)	T_g (ºC)	Tensile strength (MPa)	Tensile modulus (MPa)	Elongation at breakage (%)
PCL	58-63	-54	20-40	200-400	>700
PGA	220-230	35	60-100	6500	<3
PLA	173-178	50-80	28-50	1200-2700	6
P3HB	180	1	36	2,500	3
P4HB	62	-46.5	50	70	1,000

The first reported homopolyester of P4HB was synthesized by *Alcaligenes eutrophus* using 4-hydroxybutyratic acid as a precursor.[175,176] Wild-type bacteria like *Comanonas acidovorans*[177] and *Hydrogenophaga pseudovorans*[178] were also found to produce P4HB. After its biosynthesis, P4HB is isolated from the microorganism and is obtained in very high purity. However, the high cost of P4HB hinders its wider applications. Hence, there have been developed strategies for the production of P4HB in recombinant *Escherichia coli* by using glycerol[179,180] or xylose[181] as the growth substrate.

In 2007, the FDA cleared a monofilament suture made from P4HB marketed under the names TephaFLEX[182] (*Tepha, Inc.*) and MonoMax®,[171]. P4HB has also been used and as scaffolds and meshes. For instance, was commercialized by Tornier as the first orthopedic soft tissue scaffold for tendon repair (BioFiber®,[183]), and it was also employed in the production of P4HB meshes for hernia repair (Phasix®,[184,185]) and plastic and reconstructive surgeries (GalaFLEX®,[186]) (**Figure 1.8.5**).

Figure 1.8.5. P4HB medical products: (**a**) Biofiber®, (**b**) Phasix® and (**c**) GalaFLEX®.

As previously mentioned, in the present work we are focusing on the study of P4HB, an absorbable monofilament suture commercialized as MonoMax® by B. Braun Surgical S.A.U. that was initially launched in 2009 (**Figure 1.8.6**). Now it is available throughout most of Europe and has been recently released in the US and several other countries.

Figure 1.8.6. P4HB commercialized as MonoMax® absorbable monofilament suture.

MonoMax® suture is derived from a poly-4-hydroxybutyrate homopolymer, which is produced by Tepha, Inc. (Lexington, MA, USA) utilizing a genetically engineered *Escherichia coli* K12 microorganism that incorporates new biosynthetic pathways[174] (**Figure 1.8.7**).

The MonoMax® suture with the desirable properties is obtained by first pelleting the P4HB polymer. These pellets are melt extracted into monofilaments, quenched and drawn through multistage orientation and hot stretched to form the suture fiber. Afterward, the monofilament fibers are cut into even lengths, packaged, and sterilized in a cold ethylene oxide sterilization cycle.[171]

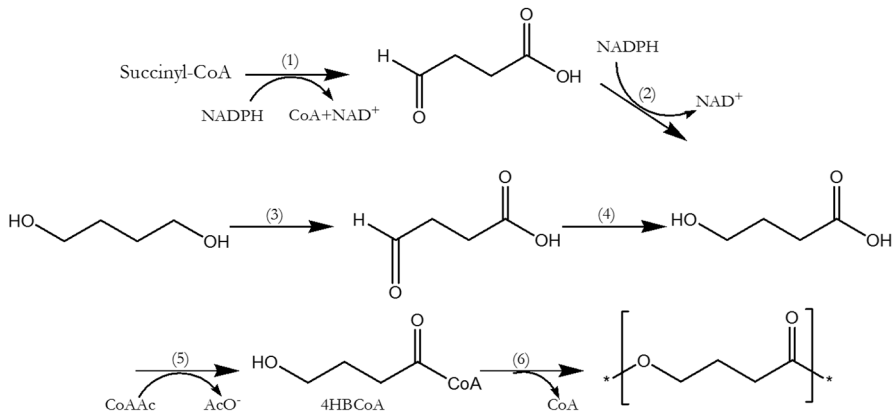

Figure 1.8.7. Metabolic pathways for the production of P4HB. The enzymes of the pathways are (**1**) succinic semialdehyde dehydrogenase; (**2**) 4-hydroxybutyrate dehydrogenase; (**3**) diol oxidoreductase; (**4**) aldehyde dehydrogenase; (**5**) coenzyme A transferase; and (**6**) PHA synthetase.

The P4HB suture is available in violet color and USP sizes 2-0, 0, and 1. This suture is indicated for soft tissue approximation and/or ligation use, especially for the closure of the abdominal wall. Furthermore, it can retain at least 50% of its initial tensile strength in vivo after 90 days, which is the highest among all commercially available monofilament absorbable sutures. The P4HB suture is also slightly elastic, in contrast with other synthetic absorbable sutures, such as PGA and PLA, which allows the suture to stretch a small amount under stress. This property prevents wound dehiscence by reducing the amount of tissue tearing at the wound edge. Finally, the lower modulus value of the MonoMax® suture makes it very pliable and flexible.[182]

Finally, it has been verified through *in vivo* biocompatibility tests that the P4HB suture degrades slowly and has no evidence of toxicity since its hydrolysis yields 4-hydroxybutyric acid, which is a common metabolite in the human body.

1.9 REFERENCES

(1) Hassan, M. N.; Rahman, R. A.; Chong, T. L.; Zakaria, Z.; Awang, M.; Hassan, M. N. Waste Recycling in Malaysia: Problems and Prospects. *Waste Manag. Res.* **2000**, *18* (4), 320–328. https://doi.org/10.1034/j.1399-3070.2000.00133.x.

(2) Narayan, R. Drivers for Biodegradable/Compostable Plastics and Role of Composting in Waste Management and Sustainable Agriculture; Report Paper. *Orbit J.* **2001**, *1* (1), 1–9.

(3) Bordes, P.; Pollet, E.; Avérous, L. Nano-Biocomposites: Biodegradable Polyester/Nanoclay Systems. *Prog. Polym. Sci.* **2009**, *34* (2), 125–155. https://doi.org/10.1016/j.progpolymsci.2008.10.002.

(4) Franceschi, E.; Cezaro, A. de; Ferreira, S. R. S.; Kunita, M. H.; Muniz, E. C.; Rubira, A. F.; Oliveira, J. V. Biopolymers Based on Renewable Resources A Review. *Open Chem. Eng. J.* **2014**, *5* (1), 11–20. https://doi.org/10.2174/1874123101004010011.

(5) Lucas, N.; Bienaime, C.; Belloy, C.; Queneudec, M.; Silvestre, F.; Nava-Saucedo, J. E. Polymer Biodegradation: Mechanisms and Estimation Techniques - A Review. *Chemosphere* **2008**, *73* (4), 429–442. https://doi.org/10.1016/j.chemosphere.2008.06.064.

(6) Chandra, R.; Rustgi, R. Biodegradable Polymers. *Prog. Polym. Sci.* **1998**, *23* (7), 1273–1335. https://doi.org/10.1016/S0079-6700(97)00039-7.

(7) Avérous, L. Biodegradable Multiphase Systems Based on Plasticized Starch: A Review. *J. Macromol. Sci. - Polym. Rev.* **2004**, *44* (3), 231–274. https://doi.org/10.1081/MC-200029326.

(8) Kaplan, D. L. *Macromolecular Systems - Materials Approach*; 1998. https://doi.org/10.10007/978-3-662-04068-3.

(9) Zhang, X.; Gozukara, Y.; Sangwan, P.; Gao, D.; Bateman, S. Biodegradation of Chemically Modified Wheat Gluten-Based Natural Polymer Materials. *Polym. Degrad. Stab.* **2010**, *95* (12), 2309–2317. https://doi.org/10.1016/j.polymdegradstab.2010.09.001.

(10) Raquez, J. M.; Habibi, Y.; Murariu, M.; Dubois, P. Polylactide (PLA)-Based Nanocomposites. *Prog. Polym. Sci.* **2013**, *38* (10–11), 1504–1542. https://doi.org/10.1016/j.progpolymsci.2013.05.014.

(11) Rao, M. G.; Bharathi, P.; Akila, R. A Comprehensive Review on Osteoporosis. *J. Trauma* **2015**, *10* (1), 3–12.

(12) Eklund, P.; Beckers, M.; Jansson, U.; Högberg, H.; Hultman, L. Linköping University Post Print The M n + 1 AX n Phases : Materials Science and Thin-Film Processing. *Mater. Sci. thin-film Process.* **2010**, No. 518, 1851–1878. https://doi.org/10.1016/j.tsf.2009.07.184.

(13) Mensitieri, G.; Di Maio, E.; Buonocore, G. G.; Nedi, I.; Oliviero, M.; Sansone, L.; Iannace, S. Processing and Shelf Life Issues of Selected Food Packaging Materials and Structures from Renewable Resources. *Trends Food Sci. Technol.* **2011**, *22* (2–3), 72–80. https://doi.org/10.1016/j.tifs.2010.10.001.

(14) Gao, X.; Chen, J. C.; Wu, Q.; Chen, G. Q. Polyhydroxyalkanoates as a

Source of Chemicals, Polymers, and Biofuels. *Curr. Opin. Biotechnol.* **2011**, *22* (6), 768–774. https://doi.org/10.1016/j.copbio.2011.06.005.

(15) Williams, D. F. On the Nature of Biomaterials. *Biomaterials* **2009**, *30* (30), 5897–5909. https://doi.org/10.1016/j.biomaterials.2009.07.027.

(16) Ulery, B. D.; Nair, L. S.; Laurencin, C. T. Biomedical Applications of Biodegradable Polymers. *J. Polym. Sci. Part B Polym. Phys.* **2011**, *49* (12), 832–864. https://doi.org/10.1002/polb.22259.

(17) Middleton, J. C.; Tipton, A. J. Synthetic Biodegradable Polymers as Orthopedic Devices. *Biomaterials* **2000**, *21* (23), 2335–2346. https://doi.org/10.1016/S0142-9612(00)00101-0.

(18) Tajirian, A. L.; Goldberg, D. J. A Review of Sutures and Other Skin Closure Materials. *J. Cosmet. Laser Ther.* **2010**, *12* (6), 296–302. https://doi.org/10.3109/14764172.2010.538413.

(19) Gunatillake, P. A.; Adhikari, R.; Gadegaard, N. Biodegradable Synthetic Polymers for Tissue Engineering. *Eur. Cells Mater.* **2003**, *5*, 1–16. https://doi.org/10.22203/eCM.v005a01.

(20) Kim, S.; Kim, J.; Jeon, O.; Chan, I.; Park, K. Engineered Polymers for Advanced Drug Delivery. *Eur. J. Pharm. Biopharm.* **2009**, *71* (3), 420–430. https://doi.org/10.1016/j.ejpb.2008.09.021.

(21) Kundu, P. P.; Sharma, V. Synthetic Polymeric Vectors in Gene Therapy. *Curr. Opin. Solid State Mater. Sci.* **2008**, *12* (5–6), 89–102. https://doi.org/10.1016/j.cossms.2009.01.005.

(22) Ratner, B. D.; Bryant, S. J. Biomaterials: Where We Have Been and Where We Are Going. *Annu. Rev. Biomed. Eng.* **2004**, *6* (1), 41–75. https://doi.org/10.1146/annurev.bioeng.6.040803.140027.

(23) Tamada, J. A.; Langer, R. Erosion Kinetics of Hydrolytically Degradable Polymers. *Proc. Natl. Acad. Sci. U. S. A.* **1993**, *90* (2), 552–556. https://doi.org/10.1073/pnas.90.2.552.

(24) Padsalgikar, A. D. Biological Properties of Species. In *Plastics in Medical Devices for Cardiovascular Applications.*; Elsevier Inc., 2017; pp 83–102. https://doi.org/10.4159/harvard.9780674865327.c6.

(25) Lin, C. C.; Anseth, K. S. The Biodegradation of Biodegradable Polymeric Biomaterials. In *Biomaterials Science: An Introduction to Materials: Third Edition*; Elsevier, 2013; pp 716–728. https://doi.org/10.1016/B978-0-08-087780-8.00061-9.

(26) Kornberg, H. L.; Krebs, H. A. Large Periods in Polyethylene: The Origin of Low-Angle X-Ray Scattering. *Nature* **1957**, *180*, 1289–1290.

(27) Pennings, A. J. Polymer Crystallization. *J. Cryst. Growth* **1980**, *48* (4), 574–581. https://doi.org/10.1016/0022-0248(80)90268-7.

(28) Zhang, M. C.; Guo, B. H.; Xu, J. *A Review on Polymer Crystallization Theories*; 2017; Vol. 7. https://doi.org/10.3390/cryst7010004.

(29) De Rosa, C.; Auriemma, F.; Malafronte, A.; Scoti, M. Crystal Structures and Polymorphism of Polymers: Influence of Defects and Disorder. *Polym. Cryst.* **2018**, *1* (4), 1–21. https://doi.org/10.1002/pcr2.10015.

(30) Michell, R. M.; Blaszczyk-Lezak, I.; Mijangos, C.; Müller, A. J. Confinement Effects on Polymer Crystallization: From Droplets to

Alumina Nanopores. *Polymer (Guildf).* **2013**, *54* (16), 4059–4077. https://doi.org/10.1016/j.polymer.2013.05.029.
(31) Rabiej, S.; Wlochowicz, A. SAXS and WAXS Investigations of the Crystallinity in Polymers. *Die Angew. Makromol. Chemie* **1990**, *175* (1), 81–97. https://doi.org/10.1002/apmc.1990.051750107.
(32) Blaine, R. L. Determination of Polyethylene Crystallinity by DSC. *TA Instruments* **2002**, *2002* (09), 1–3.
(33) Hronský, V.; Koval'Aková, M.; Vrábel, P.; Uhrínová, M.; Olčák, D. Estimation of the Degree of Crystallinity of Partially Crystalline Polypropylenes Using 13C NMR. *Acta Phys. Pol. A* **2014**, *126* (1), 409–410. https://doi.org/10.12693/APhysPolA.126.409.
(34) Sharma, J. Characterization of Polymer Blends by X-Ray Scattering: SAXS and WAXS. *Charact. Polym. Blends Miscibility, Morphol. Interfaces* **2015**, *9783527331*, 209–236. https://doi.org/10.1002/9783527645602.ch06.
(35) Chu, B.; Hsiao, B. S. Small-Angle X-Ray Scattering of Polymers. *Chem. Rev.* **2001**, *101* (6), 1727–1761. https://doi.org/10.1021/cr9900376.
(36) Khait, K.; Torkelson, J. M. A New Polymer Processing Technology for Polymer Blends with Unmatched Viscosity: Solid-State Shear Pulverization (S3P). *Int. Polym. Process.* **2000**, *15* (4), 343–347. https://doi.org/10.3139/217.1617.
(37) Ibrahim Khan, M. A. J.; Mazumder. Polymer Blends. *Introd. to Polym. Compd. Raw Mater. (Vol 1)* **2005**, *1* (August), 1–59.
(38) Patrício, T.; Glória, A.; Bártolo, P. Mechanical and Biological Behaviour of PCL and PCL/PLA Scaffolds for Tissue Engineering Applications. *Chem. Eng. Trans.* **2013**, *32*, 1645–1650. https://doi.org/10.3303/CET1332275.
(39) Del Valle, L. J.; Camps, R.; Díaz, A.; Franco, L.; Rodríguez-Galán, A.; Puiggalí, J. Electrospinning of Polylactide and Polycaprolactone Mixtures for Preparation of Materials with Tunable Drug Release Properties. *J. Polym. Res.* **2011**, *18*, 1903–1917. https://doi.org/10.1007/s10965-011-9597-3.
(40) Arrieta, M. P.; Samper, M. D.; Aldas, M.; López, J. On the Use of PLA-PHB Blends for Sustainable Food Packaging Applications. *Materials (Basel).* **2017**, *10* (9), 1–26. https://doi.org/10.3390/ma10091008.
(41) Paul, D.; Bucknall, C. *Polymer Blends, Formulation and Performance, Vol 1 and 2.*, 1st ed.; Wiley-Interscience, Ed.; John Wiley and sons; New York, USA, 2000.
(42) Quiles-Carrillo, L.; Fenollar, O.; Balart, R.; Torres-Giner, S.; Rallini, M.; Dominici, F.; Torre, L. A Comparative Study on the Reactive Compatibilization of Melt-Processed Polyamide 1010/Polylactide Blends by Multi-Functionalized Additives Derived from Linseed Oil and Petroleum. *Express Polym. Lett.* **2020**, *14* (6), 583–604. https://doi.org/10.3144/expresspolymlett.2020.48.
(43) Skalak, R. Tissue Engineering. **1993**, 1112–1113.
(44) Langer, R.; Vacanti, J. P. Tissue Engineering. *Science (80-.).* **1993**, *260*

(5110), 920–926. https://doi.org/10.1126/science.8493529.

(45) Wintermantel E; Mayer J; Blum J; Eckert KL; Luscher P; Mathey M. Tissue Engineering Scaffolds Using Superstructures. *Biomaterials* **1996**, *17* (2), 83–91.

(46) Simón-yarza, T.; Garbayo, E.; Tamayo, E.; Prósper, F.; Blanco-prieto*, M. J. Chapter 9.1. Drug Delivery in Tissue Engineering: General Concepts. **2012**, No. July, 501–526. https://doi.org/10.1039/9781849735292-00501.

(47) Garg, T.; Singh, O.; Arora, S.; Murthy, R. S. R. Scaffold: A Novel Carrier for Cell and Drug Delivery. *Crit. Rev. Ther. Drug Carrier Syst.* **2012**, *29* (1), 1–63. https://doi.org/10.1615/CritRevTherDrugCarrierSyst.v29.i1.10.

(48) Calori, G. M.; Donati, D.; Di Bella, C.; Tagliabue, L. Bone Morphogenetic Proteins and Tissue Engineering: Future Directions. *Injury* **2009**, *40 Suppl 3*, S67–S76. https://doi.org/10.1016/s0020-1383(09)70015-4.

(49) Madry, H.; Rey-Rico, A.; Venkatesan, J. K.; Johnstone, B.; Cucchiarini, M. Transforming Growth Factor Beta-Releasing Scaffolds for Cartilage Tissue Engineering. *Tissue Eng. - Part B Rev.* **2014**, *20* (2), 106–125. https://doi.org/10.1089/ten.teb.2013.0271.

(50) Zhang, Y.; Cheng, X.; Wang, J.; Wang, Y.; Shi, B.; Huang, C.; Yang, X.; Liu, T. Novel Chitosan/Collagen Scaffold Containing Transforming Growth Factor-B1 DNA for Periodontal Tissue Engineering. *Biochem. Biophys. Res. Commun.* **2006**, *344* (1), 362–369. https://doi.org/10.1016/j.bbrc.2006.03.106.

(51) Yun, Y. R.; Won, J. E.; Jeon, E.; Lee, S.; Kang, W.; Jo, H.; Jang, J. H.; Shin, U. S.; Kim, H. W. Fibroblast Growth Factors: Biology, Function, and Application for Tissue Regeneration. *J. Tissue Eng.* **2010**, *1* (1), 1–18. https://doi.org/10.4061/2010/218142.

(52) Hardwicke, J.; Schmaljohann, D.; Boyce, D.; Thomas, D. Epidermal Growth Factor Therapy and Wound Healing - Past, Present and Future Perspectives. *Surgeon* **2008**, *6* (3), 172–177. https://doi.org/10.1016/S1479-666X(08)80114-X.

(53) Lifirsu, E. S.; Ramalingam, M.; Haidar, Z. S. Vascular Endothelial Growth Factors in Tissue Engineering: Challenges and Prospects for Therapeutic Angiogenesis. In *Integrated Biomaterials in Tissue Engineering*; 2012; pp 275–293.

(54) Giannobile, W. V; Lee, C. S.; Tomala, M. P.; Tejeda, K. M.; Zhu, Z. Platelet-Derived Growth Factor (PDGF) Periodontal Tissue Engineering. *J Periodontol* **2001**, *72* (6), 815–823.

(55) Gao, Y.; Cao, W. L.; Wang, X. Y.; Gong, Y. D.; Tian, J. M.; Zhao, N. M.; Zhang, X. F. Characterization and Osteoblast-like Cell Compatibility of Porous Scaffolds: Bovine Hydroxyapatite and Novel Hydroxyapatite Artificial Bone. *J. Mater. Sci. Mater. Med.* **2006**, *17* (9), 815–823. https://doi.org/10.1007/s10856-006-9840-3.

(56) Leukers, B.; Gülkan, H.; Irsen, S. H.; Milz, S.; Tille, C.; Schieker, M.; Seitz, H. Hydroxyapatite Scaffolds for Bone Tissue Engineering Made

by 3D Printing. *J. Mater. Sci. Mater. Med.* **2005**, *16*, 1121–1124. https://doi.org/10.1007/s10856-005-4716-5.

(57) Tarafder, S.; Balla, V. K.; Davies, N. M.; Bandyopadhyay, A.; Bose, S. Microwave-Sintered 3D Printed Tricalcium Phosphate Scaffolds for Bone Tissue Engineering Solaiman. *J. Tissue Eng. Regen. Med.* **2012**, 1–11. https://doi.org/10.1002/term.

(58) Miranda, P.; Saiz, E.; Gryn, K.; Tomsia, A. P. Sintering and Robocasting of β-Tricalcium Phosphate Scaffolds for Orthopaedic Applications. *Acta Biomater.* **2006**, *2* (4), 457–466. https://doi.org/10.1016/j.actbio.2006.02.004.

(59) Skerra, A. Engineered Protein Scaffolds for Molecular Recognition. *J. Mol. Recognit.* **2000**, *13* (4), 167–187. https://doi.org/10.1002/1099-1352(200007/08)13:4<167::AID-JMR502>3.0.CO;2-9.

(60) Moe, O. W. Scaffolds: Orchestrating Proteins to Achieve Concerted Function. *Kidney Int.* **2003**, *64* (5), 1916–1917. https://doi.org/10.1046/j.1523-1755.2003.00346.x.

(61) Prabu, P.; Dharmaraj, N.; Aryal, S.; Lee, B. M.; Ramesh, V.; Kim, .Y. Preparation and Drug Release Activity of Scaffolds Containing Collagen and Poly(Caprolactone). *J. Biomed. Mater. Res. Part A* **2006**, *79A* (1), 153–158. https://doi.org/10.1002/jbm.a.

(62) Grover, C. N.; Cameron, R. E.; Best, S. M. Investigating the Morphological, Mechanical and Degradation Properties of Scaffolds Comprising Collagen, Gelatin and Elastin for Use in Soft Tissue Engineering. *J. Mech. Behav. Biomed. Mater.* **2012**, *10*, 62–74. https://doi.org/10.1016/j.jmbbm.2012.02.028.

(63) Ghasemi-Mobarakeh, L.; Prabhakaran, M. P.; Morshed, M.; Nasr-Esfahani, M. H.; Ramakrishna, S. Electrospun Poly(ε-Caprolactone)/Gelatin Nanofibrous Scaffolds for Nerve Tissue Engineering. *Biomaterials* **2008**, *29* (34), 4532–4539. https://doi.org/10.1016/j.biomaterials.2008.08.007.

(64) Zhang, Y.; Ouyang, H.; Chwee, T. L.; Ramakrishna, S.; Huang, Z. M. Electrospinning of Gelatin Fibers and Gelatin/PCL Composite Fibrous Scaffolds. *J. Biomed. Mater. Res. - Part B Appl. Biomater.* **2005**, *72* (1), 156–165. https://doi.org/10.1002/jbm.b.30128.

(65) Shin, H. J.; Lee, C. H.; Cho, I. H.; Kim, Y.-J.; Lee, Y.-J.; Kim, I. A.; Park, K.-D.; Yui, N.; Shin, J.-W. Electrospun PLGA Nanofiber Scaffolds for Articular Cartilage Reconstruction: Mechanical Stability, Degradation and Cellular Responses under Mechanical Stimulation in Vitro. *J. Biomater. Sci. Polym. Ed.* **2006**, *17* (1), 103–119. https://doi.org/10.1163/156856206774879126.

(66) Freed, L. E.; Vunjak-Novakovic, G.; Biron, R. J.; Eagles, D. B.; Lesnoy, D. C.; Barlow, S. K.; Langer, R. Biodegradable Polymer Scaffolds for Tissue Engineering. *Nat. Biotechnol.* **1994**, *12*, 689–693. https://doi.org/10.1038/nbt0794-689.

(67) Wang, Y. W.; Wu, Q.; Chen, J.; Chen, G. Q. Evaluation of Three-Dimensional Scaffolds Made of Blends of Hydroxyapatite and Poly(3-

Hydroxybutyrate-Co-3-Hydroxyhexanoate) for Bone Reconstruction. *Biomaterials* **2005**, *26* (8), 899–904. https://doi.org/10.1016/j.biomaterials.2004.03.035.

(68) Patrício, T.; Domingos, M.; Gloria, A.; Bártolo, P. Characterisation of PCL and PCL/PLA Scaffolds for Tissue Engineering. *Procedia CIRP* **2013**, *5*, 110–114. https://doi.org/10.1016/j.procir.2013.01.022.

(69) Yao, Q.; Cosme, J. G. L.; Xu, T.; Miszuk, J. M.; Picciani, P. H. S.; Fong, H.; Sun, H. Three Dimensional Electrospun PCL/PLA Blend Nanofibrous Scaffolds with Significantly Improved Stem Cells Osteogenic Differentiation and Cranial Bone Formation. *Biomaterials* **2017**, *115*, 115–127. https://doi.org/10.1016/j.biomaterials.2016.11.018.

(70) Curtis, A.; Wilkinson, C. Topographical Control of Cells Adam. *Biomaterial* **1997**, *18* (24), 1573–1583. https://doi.org/10.1016/j.ijantimicag.2018.01.018.

(71) Liu, X.; Peter, X. M. Polymeric Scaffolds for Bone Tissue Engineering. *Biomed. Eng. Soc.* **2004**, *32* (3), 477–486. https://doi.org/10.1093/mutage/gex033.

(72) Hutmacher, D. W. Scaffold Design and Fabrication Technologies for Engineering Tissues - State of the Art and Future Perspectives. *J. Biomater. Sci. Polym. Ed.* **2001**, *12* (1), 107–124. https://doi.org/10.1163/156856201744489.

(73) Ramier, J.; Bouderlique, T.; Stoilova, O.; Manolova, N.; Rashkov, I.; Langlois, V.; Renard, E.; Albanese, P.; Grande, D. Biocomposite Scaffolds Based on Electrospun Poly(3-Hydroxybutyrate) Nanofibers and Electrosprayed Hydroxyapatite Nanoparticles for Bone Tissue Engineering Applications. *Mater. Sci. Eng. C* **2014**, *38* (1), 161–169. https://doi.org/10.1016/j.msec.2014.01.046.

(74) Kumbar, S. G.; Nukavarapu, S. P.; James, R.; Nair, L. S.; Laurencin, C. T. Electrospun Poly(Lactic Acid-Co-Glycolic Acid) Scaffolds for Skin Tissue Engineering. *Biomaterials* **2008**, *29* (30), 4100–4107. https://doi.org/10.1016/j.biomaterials.2008.06.028.

(75) Sundaramurthi, D.; Krishnan, U. M.; Sethuraman, S. Electrospun Nanofibers as Scaffolds for Skin Tissue Engineering. *Polym. Rev.* **2014**, *54* (2), 348–376. https://doi.org/10.1080/15583724.2014.881374.

(76) Hu, J.; Sun, X.; Ma, H.; Xie, C.; Chen, Y. E.; Ma, P. X. Porous Nanofibrous PLLA Scaffolds for Vascular Tissue Engineering. *Biomaterials* **2010**, *31* (31), 7971–7977. https://doi.org/10.1016/j.biomaterials.2010.07.028.

(77) Venugopal, J.; Zhang, Y. Z.; Ramakrishna, S. Fabrication of Modified and Functionalized Polycaprolactone Nanofibre Scaffolds for Vascular Tissue Engineering. *Nanotechnology* **2005**, *16* (10), 2138–2142. https://doi.org/10.1088/0957-4484/16/10/028.

(78) Seal, B. L.; Otero, T. C.; Panitch, A. Polymeric Biomaterials for Tissue and Organ Regeneration. *Mater. Sci. Eng. R Reports* **2001**, *34* (4–5), 147–230. https://doi.org/10.1016/S0927-796X(01)00035-3.

(79) Li, W. J.; Cooper, J. A.; Mauck, R. L.; Tuan, R. S. Fabrication and Characterization of Six Electrospun Poly(α-Hydroxy Ester)-Based Fibrous Scaffolds for Tissue Engineering Applications. *Acta Biomater.* **2006**, *2* (4), 377–385. https://doi.org/10.1016/j.actbio.2006.02.005.

(80) Aubert, J. H.; Clough, R. L. Low-Density, Microcellular Polystyrene Foams. *Polymer (Guildf).* **1985**, *26* (13), 2047–2054. https://doi.org/10.1016/0032-3861(85)90186-7.

(81) Mikos, A. G.; Thorsen, A. J.; Czerwonka, L. A.; Bao, Y.; Langer, R.; Winslow, D. N.; Vacanti, J. P. Preparation and Characterization of Poly(l-Lactic Acid) Foams. *Polymer (Guildf).* **1994**, *35* (5), 1068–1077. https://doi.org/10.1016/0032-3861(94)90953-9.

(82) Hou, Q.; Grijpma, D. W.; Feijen, J. Porous Polymeric Structures for Tissue Engineering Prepared by a Coagulation, Compression Moulding and Salt Leaching Technique. *Biomaterials* **2003**, *24* (11), 1937–1947. https://doi.org/10.1016/S0142-9612(02)00562-8.

(83) Schugens, C.; Maquet, V.; Grandfils, C.; Jerome, R.; Teyssie, P. Biodegradable and Macroporous Polylactide Implants for Cell Transplantation: 1. Preparation of Macroporous Polylactide Supports by Solid-Liquid Phase Separation. *Polymer (Guildf).* **1996**, *37* (6), 1027–1038. https://doi.org/10.1016/0032-3861(96)87287-9.

(84) Schugens, C.; Maquet, V.; Grandfils, C.; Jerome, R.; Teyssie, P. Polylactide Macroporous Biodegradable Implants for Cell Transplantation. II. Preparation of Polylactide Foams by Liquid-Liquid Phase Separation. *J. Biomed. Mater. Res.* **1996**, *30* (4), 449–461. https://doi.org/10.1002/(SICI)1097-4636(199604)30:4<449::AID-JBM3>3.0.CO;2-P.

(85) Nam, Y. S.; Yoon, J. J.; Park, T. G. A Novel Fabrication Method of Macroporous Biodegradable Polymer Scaffolds Using Gas Foaming Salt as a Porogen Additive. *J. Biomed. Mater. Res.* **2000**, *53* (1), 1–7. https://doi.org/10.1002/(SICI)1097-4636(2000)53:1<1::AID-JBM1>3.0.CO;2-R.

(86) Mooney, D. J.; Baldwin, D. F.; Suht, N. P.; Vacantis, J. P.; Larger, R. Novel Approach to Fabricate Porous Sponges of Poly (D, L-Lactic-Co-Glycolic Acid) without the Use of Organic Solvents.Pdf. *Biomaterials* **1996**, *17* (14), 1417–1422.

(87) Formhals. Process and Apparatus for Preparing Artificial Treads, 1934.

(88) Whitesides, G. M.; Grzybowski, B. Self-Assembly at All Scales. *Science (80-.).* **2002**, *295* (5564), 2418–2421. https://doi.org/10.1126/science.1070821.

(89) Sachs, E.; Cima, M.; Williams, P.; Brancazio, D.; Cornie, J. Three Dimensional Printing: Rapid Tooling and Prototypes Directly from a CAD Model. *J. Manuf. Sci. Eng. Trans. ASME* **1992**, *114* (4), 481–488. https://doi.org/10.1115/1.2900701.

(90) Bhattarai, S. R.; Bhattarai, N.; Yi, H. K.; Hwang, P. H.; Cha, D. Il; Kim, H. Y. Novel Biodegradable Electrospun Membrane: Scaffold for Tissue Engineering. *Biomaterials* **2004**, *25* (13), 2595–2602. https://doi.org/

10.1016/j.biomaterials.2003.09.043.

(91) Ma, Z.; Kotaki, M.; Inai, R.; Ramakrishna, S. Potential of Nanofiber Matrix as Tissue-Engineering Scaffolds. *Tissue Eng.* **2005**, *11* (1), 101–109. https://doi.org/10.1089/ten.2005.11.101.

(92) Cooley, J. F. Apparatus for Electrically Dispersing Fluids. *US Pat. 692,631* **1902**, *693* (631), 1–6. https://doi.org/10.1016/j.joen.2014.07.033.

(93) Reneker, D. H.; Chun, I. Nanometre Diameter Fibres of Polymer, Produced by Electrospinning. *Nanotechnology* **1996**, *7* (3), 216–223. https://doi.org/10.1088/0957-4484/7/3/009.

(94) Taylor, G.; A, P. R. S. L. Electrically Driven Jets. *Proc. R. Soc. London. A. Math. Phys. Sci.* **1969**, *313* (1515), 453–475. https://doi.org/10.1098/rspa.1969.0205.

(95) Zhou, F. L.; Gong, R. H.; Porat, I. Three-Jet Electrospinning Using a Flat Spinneret. *J. Mater. Sci.* **2009**, *44* (20), 5501–5508. https://doi.org/10.1007/s10853-009-3768-1.

(96) Rutledge, G. C.; Fridrikh, S. V. Formation of Fibers by Electrospinning. *Adv. Drug Deliv. Rev.* **2007**, *59* (14), 1384–1391. https://doi.org/10.1016/j.addr.2007.04.020.

(97) Theron, A.; Zussman, E.; Yarin, A. . Electrostatic Field-Assisted Alignment of Electrospun Nanofibre. *Nanotechnology* **2001**, *12* (3), 384–390. https://doi.org/10.1088/0957-4484/12/3/329.

(98) Kim, J. S.; Reneker, D. H. Polybenzimidazole Nanofiber Produced by Electrospinning. *Polym. Eng. Sci.* **1999**, *39* (5), 849–854. https://doi.org/10.1002/pen.11473.

(99) Hansen, S. G.; Taskin, M. B.; Chen, M.; Wogensen, L.; Vinge Nygaard, J.; Axelsen, S. M. Electrospun Nanofiber Mesh with Fibroblast Growth Factor and Stem Cells for Pelvic Floor Repair. *J. Biomed. Mater. Res. - Part B Appl. Biomater.* **2020**, *108* (1), 48–55. https://doi.org/10.1002/jbm.b.34364.

(100) Stachewicz, U.; Szewczyk, P. K.; Kruk, A.; Barber, A. H.; Czyrska-Filemonowicz, A. Pore Shape and Size Dependence on Cell Growth into Electrospun Fiber Scaffolds for Tissue Engineering: 2D and 3D Analyses Using SEM and FIB-SEM Tomography. *Mater. Sci. Eng. C* **2019**, *95*, 397–408. https://doi.org/10.1016/j.msec.2017.08.076.

(101) Chung, H. J.; Park, T. G. Surface Engineered and Drug Releasing Pre-Fabricated Scaffolds for Tissue Engineering. *Adv. Drug Deliv. Rev.* **2007**, *59* (4–5), 249–262. https://doi.org/10.1016/j.addr.2007.03.015.

(102) Haider, A.; Haider, S.; Kang, I. K. A Comprehensive Review Summarizing the Effect of Electrospinning Parameters and Potential Applications of Nanofibers in Biomedical and Biotechnology. *Arab. J. Chem.* **2018**, *11* (8), 1165–1188. https://doi.org/10.1016/j.arabjc.2015.11.015.

(103) Chen, Z.; Mo, X.; Qing, F. Electrospinning of Collagen-Chitosan Complex. *Mater. Lett.* **2007**, *61* (16), 3490–3494. https://doi.org/10.1016/j.matlet.2006.11.104.

(104) Zhang, Y.; Venugopal, J. R.; El-Turki, A.; Ramakrishna, S.; Su, B.; Lim, C. T. Electrospun Biomimetic Nanocomposite Nanofibers of Hydroxyapatite/Chitosan for Bone Tissue Engineering. *Biomaterials* **2008**, *29* (32), 4314–4322. https://doi.org/10.1016/j.biomaterials.2008.07.038.

(105) Huang, Z. M.; Zhang, Y. Z.; Ramakrishna, S.; Lim, C. T. Electrospinning and Mechanical Characterization of Gelatin Nanofibers. *Polymer (Guildf).* **2004**, *45* (15), 5361–5368. https://doi.org/10.1016/j.polymer.2004.04.005.

(106) Kim, S. H.; Nam, Y. S.; Lee, T. S.; Park, W. H. Silk Fibroin Nanofiber. Electrospinning, Properties, and Structure. *Polym. J.* **2003**, *35* (2), 185–190. https://doi.org/10.1295/polymj.35.185.

(107) Williams, D. P.; Guo, K.; Rizk, S.; Williams, S. F. Ultrafine Electrospun Fibers of Poly-4-Hydroxybutyrate and Copolymers Therof, 2019.

(108) Jaworska, J.; Włodarczyk, J.; Karpeta-Jarząbek, P.; Janeczek, H.; Stojko, M.; Kasperczyk, J. Electrospun, Drug-Enriched Bioresorbable Nonwovens Based on Poly(Glycolide-ε-Caprolactone) and Poly(D,L-Lactide-Glycolide) for Urological Applications. *Polym. Degrad. Stab.* **2019**, *167*, 94–101. https://doi.org/10.1016/j.polymdegradstab.2019.06.026.

(109) Blaker, J. J.; Nazhat, S. N.; Boccaccini, A. R. Development and Characterisation of Silver-Doped Bioactive Glass-Coated Sutures for Tissue Engineering and Wound Healing Applications. *Biomaterials* **2004**, *25* (7–8), 1319–1329. https://doi.org/10.1016/j.biomaterials.2003.08.007.

(110) Torres-Giner, S. Electrospun Nanofibers for Food Packaging Applications. *Multifunct. Nanoreinforced Polym. Food Packag.* **2011**, 108–125. https://doi.org/10.1533/9780857092786.1.108.

(111) Wang, X.; Li, Y.; Ding, B. Electrospun Nanofiber-Based Sensors. In *Electrospun Nanofibers for Energy and Environmental Applications*; Springer: Berlin, Heidelberg, 2014; pp 267–297. https://doi.org/10.1007/978-3-642-54160-5.

(112) Wang, N.; Mao, X.; Zhang, S.; Yu, J.; Ding, B. Electrospun Nanofibers for Air Filtration. In *Electrospun Nanofibers for Energy and Environmental Applications*; Springer: Berlin, Heidelberg, 2014; pp 299–323. https://doi.org/10.1007/978-3-642-54160-5.

(113) Wang, R.; Hsiao, B. S.; Chu, B. Electrospun Nanofibrous Membranes for Liquid Filtration. In *Electrospun Nanofibers for Energy and Environmental Applications*; Springer: Berlin, Heidelberg, 2014; pp 325–354. https://doi.org/10.1007/978-3-642-54160-5.

(114) Raza, A.; Ge, J.; Si, Y.; Yu, J.; Sun, G.; Ding, B. Applications of Electrospun Nanofibers in Oil Spill Cleanup. In *Electrospun Nanofibers for Energy and Environmental Applications*; Springer: Berlin, Heidelberg, 2014; pp 433–447. https://doi.org/10.1007/978-3-642-54160-5.

(115) Raza, A.; Li, Y.; Sheng, J.; Yu, J.; Ding, B. Protective Clothing Based on Electrospun Nanofibrous Membranes. In *Electrospun Nanofibers for Energy and Environmental Applications*; Springer: Berlin, Heidelberg, 2014; pp

355–369. https://doi.org/10.1007/978-3-642-54160-5.
(116) Hu, X.; Liu, S.; Zhou, G.; Huang, Y.; Xie, Z.; Jing, X. Electrospinning of Polymeric Nanofibers for Drug Delivery Applications. *J. Control. Release* **2014**, *185*, 12–21. https://doi.org/10.1016/j.jconrel.2014.04.018.
(117) Abrigo, M.; Kingshott, P.; McArthur, S. L. Electrospun Polystyrene Fiber Diameter Influencing Bacterial Attachment, Proliferation, and Growth. *ACS Appl. Mater. Interfaces* **2015**, *7* (14), 7644–7652. https://doi.org/10.1021/acsami.5b00453.

(118) Singer, A. J.; Clark, R. A. F. Cutaneous Wound Healing. *N. Engl. J. Med.* **1999**, *341* (10), 738–746.
(119) Guo, S.; DiPietro, L. A. Critical Review in Oral Biology & Medicine: Factors Affecting Wound Healing. *J. Dent. Res.* **2010**, *89* (3), 219–229. https://doi.org/10.1177/0022034509359125.
(120) Steed, D. L. The Role of Growth Factors in Wound Healing. *Surg. Clin. North Am.* **1997**, *77* (3), 575–586.
(121) Krishna, C.; Pillai, S.; Sharma, C. P. Review Paper: Absorbable Polymeric Surgical Sutures: Chemistry, Production, Properties, Biodegradability, and Performance. *J. Biomater. Appl.* **2010**, *25* (4), 291–366. https://doi.org/10.1177/0885328210384890.
(122) Gfroerer, S.; Baumann, P.; Schwalbach, A. K.; Smirnoff, A. Prospective International Multicenter Observational Study of Novosyn® Quick for Skin Closures in Adults and Children (SKINNOQ). *BMC Surg.* **2019**, *19* (1), 1–9. https://doi.org/10.1186/s12893-019-0506-8.
(123) Rivera, R. F.; Fagan, M. *Laceration Repair*; Elsevier Inc., 2017. https://doi.org/10.1016/B978-0-323-46215-0.00044-6.
(124) Kamer, F. M.; Joseph, J. H. Histoacryl: Its Use in Aesthetic Facial Plastic Surgery. *Arch. Otolaryngol. Neck Surg.* **1989**, *115* (2), 193–197. https://doi.org/10.1001/archotol.1989.01860260067016.
(125) Gusman, D. N. *Suture Materials and Techniques*, Second Edi.; Elsevier Ltd, 2012. https://doi.org/10.1016/B978-0-7020-3136-6.00009-6.
(126) Baylón, K.; Rodríguez-Camarillo, P.; Elías-Zúñiga, A.; Díaz-Elizondo, J. A.; Gilkerson, R.; Lozano, K. Past, Present and Future of Surgical Meshes: A Review. *Membranes (Basel).* **2017**, *7* (3), 1–23. https://doi.org/10.3390/membranes7030047.
(127) Paajanen, H. A Single-Surgeon Randomized Trial Comparing Three Composite Meshes on Chronic Pain after Lichtenstein Hernia Repair in Local Anesthesia. *Hernia* **2007**, *11* (4), 335–339. https://doi.org/10.1007/s10029-007-0236-1.
(128) Chu, C. C.; Von Fraunhofer, J. A.; Greisler, H. P. *Wound Closure Biomaterials and Devices*; CRC Press, 1997.
(129) Somerville, N. Ethicon Wound Closure Manual. *J Ethicon* **1994**.
(130) Bartholomew, R. S. PDS (Polydioxanone Suture): A New Synthetic Absorbale Suture in Cataract Surgery. A Preliminary Study. *Ophthalmologica* **1981**, *2* (183), 81–85. https://doi.org/10.1159/000309144.

(131) Dennis, C.; Sethu, S.; Nayak, S.; Mohan, L.; Morsi, Y.; Manivasagam, G. Suture Materials - Current and Emerging Trends. *J. Biomed. Mater. Res. - Part A* **2016**, *104* (6), 1544–1559. https://doi.org/10.1002/jbm.a.35683.
(132) Trott, A. T. Instruments, Suture Materials, and Closure Choices. In *Wounds and Lacerations*; 2012; pp 82–94. https://doi.org/10.1016/b978-0-323-07418-6.00008-3.
(133) Bennett, R. G.; Angeles, M. D. L. Selection of Wound Closure Materials. *J. Am. Acad. Dermatol.* **1988**, *18*, 619–637. https://doi.org/10.1016/s0190-9622(88)70083-3.
(134) Rodeheaver, G. .; Nesbit, W. S.; Edlich, R. F. Novafil. A Dynamic Suture for Wound Closure. *Ann. Surg.* **1986**, *204* (2), 193–199.
(135) Listner, G. J.; Park, K. Polypropylene Monofilament Sutures. 3,630,205, 1971.
(136) Hochberg, J.; Meyer, K. M.; Marion, M. D. Suture Choice and Other Methods of Skin Closure. *Surg. Clin. North Am.* **2009**, *89* (3), 627–641. https://doi.org/10.1016/j.suc.2009.03.001.
(137) Harloff, J. *Application of Polymers for Surgical Sutures*; 1995.
(138) Amass, W.; Amass, A.; Tighe, B. A Review of Biodegradable Polymers: Uses, Current Developments in the Synthesis and Characterization of Biodegradable Polyesters, Blends of Biodegradable Polymers and Recent Advances in Biodegradation Studies. *Polym. Int.* **1998**, *47* (2), 89–144. https://doi.org/10.1002/(SICI)1097-0126(1998100)47:2<89::AID-PI86>3.0.CO;2-F.
(139) Burg, K. *Poly(a-Ester)S*, 1st ed.; Elsevier Inc., 2014. https://doi.org/10.1016/B978-0-12-396983-5.00006-5.
(140) Domb, A. J.; Khan, W. *Biodegradable Polymers. Polymeric Biomaterials: Structure and Function*, third.; Popa, V., Ed.; CRC Press, 2013.
(141) Maurus, P. B.; Kaeding, C. C. Bioabsorbable Implant Material Review. *Oper. Tech. Sports Med.* **2004**, *12* (3), 158–160. https://doi.org/10.1053/j.otsm.2004.07.015.
(142) Lee, S. H.; Kim, B. S.; Kim, S. H.; Choi, S. W.; Jeong, S. I.; Kwon, I. K.; Kang, S. W.; Nikolovski, J.; Mooney, D. J.; Han, Y. K.; et al. Elastic Biodegradable Poly(Glycolide-Co-Caprolactone) Scaffold for Tissue Engineering. *J. Biomed. Mater. Res. - Part A* **2003**, *66* (1), 29–37. https://doi.org/10.1002/jbm.a.10497.
(143) Zong, X.; Ran, S.; Kim, K. S.; Fang, D.; Hsiao, B. S.; Chu, B. Structure and Morphology Changes during in Vitro Degradation of Electrospun Poly(Glycolide-Co-Lactide) Nanofiber Membrane. *Biomacromolecules* **2003**, *4* (2), 416–423. https://doi.org/10.1021/bm025717o.
(144) Noorsal, K.; Mantle, M. D.; Gladden, L. F.; Cameron, R. E. Degradation and Drug-Release Studies of a Poly(Glycolide-Co-Trimethylene Carbonate) Copolymer (Maxon). *J. Appl. Polym. Sci.* **2005**, *95* (3), 475–486. https://doi.org/10.1002/app.21108.
(145) Heimann, P.; Solhaug, J. H. Dexon--a New Absorbable, Synthetic Suture Material for General Surgical Use. *J. Nor. Med. Assoc.* **1974**.
(146) D.Sutures. Petcryl https://www.dolphinsutures.com/pga-sutures.

(147) B.Braun. Safil https://www.bbraun.com/en/products/b0/safil.html.
(148) Patlolla, A.; Collins, G.; Livingston Arinzeh, T. Solvent-Dependent Properties of Electrospun Fibrous Composites for Bone Tissue Regeneration. *Acta Biomater.* **2010**, *6* (1), 90–101. https://doi.org/10.1016/j.actbio.2009.07.028.
(149) Keridou, I.; Franco, L.; Turon, P.; del Valle, L. J.; Puiggalí, J. Scaffolds with Tunable Properties Constituted by Electrospun Nanofibers of Polyglycolide and Poly(ε-Caprolactone). *Macromol. Mater. Eng.* **2018**, *303* (7), 1–14. https://doi.org/10.1002/mame.201800100.
(150) Gunatillake, P.; Mayadunne, R.; Adhikari, R. *Recent Developments in Biodegradable Synthetic Polymers*; 2006; Vol. 12. https://doi.org/10.1016/S1387-2656(06)12009-8.
(151) Can, E.; Udenir, G.; Kanneci, A. I.; Kose, G.; Bucak, S. Investigation of PLLA/PCL Blends and Paclitaxel Release Profiles. *AAPS PharmSciTech* **2011**, *12* (4), 1442–1453. https://doi.org/10.1208/s12249-011-9714-y.
(152) Lebourg, M.; Antón, J. S.; Ribelles, J. L. G. Porous Membranes of PLLA-PCL Blend for Tissue Engineering Applications. *Eur. Polym. J.* **2008**, *44* (7), 2207–2218. https://doi.org/10.1016/j.eurpolymj.2008.04.033.
(153) Aghdam, R. M.; Najarian, S.; Shakhesi, S.; Khanlari, S.; Shaabani, K.; Sharifi, S. Investigating the Effect of PGA on Physical and Mechanical Properties of Electrospun PCL/PGA Blend Nanofibers. *J. Appl. Polym. Sci.* **2011**, *124*, 123–131. https://doi.org/10.1002/app.
(154) Can, E.; Bucak, S.; Kinaci, E.; Çalikoğlu, A. C.; Köse, G. T. Polybutylene Succinate (PBS) - Polycaprolactone (PCL) Blends Compatibilized with Poly(Ethylene Oxide)-Block-Poly(Propylene Oxide)-Block-Poly(Ethylene Oxide) (PEO-PPO-PEO) Copolymer for Biomaterial Applications. *Polym. - Plast. Technol. Eng.* **2014**, *53* (11), 1178–1193. https://doi.org/10.1080/03602559.2014.886119.
(155) Oberhoffner, S.; Planck, I. H. Triblock Terpolymer, Its Use for Surgical Suture Material and Process for Its Production. 6,048,947, 2000.
(156) Bezwada, R. S.; Jamiolkowski, D. D.; Lee, I.-Y.; Agarwal, V.; Persivale, J.; Trenka-Benthin, S.; Emeta, M.; Suryadevara, J.; Yang, A.; Liu, S. Monocryl@ Suture, a New Ultra-Pliable Absorbable Monofilament Suture. *Klio* **1995**, *16* (15), 1141–1148. https://doi.org/10.1524/klio.2008.0002.
(157) Chu, C. C. *Materials for Absorbable and Nonabsorbable Surgical Sutures*; Woodhead Publishing Limited, 2013. https://doi.org/10.1533/9780857095602.2.275.
(158) Pineros-Fernandez, A.; Drake, D. B.; Rodeheaver, P. A.; Moody, D. L.; Edlich, R.; Rodeheaver, G. T. CAPROSYN*, Another Major Advance in Synthetic Monofilament Absorbable Suture. *Long-Term Eff. Med. Implant.* **2004**, *14* (5).
(159) Avérous, L. Synthesis, Properties, Environmental and Biomedical Applications of Polylactic Acid. *Handb. Biopolym. Biodegrad. Plast. Prop. Process. Appl.* **2013**, No. 2008, 171–188. https://doi.org/10.1016/B978-

1-4557-2834-3.00009-4.

(160) Lou, C. W.; Yao, C. H.; Chen, Y. S.; Hsieh, T. C.; Lin, J. H.; Hsing, W. H. Manufacturing and Properties of PLA Absorbable Surgical Suture. *Text. Res. J.* **2008**, *78* (11), 958–965. https://doi.org/10.1177/0040517507087856.

(161) Krishna, C.; Pillai, S.; Sharma, C. P. Review Paper: Absorbable Polymeric Surgical Sutures: Chemistry, Production, Properties, Biodegradability and Performance. *J. Biomater. Appl.* **2010**, *25*, 291–366. https://doi.org/10.1177/0885328210384890.

(162) Wang, Y.; Yin, J.; Chen, G. Q. Polyhydroxyalkanoates, Challenges and Opportunities. *Curr. Opin. Biotechnol.* **2014**, *30*, 59–65. https://doi.org/10.1016/j.copbio.2014.06.001.

(163) Jendrossek, D. Microbial Degradation of Polyesters: A Review on Extracellular Poly(Hydroxy Alkanoic Acid) Depolymerases. *Polym. Degrad. Stab.* **1998**, *59* (1–3), 317–325. https://doi.org/10.1016/s0141-3910(97)00190-0.

(164) Williams, S. F.; Martin, D. P.; Horowitz, D. M.; Peoples, O. P. PHA Applications: Addressing the Price Performance Issue I. Tissue Engineering. *Int. J. Biol. Macromol.* **1999**, *25*, 111–121. https://doi.org/10.1016/S0141-8130(99)00022-7.

(165) Chen, G. Q.; Wu, Q. The Application of Polyhydroxyalkanoates as Tissue Engineering Materials. *Biomaterials* **2005**, *26* (33), 6565–6578. https://doi.org/10.1016/j.biomaterials.2005.04.036.

(166) Nobes, G. A. R.; Marchessault, R. H. Polyhydroxyal Kanoates : Materials for Delivery Systems. **1998**, 167–177.

(167) Zhang, J.; Shishatskaya, E. I.; Volova, T. G.; da Silva, L. F.; Chen, G. Q. Polyhydroxyalkanoates (PHA) for Therapeutic Applications. *Mater. Sci. Eng. C* **2018**, *86*, 144–150. https://doi.org/10.1016/j.msec.2017.12.035.

(168) Valappil, S. P.; Misra, S. K.; Boccaccini, A.; Roy, I. Biomedical Applications of Polyhydroxyalkanoates, an Overview of Animal Testing and in Vivo Responses. *Expert Rev. Med. Devices* **2006**, *3* (6), 853–868. https://doi.org/10.1586/17434440.3.6.853.

(169) Holmes PA. Application of PHB: A Microbially Produced Biodegradable Thermoplastic. *Phys. Technol.* **1985**, *32* (16), 32–36.

(170) Asrar, J.; Gruys, K. J. Biodegradable Polymer (Biopol®). **2005**.

(171) Odermatt, E. K.; Funk, L.; Bargon, R.; Martin, D. P.; Rizk, S.; Williams, S. F. MonoMax Suture: A New Long-Term Absorbable Monofilament Suture Made from Poly-4-Hydroxybutyrate. *Int. J. Polym. Sci.* **2012**, *2012*, 1–12. https://doi.org/10.1155/2012/216137.

(172) Foster, L. J. R.; Sanguanchaipaiwong, V.; Gabelish, C. L.; Hook, J.; Stenzel, M. A Natural-Synthetic Hybrid Copolymer of Polyhydroxy octanoate-Diethylene Glycol: Biosynthesis and Properties. *Polymer (Guildf).* **2005**, *46* (17), 6587–6594. https://doi.org/10.1016/j.polymer.2005.05.012.

(173) Martin, D. P.; Williams, S. F. Medical Applications of Poly-4-Hydroxybutyrate: A Strong Flexible Absorbable Biomaterial. *Biochem.*

Eng. J. **2003**, *16*, 97–105. https://doi.org/10.1016/S1369-703X(03)00040-8.

(174) Martin, D. P.; Williams, S. F. Medical Applications of Poly-4-Hydroxybutyrate: A Strong Flexible Absorbable Biomaterial. *Biochem. Eng. J.* **2003**, *16* (2), 97–105. https://doi.org/10.1016/S1369-703X(03)00040-8.

(175) Kunioka, M.; Kawaguchi, Y.; Doi, Y. Production of Biodegradable Copolyesters of 3-Hydroxybutyrate and 4-Hydroxybutyrate by Alcaligenes Eutrophus. *Appl. Microbiol. Biotechnol.* **1989**, *30* (6), 569–573. https://doi.org/10.1007/BF00255361.

(176) Nakamura, S.; Doi, Y. Microbial Synthesis and Characterization of Poly(3- Hydroxybutyrate-Co-4-Hydroxybutyrate. *Macromolecules* **1992**, *25* (17), 4237–4241.

(177) Sudesh, K.; Fukui, T.; Taguchi, K.; Iwata, T.; Doi, Y. Improved Production of Poly(4-Hydroxybutyrate) by Comamonas Acidovorans and Its Freeze-Fracture Morphology. *Int. J. Biol. Macromol.* **1999**, *25* (1–3), 79–85. https://doi.org/10.1016/S0141-8130(99)00018-5.

(178) Choi, M. H.; Yoon, S. C.; Lenz, R. W. Production of Poly(3-Hydroxybutyric Acid-Co-4-Hydroxybutyric Acid) and Poly(4-Hydroxybutyric Acid) without Subsequent Degradation by Hydrogenophaga Pseudoflava. *Appl. Environ. Microbiol.* **1999**, *65* (4), 1570–1577. https://doi.org/10.1128/aem.65.4.1570-1577.1999.

(179) Le Meur, S.; Zinn, M.; Egli, T.; Thöny-Meyer, L.; Ren, Q. Improved Productivity of Poly (4-Hydroxybutyrate) (P4HB) in Recombinant Escherichia Coli Using Glycerol as the Growth Substrate with Fed-Batch Culture. *Microb. Cell Fact.* **2014**, *13*, 131. https://doi.org/10.1186/s12934-014-0131-2.

(180) Chen, G.-Q.; Shi, Z.-Y.; Jiang, W.-J.; Zhou, X.-Y.; Yuan, X.-X.; Wu, L.-P.; Chen, J.-C.; Meng, D.-C. Hyperproduction of Poly(4-Hydroxybutyrate) from Glucose by Recombinant Escherichia Coli. *Microb. Cell Fact.* **2012**, *11* (1), 54. https://doi.org/10.1186/1475-2859-11-54.

(181) Le Meur, S.; Zinn, M.; Egli, T.; Thöny-Meyer, L.; Ren, Q. Poly(4-Hydroxybutyrate) (P4HB) Production in Recombinant Escherichia Coli: P4HB Synthesis Is Uncoupled with Cell Growth. *Microb. Cell Fact.* **2013**, *12*, 1–11. https://doi.org/10.1186/1475-2859-12-123.

(182) Williams, S. F.; Rizk, S.; Martin, D. P. Poly-4-Hydroxybutyrate (P4HB): A New Generation of Resorbable Medical Devices for Tissue Repair and Regeneration. *Biomed. Eng. (NY).* **2013**, *58* (5), 439–452. https://doi.org/10.1515/bmt-2013-0009.

(183) Tornier, announces launch of BioFiber® Surgical Mesh for tendon repair at arthroscopic surgery conference https://www.businesswire.com/news/home/20110414005940/en/Tornier-Announces-Launch-BioFiber®-Surgical-Mesh-Tendon (accessed Jul 2, 2020).

(184) Martin, D. P.; Badhwar, A.; Shah, D. V.; Rizk, S.; Eldridge, S. N.; Gagne, D. H.; Ganatra, A.; Darois, R. E.; Williams, S. F.; Tai, H. C.; et al.

Characterization of Poly-4-Hydroxybutyrate Mesh for Hernia Repair Applications. *J. Surg. Res.* **2013**, *184* (2), 766–773. https://doi.org/10.1016/j.jss.2013.03.044.

(185) Levy, A. S.; Bogue, J. T.; Morrison, K. A.; Lieberman, M. D.; Pomp, A.; Spector, J. A. P4HB : The Ideal Mesh for Complex Abdominal Wall Reconstruction ? *PRS Glob. Open* **2016**, 116–116.

(186) Williams, S. F.; Martin, D. P.; Moses, A. C. The History of GalaFLEX P4HB Scaffold. *Aesthetic Surg. J.* **2016**, *36*, S33–S42. https://doi.org/10.1093/asj/sjw141.

2. OBJECTIVES

2. OBJECTIVES

Part of this work has been executed under the collaborative research project established between the PSEP (Synthetic polymers: Structure and properties. Biodegradable polymers) group of the Polytechnic University of Catalonia and B. Braun Surgical S.A.U. (Center of Excellence for Closure Technologies) with specific biomedical applications by evolving and investigating polymeric systems.

The main goal of this work corresponds to the study of poly-4-hydroxybutyrate (P4HB) (commercially marketed as MonoMax® and TephaFLEX, by B. Braun Surgical S.A.U. and Tepha, respectively) as well as blends of related polyesters such as polyglycolide (PGA), poly (ε-caprolactone) (PCL) and polylactide (PLA).

Up to now, P4HB has been scarcely studied, unlike the extensive information that exists on its analog polyester, P3HB, which is the most common polyhydroxyalkanoate. P4HB is a biopolymer currently used as a bioresorbable soft tissue reinforcement since its high elasticity makes it suitable for being used as wound closure in abdominal surgery.

Particularly, the main objectives of this work are:

Study of the physicochemical, thermal, and mechanical properties of P4HB carrying on a detailed crystallization study of P4HB and the determination of the corresponding kinetics by using both calorimetry and optical microscopy techniques. This feature is important because it enables the control of the material's crystallinity and its final properties during the processing of the material.

Study on the microstructure and crystalline morphology of annealed fibers, films, and electrospun nanofibers of P4HB. A complete study was performed by synchrotron radiation to analyze the different lamellar thickness and other related parameters.

Based on the interest as biomedical product, another specific objective will be the comprehension of the relationships between crystalline morphology and

degradability, by studying the effect of the hydrolytic degradation of annealed fibers and films of P4HB considering media of different pH values and temperatures and evaluation of the enzymatic degradation at physiological conditions using two different lipases: *Pseudomonas cepacia* and *Rhizopus oryzae*. Furthermore, evaluation of the polymer solution conditions, processing parameters, and optimal experimental set-up configurations to produce suitable P4HB scaffolds by electrospinning and comparison with the annealed fibers and melted film.

A second general objective will be the study of different scaffolds combining polymers used in the biomedical field. An assessment of production, characterization, and optimization of the processing conditions of PGA/PCL electrospun scaffolds with tuned properties, as well as the incorporation of different pharmacological agents to study its release and antibacterial activity.

A final objective is the development of reinforced polymeric blends of PLA/PA to obtain matrices with improved properties. Specifically, it is focused on the study of immiscible PLA/PA610 blends by using a PLA modified to improve its rheological properties and get a finer and more homogeneous PA microstructure to favor the interfacial adhesion. The aim is to focus on the evaluation of the potential nucleation effect of the confined PA domains on the crystallization of PLA by studying the morphological and crystallization behavior under dynamic and isothermal conditions. Moreover, to study the influence of the presence of melted PLA phase on the final crystalline structure of the PA. In summary, to investigate how effective is the disperse phase of semi-crystalline polyamide in promoting PLA crystallization.

3. CRYSTALLIZATION STUDIES OF THE POLY-4-HYDROXYBUTYRATE

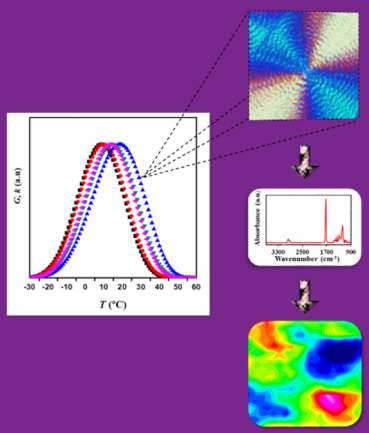

The present work deals with the study of crystallization, from the melt and the amorphous states, and the determination of the corresponding kinetics which is crucial to control the crystallinity of the material and its final properties during the processing.

Thermal properties and crystallization kinetics of poly-4-hydroxybutyrate (P4HB) under both, isothermal and non-isothermal conditions have been studied by means of differential scanning calorimetry (DSC) and polarizing optical microscopy (POM). The polymer shows the typical complex melting behavior associated with different lamellar populations. Annealing processes had great repercussions on properties and the morphology of constitutive lamellae as verified by X-ray scattering data. The isothermal data corresponded to a limited region (i.e., 24–38 ºC and 37–49 ºC for DSC and POM observations, respectively) where the polymer crystallized according to a single regime. A wider temperature range could be covered by non-isothermal experiments. Negative and ringed spherulites were always obtained from both isothermal and non-isothermal crystallization of P4HB from the melt. Infrared microspectroscopy was applied to determine differences in the molecular orientation inside a specific ring according to the spherulite sectorization or between different rings along a determined spherulitic radius.

In the case of the isothermal study of P4HB, primary nucleation was increased during crystallization and when temperature decreased. Similar crystallization parameters were deduced from DSC and POM analyses (e.g., secondary nucleation parameters of 1.69×10^5 K^2 and 1.58×10^5 K^2, respectively). The effect of sporadic nucleation was therefore minimized in the experimental crystallization temperature range and a good proportionality between overall crystallization rate (k) and rate (G) was inferred. Similar bell-shaped curves were postulated to express the temperature dependence of both k and G rates, corresponding to the maximum of these curves close to a crystallization temperature of 14-15 ºC

DSC, Avrami, Ozawa, Mo, Cazé, and Friedman methodologies were applied to study the non-isothermal crystallization by means of DSC. The

isoconversional approach developed by Vyazovkin allowed also the determination of a secondary nucleation parameter of 2.10 × 10^5 K^2 and crystal growth rate

Similar values (i.e., 2.22 × 10^5 K^2 and 9 °C) were from non-isothermal Avrami parameters. The texture of spherulites was dependent on the crystallization temperature, and specifically, the interring spacing decreased with the decrease of the crystallization temperature (T_c). Synchrotron data indicated that the thickness of the constitutive lamellae varied with the cooling rate, being deduced as a lamellar insertion mechanism that became more relevant when the cooling rate increased. Analysis of the POM data gave secondary nucleation constant and a bell-shaped G-T_c dependence that was in relative agreement with DSC analysi

3.1 ISOTHERMAL CRYSTALLIZATION KINETICS OF POLY-4-HYDROXYBUTYRATE BIOMATERIAL BY MEANS OF DIFFERENTIAL CALORIMETRY AND POLARIZED OPTICAL MICROSCOPY

3.1.1 INTRODUCTION

Poly-4-hydroxybutyrate (P4HB) is a new generation biopolymer widely employed as a bioresorbable soft tissue reinforcement[1] due to its excellent mechanical and acceptable thermal properties, including high thermal stability.[2] Probably, the main drawback of P4HB is associated with its cost of production and purification, with chemical synthesis being discarded for large scale production.[3] P4HB is biosynthesized by a fermentation process (e.g., by means of recombinant *Escherichia coli* K12[1,4] and used by microorganisms as energy reserve material.

The main characteristic of P4HB is its high elasticity which contrasts with the high stiffness of the most employed reabsorbable devices: polyglycolide (PGA) and polylactide (PLA). P4HB can be employed directly as a suture or knitted into a scaffold. The high elasticity confers upon P4HB special advantages for being employed as abdominal wall closure material. In addition, P4HB has an interest in a wide range of biomedical applications, such as patching materials for treatments of congenital cardiovascular defects, heart valves, vascular grafts, and bulking agents[1]. The first commercial P4HB device was a bioresorbable suture launched in 2009 under the trademark of MonoMax® by B. Braun Surgical S.A.U.[5] Subsequently, P4HB was commercialized by Tornier as a soft scaffold for tendon repair (BioFiber®,[6]), it was also utilized in the production of P4HB meshes for hernia repair (Phasix®,[7]) and reconstructive surgeries (GalaFLEX®,[8,9]).

P4HB sutures are processed through melt spinning in the form of both monofilament and multifilament fibers, although injection molding, extrusion, and melt blowing have also been employed for other general applications. The

material is characterized by a moderate degradation rate (i.e., intermediate between polyglycolide and polylactide), neutral and biocompatible degradation products, rapid tissue in-growth, and low bacterial adherence. In vivo biocompatibility tests of P4HB are highly favorable since its hydrolysis yields 4-hydroxybutyric acid, which is a common metabolite in the human body[10]. Mechanical properties of P4HB are highly dependent not only on the degree of orientation,[8] but also on the molecular weight.[11] Specifically, tensile strength, Young modulus, and elongation at break can change from 50 MPa, 70 MPa, and 1000% to 800 MPa, 670 MPa, and 90%, respectively. Comparing to related aliphatic polyesters, like PGA (i.e., one methylene group unit) and PCL (i.e., five methylene group units) the mechanical properties of P4HB (three methylene group units) are different.[8,12,13] Thus, a correlation between the Young modulus and the elongation at break with the number of methylene groups cannot be found. Specifically, P4HB with an intermediate repeat unit length has the lowest modulus (i.e., typical values are 70 MPa, 6900 MPa, and 400 MPa for P4HB, PGA, and PCL, respectively) and the highest elongation (i.e., typical values are 1000%, <3% and 80% for P4HB, PGA, and PCL, respectively).[1]

P4HB is a semicrystalline polymer with a structure defined by an orthorhombic unit cell (a = 0.775 nm, b = 0.477 nm, and c (fiber axis) = 1.199 nm) containing two antiparallel chain segments, a $P2_12_12_1$ space group, and a slightly distorted all-trans conformation.[14,15] Molecular structure has been determined from X-ray diffraction patterns of annealed fibers[15,16] and electron diffraction patterns of solution crystallized lamellae.[15,16]

Enzymatic degradation studies have extensively been studied for poly-3-hydroxybutyric acid and their copolymers with other poly(hydroxyalkanoate)s, including P4HB.[17] Results pointed out that degradation rate was highly influenced by the degree of crystallinity but also the crystal morphology (mainly the lamellar thickness) played a fundamental role. Therefore, control of crystalline dimensions during processing has a significant role in the subsequent biomedical applications of such materials.

Degradation studies performed with oriented and disoriented P4HB revealed also great differences that were a consequence of the polymer morphology and the orientation of the sample. Thus, disoriented fibers showed a highly significant loss of tensile strength after only four weeks of implantation (residual strength close to 18%) while oriented fibers can retain a good performance for eight weeks, with the in vivo strength retention being close to 50% after 12 weeks.[8] Materials were degraded by surface erosion as revealed by inspecting the morphology and the scarce variation of the molecular weight of the remaining fiber fragments. Enzymatic degradation of lamellar crystals has also been evaluated[16] and we observed that lipase from *Pseudomonas sp.* and PHB depolymerase from *Pseudomonas stutzari* degraded single lamellae from the crystal edges rather than the chain-folded surfaces.

The studies performed with P4HB are mainly concerned with its applications and are limited to those involved in the physical characterization. This fact is not logical considering the above indicated peculiar mechanical behavior and the great variability of properties according to the processing conditions. The present work tries to delve into fundamental questions underling as the study of crystallization, from the melt and the amorphous states, and the determination of the corresponding kinetics. This aspect is crucial to be able to control the crystallinity of the material and its final properties during the processing. To the best of our knowledge and surprise, no concrete study covering this aspect has currently been performed with P4HB.

3.1.2 MATERIALS AND METHODS

Commercially available sutures of P4HB (MonoMax®, USP 1) were kindly supplied by B. Braun Surgical S.A.U. The weight and number average molecular weights of MonoMax® samples were 215,000 and 68,000 g/mol, as determined by size exclusion chromatography (GPC).

Molecular weight was estimated by size exclusion chromatography (GPC) using a liquid chromatograph (Shimadzu, model LC-8A Tokyo, Japan)

equipped with an Empower computer program (Waters). A PL HFIP gel column (Polymer Lab, Agilent Technologies Deutschland GmbH, Böblingen, Germany) and a refractive index detector (Shimadzu RID-10A, Tokyo, Japan) were employed. The polymer was dissolved and eluted in 1,1,1,3,3,3-hexafluoroisopropanol (HFIP) containing CF_3COONa (0.05 M) at a flow rate of 0.5 mL/min (injected volume 100 μL, sample concentration 2.0 mg/mL). The number and weight average molecular weights were calculated using polymethyl methacrylate standards.

Calorimetric data were obtained by differential scanning calorimetry with a TA Instruments Q100 series equipped with a refrigerated cooling system (RCS) operating at temperatures from −50 °C to 150 °C. Calibration was performed with indium. Experiments were conducted under a flow of dry nitrogen with a sample weight of approximately 5 mg. Basic thermal characterization was performed following a four-run protocol consisting of a heating run (10 °C/min) a cooling run (10 °C/min) after keeping the sample in the melt state for one minute, a subsequent heating run (10 °C/min) of the melt crystallized sample and finally a heating run (10 °C/min) of a sample cooled at the maximum rate allowed by the equipment.

For the study of isothermal crystallization from the melt state, the sample was heated up to 100 °C (i.e., around 30 °C above the melting peak) at a heating rate of 10 °C/min. The sample was held for 5 min at 100 °C to erase sample history and subsequently cooled at a rate of 50 °C/min to the selected isothermal temperature where it was kept until baseline was attained. For cold crystallization experiments, samples were firstly quenched from the melt state and then heated to the selected isothermal temperature.

The spherulitic growth rate was determined by optical microscopy using a Zeiss Axioskop 40 Pol light polarizing microscope (Carl Zeiss, Göttingen, Germany) equipped with a Linkam temperature control system configured by a THMS 600 heating and freezing stage connected to an LNP 94 liquid nitrogen cooling system. Spherulites were grown from homogeneous thin films prepared by evaporation of dilute solutions of the polymer in HFIP (0.1 g/mL). The

films were dried in a vacuum until a constant weight was achieved. Small sections of these films were pressed or smeared between two cover slides to get thicknesses close to 10 μm. Subsequently, the samples were inserted into the hot stage and kept at 100 °C for 5 min to eliminate sample history effects. Crystallization from the melt was evaluated after a fast cooling to the selected crystallization temperature. The spherulitic growth rate was determined by optical microscopy taking images with a Zeiss AxioCam MRC5 digital camera (Carl Zeiss, Göttingen, Germany) every five min. The plot of the measured spherulite radius versus time allows deducing the growth rate at each selected temperature from the corresponding slope. A first-order red tint plate was employed to determine the sign of spherulitic birefringence under crossed polarizers.

Wide-angle X-ray diffraction (WAXD) and Small-angle X-ray scattering (SAXS) data were obtained at the NCD beamline (BL11) of the ALBA synchrotron facility (Cerdanyola del Vallès, Barcelona, Spain), by using a wavelength of 0.100 nm. A WAXD LX255-HS detector from Rayonix and an ImXPAD S1400 photon-counting detector were employed. Polymer samples were confined between Kapton films. WAXD and SAXS diffraction patterns were calibrated with Cr_2O_3 and silver behenate (AgBh), respectively. The correlation function and the corresponding parameters were calculated with the CORFUNC program for Fibre Diffraction/Non-Crystalline Diffraction provided by the Collaborative Computational Project 13. Deconvolution of WAXD peaks was performed using the PeakFit 4.0 program.

Synchrotron-based infrared microspectroscopy measurements (transmission mode) have been performed at the infrared beamline MIRAS of ALBA synchrotron using the Hyperion 3000 microscope coupled to Vertex 70 spectrometer (Bruker, Germany) at 4 cm^{-1} resolution with 256 co-added scans per spectrum. In this case, the spherulites were grown from films prepared directly over infrared transparent windows of CaF_2 of 13mm diameter and 0.5 thickness. All spectra were obtained using a single masking aperture size of 8 μm × 8 μm. In addition to the intrinsic quasi-linear light polarization of

synchrotron radiation, the synchrotron light was also polarized at 0° or 90° by a ZnSe holographic wire grid polarizer (Acal BFi Germany GmbH).

3.1.3 Results and Discussion

3.1.3.1 Thermal Properties of P4HB

The thermal behavior of commercial P4HB sutures is shown in **Figure 3.1.1**:

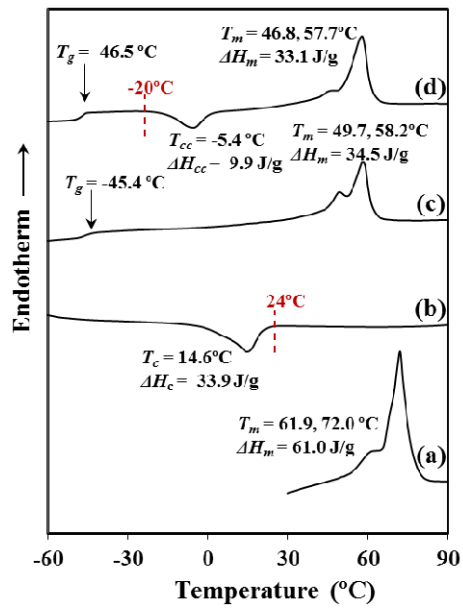

Figure 3.1.1. A sequence of calorimetric and heating runs performed with the initial commercial suture of poly-4-hydroxybutyrate (P4HB): (**a**) First heating run performed at 10 °C/min; (**b**) Cooling run at 10 °C/min after keeping the sample in the melt state for one min; (**c**) Heating run at 10 °C/min of the above melt crystallized samples and (**d**) Heating run at 10 °C/min of a sample quenched from the melt at the maximum rate allowed by the equipment.

The following points are noticeable:

1. P4HB shows a complex fusion that depends on the processing conditions. Specifically, the fusion of the processed suture is highly different from that determined from a melt crystallized (i.e., second heating run) and even a cold crystallized (i.e., third heating run corresponding to a melt quenched sample) sample. In all cases, a

double melting point can be observed, but a remarkable shift to higher temperatures is detected for the initial suture in comparison with the melted and cold crystallized samples. Note that the temperature of the maximum intensity peak increases from 58 °C to 72 °C and the temperature of the lower peak that moves from 47–50 °C to 62 °C. In summary, temperature increases by approximately 10 °C for both melting peaks. These peaks can be associated with a typical lamellar reordering process where thinner lamellae become thicker[18]. Note that P4HB does not exhibit polymorphism and consequently endothermic peaks associated with structural changes can be discarded.

2. Crystallization from both the melt and the glassy state (i.e., that attained by a fast cooling to temperatures lower than the glass transition temperature) is a complex process that requires a long time and a thermal annealing process to improve crystallinity. Note that the crystallization enthalpy determined for a slow cooling run (10 °C/min, **Figure 3.1.1**) from the melt state was around 57% of the melting enthalpy determined for the commercial annealed sample (i.e., 34.5 J/g with respect to 61 J/g). Nevertheless, a significant crystallization takes place even if the sample is quenched from the melt (i.e., (33.1–9.9) J/g was determined in the third heating run given in **Figure 3.1.1**, a value that corresponds to 38% of the maximum enthalpy).
3. Significant differences are observed between second and third heating runs. Amorphous content is logically higher for the fast crystallized sample as evidenced from the increase of C_p (i.e., 0.2718 J/g·°C with respect to 0.3233 J/g·°C) at the glass transition temperature (−46.5 °C). Calorimetric (DSC) traces indicate also a lower perfection of the thin lamellar crystals for the quenched sample since the lamellar reordering process was enhanced (i.e., a lower relative intensity for the low temperature melting peak is derived in this case).

4. Final crystallinities attained for samples crystallized from the melt and the glassy states become similar due to the cold crystallization process that only develops during heating in the second case.

The given results point out the great difficulty of P4HB to render a high crystallinity and also to develop perfect crystals. Probably, the high polymer molecular weight renders a high melt viscosity and a large number of chain entanglements. Logically, low chain mobility is expected and consequently, there is a great difficulty to both complete crystallization and the development of thick crystals with low defects during the final reordering process.

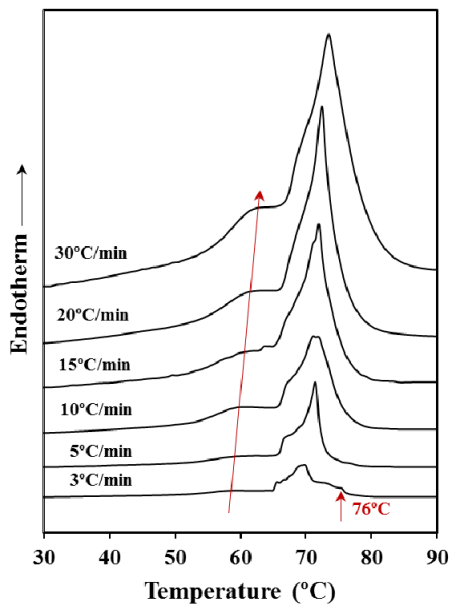

Figure 3.1.2. Calorimetric (DSC) heating runs performed at the indicated rates with the commercial P4HB (Poly-4-hydroxybutyrate) suture.

Figure 3.1.2 shows that the heating rate has a clear influence on the melting process even if the sample was previously annealed. Note the great difference in the melting process between samples heated at rates of 3 and 30 °C/min and the gradual change observed for intermediate rates. Thus, the low temperature melting peak gradually moved to the right (i.e., to a higher temperature) and increased its relative intensity with respect to the larger peak as the heating rate was increased. These features suggest a worse heat

transmission (i.e., the increase of the peak temperature) and a lower capacity suffer a reordering process during heating that leads to thicker lamellae with an increased melting point. More interestingly, the high-temperature peak appears split giving rise to multiple peaks when the heating rate was the lowest one (i.e., 3 °C/min). Specifically, it should be pointed out that a peak associated with highly reorganized lamellae appears clearly defined at a temperature close to 76 °C.

3.1.3.2 X-Ray Diffraction Analysis of P4HB

WAXD diffraction patterns of P4HB showed two predominant peaks at 0.406 and 0.388 nm (i.e., those corresponding to the (110) and (200) reflections of the reported orthorhombic structure) independently of the way as the polymer was prepared (**Figure 3.1.3a**). Nevertheless, some minor differences between the profiles of the original suture and the melt crystallized sample were found. These mainly corresponded to the broad amorphous halo centered at 0.421 nm that could only be observed in the profile of the melt crystallized sample. On the contrary, large differences were found in the SAXS profiles (**Figure 3.1.3b**) where peak values of 9.5 nm to 10.5 nm were determined for the melt crystallized film and the processed suture. These values demonstrated the large differences in the supramolecular order (i.e., lamellar morphology) that could be induced by the thermal treatment.

The diffraction peak of the melt crystallized film was less intense and broader indicating a worse contrast between the electronic densities corresponding to the amorphous lamellar surface and the crystalline lamellar core and even a large dispersity of the lamellar thickness.[19] Specific contributions of the crystalline lamellar core and the amorphous folding surfaces were determined through the γ (r) one-dimensional correlation function.[20]

$$\gamma(r) = \int_0^\infty q^2 I(q) \cos(qr) dq \Big/ \int_0^\infty q^2 I(q) dq \qquad (1)$$

where $I(q)$ is the intensity at each value of the q scattering vector (=[$4\pi/\lambda$] sin θ, with λ and θ being the wavelength and the Bragg angle, respectively).

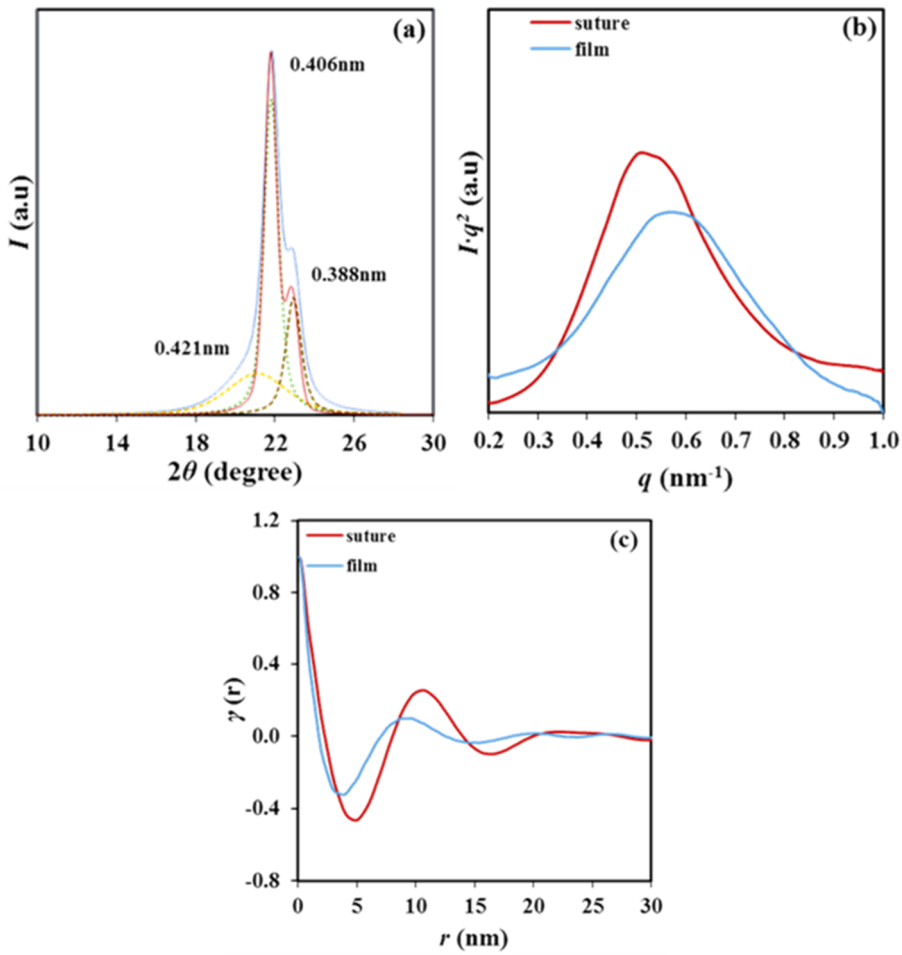

Figure 3.1.3. Wide-angle X-ray diffraction (WAXD) profiles (**a**); Small-angle X-ray scattering (SAXS) profiles (**b**) and correlation functions (**c**) of the initial commercial P4HB suture (red line) and a P4HB melt crystallized sample (blue line). Deconvoluted WAXD peaks are only indicated for the melt crystallized sample.

The correlation function (**Figure 3.1.3c**) showed better-defined peaks for the processed suture as a consequence of the higher contrast between electronic densities of crystalline and amorphous phases. Calculated values of the long period, L_p, the amorphous layer thickness, l_a and the crystalline lamellar thickness, l_c, indicated an increase of all parameters after the annealing process.

Specifically, changes from 8.8 nm to 10.5 nm, 1.7 nm to 2.6 nm, and 7.1 nm to 7.9 nm were determined for L_p, l_a, and l_c, respectively. Therefore, the crystalline region increased significantly and agreed with the increase of the melting temperature. At the same time, the dimension of the folding surface increased and became more disordered as deduced from its lower electron density (i.e., higher contrast). Changes are clarified by considering the crystallinity within the lamellar stacks (i.e., $\chi^{SAXS} = l_c/L_p$), which decreased from 80.6% to 75% after annealing as a consequence of the major impact caused by the disordered lamellar surface.

3.1.3.3 Equilibrium Melting Point of P4HB

Equilibrium melting temperature (T_m^0) is a crucial parameter to perform an analysis of the crystallization process and specifically to evaluate the nucleation capacity of the surface of growing crystals as well as the degree of supercooling ($T_m^0 - T_c$) at which crystallization is taking place. This temperature is associated with the theoretical fusion of crystals having an infinite thickness and can be estimated through the Hoffman-Weeks extrapolation.[21] This is a commonly accepted method due to its simplicity and straightforward experimental implementation. The method is based on **Equation (2)**, which was deduced from a combination of the well-known Gibbs-Thomson equation and secondary nucleation theory.[22] The equation indicates that the melting temperature, T_m, of a crystal varies with the temperature at which it was formed due to variation of the lamellar thickness. Specifically, the equation relates the melting and the crystallization temperature, T_c, through the equilibrium melting temperature and the thickening coefficient, γ, defined as the ratio between the thickness of the grown crystal, l_c, and the initial thickness of a "virgin lamella" l_g^*:

$$T_m = T_m^0 (1 - 1/\gamma) + T_c/\gamma \quad \textbf{(2)}$$

A straight line can be obtained by plotting T_m as a function of T_c, with the equilibrium temperature corresponding to the intersection of this line with the $T_m = T_c$ line. The validity of **Equation (2)** implies that lamellar crystals thicken

at a specific crystallization temperature, which also influences the thickening parameter.

Figure 3.1.4 shows the evolution of the melting peak of P4HB when it was crystallized at different temperatures. It is clear that the low temperature melting peak, which is associated with the initial melt of crystallized lamellae, shifted to higher temperatures with increasing crystallization temperature. On the contrary, the high temperature melting peak remains at a practically constant temperature since it corresponds to the fusion of reordered lamellae that are mainly formed during the heating process. Note also that at high crystallization temperatures the two melting peaks appear practically overlapped giving the false impression that the high-temperature peak moves to lower temperatures.

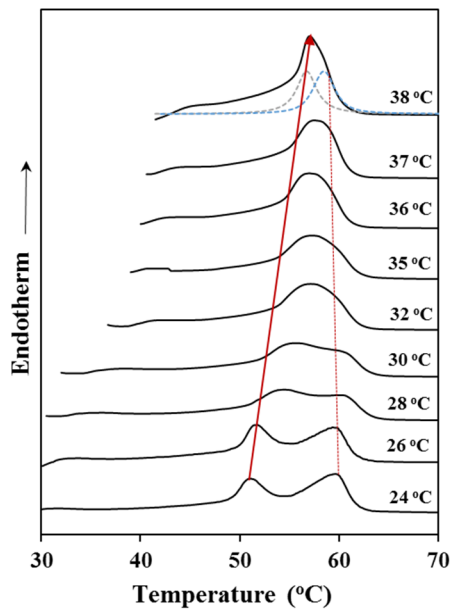

Figure 3.1.4. DSC heating runs of P4HB previously crystallized at the indicated temperatures.

Deconvolution of DSC profiles (as shown for the crystallization performed at 38 °C) allowed determining the peak temperatures used for the Hoffman-Weeks plot. In addition, the relative intensity of the former peak increased as the crystallization temperature did as a consequence of the greater stability of

the corresponding thin crystals (i.e., the lower capacity to undertake a lamellar reordering process).

Figure 3.1.5 shows the Hoffman-Weeks plot obtained from the temperature evolution of the former melting peak. The equilibrium melting temperature was 79.9 °C, a slightly higher value than the maximum peak temperature (76 °C) detected in the slow heating run of the commercial suture (**Figure 3.1.2**).

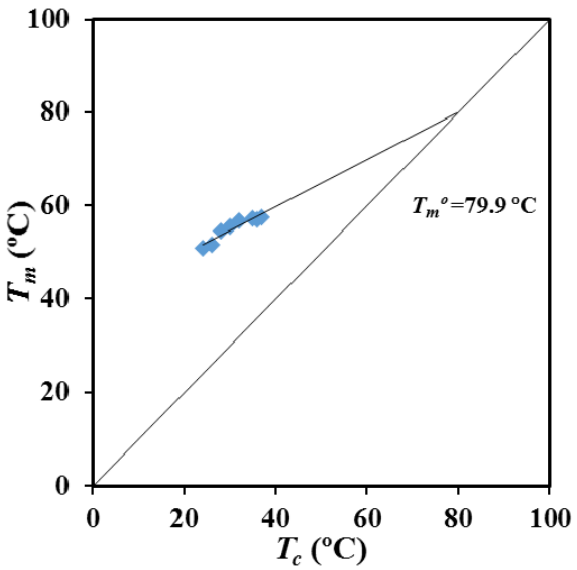

Figure 3.1.5. Hoffman-Weeks plot for P4HB considering the temperatures of its first melting peak.

3.1.3.4 Isothermal Crystallization Kinetics of P4HB Evaluated by Calorimetric Data

Kinetic crystallization analysis of P4HB was performed by cooling the samples from the melt state at selected isothermal temperatures and also by isothermal cold crystallization since in this case the polymer was not completely crystallized during the previous fast cooling from the melt. Note, however, that cold crystallization should proceed under constraints imposed by the great crystalline fraction developed during the cooling run.

Crystallization experiments from the melt state were successfully carried out in the narrow 24–38 °C temperature interval. Experimental problems

concerning the time required to get a complete crystallization limited the highest temperature, while the lowest one was selected to avoid any trace of crystallization before reaching this temperature. The DSC cooling run shown in **Figure 3.1.1** indicates the impossibility to start at temperatures lower than 24 °C. **Figure 3.1.6a** shows the variation of the DSC exothermic peaks with crystallization temperature. Logically, these peaks became narrower and shifted to lower times as the crystallization temperature decreased. Cold crystallization experiments were performed in the interval between −26 °C and −20 °C where peaks were still detectable (**Figure 3.1.6b**).

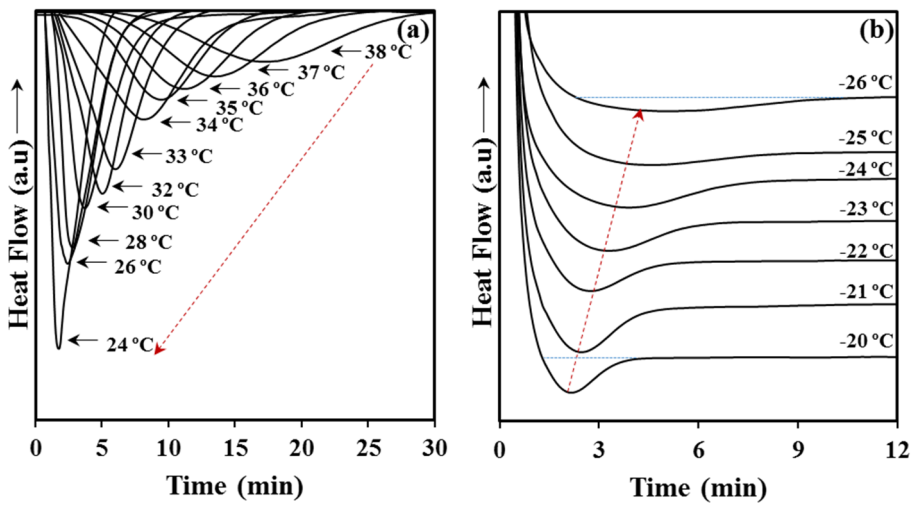

Figure 3.3.1.6. Exothermic DSC peaks corresponding to the isothermal crystallization from the melt state performed between 24 °C and 38 °C (**a**) and the cold crystallization performed between −26 °C and −20 °C (**b**).

Note that at lower temperatures the exothermic process required long times, where broad peaks were therefore derived, whereas at higher temperatures crystallization took place before reaching the selected temperature (see for example the temperature corresponding to the start of cold crystallization in **Figure 3.1.1d**).In general, cold crystallization exothermic peaks had low intensity as a consequence of the previous crystallization during quenching and the final reduced amorphous fraction in the sample. Peaks

broadened and shifted to higher times with the decrease of the selected crystallization temperature.

The time evolution of the relative degree of crystallinity, $\chi(t-t_0)$, was determined from the corresponding crystallization exotherms (**Figure 3.1.7**) through the ratio area: of the exotherm up to time $t - t_0$ divided by the total exotherm area, i.e.,

$$\chi(t - t_0) = \int_{t0}^{t} (dH / dt)dt \Big/ \int_{t0}^{\infty} (dH / dt)dt \qquad (3)$$

where dH/dt is the heat flow rate and t_0 the induction time. The development of crystallinity always showed a characteristic sigmoidal dependence on time, as plotted in **Figure 3.1.7a** and **3.1.7b** for melt and cold crystallization experiments, respectively.

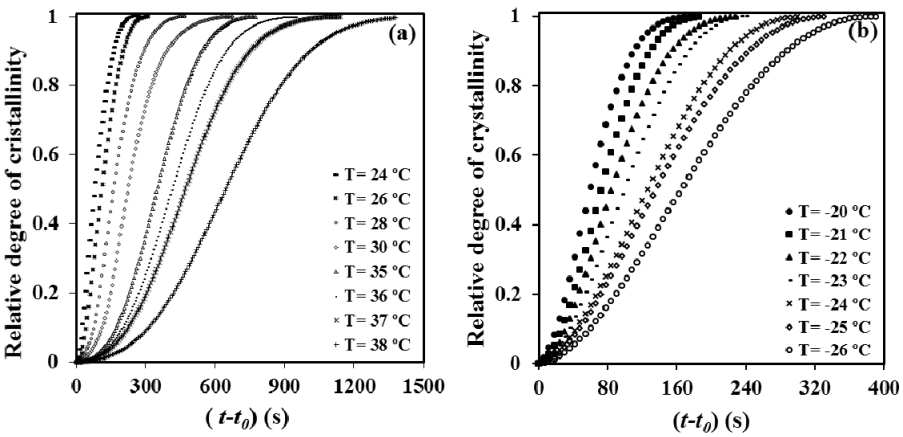

Figure 3.1.7. Evolution of the relative crystallinity over time for isothermal crystallization of P4HB at the indicated temperatures. (**a**) Samples coming from the melt state; (**b**) Glassy sample obtained from a fast cooling from the melt.

These data were analyzed assuming the well-known Avrami equation[23,24] for primary crystallization:

$$1 - (t-t_0) = \exp[-Z\,(t-t_0)^n] \qquad (4)$$

where Z is the temperature-dependent rate constant and n the Avrami exponent whose value varies according to the crystallization mechanism. A normalized

rate constant, $k = Z^{1/n}$, is usually evaluated for comparison purposes since its dimension ($time^{-1}$) is independent of the value of the Avrami exponent.

Table 3.1.1 summarizes the main kinetic parameters of the primary crystallization process from the melt state, as deduced from the plots of $\log\{-\ln[1 - \chi\ (t - t_0)]\}$ against $\log(t - t_0)$ (**Figure 3.8a**). The values of the Avrami exponent lay in a narrow range, from 2.35 to 2.62, with 2.56 being the average value. In general, the exponent increased with the crystallization temperature and suggests the occurrence at the higher temperatures of a predetermined (heterogeneous) nucleation with spherical growth under geometric constraints since the theoretical value should be equal to 3. Both sporadic (heterogeneous) and homogeneous nucleation can be discarded as a higher exponent, close to 4, should be derived. Furthermore, homogeneous nucleation usually requires high undercooling, which is not the case.

Table .3.1.1. Isothermal crystallization kinetic parameters deduced from calorimetric (DSC) experiments for poly-4-hydroxybutyrate (P4HB).

T_c (°C)	n	$Z \times 10^6$ (s^{-n})	$k \times 10^3$ (s^{-1})	$\tau_{1/2}$ (s)
−26	1.95	33.50	5.13	164
−25	1.97	40.18	5.94	130
−24	1.91	70.68	6.71	113
−23	1.94	99.20	8.58	95
−22	1.93	134.25	9.89	78
−21	1.95	167.69	11.61	71
−20	1.84	381.86	13.98	65
28	2.35	3.99	5.03	177
30	2.52	0.74	3.72	392
35	2.71	0.09	2.49	341
36	2.63	0.09	2.10	382
37	2.56	0.10	1.84	481
38	2.62	0.03	1.35	722

Table 3.1.1 shows also that rather constant exponents between 1.84 and 1.97 (mean value of 1.93) were determined from the Avrami analysis of the cold crystallization process (**Figure 3.1.8b**). In this case, as above explained, crystallization must take place under high constrictions due to the existence of a high ratio of P4HB crystallites produced during the previous cooling process. The value of the exponent became lower than that determined from melt

crystallizations and its temperature dependence did not follow any defined trend.

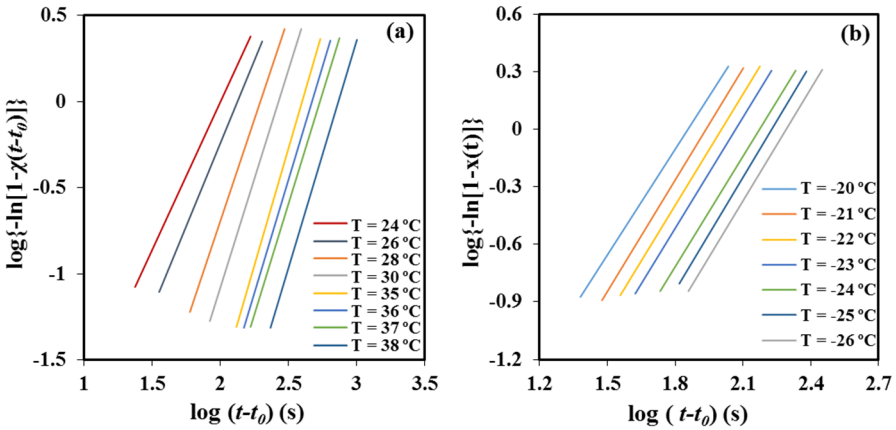

Figure 3.1.8. Avrami plots obtained from isothermal melt (**a**) and cold (**b**) crystallizations.

Z and *k* values evaluated from both kinds of crystallizations are also summarized in **Table 3.1.1**. Logically, the crystallization rate took the lowest values at the highest and the lowest assayed temperatures as a consequence of the restricted effective nucleation and the limited chain mobility, respectively. The maximum rate is expected between -20 °C and 24 °C considering a typical bell-shaped dependence with the temperature, as then will be explained. **Figure 3.1.9a** shows the variation of the overall crystallization rate with crystallization temperature. Melt crystallization data define the right side of the bell-shaped curve that is governed by the secondary nucleation process. Values of cold crystallization were not consistent with the typical representation since overall crystallization rates under the indicated constrictions were significantly higher than expected for normal growth.

The values of the corresponding reciprocal crystallization half-times ($1/\tau_{1/2}$), calculated as the inverse of the difference between crystallization start time (i.e., t_0) and the time required to achieve a relative crystallinity of 0.5, are also given in **Table 3.1.1**. This parameter is a direct indicator of the crystallization process, and therefore can be used to check the accuracy of

Avrami analysis by comparison with the theoretical kinetic value (i.e., $1/\tau_{1/2} = (Z/\ln 2)^{1/n}$). **Figure 3.1.9b** demonstrated also the validity of the Avrami analysis for melt and cold crystallization since the temperature evolution of the overall crystallization rate, k, was very similar to that found for the experimental crystallization data.

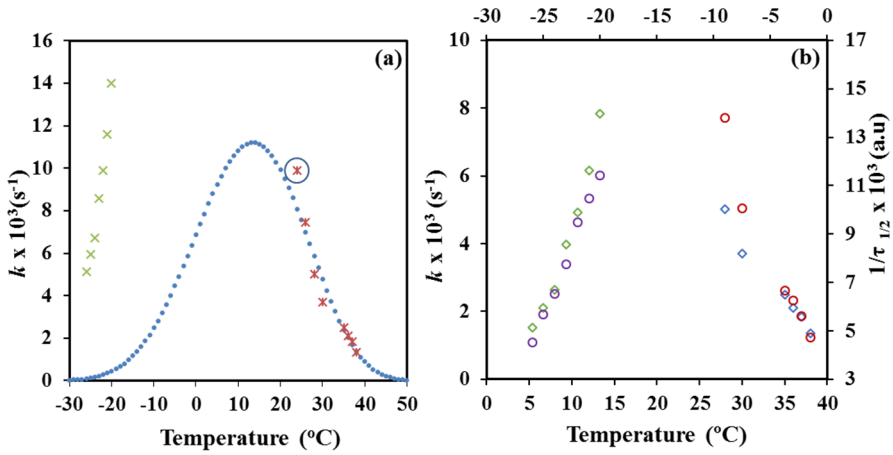

Figure 3.1.9. (**a**) Experimental (×) and simulated (●) temperature dependence of the overall crystallization rate of P4HB for isothermal melt crystallization. For the sake of completeness experimental cold crystallization data are also plotted (×); (**b**) Temperature dependence of the overall crystallization rates (◊, ◊) and the reciprocal crystallization half-times (o, o) of P4HB for melt and cold crystallizations.

3.1.3.5 Spherulitic Morphologies of P4HB

Crystallization of P4HB from the melt state rendered spherulitic morphologies with a banded texture (**Figure 3.1.10a**) at all assayed temperatures (i.e., between 36 °C and 49 °C). This kind of morphology is usually observed in the crystallization of different polymers and has merited different explanations based on the development of interlamellar screw dislocations,[25,26] the continuous twisting of lamellae,[27] the rhythmic growth derived from the presence of depletion zones in the growth front[28] and the presence of different polymorphic structures.[29] It has also been postulated that final morphology is a consequence of a balance between the diffusion rate (v_d) of the melted polymer and the crystallization rate (v_c).[30,31] These rates are defined by:

$$v_d = \mathrm{d}/\mathrm{d}t[6D(T_c)t]^{1/2} \quad (5)$$

$$v_c = G_0 \times \exp[-U^*/(R \times (T_c - T_\infty))] \times \exp[K_g/T_c\Delta T f] \quad (6)$$

Where D is the whole chain diffusion constant, T_c is the crystallization temperature, t is the whole diffusion time, G_0 is a preexponential factor, generally assumed to be constant, U^* is the transport activation energy, T_∞ is the temperature at which all motions are associated with viscous flow cease, f is a factor which corrects for variation in the heat of fusion with temperature below the equilibrium melt point and taken as $2T/(T_m^0 + T_\infty)$, ΔT is the supercooling degree, and K_g is the secondary nucleation parameter which is related to the growth regime. Banded morphologies are usually observed when v_d becomes lower than v_c.[30–32] Note that independently of a possible lamellar twisting, a slow diffusion rate together with the volume shrinkage during solidification should cause a depletion zone at the growth fronts. Therefore, ridge and valley topographic textures with different width should be derived, it is also indicated in the crystallization of the related poly(3-hydroxybutyrate) (P3HB)[31] that banding with highly zigzag irregularities is formed at the highest crystallization temperature range.

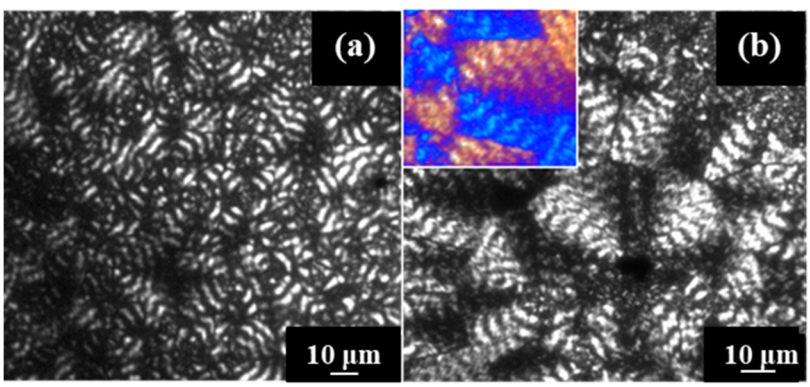

Figure 3.1.10. Optical micrographs showing P4HB spherulites crystallized at 36 °C (**a**) and 47 °C (**b**). The inset of (**b**) corresponds to a micrograph taken with a red tint plate to determine the spherulite sign.

The observed spherulitic morphologies revealed an increase of the zigzag irregularities of each band when the temperature was increased, as well as, the

differences between the width of birefringent and non-birefringent bands (i.e., the non-birefringent bands became narrower) (**Figure 3.1.10**). Spacing between bands was always close to 4–5 μm, a characteristic decrease with a temperature was not detected, probably as a consequence of the reduced temperature range at which spherulites were studied. Spherulites always showed a negative birefringence (inset of **Figure 3.1.10b**) characteristic of aliphatic polyesters.

3.1.3.6 Crystal Growth Rate and Primary Nucleation of P4HB

Kinetics of crystallization of P4HB from the melt state could be studied by optical microscopy but not for the glassy state since a high crystallinity was developed during the previous cooling run. The study of the development of spherulites was therefore precluded despite some cold crystallization taking place when samples were heated at the appropriate temperatures.

Figure 3.1.11 and optical micrographs given in **Figure 3.1.12** show the great change of the nucleation density for melt crystallization when the selected isothermal temperature was varied, even in the very narrow temperature interval at which experiments could be performed (i.e., between 36 °C and 49 °C).

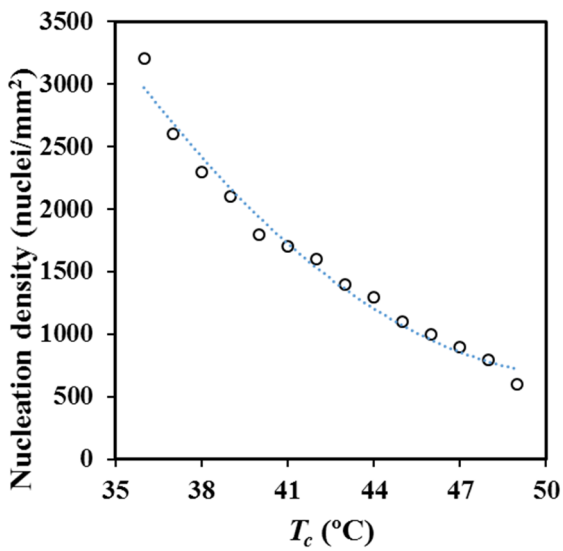

Figure 3.1.11. Temperature dependence of the primary nucleation density for crystallization performed from the melt state.

Nucleation densities were determined by counting the number of spherulites observed in representative areas of optical micrographs. Primary nucleation density was exponentially increased from 600 nuclei/mm^2 to 3200 nuclei/mm^2 when crystallization temperature was reduced from 49 °C to 36 °C. Crystal grown measurements were not possible at lower temperatures than 36 °C due to the small size of the derived spherulites.

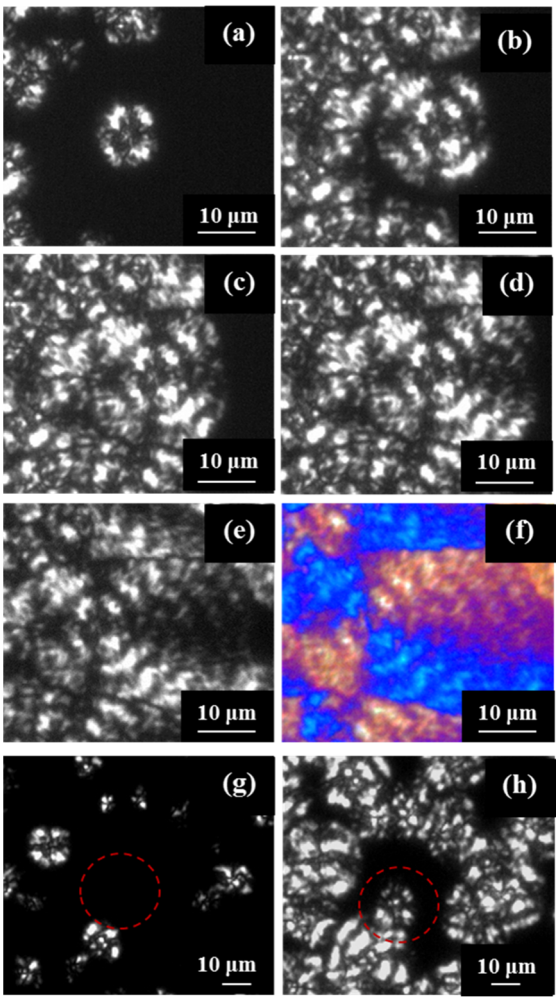

Figure 3.1.12. Optical micrographs showing P4HB spherulites crystallized at 47 °C for (**a**) 100 min, (**b**) 150 min, (**c**) 180 min, (**d**) 250 min, (**e**) 350 min and (**f**) 350 min. In the case of (**f**), the micrograph has been taken with a red tint plate. Comparison of micrographs taken after 47 min (**g**) and 80 min (**h**) for the crystallization performed at 46 °C. The dashed red circle points out the region where the apparition of a new spherulite is clear.

The number of spherulites increased during the isothermal crystallization process (as shown in **Figure 3.1.12** where micrographs taken at different crystallization times for an isothermal process are compared). Therefore, P4HB follows a thermal crystallization (i.e., the number of active nuclei increased with time), probably as a consequence of heterogeneous and sporadic nucleation since alternative homogeneous nucleation can be discarded considering both the low degree of supercooling and the Avrami exponent values deduced from the calorimetric analysis.

The radii of the spherulites grew linearly with time until impingement, as shown in **Figure 3.1.13a** and **3.1.13b** for crystallization experiments performed in the above-indicated temperature range. Final radii varied in this case between 6.5 and 27 μm and logically decreased at higher primary nucleation densities (i.e., at lower crystallization temperatures). Nevertheless, the spherulitic diameter was relatively small even at the higher assayed temperature since the nucleation density was still high.

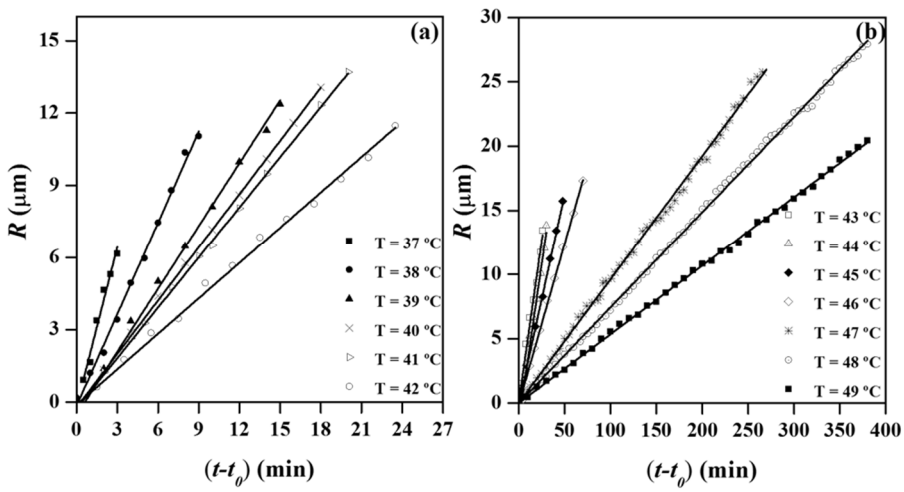

Figure 3.1.13. Variation of the spherulitic radius with crystallization time for temperatures between 37 °C and 42 °C (**a**) and 43 °C and 49 °C (**b**).

It is worthy to note that a discontinuous growth of spherulites was not detected and consequently a ridge and valley structure of the spherulite linked to depletion zones and fluctuations on the melt thin film, as postulated for

P3HB polymers,[33] could not be demonstrated in our case. Nevertheless, plots corresponding to higher temperature crystallized samples (e.g., 47 °C) showed small periodic fluctuations that although not being conclusively pointed towards the indicated interpretation. Small band spacing of P4HB and limitations of the experimental technique must be taken into account in this regard.

3.1.3.7 Secondary Nucleation Constant from DSC and Optical Microscopy Observations

The crystal growth rate, G, was analyzed by means of the Lauritzen-Hoffman (LH) equation in order to deduce the corresponding kinetic parameters.[34]

$$G = G_0 \times \exp[-U^*/(R\,(T_c - T_\infty))] \times \exp[-K_g/(T_c(\Delta T)f)] \quad (7)$$

A similar equation can also be derived by considering the overall crystallization rate as deduced from DSC data:

$$k = k_0 \times \exp[-U^*/(R\,(T_c - T_\infty))] \times \exp[-K_g/(T_c(\Delta T)f)] \quad (8)$$

The validity of this last approach implies a proportionality between k and G values, which in general is accepted for athermal crystallizations and becomes progressively wrong as primary nucleation varied during the crystallization process.[35–38]

Following LH equation, the experimental spherulitic growth rates and overall growth rates of P4HB were plotted as $\ln G + U^*/R(T_c - T_\infty)$ versus $1/(T_c(\Delta T)f)$ (**Figure 3.1.14a**) and $\ln k + U^*/R(T_c - T_\infty)$ versus $1/(T_c(\Delta T)f)$ (**Figure 3.1.14b**). The plots were fitted with straight lines ($r^2 = 0.99$) when the "universal" values reported by Suzuki and Kovacs[39] (i.e., $U^* = 1500$ cal/mol and $T_\infty = T_g - 30$ K) were used in the calculation.

Kinetic features at low supercoolings are governed by the nucleation term, and consequently, crystallization rates could become relatively insensitive to both U^* and T_∞ parameters. Plot allowed estimating secondary nucleation constants of 1.58×10^5 K^2 (from polarizing optical microscopy (POM) measurements) and 1.69×10^5 K^2 (from DSC data). The good agreement that

is found allows us to infer that the applied approximation (i.e., the proportionality between G and k) seems correct and consequently the impact caused by the thermal nucleation is scarce. Probably, all primary nuclei became active when the exothermic crystallization peak starts to appear (i.e., after the induction time) and consequently a minimum discrepancy between the derived K_g values is found.

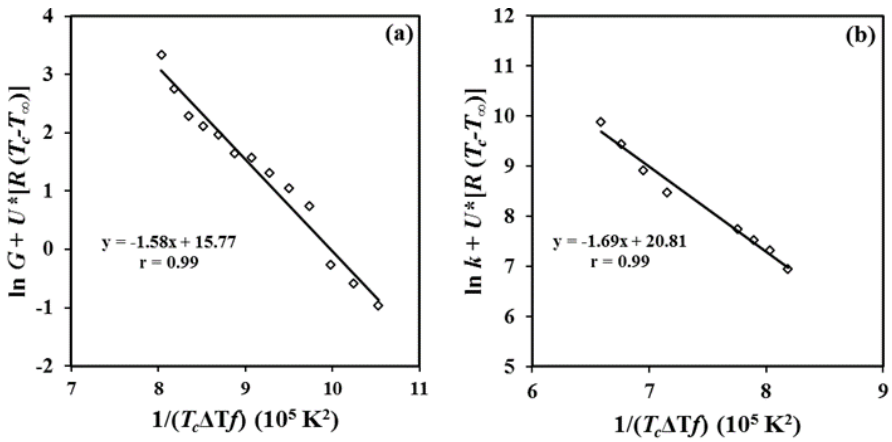

Figure 3.1.14. Lauritzen-Hoffman plots for the crystal growth rate (**a**) and the overall crystallization rate (**b**) for the isothermal crystallization of P4HB.

Equations (7) and **(8)**, and the estimated U^*, T_∞, K_g, G_0, and k_0 parameters were used to estimate G and k values at different crystallization temperatures. The plot in **Figure 3.1.15** shows, in both cases, the conventional bell-shaped curve expected from the interplay between segmental mobility and secondary nucleation.

A satisfactory agreement was observed between the simulated curves obtained from DSC and POM data, as well as, between the limited experimental data and the simulated curves. The simulated curves also allowed estimating the crystallization temperatures at which crystal growth and overall crystallization rates became maxima (i.e., 14 °C (POM) and 15 °C (DSC).

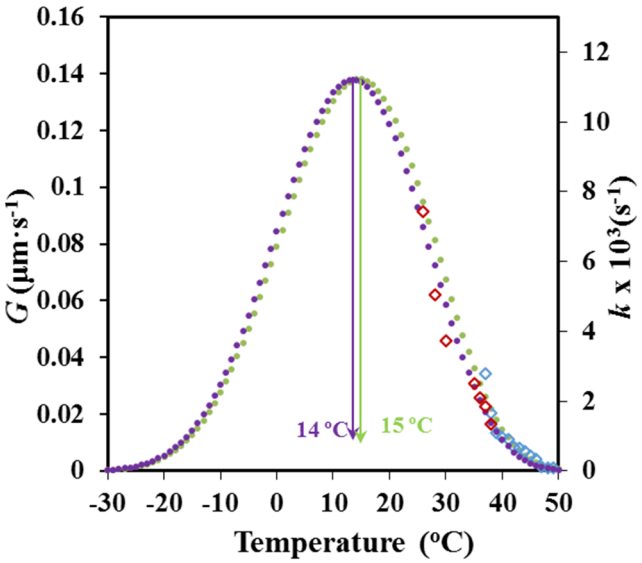

Figure 3.1.15. Temperature dependence of the crystal growth (●, ◊) and overall crystallization (●, ◊) rate. Simulated data is represented by circles and experimental data by rhombus.

3.1.3.8 Infrared Microspectroscopic Studies of P4HB Ringed Spherulites

Microspectroscopic experiments were undertaken to get insight into the hypothesis concerning the structure of ringed P4HB spherulites. **Figure 3.1.16** shows the typical Fourier-transform infrared spectroscopy (FTIR) spectra of a commercial P4HB suture where characteristic stretching bands of methylene groups (2962 and 2898 cm^{-1}) and ester groups (C=O at 1722 cm^{-1}, and asymmetric and symmetric C–O at 1203 cm^{-1} and 1168 cm^{-1}, respectively) can be detected.

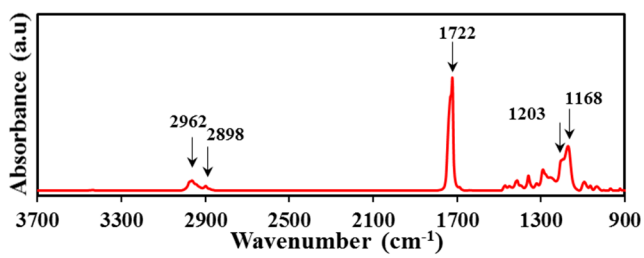

Figure 3.1.16. FTIR spectra of the P4HB suture with the labeling of main bands

The solvent casting of chloroform diluted solutions gave rise to films with a thickness lower than 5 μm that could be analyzed by transmission Fourier transform infrared microspectroscopy. Polarized optical microscopy images showed the development of spherulites (**Figure 3.1.17a**) with well-differentiated dark and bright rings. Chemical images of the spherulites were obtained from the integration of the different infrared peaks (see insets of **Figure 3.1.17a**). In general, spherulitic sectorization was not observed in the chemical images when typical bands were considered, for example, the C=O band (i.e., see the inset of **Figure 3.1.17a**). In this case, the intensity of the peak was practically constant, with the only detected variation being a consequence of the not completely uniform thickness of the cast film.

However, a detailed analysis was successful and a clear sectorization was derived by considering some minor intensity peaks as the high wavenumber shoulder of the 2973 cm^{-1} CH_2 band. Interpretation of the peak is in progress, but the result points out the different orientation of the chemical bond that gives rise to a typical cross with two sectors with higher intensity (red) and two with the lower intensity (blue).

The indicated peak was also considered to discern, if some differences can be detected, between dark and bright rings. **Figure 3.1.17b** shows the specific microzones (color points) that were analyzed and the corresponding microinfrared spectra. Main peaks had always the same intensity in agreement with the previous discussion and only small differences could be detected for the indicated minor peaks. These differences were only found along each specific ring (see shoulders corresponding to the zones indicated by the red, light blue, and pink circles) but not along a specific spherulite radius. Thus, the indicated shoulder had the same intensity for dark (e.g., orange circle) and bright (e.g., violet circle) ring of a radius of the low-intensity sector as well as for the dark (e.g., green circle) and bright (e.g., red circle) ring of a radius of the high-intensity sector. In summary, the microinfrared spectra analysis is not consistent with a typical twisting of constitutive lamellae since clear differences should be

expected between spectra recorded at a determined radius as a consequence of a periodic change in the orientation of chemical bonds.

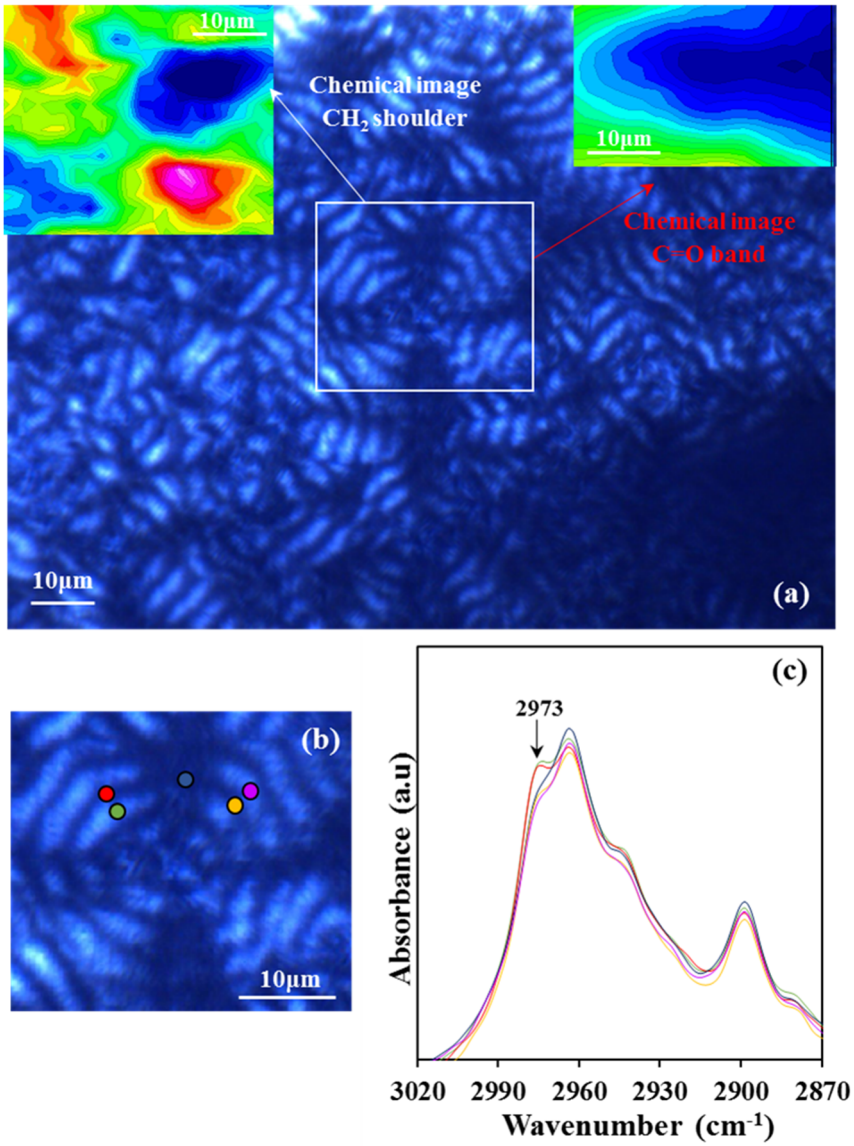

Figure 3.1.17. (**a**) Optical polarized micrographs showing spherulites developed in a solvent casting film. Insets show the chemical image obtained from C=O and CH_2 (shoulder) bands; (**c**) Micrographs showing a representative banded spherulite and the specific microdomains where FTIR spectra were recorded; (**d**) Microinfrared spectra taken from the indicated microdomains (keeping the color code). Different magnifications and wavenumber regions are showed.

3.1.4 CONCLUSIONS

P4HB shows a complex melting peak associated with different lamellar populations and that is strongly dependent on the processing conditions. Thus, the temperature associated with the predominant melting peak can be increased by more than 12 °C after an annealing process. SAXS experiments demonstrated clear differences in the lamellar supramolecular order between annealed and melt crystallized samples. Lamellar thickness and contrast, between amorphous and crystalline regions, become higher for the annealed samples. These samples showed also a higher macroscopic crystallinity, although the order within lamellar stacks decreases due to the high increase of the amorphous lamellar thickness. An equilibrium melting temperature of 79.9 °C was deduced from the typical Hoffman-Weeks analysis.

DSC analysis of the isothermal crystallization of P4HB from the melt state allowed determining an average Avrami exponent of 2.56 and single secondary nucleation constant of 1.69×10^5 K^2. P4HB experimented with a cold crystallization process from the glassy state that occurred under high geometrical constrictions and leads to a decrease of the exponent to a value of 1.93.

Primary nucleation increased by lowering the crystallization temperature, and even during an isothermal experiment. Nevertheless, the impact of the sporadic nucleation was reduced as could be deduced from the Avrami exponent and also by the value of the secondary nucleation constant (1.58×10^5 K^2) that is in full agreement with that determined from DSC experiments. Similar bell-shaped curves defined the dependence of the crystal growth and the overall crystallization rate, with 14-15 °C being the inferred temperatures for those associated with the maximum rates.

Optical microscopy observations indicate that P4HB crystallized from the melt gives rise to banded spherulites with clear differences between the widths of black and white rings and an interring spacing. Infrared microspectroscopy

analysis indicated that chemical bonds had the same orientation in the dark and bright rings supporting a model based on rhythmic growth.

3.1.5 REFERENCES

(1) Martin, D. P.; Williams, S. F. Medical-Applications-of-Poly-4-Hydroxybutyrate. *Biochemical Engineering Journal*. 2003, pp 97–105.

(2) Abate, R.; Ballistreri, A.; Montando, G.; Impallomeni, G. Thermal Degradation of Microbial Poly(4-Hydroxybutyrate). *Macromolecules* **1994**, *27* (2), 332–336. https://doi.org/10.1021/ma00080a004.

(3) Houk, K. N.; Jabbari, A.; Hall, H. K.; Aleman, C. Why δ-Valerolactone Polymerizes and Gamma-Butyrolactone Does Not. *J. Org. Chem.* **2008**, *73* (7), 2674–2678. https://doi.org/10.1021/jo702567v.

(4) Le Meur, S.; Zinn, M.; Egli, T.; Thöny-Meyer, L.; Ren, Q. Poly(4-Hydroxybutyrate) (P4HB) Production in Recombinant Escherichia Coli: P4HB Synthesis Is Uncoupled with Cell Growth. *Microb. Cell Fact.* **2013**, *12*, 1–11. https://doi.org/10.1186/1475-2859-12-123.

(5) Odermatt, E. K.; Funk, L.; Bargon, R.; Martin, D. P.; Rizk, S.; Williams, S. F. MonoMax Suture: A New Long-Term Absorbable Monofilament Suture Made from Poly-4-Hydroxybutyrate. *Int. J. Polym. Sci.* **2012**, *2012*, 1–12. https://doi.org/10.1155/2012/216137.

(6) Tornier, announces Launch of BioFiber® Surgical Mesh for Tendon Repair at Arthroscopic Surgery Conference https://www.businesswire.com/news/home/20110414005940/en/Tornier-Announces-Launch-BioFiber®-Surgical-Mesh-Tendon.

(7) Deeken, C. R.; Matthews, B. D. Characterization of the Mechanical Strength, Resorption Properties, and Histologic Characteristics of a Fully Absorbable Material (Poly-4-Hydroxybutyrate-PHASIX Mesh) in a Porcine Model of Hernia Repair. *ISRN Surg* **2013**, *2013*, 1–12. https://doi.org/10.1155/2013/238067.

(8) Williams, S. F.; Rizk, S.; Martin, D. P. Poly-4-Hydroxybutyrate (P4HB): A New Generation of Resorbable Medical Devices for Tissue Repair and Regeneration. *Biomed. Tech.* **2013**, *58* (5), 439–452. https://doi.org/10.1515/bmt-2013-0009.

(9) Angelos PC; Thakkar, N.; A, S.; Toriumi, D. Use of Poly-4-Hydroxybutyrate Mesh in Rhytidectomy: A Retrospective Review and Cadaveric Study of Biomechanical Strength Testing. In *Presentation at the American Academy of Facial Plastic and Reconstructive Surgery Meeting*; Washington DC, 2012.

(10) Nelson, T.; Kaufman, E.; Kline, J.; Sokoloff, L. The Extraneural Distribution of Γ-Hydroxybutyrate. *J. Neurochem.* **1981**, *37* (5), 1345–1348. https://doi.org/10.1111/j.1471-4159.1981.tb04689.x.

(11) Boesel, L. F.; Meur, S. Le; Thöny-Meyer, L.; Ren, Q. The Effect of Molecular Weight on the Material Properties of Biosynthesized Poly(4-Hydroxybutyrate). *Int. J. Biol. Macromol.* **2014**, *71*, 124–130. https://doi.org/10.1016/j.ijbiomac.2014.04.015.

(12) Engelberg, I.; Kohn, J. Physico-Mechanical Properties of Degradable Polymers Used in Medical Applications: A Comparative Study. *Biomaterials* **1991**, *12* (3), 292–304. https://doi.org/10.1016/0142-9612(91)90037-B.

(13) Velde, K. Van De; Kiekens, P. Biopolymers: Overview of Several Properties and Consequences on Their Applications. *eb - Elektrische Bahnen* **2001**, *99* (12), 483.

(14) Mitomo, H.; Kobayashi, S.; Morishita, N.; Doi, Y. . *Polym. Prepr.* **1995**, *44*, 3156.

(15) Su, F.; Iwata, T.; Sudesh, K.; Doi, Y. Electron and X-Ray Diffraction Study on Poly(4-Hydroxybutyrate). *Polymer (Guildf).* **2001**, *42* (21), 8915–8918. https://doi.org/10.1016/S0032-3861(01)00412-8.

(16) Su, F.; Iwata, T.; Tanaka, F.; Doi, Y. Crystal Structure and Enzymatic Degradation of Poly(4-Hydroxybutyrate). *Macromolecules* **2003**, *36* (17), 6401–6409. https://doi.org/10.1021/ma034546s.

(17) Koyama, N.; Doi, Y. Effects of Solid-State Structures on the Enzymatic Degradability of Bacterial Poly(Hydroxyalkanoic Acids). *Macromolecules* **1997**, *30* (4), 826–832. https://doi.org/10.1021/ma961195r.

(18) Alamo, R.; Mandelkern, L. Origins of Endothermic Peaks in Differential Scanning Calorimetry. *J. Polym. Sci. Part B Polym. Phys.* **1986**, *24* (9), 2087–2105. https://doi.org/10.1002/polb.1986.090240914.

(19) Morales-Gámez, L.; Soto, D.; Franco, L.; Puiggalí, J. Brill Transition and Melt Crystallization of Nylon 56: An Odd-Even Polyamide with Two Hydrogen-Bonding Directions. *Polymer (Guildf).* **2010**, *51* (24), 5788–5798. https://doi.org/10.1016/j.polymer.2010.09.074.

(20) Vonk, C. G. A General Computer Program for the Processing of Small-Angle X-Ray Scattering Data. *J. Appl. Crystallogr.* **1975**, *8*, 340–341.

(21) Hoffman, J. D.; Weeks, J. J. Melting Process and the Equilibrium Melting Temperature of Polychlorotrifluoroethylene. *J. Res. Natl. Bur. Stand. Sect. A Phys. Chem.* **1962**, *66A* (1), 13. https://doi.org/10.6028/jres.066a.003.

(22) Hoffman, J. D.; Davis, G. T.; Lauritzen, J. I. The Rate of Crystallization of Linear Polymers with Chain Folding. *Treatise Solid State Chem.* **1976**, No. Chapter 7, 497-614. https://doi.org/10.1007/978-1-4684-2664-9_7.

(23) Avrami, M. Kinetics of Phase Change. I: General Theory. *J. Chem. Phys.* **1939**, *7* (12), 1103–1112. https://doi.org/10.1063/1.1750380.

(24) Avrami, M. Kinetics of Phase Change. II Transformation-Time Relations for Random Distribution of Nuclei. *J. Chem. Phys.* **1940**, *8* (2), 212–224. https://doi.org/10.1063/1.1750631.

(25) Schultz, J. M.; Kinloch, D. R. Transverse Screw Dislocations: A Source of Twist in Crystalline Polymer Ribbons. *Polymer (Guildf).* **1969**, *10* (C), 271–278. https://doi.org/10.1016/0032-3861(69)90039-1.

(26) Bassett, D. C.; Olley, R. H.; Al Raheil, I. A. M. On Isolated Lamellae of Melt-Crystallized Polyethylene. *Polymer (Guildf).* **1988**, *29* (9), 1539–1543. https://doi.org/10.1016/0032-3861(88)90259-5.

(27) Barham, P. J.; Keller, A.; Otun, E. L.; Holmes, P. A. Crystallization and Morphology of a Bacterial Thermoplastic: Poly-3-Hydroxy butyrate. *J. Mater. Sci.* **1984**, *19* (9), 2781–2794. https://doi.org/10.1007/BF01026954.

(28) Kyu, T.; Chiu, H. W.; Guenthner, A. J.; Okabe, Y.; Saito, H.; Inoue, T. Rhythmic Growth of Target and Spiral Spherulites of Crystalline Polymer Blends. *Phys. Rev. Lett.* **1999**, *83* (14), 2749–2752. https://doi.org/10.1103/PhysRevLett.83.2749.

(29) Zhao, L.; Wang, X.; Li, L.; Gan, Z. Structural Analysis of Poly (Butylene Adipate) Banded Spherulites from Their Biodegradation Behavior. *Polymer (Guildf).* **2007**, *48* (20), 6152–6161. https://doi.org/10.1016/j.polymer.2007.07.055.

(30) Jungnickel, B. 12 Crystallization Kinetical Peculiarities Immiscible Blends : **2003**, *6*, 208–237.

(31) Ding, G.; Liu, J. Morphological Varieties and Kinetic Behaviors of Poly(3-Hydroxybutyrate) (PHB) Spherulites Crystallized Isother mally from Thin Melt Film. *Colloid Polym. Sci.* **2013**, *291* (6), 1547–1554. https://doi.org/10.1007/s00396-012-2882-9.

(32) Duan, Y.; Jiang, Y.; Jiang, S.; Li, L.; Yan, S.; Schultz, J. M. Depletion-Induced Nonbirefringent Banding in Thin Isotactic Polystyrene Thin Films. *Macromolecules* **2004**, *37* (24), 9283–9286. https://doi.org/10.1021/ma0483165.

(33) Okabe, Y.; Kyu, T.; Saito, H.; Inoue, T. Spiral Crystal Growth in Blends of Poly (Vinylidene Fluoride) and Poly (Vinyl Acetate). *Macromolecules* **1998**, *31* (98), 5823–5829.

(34) Lauritzen, J. I.; Hoffman, J. D. Extension of Theory of Growth of Chain-Folded Polymer Crystals to Large Undercoolings. *J. Appl. Phys.* **1973**, *44* (10), 4340–4352. https://doi.org/10.1063/1.1661962.

(35) Chan, T. W.; Isayev, A. I. Quiescent Polymer Crystallization: Modelling and Measurements. *Polym. Eng. Sci.* **1994**, *34* (6), 461–471. https://doi.org/10.1002/pen.760340602.

(36) Fatou, J. G.; Marco, C.; Mandelkern, L. The Crystallization Kinetics of Low-Molecular-Weight Polyethylene Fractions. *Polymer (Guildf).* **1990**, *31* (5), 890–898. https://doi.org/10.1016/0032-3861(90)90052-Z.

(37) Lu, H.; Qiao, J.; Yang, Y. Effect of Isotacticity Distribution on Crystallization Kinetics of Polypropylene. *Polym. Int.* **2002**, *51* (12), 1304–1309. https://doi.org/10.1002/pi.856.

(38) Kenny, J. M.; Maffezzoli, A.; Nicolais, L. A New Kinetic Model for Polymer Crystallization Derived by Calorimetric Analysis. *Thermo chim. Acta* **1993**, *227* (C), 83–95. https://doi.org/10.1016/0040-6031(93)80252-6.

(39) Suzuki, T.; Kovacs, A. J. Temperature Dependence of Spherulitic Growth Rate of Isotactic Polystyrene. A Critical Comparison with the Kinetic Theory of Surface Nucleation. **1970**, *1* (1), 82–100.

3.2 NON-ISOTHERMAL CRYSTALLIZATION OF POLY-4-HYDROXYBUTYRATE BIOPOLYMER

3.2.1 INTRODUCTION

Poly-4-hydroxybutyrate (P4HB) is a biodegradable, linear, and aliphatic polyester with interesting applications in the biomedical field. This is mainly associated with its use as a wound closure material.[1] This hydroxyalkanoate (HA) derivative can easily be produced from microorganisms (e.g., *Escherichia coli K12*) by recombinant fermentation under a deficit of nutrients or other stress limitations.[2–4] Basically, the polymer is employed by microorganisms (as other polyhydroxyalkanoates (PHAs), such as poly-3-hydroxybutyrate (P3HB) and polyhydroxyvalerate (PHV), as an energy storage form produced by the carbon assimilation from glucose or starch sources. Biosynthesis is the only practical pathway to produce P4HB, since samples with a reasonable molecular weight cannot be obtained from conventional chemical synthesis (e.g., ring-opening polymerization of butyrolactone).[5,6]

P4HB has exceptional mechanical properties that allow the preparation of strong fibers with good retention in vivo.[7] The use of P4HB for soft tissue ligation was approved by the food and drug administration (FDA) in 2007, being commercialized as a long-term absorbable monofilament suture under the trademark of MonoMax® (B. Braun Surgical S. A.U.). P4HB is the only PHA allowed for regulatory agencies (e.g., USFDA and EU) to be used in clinical applications,[8,9] such as reconstructive surgery, materials for cardiovascular applications, such as vascular grafts and stents,[10] and devices for repair of hernias,[11] ligaments, and tendons, are other well-known applications of P4HB.[1]

Probably the most remarkable feature of P4HB is not only its high ductility and flexibility (i.e., the elongation at break can reach a value of 1000%) but also the great interest in the preparation of copolymers with other HAs. Thus, the highly brittle and crystalline P3HB can easily be modified by copolymerization

with different molar fractions of the 4HB monomer to obtain a group of materials with suitable mechanical strength and properties, including degradation rate.[12]

On the other hand, P4HB (-[O(CH_2)$_3$CO]$_n$-) has different properties than the similar linear polyesters with a lower (i.e., polyglycolide, -[OCH_2CO]$_n$-, PGA) and higher (i.e., poly(ε-caprolactone), -[O(CH_2)$_5$CO]$_n$-, PCL) number of carbon atoms in their chemical repeat unit. Surprisingly, a continuous evolution of properties with the length of the repeat unit is not observed even while maintaining its parity, that is avoiding great changes of the crystalline structure. For example, typical elongation at break values are <3%, 1000%, and 80%, while elastic modulus values are 6900 MPa, 70 Mpa, and 400 MPa for PGA, P4HB, and PCL, respectively.[10] Differences in the degradation rate are clear (e.g., fast and slow for PGA and P4HB, respectively), and it is of interest to explore the use of combinations of such materials to tune the final degradability of the material.[13]

The peculiar properties of P4HB have attracted great attention for the development of new materials for applications in the biomedical field. However, research concerning physical characterization is surprisingly relatively scarce, especially considering that the above-indicated differences with related polyesters. To the best of our knowledge works concerning the physical characterization of P4HB only include the study of its crystalline structure by both X-ray and electron diffraction techniques,[14–16] morphologic studies,[16] evaluation of hydrolytic and enzymatic degradation mechanisms,[16,17] and determination of basic thermal and mechanical properties.[1]

The thermal properties of P4HB are strongly dependent on the preparation conditions. Samples are crystalline and have shown a preferential melting peak at 72 °C after annealing at an appropriate temperature**,** under stress conditions, or from solution crystallization. By contrast, a decrease in the melting temperature at 58 °C is characteristic when samples are crystallized after melting. Control of the crystallization process seems fundamental considering the relatively low melting point that becomes close to room temperature and

the derived applications where crystallinity plays a significant role (i.e., degradation rate and even elastic behavior). Isothermal crystallization studies of P4HB have recently been carried out considering both calorimetric (DSC) and optical microscopy (POM) experimental data.[18] The obtained data covered a very narrow range of crystallization temperatures (i.e., 24–38 °C and 37–49 °C for DSC and POM observations, respectively) due to experimental limitations (e.g., high primary nucleation and slow crystallization rate at low and high temperatures, respectively). Results indicated a crystallization process from the melt state defined by an averaged Avrami exponent of 2.56. Crystallization occurred according to a single regime characterized by secondary nucleation constant of 1.69×10^5 K^2 (from DSC data) and 1.58×10^5 K^2 (from POM data).

Nowadays, efforts are focused on understanding the non-isothermal crystallization behavior of semi-crystalline polymers since this is more appropriate to describe the usual processing conditions and can even be useful in the description of the crystallization process for a wider temperature range. Different methodologies have been developed to carry out the evaluation of non-isothermal crystallization from DSC and POM experimental data. Results are in general controversial when different methods are compared, especially when interpretation and theoretical approximations are not clear. The goals of the present section are (a) the specific study of non-isothermal crystallization of P4HB, a polymer with increasing applied interest and with a crystallization process scarcely studied; (b) a comparison of the non-isothermal process with isothermal crystallization data evaluated above, and (c) the evaluation of the more significant highlights given by the different theories derived from DSC and POM data.

3.2.2 MATERIALS AND METHODS

3.2.2.1 Materials

Commercially available sutures of P4HB (MonoMax®, violet sample, USP 1) were kindly supplied by B. Braun Surgical S.A.U. The weight and number

average of molecular weights of MonoMax® samples were 215,000 and 68,000 g/mol, as determined by size exclusion chromatography (GPC).

3.2.2.2 Measurements

Molecular weight was estimated at room temperature by size exclusion chromatography (GPC) using a liquid chromatograph (model LC-8A, Shimadzu, Tokyo, Japan) equipped with an Empower computer program (Waters, Milford, Massachusetts, USA). A PL HFIP gel column (Polymer Lab, Agilent Technologies Deutschland GmbH, Böblingen, Germany) and a refractive index detector (Shimadzu RID-10A) were employed. The polymer was dissolved and eluted in 1,1,1,3,3,3-hexafluoroisopropanol containing CF_3COONa (0.05 M) at a flow rate of 0.5 mL/min (injected volume 100 µL, sample concentration 2.0 mg/mL). The number and weight average of molecular weights were estimated using polymethyl methacrylate standards.

Calorimetric data were obtained by differential scanning calorimetry with a TA Instruments Q100 series with T_{zero} technology and equipped with a refrigerated cooling system (RCS). Experiments were conducted under a flow of dry nitrogen with a sample weight of approximately 5 mg, and calibration was performed with indium. T_{zero} calibration required two experiments: The first was performed without samples while sapphire disks were used in the second. Non-isothermal crystallization studies were performed by cooling previously molten samples (5 min at 100 °C) at rates varying from 5 to 1 °C/min.

The spherulitic growth rate was determined by optical microscopy using a Zeiss Axioskop 40 Pol light polarizing microscope equipped with a Linkam temperature control system configured by a THMS 600 heating and freezing stage connected to an LNP 94 liquid nitrogen cooling system. Spherulites were grown from homogeneous thin films prepared from the melt. Small sections of these films were pressed or smeared between two cover slides and inserted into the hot stage, producing samples with thicknesses close to 10 µm in all cases. Samples were kept at approximately 100 °C for 5 min to eliminate sample history effects. Then the sample was quickly cooled to 45 °C and led to

isothermally grown for 60 min to generate enough nuclei for measurements and avoid the induction step. Subsequently, the radius of growing spherulites was monitored during crystallization with micrographs taken with a Zeiss AxiosCam MRC5 digital camera at appropriate time intervals. A first-order red tint plate was employed to determine the sign of spherulite birefringence under crossed polarizers.

Wide-angle X-ray diffraction (WAXD) and small-angle X-ray scattering patterns (SAXS) data were obtained at the NCD beamline (BL11) of the ALBA synchrotron facility (Cerdanyola del Vallès, Barcelona, Spain), by using a wavelength of 0.100 nm. A WAXD LX255-HS detector from Rayonix and an ImXPAD S1400 photon-counting detector were employed. Polymer samples were confined between Kapton films. WAXD and SAXS diffraction patterns were calibrated with Cr_2O_3 and silver behenate (AgBh), respectively. WAXD peaks were deconvoluted with the PeakFit v4 program by Jandel Scientific Software. The correlation function and corresponding parameters were calculated with the CORFUNC program for Fiber Diffraction/Non-Crystalline Diffraction provided by the Collaborative Computational Project 13.

3.2.3 RESULTS AND DISCUSSION

3.2.3.1 Limitations of the Avrami Analysis of Non-isothermal Crystallization of P4HB

Figure 3.2.1 shows the dynamic DSC exotherms obtained by cooling melted P4HB samples at different rates. Logically, peaks moved progressively to lower temperatures as the cooling rate increased.

Calorimetric data allowed the determination of the relative degree of crystallinity at any temperature, $\chi(T)$, for all cooling rates by the expression

$$\chi(T) = \frac{\int_{T_0}^{T} (dH_c/dT)dT}{\int_{T_0}^{T_\infty} (dH_c/dT)dT} \quad (1)$$

where dH_c is the enthalpy of crystallization released within an infinitesimal temperature range dT, T_0 denotes the initial crystallization temperature, and T_∞ is the temperature required to complete the crystallization process. Thus, the denominator corresponds to the overall enthalpy of crystallization for specific heating/cooling conditions. Note that this relative crystallinity is higher than the real extent of crystallization, which is limited by the slow dynamics of polymeric molecular chains.

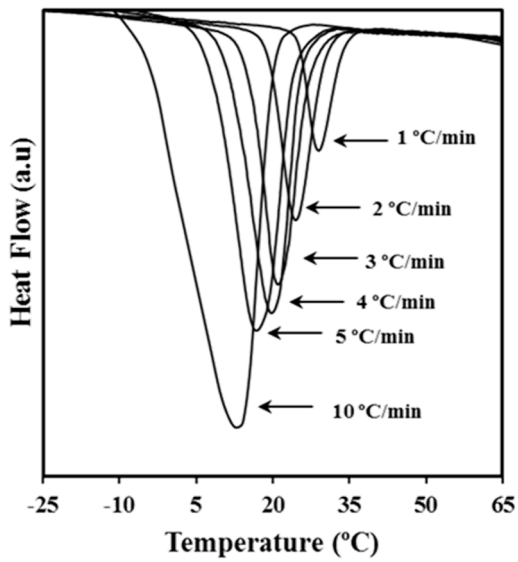

Figure 3.2.1. Dynamic differential scanning calorimetry (DSC) curves obtained at the indicated cooling rates for poly-4-hydroxybutyrate (P4HB) crystallization from the melt state.

The time dependence of the degree of crystallinity (**Figure 3.2.2a**) can be derived considering the relationship

$$(t - t_0) = (T - T_0)/\varphi \qquad (2)$$

where T_0 is the temperature when crystallization begins ($t = t_0$) and φ is the cooling rate.

The typical Avrami analysis can be applied to these non-isothermal experiments based on **Equation 3.**

$$1 - \chi(t - t_0) = \exp -Z\,(t - t_0)^n], \qquad (3)$$

where Z is the temperature-dependent rate constant and n the Avrami exponent.

This exponent has a physical sense for isothermal crystallization of semi-crystalline polymers despite being initially postulated for the study of the phase transformation of metals.[19,20] It has been established that the exponent varies according to the dimensionality of the crystal growth and the type of nucleation.[21] Namely, time-dependent thermal nucleation (i.e., homogeneous nucleation and sporadic heterogeneous nucleation) can be differentiated from athermal nucleation (i.e., instantaneous heterogeneous nucleation) after evaluating the crystal dimensionality. Unfortunately, the direct application of the Avrami equation to the evaluation of non-isothermal crystallization merely corresponds to a mathematical fitting. This allows the evaluation of the variation of crystallinity with crystallization time, but parameters lose their physical meaning since, for example, values of the exponent become usually higher than four.

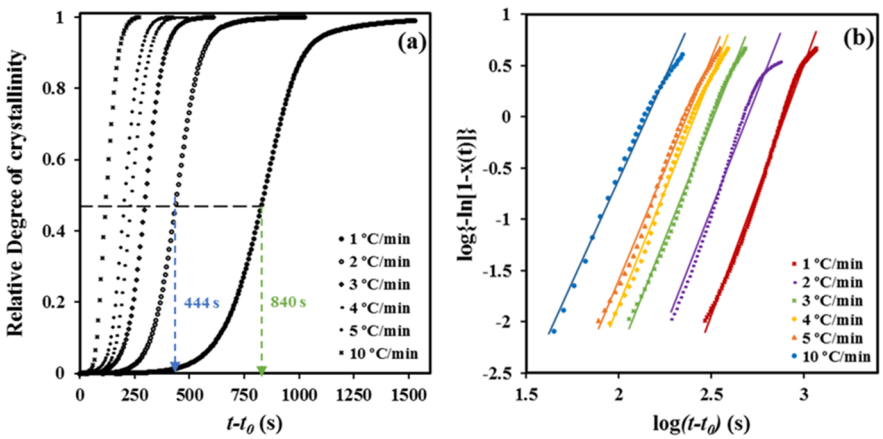

Figure 3.2.2. Time evolution of relative crystallinity (**a**) and Avrami plots, (**b**) at the indicated cooling rates for the non-isothermal crystallization of P4HB.

Plots of log $\{-\ln [1 - \chi (t - t_0)]\}$ versus log $(t - t_0)$ showed good linearity (**Figure 3.2.2b**) before the start of the secondary crystallization process associated with the impingement of spherulitic crystals (i.e., the decrease of the

dimensionality of the crystal growth). The linearity is observed, in our case, up to a relative crystallinity of 0.92.

Table 3.2.1. Non-isothermal crystallization kinetic parameters deduced from differential scanning calorimetry (DSC) experiments for poly-4-hydroxybutyrate (P4HB).

Φ (°C/min)	n	Z (s^{-n})	$k \times 10^3$ (s^{-1})	$\tau_{1/2}$ (s)	$(1/\tau_{1/2}) \times 10^3$ (s^{-1})	$(Z/\ln 2)^{1/n} \times 10^3$ (s^{-1})
1	5.67	4.42×10^{-17}	1.30	840	1.19	1.39
2	5.18	1.47×10^{-14}	1.95	444	2.25	2.28
3	4.92	4.83×10^{-13}	3.13	300	3.33	3.37
4	4.24	6.89×10^{-11}	4.00	231	4.33	4.36
5	4.21	1.22×10^{-10}	4.42	207	4.83	4.82
10	3.98	2.54×10^{-9}	6.92	120	8.33	7.59

Table 3.2.1 summarizes the main kinetic parameters deduced from the Avrami analysis, including the overall crystallization rate, k, calculated as $Z^{1/n}$. This rate has units of s^{-1} and consequently, can be used to compare data from crystallizations having different Avrami exponents. Note that the usually employed Z parameter is not useful since it has units of s^{-n} (i.e., it is dependent on the change of nucleation mechanism and crystal growth dimensionality). Logically, the crystallization became faster as the cooling rate increased, and specifically, a change from 1.30×10^3 to 4.40×10^3 was detected when the rate was increased from 1 °C/min to 5 °C/min. The generally observed trend was the decrease of the Avrami exponent (being 5.0 the average value) when the cooling rates were increasing. This is higher than the postulated value for a maximum crystal dimensionality and a homogeneous (or even a sporadic heterogeneous) nucleation, making the deduction of the crystallization mechanism as above indicated impossible. Nevertheless, the observed decrease suggests that the dimensionality decreased as crystallization was conducted faster. Reported data for the non-isothermal crystallization of the related PCL polyester also gave a high Avrami exponent (i.e., n between 3 and 4), although

it was interpreted as a three-dimensional spherulitic growth with homogeneous nucleation.[22]

Table 3.2.1 also shows a satisfying agreement between the reciprocal crystallization half-times ($1/\tau_{1/2}$) that were directly determined from the experimental data and those that were deduced from the Avrami parameters (i.e., $1/\tau_{1/2} = ((Z/\ln 2)^{1/n})$. The deduced parameters are at least appropriate to simulate the non-isothermal crystallization process.

3.2.3.2 Alternatives to the Avrami Analysis for the Non-isothermal Crystallization of P4HB

Ozawa[23] proposed a modified Avrami equation that directly considers the effect of the cooling rate. The approach assumes that a non-isothermal process is the result of an infinite number of small isothermal steps. The Ozawa equation was formulated by applying the mathematical derivation of Evans[24] to the Avrami equation and considering a constant cooling rate.

$$1 - \chi(T) = \exp(-R(T)/\varphi^m) \quad (4)$$

where $R(T)$ is a cooling function that depends on the temperature of the process and m is the so-named Ozawa exponent. The difference of the exponent with the above indicated Avrami exponent is not clear, and generally, it has been interpreted in the same way.[25]

The exponent can be deduced from the plot of $\log\{-\ln[1 - \chi(T)]\}$ versus $\log\varphi$ for conversions determined at the same temperature and different cooling rates. The main limitation of the method is that the linearity is observed for a restricted range of cooling rates, as can be observed in **Figure 3.2.3**. The absence of linearity becomes more evident as the process becomes faster (i.e., the temperature is lower). In other words, the analysis is highly sensitive to the variation between primary and secondary crystallization processes. It was noted in the previous section that secondary crystallization only becomes significant when the degree of crystallinity becomes very high. Thus, plots performed at high crystallization temperatures are linear over a wide range of cooling rates

due to the slow crystallization and the difficulty of entering into the secondary crystallization region.

The slopes of the different straight segments shown in **Figure 3.2.3** are close to −3.5, which suggests athermal nucleation and three-dimensional spherulitic growth. The value of the Avrami exponent is in clear contradiction with the reported values from isothermal studies, a feature that is congruent with the previous discussion and that points out the limitation of the application of the Avrami analysis to non-isothermal crystallization studies.

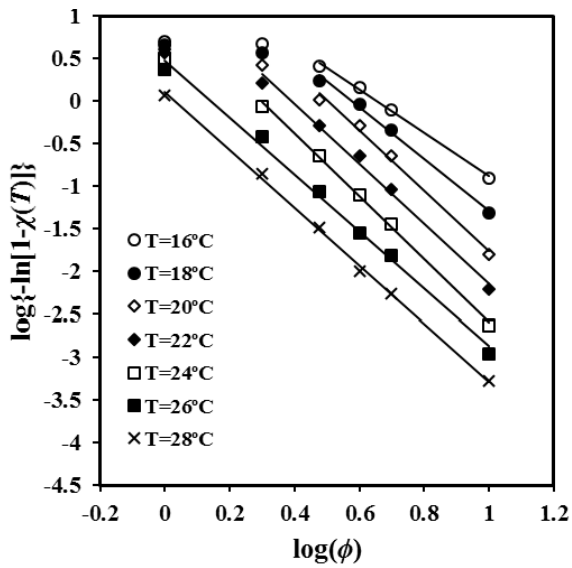

Figure 3.2.3. Plots of log{−ln [1 − $\chi(T)$]} versus logφ for non-isothermal crystallizations of P4HB at the indicated temperatures.

The values of the exponent decreased at low crystallization temperatures when cooling rates were low as a consequence of the increasing secondary crystallization. Thus, exponents of 1.44, 1.87, and 2.35 were determined in the cooling rate region between 2 and 3 °C/min for temperatures of 16 °C, 18 °C, and 20 °C, respectively. Low values of 1.14 and 1.87 were estimated in the cooling rate region between 1 and 2 °C/min for temperatures of 22 °C and 24 °C, respectively.

Optical micrographs (**Figures 3.2.4** and **3.2.5**) taken during the non-isothermal crystallization clearly show the development of banded spherulites

with a negative birefringence and increasing nucleation as a consequence of the temperature decrease. For instance, the dashed circles that are observed indicate the apparition of new nuclei and spherulites during the crystallization that was performed at a representative cooling rate of 0.5 °C/min. These non-isothermal experiments cannot demonstrate that the crystallization takes place according to an athermal process (i.e., the apparition of new nuclei during crystallization at a given temperature), but this feature was corroborated in the previous isothermal crystallization studies.

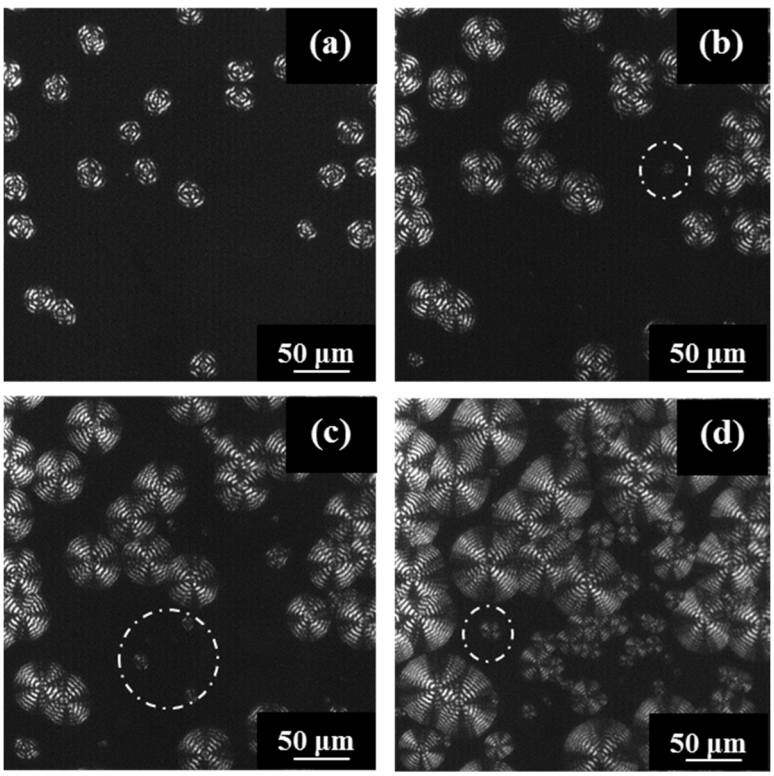

Figure 3.2.4. Optical micrographs of P4HB spherulites formed at the indicated non-isothermal crystallization times by cooling the sample at a rate of 0.5 °C/min from 45 °C, where some spherulites were isothermally grown (60 min) from the melt state. Micrographs were taken at temperatures of 44 °C (**a**), 38 °C (**b**), 36 °C (**c**), and 33 °C (**d**).

The spherulitic texture was variable (e.g., the width of bands shown in **Figure 3.2.5** continuously decreased during the crystallization that began at 45

°C and finished at 29 °C), since changes were expected between regions crystallized at high and low temperatures.

Liu et al.[26] postulated an alternative calorimetric analysis based on the combination of typical Avrami and Ozawa treatments. **Equation 5** (also known as the Mo equation) was derived.

$$\log \varphi = \log F(T) - a \log (t - t_0) \quad \textbf{(5)}$$

where $F(T)$ is a new kinetic function, defined as $[\chi(T)/Z(T)]^{1/m}$, and a is the ratio between apparent Avrami and Ozawa exponents (n/m).

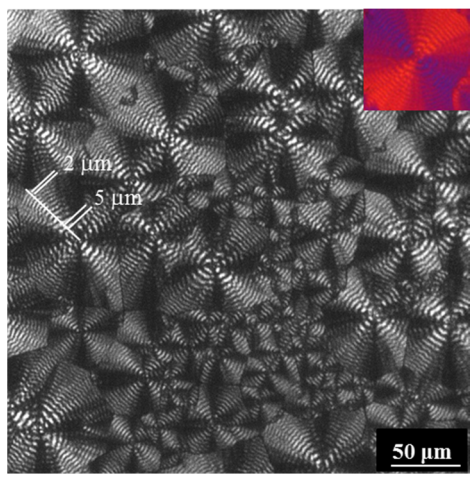

Figure 3.2.5. Optical micrograph at the end of the non-isothermal crystallization (0.5 °C/min) of P4HB. The decrease in the interring spacing during crystallization is evident. Inset shows a micrograph taken with a first-order red tint plate to determine the birefringence sign.

The main problem of the model is the non-clear physical sense of $F(T)$, which was defined as the cooling rate that must be chosen at a unit crystallization time to reach a certain crystallinity. $F(T)$ increases with increasing crystallinity, indicating that a higher cooling rate is required. The main interest of Liu analysis concerns the evaluation/quantification of how the modifications of a system (e.g., incorporation of additives) may be reflected in a more difficult crystallization (i.e., higher $F(T)$ values for a given crystallinity).

A plot of log φ versus log $(t - t_0)$ yields a series of straight lines (**Figure 3.2.6**) that suggest the validity of the Mo equation for the P4HB system. The

intercept and slope of these lines can be used to estimate the kinematic parameters. The values of $F(T)$ (**Table 3.2.2**) increased with crystallinity, indicating that the motion of molecular chains became slower, making the formation of crystals more difficult.

The second piece of information derived from the Liu and Mo analysis concerns the n/m ratio, which theoretically should be equal to 1 if the equivalence of exponents is assumed. Different non-isothermal studies revealed presumably a good equivalence between both exponents.[25,27–29]

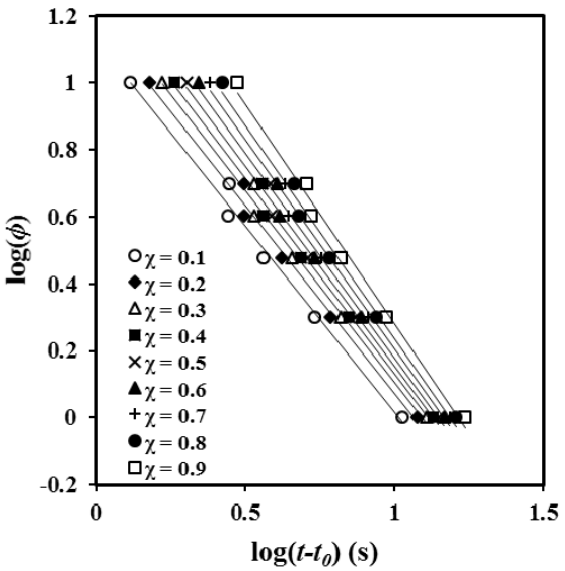

Figure 3.2.6. Plots of log φ versus log$(t - t_0)$ at the indicated crystallinities for non-isothermal crystallization of P4HB.

Table 3.2.2. Values of kinetic parameters at a given crystallinity estimated from the combined Liu model for non-isothermal crystallization of P4HB.

$\chi(T)$	α'	$F(T)$	r^2
0.1	−1.11	13.41	0.988
0.2	−1.12	15.70	0.990
0.3	−1.14	17.62	0.991
0.4	−1.16	19.74	0.991
0.5	−1.19	22.14	0.991
0.6	−1.22	24.85	0.990
0.7	−1.24	28.03	0.990

0.8	−1.28	32.30	0.989
0.9	−1.31	38.65	0.989

[1] *r*: correlation factor.

Table 3.2.2 shows that the values of *a* were almost constant and close to 1 (i.e., between 1.11 and 1.31). Nevertheless, the *a* values slightly increased with crystallinity (i.e., an increased dissimilarity between Avrami and Ozawa exponents was observed when crystallinity increased). Specifically, the Avrami exponent became regularly higher than the Ozawa exponent. Note that **Figure 3.2.3** demonstrates that the Ozawa exponent changed and dramatically decreased at high crystallinity as a consequence of the great contribution of secondary crystallization**.** Previous studies performed with the related PCL polyester indicated a ratio higher than 1 and specifically an increase from 1.41 to 1.65 for conversions varying from 0.2 and 0.8.[22]

Cazé has also developed a methodology able to render an average value of the Avrami exponent for all the crystallization process.[30] The method hypothesizes that crystallization exotherms follow a Gaussian curve and considers three temperature inflection points: the onset temperature, the peak temperature, and the end crystallization temperature. The approach assumes that these three temperatures vary linearly with the cooling rate. A theoretical peak temperature T'_p and a new constant a' can be estimated, assuming the following equation:

$$\ln [1 - \ln (1 - \chi (T))] = a' (T - T'_p) \quad \textbf{(6)}$$

Plots of ln [1 − ln (1 − χ (*T*))] versus *T* at different cooling rates (**Figure 3.2.7a**) are linear and allow the indicated parameters (i.e., a' and T'_p) to be calculated (**Table 3.2.3**). It is worth noting that **Equation 6** is confined to the primary crystallization regime. The range of crystallinities starts at 2% to ensure precision and cover data in such a way that the correlation coefficient is greater than 0.99. **Table 3.2.3** also shows a favorable agreement between the peak temperature that was estimated assuming the Cazé model and that directly determined from the experimental DSC data.

The deduced peak temperatures can then be related to the cooling rate (**Figure 3.2.7b**) by the expression

$$T'_p = (m/a') \ln \varphi - b'a' \quad (7)$$

where b' is a new constant.

The plot of T'_p versus ln $\varphi a'$ (**Figure 3.2.7b**) gives straight lines with a slope equal to the estimated Ozawa exponent m. The values obtained for P4HB are close to 2.13, which has a physical meaning and appears very close to those deduced from the isothermal analysis[18] (i.e., exponents varied between 2.35 and 2.62, with 2.56 being the average value). Note that the derived value of m corresponds to an Avrami exponent of 2.57 to 2.87 if the nm ratio deduced from the Liu model is applied. The obtained results support the suitability of the Cazé methodology, as previously reported in the non-isothermal study of different polymers.[31]

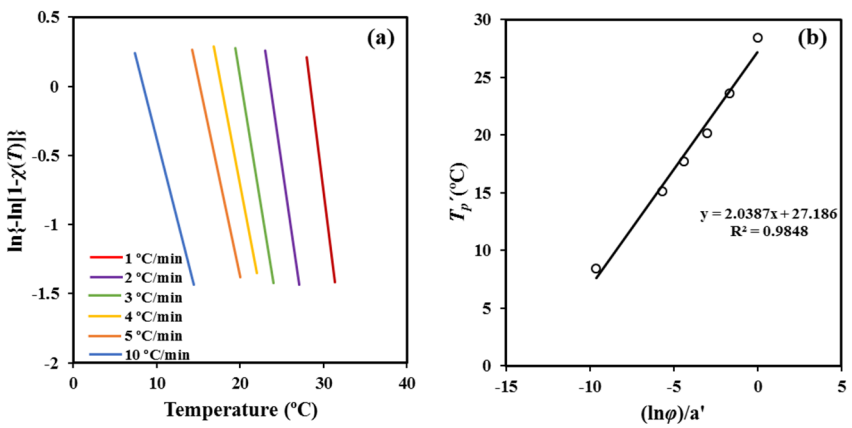

Figure 3.2.7. Plots of ln{−ln[1 − $\chi(T)$]} against temperature for non-isothermal crystallization of P4HB with cooling rates as a parameter (**a**). Determination of the Avrami exponent using linear plots of T_p' against (ln φ)/a' (**b**).

Table 3.2.3. Characteristic crystallization parameters obtained for P4HB by using the methodology developed by Cazé et al.[30].

φ (°C/min)	a'	T_p' (°C)	T_p [a] (°C)
1	−0.49	28.43	28.92
2	−0.41	23.63	24.18
3	−0.37	20.15	20.86

4	−0.32	17.72	19.68
5	−0.28	15.14	16.87
10	−0.24	−9.61	13.27

[a] Temperature determined for the exothermic peak observed in the cooling scans.

3.2.3.3 Isoconversional Methods. Activation Energy

Evaluation of the activation energy of a non-isothermal crystallization from the melt was performed by using the isoconversional method of Friedman. [32] This considers that the energy barrier of crystallization can vary during the non-isothermal melt crystallization according to **Equation 8**.

$$d\chi(T)/dt = A \exp(-\Delta E/RT) f[\chi(T)] \quad (8)$$

where A is a preexponential factor, and $f[\chi(T)]$ is the crystallization model. This method assumes that the activation energy is only constant at a given extent of conversion and for the narrow temperature region associated with this conversion.

The temperature-dependent activation energy is a consequence of the non-Arrhenius behavior expected for the crystallization process. In this sense, it should be indicated that a mistake is derived when other simpler isoconversional methods, such as Kissinger,[33] Kissinger–Akahira–Sunose,[34] Ozawa,[35] and Flynn and Wall,[36] are applied. These methods were also problematic, as indicated by Vyazovkin for crystallization processes that are defined by cooling rate values.[25,37]

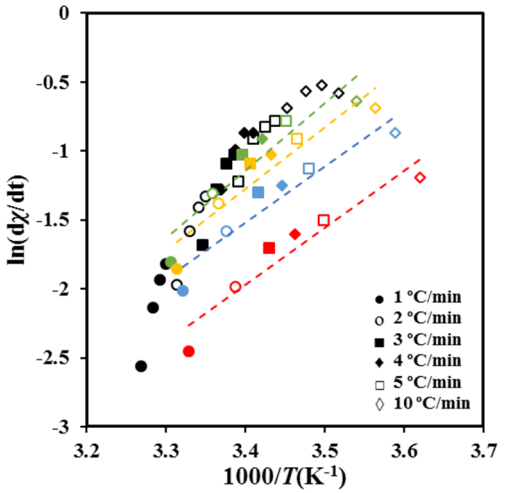

Figure 3.2.8. Plots of $\ln(d\chi/dt)_\chi$ versus $1/T$ for non-isothermal crystallization of P4HB at the indicated cooling rates. Data corresponding to different relative degrees of crystallinity are represented using symbols and lines of different colors (i.e., green, yellow, blue, and red correspond to 0.5, 0.6, 0.7, and 0.8 values, respectively).

Crystallization experiments performed at different cooling rates allow obtaining values for $\ln [d\chi(T)dt]$ at different temperatures and crystallization degrees. For a given conversion, the slopes of the linear plots of $\ln [d\chi(T)dt]$ versus $1/T$ (**Figure 3.2.8**) determines ΔE.

As shown in **Figure 3.2.9a**, the deduced values of the activation energy are negative as expected in the temperature range from the melting point down to the temperature of the maximum crystallization rate. The energy sign indicates that crystallization rates increase with decreasing crystallization temperatures. It should be pointed out that the effective activation energy varies between −45 kJ/mol and −98 kJ/mol covering a wide range of energies. Published results concerning PCL showed a similar variation with a change from −49 kJ mol^{-1} to −110 kJ mol^{-1} with χ_t the ranging from 10 to 90%.[38]

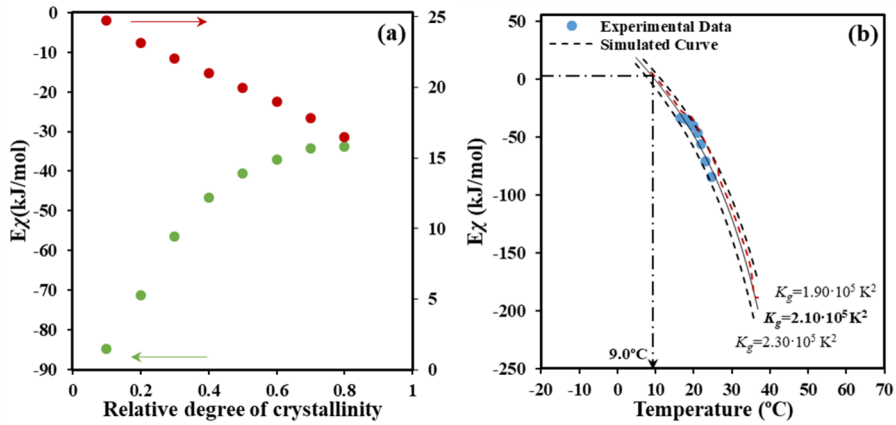

Figure 3.2.9. (**a**) Dependence of the activation energy of crystallization (●) and the average crystallization temperature (●) on crystallinity. (**b**) Experimental *Ex* vs. *T* data for non-isothermal crystallization of P4HB. The solid black line corresponds to the data calculated by **Equation 11** and the optimized crystallization parameters. Arrow indicates the expected temperature for the maximum crystallization rate (i.e., the effective activation energy becomes equal to zero).

Finally, the activation energy can be correlated (**Figure 3.2.9b**) with the crystallization temperature by considering the average temperature associated with a given degree of crystallinity (**Figure 3.2.9a**). Note that the estimation of the activation energy is based on the application of the Arrhenius equation within small temperature regions associated with given values of the degree of crystallinity. The plot clearly shows that the activation energy was negative at temperatures higher than that associated with the maximum crystallization rate and tended to zero when temperature decreased, as extensively discussed by Vyazovkin and Dranca.[39]

3.2.3.4 Secondary Nucleation Constant from Non-isothermal Crystallization

DSC calorimetric data from non-isothermal crystallization experiments can also be employed to known crystal growth parameters as, for example, the secondary nucleation constant.

The Lauritzen–Hoffman model[40] is usually accepted to determine the crystal growth rate, *G*. According to this theory this rate is defined by two terms: (a) The transport activation energy, U^*, which expresses the difficulty of

crystallizing segments to move across the liquid–crystal interface, and (b) the secondary nucleation constant, K_g, which evaluates the formation of new particles in the presence of an established population of previously formed particles. An increase of K_g indicates a greater difficulty for the surface of a growing lamellar crystal to act as an effective nucleus.

The Lauritzen–Hoffman equation is defined by

$$G = G_0 \exp\left[-U^*/(R\,(T_c - T_\infty))\right] \times \exp\left[-K_g/(T_c(\Delta T)\,f)\right] \quad \textbf{(9)}$$

where G_0 is a constant preexponential factor, T_∞ is the temperature below which molecular motion ceases, T_c is the selected crystallization temperature, R is the gas constant, ΔT is the degree of supercooling measured as the difference between the equilibrium melting temperature (T_m^0) and T_c (i.e., $\Delta T = T_m^0 - T_c$), and f is a correction factor accounting for the variation in the bulk melting enthalpy per unit volume with temperature ($f = 2T_c/(T_m^0 + T_c)$).

The temperature dependence of G follows a bell-shaped curve due to the two exponential terms of **Equation 9**. In general, crystallizations from the melt takes place at relatively low degrees of supercooling (right region of the curve) where the influence of the transport term is not highly relevant. In this case, it is usual to perform calculations with standard U^* and T_∞ values as those reported by Suzuki and Kovacs[41] (i.e., $U^* = 1500$ cal/mol and $T_\infty = T_g - 30$ K).

Hoffman and Lauritzen parameters can also be derived from non-isothermal crystallizations by using an isoconversional approach developed by Vyazovkin et al.[42] that has been satisfactorily tested for different polymers, such as poly(ethylene terephthalate),[42] poly(butylene naphthalate),[43] and poly(ethylene naphthalate).[39]

This isoconversional method is based on an explicit dependence of the activation energy on temperature (**Equation 8**) that was derived assuming an equivalence of the temperature coefficients of the growth rate and the heat flow[44] (**Equation 9**).

$$\Delta E_\chi = [U^*T^2/(T - T_\infty)^2] + [K_g R((T_m^0)^2 - T^2 - T_m^0 T)/((T_m^0 - T)^2 T)] \quad \textbf{(10)}$$

$$d(\ln \varphi)/T = d(\ln G)/T \quad (11)$$

The experimental temperature dependence of the activation energy that was determined in the previous section can be related to the theoretical one calculated from the right side of **Equation 8**. U^* and K_g parameters are selected to get the best fit between theoretical and experimental data, which is the process simplified when standard U^* values can be employed. T_m^0 and T_g were taken equal to 79.9 and -45.4 °C, as previously evaluated from the calorimetric analysis of P4HB.[18]

Figure 3.2.9b shows that a reasonable fit between experimental and predicted values is attained with the set of parameters: U^* = 1500 cal/mol, $T_\infty = T_g - 30$ K, and $K_g = 2.10 \times 10^5$ K^2. For the sake of completeness simulated curves for K_g values of 2.30×10^5 K^2 and 1.90×10^5 K^2 are also plotted (dashed lines), illustrating the impact caused by small changes in the nucleation parameter. In the same way, the non-significant influence caused by a change in U^* is also shown by the red dashed line calculated for U^* = 1800 cal/mol, $T_\infty = T_g - 30$ K, and $K_g = 2.10 \times 10^5$ K^2. Interestingly, the deduced parameters from the non-isothermal DSC data became very close to those evaluated from isothermal DSC experiments and direct POM measurements on the spherulitic growth. In this case values of the selected set of parameters became U^* = 1500 cal/mol, $T_\infty = T_g - 30$ K, and $K_g = 1.69 \times 10^5$ K^2 (DSC) and 1.58×10^5 K^2 (POM), which appear in acceptable agreement with those determined by the isoconversional methodology.

Figure 3.2.9b also shows that the activation energy becomes zero at a temperature of 9.0 °C. This zero of energy is associated with the maximum crystallization rate and therefore, should correspond to the maximum of the bell-shaped $G - T$ curve. Note that at higher temperatures (i.e., the region dominated by the secondary nucleation) the activation energy becomes negative and progressively increases with decreasing the temperature. This feature means that the crystallization rate is enhanced with decreasing temperatures as discussed at length by Vyazovkin and Dranca.[39] At lower temperatures than

those corresponding to the maximum rate, the activation energy becomes positive, indicating that G decreases when crystallization temperature decreases. Results of the non-isothermal study show an impressive agreement with the maximum growth rate determined from isothermal measurements from both optical microscopy (i.e., 15.0 °C) and even the calorimetric data (i.e., 14.0 °C).[18]

Overall, crystallization rates determined from DSC data and applying the Avrami analysis (**Table 3.2.1**) can be employed to determine the Lauritzen and Hoffman parameters, considering a proportionality between k and G values. In this case, **Equation 12** can be applied.

$$k = k_0 \exp\left[-U^*/(R\,(T_c - T_\infty))\right] \times \exp\left[-K_g/(T_c(\Delta T)\,f)\right]. \qquad \textbf{(12)}$$

In addition, the temperature associated with each k value was taken as a rough approximation of the peak temperature determined for the DSC runs performed at the corresponding cooling rates.

The plot of $\ln k + U^*/(R\,(T_c - T_\infty))$ versus $1/[T_c\,(\Delta T)\,f]$ gave a straight line with a slope (i.e., the K_g value) of 2.22×10^5 K^2. It is very interesting to point out the great agreement with the secondary nucleation constant determined from the evaluation of activation energies.

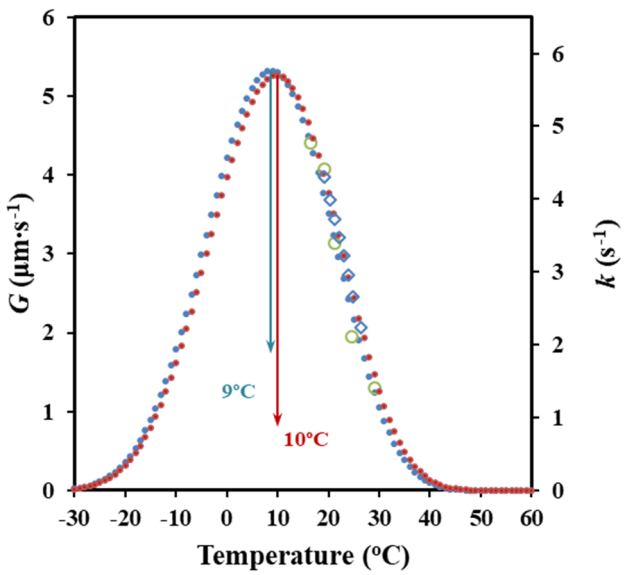

Figure 3.2.10. Comparison between bell-shaped curves of G/k temperature dependence obtained from DSC data and the two non-isothermal methodologies (from Avrami analysis (●) and activation energy (●) with their respective experimental results (o) (◊). An arbitrary value of G_0 has been selected to fit the maximum rate of both curves.

The similarity between both analyses can also be observed in **Figure 3.2.10**, where simulated bell-shaped curves from both sets of data are plotted. The advantages of the isoconversional method are clear since additional information concerning energies are obtained and approximations related to temperature, associated with each cooling rate, avoided.

3.2.3.5 Non-isothermal Crystallization Studies by Optical Microscopy

Spherulitic growth rates for non-isothermal crystallizations can also be determined by optical microscopy.[45–47] In this case the evolution of the spherulite radius (R) with temperature (T) is followed for a constant cooling rate (dT/dt).[45,46] Specifically, the growth rate is given by **Equation 13**. It is necessary to select an appropriate cooling rate to get the maximum information concerning the $G - T_c$ curve. Furthermore, a set of cooling rates can be employed if necessary to extend the curve to higher or lower temperatures.

$$G = dR/dt = (dR/dT) \times (dT/dt) \quad \textbf{(13)}$$

Evolution of the radius versus crystallization temperature during each selected cooling run allows obtaining a plot which is then fitted to polynomial equations. The selected equation corresponds to the lower order that renders a good regression coefficient (r). Growing rates (dR/dT) are then calculated at each crystallization temperature from the first derivative function of the polynomial equation. Experimental problems lie in the choice of the cooling rate required to maximize the crystallization temperature range where radii can be well measured, making necessary, in some cases, the use of various rates.

Figure 3.2.11a shows the evolution of the crystal growth rate of P4HB spherulites with crystallization temperature for a cooling rate of 0.5 °C/min. This rate allowed to cover a wide range of experimental data that are

comparable with those available from non-isothermal DSC experiments. This range was also clearly higher than that defined by both DSC and POM isothermal crystallizations.[18] Therefore, a kinetic analysis was carried out considering only the cooling rate of 0.5 °C/min. A second-order equation (R = 0.1091 T^2 − 10.238 T + 239.89) gave a correlation coefficient of r^2 = 0.996, which was slightly better than those calculated for higher-order equations.

Equation 7 can be applied to obtain crystallization parameters by considering the above-deduced $G - T_c$ data. Thus, the representation of ln G + $U^*/(R\,(T_c - T_\infty))$ versus $1/[T_c(\Delta T)f]$ gave a straight line with an intercept at the origin at ln G_0 and a negative slope equal to K_g (**Figure 3.2.11b**). A single value of K_g was observed in agreement with the above reported DSC data. This single value is a clear indication of a process that took place according to a single crystallization regime. The Lauritzen–Hoffman theory postulated the possibility of three regimes according to the type of nucleation on the crystal surface, being in some cases even related to different morphologies (e.g., axialites, banded/ringed spherulites, and non-ringed ones). Regime II is usually associated with ringed spherulites as those observed for P4HB in the considered temperature range. This regime II obeys a nucleation rate on the crystal surface that is comparable or even greater than the lateral growth rate.

U^* = 1500 cal/mol and $T_\infty = T_g - 30$ K values gave a straight line with r^2 = 0.995 and a K_g parameter of 1.25 × 10^5 K^2. Note that this constant is in complete agreement with that determined by the isoconversional methodology and even the Avrami analysis. Nevertheless, the higher discrepancy was derived from this methodology. It seems that the method has a great advantage due to its simplicity, but some cautions must be taken into account concerning the precision of the derived results. It should be pointed out that POM analyses are independent of the nucleation rate and that some discrepancies with DSC measurements can also be justified.

It is also interesting to note that K_g values determined from isothermal and non-isothermal crystallizations using DSC or POM data are close, with 1.7 ± 0.5 × 10^5 K^2 being the average value. In the same way, temperatures

corresponding to the maximum of the bell-shaped curves that express the dependence of crystal growth rate or the overall crystallization rate on the crystallization temperature showed minimum deviations (i.e., 13 ± 5 °C).

Figure 3.2.11a compares the plots of the experimental and simulated *G* values versus crystallization temperature. The simulated curve was obtained by applying **Equation 9** and the deduced Lauritzen–Hoffman parameters. This curve had a typical bell shape and showed a maximum at 19 °C, which was relatively higher than the temperature deduced from the isoconversional methodology and the DSC non-isothermal data.

Figure 3.2.11c compares the bell-shaped curves obtained from all the performed crystallization studies. For the sake of simplicity, arbitrary units have been employed for the ordinate axis due to the different represented rates (i.e., *G* and *k*). A relatively good agreement was in general observed between the isothermal and the non-isothermal studies and between DSC and POM techniques. In general, non-isothermal methods have advantages derived from their higher simplicity, the larger number of available experimental data, and finally, the closest fit to realistic processing conditions. Crystallization under isothermal and non-isothermal conditions is obviously different and consequently, slight differences, such as those detected for the secondary nucleation constant and the temperature associated with the maximum crystallization rate, can be expected.

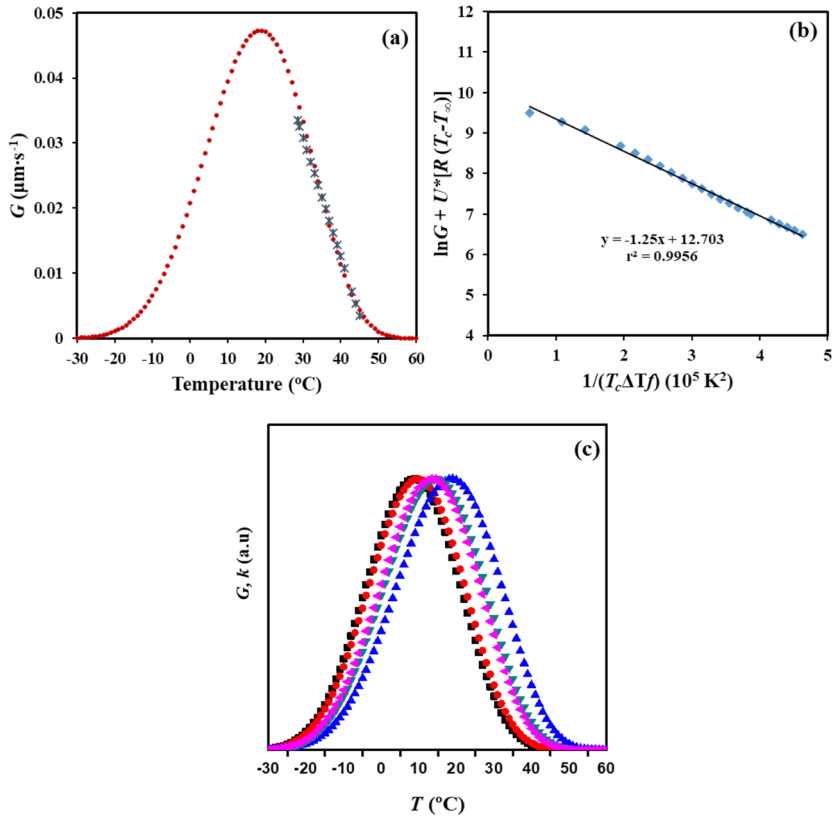

Figure 3.2.11. (**a**) Experimental and simulated dependence of the growth rate on crystallization temperature. (**b**) Plot of ln $G + U^*/R\ (T_c - T_\infty)$ versus $1/T_c\ (\Delta T)\ f$ to determine the K_g secondary nucleation parameter of P4HB. (**c**) Comparison between bell-shaped curves derived from non-isothermal DSC data ((●) from isoconversional and (■) from Avrami analyses), non-isothermal POM data (▲) and isothermal DSC data (◀) and POM (▼) data.

3.2.3.6 Synchrotron Data on Non-isothermal Crystallization of P4HB

The cooling rate has an influence on the final morphology and even on the crystallinity of P4HB despite its rapid crystallization. Thus, melting enthalpy decreased from 39.6 kJ/mol to 35.2 kJ/mol when the cooling rate increased from 1 °C/min to 5 °C/min, while spherulitic size and texture changed (**Figure 3.2.12**). The average crystallization temperature decreased with the increase of the cooling rate (**Figure 3.2.1**) and consequently, primary nucleation increased,

leading to a decrease in the spherulite size (**Figure 3.2.12**). Spacing between rings was also temperature-dependent as discussed earlier (**Figure 3.2.5**).

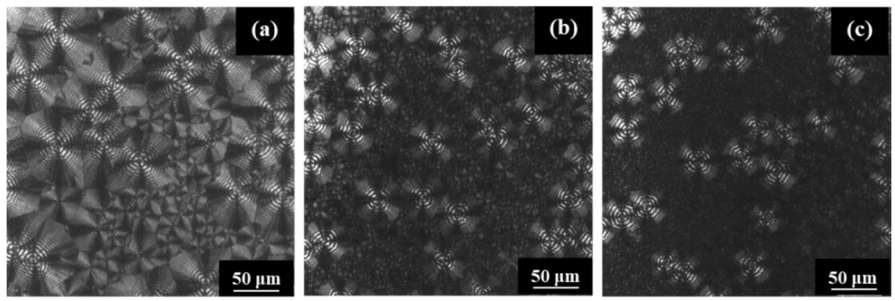

Figure 3.2.12. Optical micrographs taken at the end of the non-isothermal crystallizations of P4HB performed at cooling rates of 0.5 °C/min (**a**), 3 °C/min (**b**), and 5 °C/min (**c**).

Morphology of constitutive lamellae depends not only on the crystallization rate, as indicated for the twisting period (i.e., interring spacing), but also on the lamellar thickness. Small-angle X-ray scattering patterns (SAXS) taken in real-time during the cooling process allowed us to follow the evolution of lamellar thickness during crystallization and also allowed us to compare morphological parameters for different cooling rates through the use of the normalized correlation function:

$$\gamma(r) = \int_0^\infty q^2 I(q) \cos(qr) dq \Big/ \int_0^\infty q^2 I(q) dq \qquad (14)$$

where $I(q)$ is the intensity of the SAXS peak at each value of the scattering vector ($q = [4\pi/\lambda] \sin \theta = 2\pi/d$, θ and d being the Bragg angle and the Bragg spacing, respectively).

Long period, L_p, amorphous layer thickness, l_a, and crystalline lamellar thickness, l_c, can be determined by the normalized one-dimensional correlation function[48] and applying Vonk's model[49] and Porod's law to perform extrapolations to low and high q values.

Figure 3.2.13 shows the evolution of the SAXS peak during the non-isothermal crystallization from the melt at a representative cooling rate of 7 °C/min. This scattering peak appeared at the same temperature as the wide-

angle X-ray reflections, which are presumable for a crystallization, where the supramolecular structure (lamellae) is developed at the same time that the molecular arrangement took place. Wide-angle X-ray diffraction (WAXD) profiles show two main peaks at 0.406 nm and 0.388 nm that correspond to the (110) and (200) reflections of the orthorhombic structure (a = 0.775 nm, b = 0.477 nm, and c (fiber axis) = 1.199 nm) reported for P4HB[15].

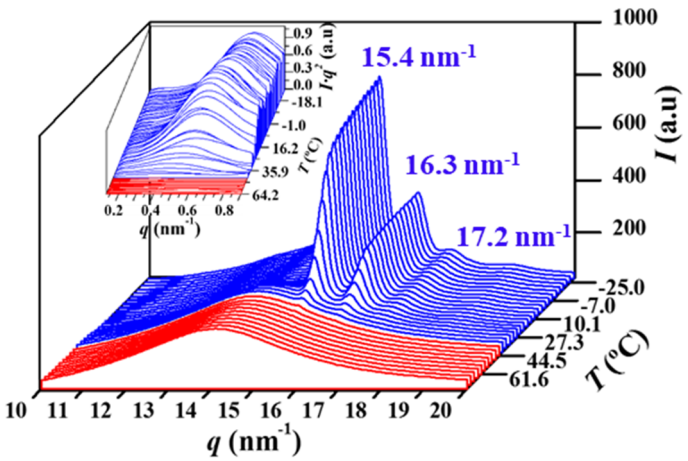

Figure 3.2.13. Three-dimensional wide-angle X-ray diffraction (WAXD) and small-angle X-ray scattering patterns (SAXS) profiles of P4HB during cooling at a rate of 7 °C/min.

Deconvolution of WAXD profiles allowed for the determination of the temperature evolution of crystallinity during cooling runs performed at three different representative rates (**Figure 3.2.14**). Results indicated that the increase of the cooling rate led to a decrease of the temperature at which crystallization started and as well as of the crystallinity (i.e., crystallinities around 65%, 60%, and 46% were determined for 3 °C/min, 7 °C/min, and 10 °C/min, respectively). Logically, the crystallization rate diminished when temperatures approached −20 °C (i.e., at some degrees above the glass transition temperature of −45.4 °C). It is also clear that samples are mainly crystallized at a lower average temperature when the cooling rate increased, and consequently, some influence on the derived lamellar morphology should be expected.

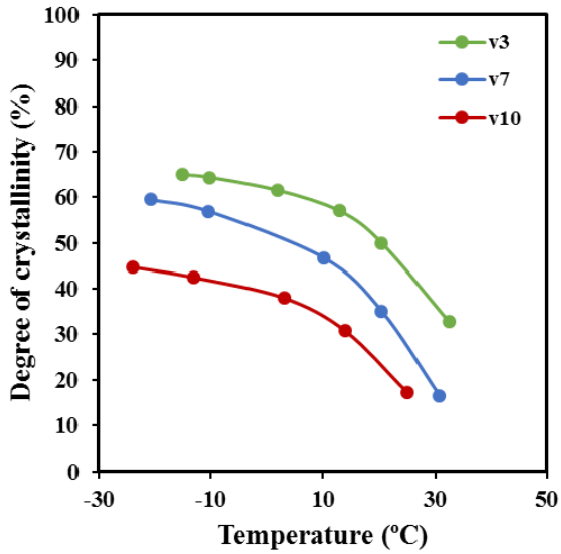

Figure 3.2.14. Evolution of the absolute degree of crystallinity determined from WAXD profiles with temperature for the indicated cooling rates.

Figure 3.2.15a compares the correlation functions corresponding to the end of crystallizations performed at 10 °C/min and 3 °C/min. Slight but significant changes can be detected, with peaks being clearly defined for the crystallization performed at the lower rate. In this case, the contrast between the amorphous and crystalline regions is increased. Lamellae became narrower (8.70 nm versus 9.70 nm for L_γ) for the crystallization performed at the lower rate, mainly as a consequence of the decrease in l_c (i.e., 7.08 nm versus 7.61 nm), although a slight decrease in l_a (i.e., 1.62 nm versus 2.09 nm) was also detected. Note that the average crystallization temperature is superior for samples crystallized at the lower cooling rate, consequently with an expected greater lamellar thickness. The opposite results that were attained can be explained due to a lamellar reinsertion mechanism that took place. This process is the consequence of the formation of thinner lamellar crystals between the loosely stacked primary lamellae and appears to be more significant when the crystallization process is slower.

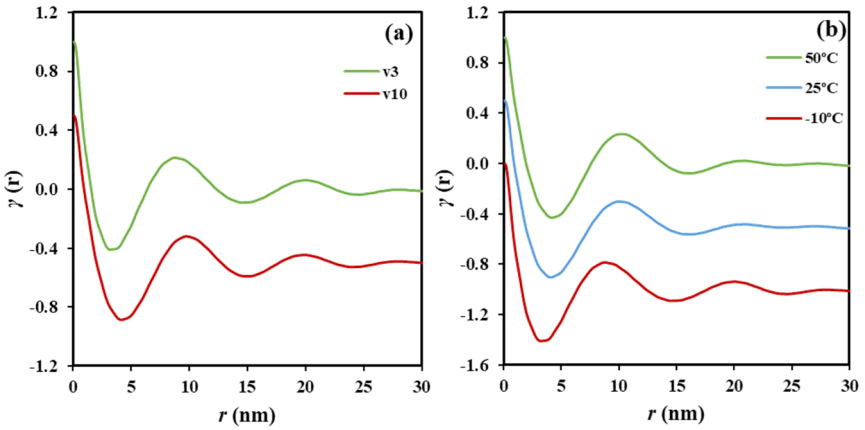

Figure 3.2.15. (**a**) Correlation functions obtained after non-isothermal crystallizations of P4HB from the melt state performed at cooling rates of 3 and 10 °C/min. (**b**) SAXS correlation functions calculated at the indicated temperatures during the cooling run (3 °C/min) of a melted P4HB sample.

Figure 3.2.15b compares the correlation function obtained at the beginning, an intermediate stage, and the end of the crystallization process performed at a rate of 3 °C/min. Lamellar spacings decreased (i.e., 10.10/9.90/8.70 for L_γ, 2.09/1.98/1.62 for l_a and 8.01/7.92/7.08 for l_c) when the temperature did. The indicated evolution (also observed for the other rates) points out a lamellar insertion mechanism and a molecular rearrangement in the amorphous layer. The bilayer model demonstrated an improvement in the molecular arrangement in the crystalline domains as visualized by the increase in the contrast of the electronic density of amorphous and crystalline layers, or even by the increase in the crystallinity within the lamellar stacks ($X_c^{SAXS} = l_c/L_\gamma$) which varied from 0.79 to 0.81.

3.2.4 CONCLUSIONS

Non-isothermal crystallization studies of P4HB were performed by calorimetric experiments and allowed the determination of crystallization parameters by considering both the classical Avrami analysis and isoconversional methods. In the first case, the determined Avrami parameters had no physical sense but gave an estimation of the variation of the overall

crystallization rate with crystallization temperature, when average crystallization temperatures were assumed for experiments performed at different cooling rates. Additionally, this approximation made feasible the evaluation of the secondary nucleation constant. The isoconversional analysis provided information concerning the activation energy and allowed the estimation of both the temperature associated with the maximum crystallization rate and the secondary nucleation constant. Both methodologies were in remarkable agreement with the derived secondary nucleation constants (i.e., 2.10×10^5 K^2 and 2.22×10^5 K^2), as well as the temperatures associated with the maximum growth rate/overall crystallization rate (i.e., 9 and 10 °C). Optical microscopy data allowed the estimation of crystal growth rates at different crystallization temperatures. Results were independent of primary nucleation and in relatively good agreement with calorimetric analyses. Discrepancies could be associated with a lower precision of the method or to the effect caused by thermal nucleation. The obtained results are also comparable with previously reported data from isothermal crystallization. In this case, DSC and POM analysis were in satisfactory agreement suggesting a scarce influence of thermal nucleation. The cooling rate had a great effect on the morphology and texture of spherulites, as well as the twisting and thickness of the constitutive lamellar crystals. WAXD synchrotron experiments allowed for the determination of final crystallinities and demonstrated a lower crystallization when the cooling rate increased. More interestingly, SAXS data indicated a lamellar insertion mechanism during crystallization that led to a decrease of the crystalline layer thickness. This process was more significant when the cooling rate decreased. The crystallinity of lamellar stacks slightly increased during the cooling run due to the similar thickness evolution of amorphous and crystalline layers.

3.2.5 REFERENCES

(1) Williams, S. F.; Rizk, S.; Martin, D. P. Poly-4-Hydroxybutyrate (P4HB): A New Generation of Resorbable Medical Devices for Tissue Repair and Regeneration. *Biomed. Eng. (NY).* **2013**, *58* (5), 439–452. https://doi.org/10.1515/bmt-2013-0009.

(2) Ackermann, J. uwe; Müller, S.; Lösche, A.; Bley, T.; Babel, W. Methylobacterium Rhodesianum Cells Tend to Double the DNA Content under Growth Limitations and Accumulate PHB. *J. Biotechnol.* **1995**, *39* (1), 9–20. https://doi.org/10.1016/0168-1656(94)00138-3.

(3) Huisman, G. W.; Skraly, F. Biological Systems for Manufacture of Polyhydroxyalkanoate Polymers Containing 4-Hydroxyacids. US 6,316,262, 2001.

(4) Dennis, D. E.; Valentin, H. E. Methods of Making Polyhydroxy alkanoates Comprising 4 -Hydroxybutyrate Monomer Units. 6,117, 658, 2000. https://doi.org/US005485919A.

(5) Hori, Y.; Yamaguchi, A.; Hagiwara, T. Chemical Synthesis of High Molecular Weight Poly(3-Hydroxybutyrate-Co-4-Hydroxybuty rate). *Polymer (Guildf).* **1995**, *36* (24), 4703–4705. https://doi.org/10.1016/0032-3861(95)96838-Y.

(6) Houk, K. N.; Jabbari, A.; Hall, H. K.; Aleman, C. Why δ-Valerolactone Polymerizes and Gamma-Butyrolactone Does Not. *J. Org. Chem.* **2008**, *73* (7), 2674–2678. https://doi.org/10.1021/jo702567v.

(7) Odermatt, E. K.; Funk, L.; Bargon, R.; Martin, D. P.; Rizk, S.; Williams, S. F. MonoMax Suture: A New Long-Term Absorbable Monofilament Suture Made from Poly-4-Hydroxybutyrate. *Int. J. Polym. Sci.* **2012**, *2012*, 1–12. https://doi.org/10.1155/2012/216137.

(8) Zhou, X.-Y.; Yuan, X.-X.; Shi, Z.-Y.; Meng, D.-C.; Jiang, W.-J.; Wu, L.-P.; Chen, J.-C.; Chen, G.-Q. Hyperproduction of Poly(4-Hydroxy butyrate) from Glucose by Recombinant Escherichia Coli. *Microb. Cell Fact.* **2012**, *11* (1), 54. https://doi.org/10.1186/1475-2859-11-54.

(9) Chen, G. Q.; Wu, Q. The Application of Polyhydroxyalkanoates as Tissue Engineering Materials. *Biomaterials* **2005**, *26* (33), 6565–6578. https://doi.org/10.1016/j.biomaterials.2005.04.036.

(10) Martin, D. P.; Williams, S. F. Medical Applications of Poly-4-Hydroxybutyrate: A Strong Flexible Absorbable Biomaterial. *Biochem. Eng. J.* **2003**, *16*, 97–105. https://doi.org/10.1016/S1369-703X(03)00040-8.

(11) Plymale, M. A.; Davenport, D. L.; Dugan, A.; Zachem, A.; Roth, J. S. Ventral Hernia Repair with Poly-4-Hydroxybutyrate Mesh. *Surg.*

Endosc. **2018**, *32* (4), 1689–1694. https://doi.org/10.1007/s00464-017-5848-7.

(12) Rao, U.; Sridhar, R.; Sehgal, P. K. Biosynthesis and Biocompatibility of Poly(3-Hydroxybutyrate-Co-4-Hydroxybutyrate) Produced by Cupriavidus Necator from Spent Palm Oil. *Biochem. Eng. J.* **2010**, *49* (1), 13–20. https://doi.org/10.1016/j.bej.2009.11.005.

(13) Generali, M.; Kehl, D.; Capulli, A. K.; Parker, K. K.; Hoerstrup, S. P.; Weber, B. Comparative Analysis of Poly-Glycolic Acid-Based Hybrid Polymer Starter Matrices for in Vitro Tissue Engineering. *Colloids Surfaces B Biointerfaces* **2017**, *158*, 203–212. https://doi.org/10.1016/j.colsurfb.2017.06.046.

(14) Mitomo, H.; Kobayashi, S.; Morishita, N.; Doi, Y. . *Polym. Prepr.* **1995**, *44*, 3156.

(15) Su, F.; Iwata, T.; Sudesh, K.; Doi, Y. Electron and X-Ray Diffraction Study on Poly(4-Hydroxybutyrate). *Polymer (Guildf).* **2001**, *42* (21), 8915–8918. https://doi.org/10.1016/S0032-3861(01)00412-8.

(16) Su, F.; Iwata, T.; Tanaka, F.; Doi, Y. Crystal Structure and Enzymatic Degradation of Poly(4-Hydroxybutyrate). *Macromolecules* **2003**, *36* (17), 6401–6409. https://doi.org/10.1021/ma034546s.

(17) Koyama, N.; Doi, Y. Effects of Solid-State Structures on the Enzymatic Degradability of Bacterial Poly(Hydroxyalkanoic Acids). *Macromolecules* **1997**, *30* (4), 826–832. https://doi.org/10.1021/ma961195r.

(18) Keridou, I.; del Valle, L. J.; Funk, L.; Turon, P.; Yousef, I.; Franco, L.; Puiggalí, J. Isothermal Crystallization Kinetics of Poly(4-Hydroxybutyrate) Biopolymer. *Polym. Morphol. Princ. Charact. Process.* **2019**, *12* (2488), 1–20. https://doi.org/10.3390/ma12152488.

(19) Avrami, M. Kinetics of Phase Change. I: General Theory. *J. Chem. Phys.* **1939**, *7* (12), 1103–1112. https://doi.org/10.1063/1.1750380.

(20) Avrami, M. Kinetics of Phase Change. II Transformation-Time Relations for Random Distribution of Nuclei. *J. Chem. Phys.* **1940**, *8* (2), 212–224. https://doi.org/10.1063/1.1750631.

(21) Mandelkern, L. *Crystallization of Polymers: Volume 2, Kinetics and Mechanisms.*; Cambridge University Press, 2004.

(22) Limwanich, W.; Phetsuk, S.; Meepowpan, P.; Kungwan, N. Kinetics Studies of Non-Isothermal Melt Crystallization of Poly (ε -Caprolactone) and Poly (L-Lactide). *Chiang Mai J. Sci.* **2016**, *43* (2), 329–338.

(23) Ozawa, T. Kinetics of Non-Isothermal Crystallization. *Polymer (Guildf).* **1971**, *12* (3), 150–158.

(24) Evans, U. R. The Laws of Expanding Circles and Spheres in Relation to the Lateral Growth of Surface Films and the Grain-Size of Metals.

Trans. Faraday Soc. **1945**, *41*, 365.

(25) Vyazovkin, S. Nonisothermal Crystallization of Polymers: Getting More out of Kinetic Analysis of Differential Scanning Calorimetry Data. *Polym. Cryst.* **2018**, *1* (2), e10003. https://doi.org/10.1002/pcr2.10003.

(26) Liu, T.; Mo, Z.; Wang, S.; Zhang, H. Non-Isothermal Melt and Cold Crystallization Kinetics of Poly(Aryl Ether Ether Ketone Ketone). *Polym. Eng. Sci.* **1997**, *37* (3), 568–575. https://doi.org/10.1016/S0014-3057(97)00016-5.

(27) Márquez, Y.; Franco, L.; Turon, P.; Martínez, J. C.; Puiggalí, J. Study of Non-Isothermal Crystallization of Polydioxanone and Analysis of Morphological Changes Occurring during Heating and Cooling Processes. *Polymers (Basel).* **2016**, *8* (10), 351. https://doi.org/10.3390/polym8100351.

(28) Tarani, E.; Wurm, A.; Schick, C.; Bikiaris, D. N.; Chrissafis, K.; Vourlias, G. Effect of Graphene Nanoplatelets Diameter on Non-Isothermal Crystallization Kinetics and Melting Behavior of High Density Polyethylene Nanocomposites. *Thermochim. Acta* **2016**, *643*, 94–103. https://doi.org/10.1016/j.tca.2016.09.018.

(29) Jape, S. P.; Deshpande, V. D. Nonisothermal Crystallization Kinetics of Nylon 66/LCP Blends. *Thermochim. Acta* **2017**, *655*, 1–12. https://doi.org/10.1016/j.tca.2017.06.007.

(30) Cazé, C.; Devaux, E.; Crespy, A.; Cavrot, J. P. A New Method to Determine the Avrami Exponent by d.s.c. Studies of Non-Isothermal Crystallization from the Molten State. *Polymer (Guildf).* **1997**, *38* (3), 497–502. https://doi.org/10.1016/S0032-3861(96)00552-6.

(31) Márquez, Y.; Franco, L.; Turon, P.; Puiggalí, J. Isothermal and Non-Isothermal Crystallization Kinetics of a Polyglycolide Copolymer Having a Tricomponent Middle Soft Segment. *Thermochim. Acta* **2014**, *585*, 71–80. https://doi.org/10.1016/j.tca.2014.03.049.

(32) Friedman, H. L. Kinetics of Thermal Degradation of Char-Forming Plastics from Thermogravimetry. Application to a Phenolic Plastic. *J. Polym. Sci. Part C* **1964**, *6* (1), 183–195. https://doi.org/10.1002/polc.5070060121.

(33) Kissinger, H. E. Reaction Kinetics in Differential Thermal Analysis. *Anal. Chem.* **1957**, *29* (11), 1702–1706. https://doi.org/10.1021/ac60131a045.

(34) Akahira, T.; Sunose, T. Joint Convention of Four Electrical Institutes. *Sci. Technol.* **1971**, *16*, 22–31.

(35) Takeo, O. A New Method of Analyzing Thermogravimetric Data. *Bull. Chem. Soc. Jpn.* **1965**, *38* (11), 1881–1886. https://doi.org/10.1246/bcsj.38.1881.

(36) Flynn, J.; Wall, L. General Trement of the Therogravimetry of Polymers. *J. Res. Natl. Bur. Stand. (1934).* **1966**, *70A* (6), 487–523.

(37) Vyazovkin, S. Is the Kissinger Equation Applicable to the Processes That Occur on Cooling? *Macromol. Rapid Commun.* **2002**, *23* (13), 771–775. https://doi.org/10.1002/1521-3927(20020901)23:13<771::AID-MARC771>3.0.CO;2-G.

(38) Pires, L. S. O.; Fernandes, M. H. F. V.; de Oliveira, J. M. M. Crystallization Kinetics of PCL and PCL–Glass Composites for Additive Manufacturing. *J. Therm. Anal. Calorim.* **2018**, *134* (3), 2115–2125. https://doi.org/10.1007/s10973-018-7307-7.

(39) Vyazovkin, S.; Dranca, I. Isoconversional Analysis of Combined Melt and Glass Crystallization Data. *Macromol. Chem. Phys.* **2006**, *207* (1), 20–25. https://doi.org/10.1002/macp.200500419.

(40) Lauritzen, J. I.; Hoffman, J. D. Extension of Theory of Growth of Chain-Folded Polymer Crystals to Large Undercoolings. *J. Appl. Phys.* **1973**, *44* (10), 4340–4352. https://doi.org/10.1063/1.1661962.

(41) Suzuki, T.; Kovacs, A. J. Temperature Dependence of Spherulitic Growth Rate of Isotactic Polystyrene. A Critical Comparison with the Kinetic Theory of Surface Nucleation. **1970**, *1* (1), 82–100.

(42) Vyazovkin, S.; Sbirrazzuoli, N. Isoconversional Approach to Evaluating the Hoffman-Lauritzen Parameters (U* and Kg) from the Overall Rates of Nonisothermal Crystallization. *Macromol. Rapid Commun.* **2004**, *25* (6), 733–738. https://doi.org/10.1002/marc.200300295.

(43) Achilias, D. S.; Papageorgiou, G. Z.; Karayannidis, G. P. Evaluation of the Isoconversional Approach to Estimating the Hoffman-Lauritzen Parameters from the Overall Rates of Non-Isothermal Crystallization of Polymers. *Macromol. Chem. Phys.* **2005**, *206* (15), 1511–1519. https://doi.org/10.1002/macp.200500175.

(44) Toda, A.; Oda, T.; Hikosaka, M.; Saruyama, Y. A New Method of Analysing Transformation Kinetics with Temperature Modulated Differential Scanning Calorimetry: Application to Polymer Crystal Growth. *Polymer (Guildf).* **1997**, *38* (1), 231–233. https://doi.org/10.1016/S0032-3861(96)00627-1.

(45) Chen, M.; Chung, C. T. Analysis of Crystallization Kinetics of Poly(Ether Ether Ketone) by a Nonisothermal Method. *J. Polym. Sci. Part B Polym. Phys.* **1998**, *36* (13), 2393–2399. https://doi.org/10.1002/(SICI)1099-0488(19980930)36:13<2393::AID-POLB14>3.0.CO;2-Z.

(46) Di Lorenzo, M. L.; Cimmino, S.; Silvestre, C. Nonisothermal Crystallization of Isotactic Polypropylene Blended with Poly(α-Pinene). 2. Growth Rates. *Macromolecules* **2000**, *33* (10), 3828–3832.

https://doi.org/10.1021/ma992037d.

(47) Lorenzo, D. M. L. Determination of Spherulite Growth Rates of Poly(L-Lactic Acid) Using Combined Isothermal and Non-Isothermal Procedures. *Polymer (Guildf).* **2001**, *42* (23), 9441–9446. https://doi.org/10.1016/S0032-3861(01)00499-2.

(48) Vonk, C. G.; Kortleve, G. X-Ray Small-Angle Scattering of Bulk Polyethylene. *Kolloid Z Z Polym* **1967**, *220*, 19–24.

(49) Vonk, C. G. A General Computer Program for the Processing of Small-Angle X-Ray Scattering Data. *J. Appl. Crystallogr.* **1975**, *8*, 340–341.

4. Degradation studies of poly-4-hydroxy butyrate.

Hydrolytic degradation of annealed fibers and films of poly-4-hydroxybutyrate (P4HB) has been studied considering media of different pH values (i.e., 3, 7, and 10) and temperatures (i.e., 37 and 55 °C), in order to comprehend the relationships between crystalline morphology and degradability. Enzymatic degradation has also been evaluated at physiological conditions using two different lipases: *Pseudomonas cepacia* and *Rhizopus oryzae*.

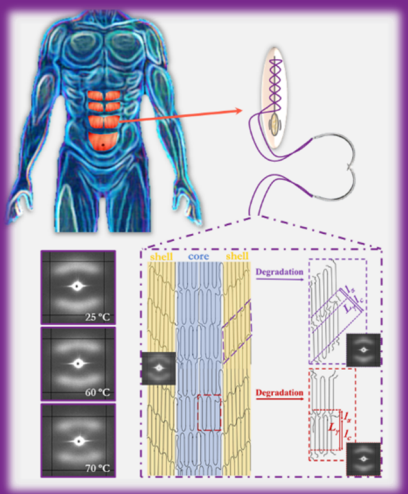

Different bulk and surface erosion mechanisms with random chain scissions and successive removal of monomer units have been supported through weight loss measurements, molecular weight determinations by GPC and NMR spectroscopy, and finally, changes in thermal properties by DSC.

In the case of annealed fibers, small-angle X-ray diffraction studies revealed a supramolecular structure with two different types of lamellar stacks. These were caused by the distinct shear stresses that the core and the shell of the fiber suffered during the severe annealing process. External lamellae were characterized by surfaces tilted 45◦ with respect to the stretching direction and a higher thickness, while the inner lamellae were more imperfect and had their surfaces perpendicularly oriented to the fiber axis. In all cases, WAXD data indicated that the chain molecular axis was aligned with the fiber axis and molecules were arranged according to a single orthorhombic structure. A gradual change of the microstructure was observed as a function of the progress of hydrolysis while changes were not evident under an enzymatic attack

Hydrolysis of annealed fibers mainly affected the inner lamellar stacks as revealed by the direct SAXS patterns and the analysis of correlation functions. Both lamellar crystalline and amorphous thicknesses slightly increased as well as the electronic contrast between amorphous and crystalline regions. Thermal treatments of samples exposed to the hydrolytic media revealed microstructural changes caused by degradation, with the inner lamellae being those that melted faster.

Degradation of the films influenced the melting temperature and crystallinity of samples, as well as on the lamellar geometrical parameters as evaluated by SAXS. Enzymatic degradation of the films was ideal to selectively eliminate the amorphous regions and highlight the spherulitic morphology. The presence of ringed textures was therefore evident in bright field optical micrographs in addition to SEM images, namely observations under polarized light was not necessary to distinguish the presence of banded spherulites. *Rhizopus oryzae* was revealed to be the most suitable enzyme to crop out the P4HB spherulites that form part of the initial smooth surfaces of solvent casting films. After determining the appropriate activity and exposure time, the presence of rings constituted by cooperative C-shaped edge-on lamellae and flat-on lamellae was highlighted.

4.1 MICROSTRUCTURAL CHANGES DURING DEGRADATION OF BIOBASED POLY-4-HYDROXY BUTYRATE SUTURES

4.1.1 INTRODUCTION

Synthetic bioabsorbable sutures have been commercialized since the early 1970s when braided polyglycolide sutures were developed[1]. Since then, different homopolymers and copolymers have been employed in order to provide a controlled degradation rate and a good fit with the required function as temporary wound support. Although initial sutures were processed in a braided form to reduce stiffness and facilitate manipulation, the use of resorbable monofilament forms was since the 1980s when polydioxanone sutures were developed.[2] Advantages of this form involve the reduction of problems associated with tissue drag and the decrease of infection risk derived from a capillary effect. In general, traditional monofilament sutures have a fast or medium degradation rate, with a long term decomposition profile having been developed more recently. Specifically, MonoMax® has been commercialized in 2009 for abdominal wall repair applications.[3] This suture is based on poly-4-hydroxybutyrate (P4HB) and is currently probably the most pliable monofilament suture. Specific mechanical properties of P4HB are 50 MPa, 70 MPa, and 1000% for tensile strength, tensile modulus, and elongation at break.[4] The polymer is fully biocompatible since its degradation leads to 4-hydroxybutyrate, which is a molecule resulting from the metabolism of 4-aminobutyrate (GABA). The degradation process of the polymer P4HB in the human body is initiated by hydrolysis caused by the water diffused into the polymer bulk[5], but enzymes such as lipases are also able to promote a surface attack.[5,6]

Poly(hydroxyalkanoate)s (PHA)s constitute a big family of polyesters that show common properties such as biocompatibility, biodegradability, and non-toxicity.[7] These properties together with a great elasticity justify the increasing

use of P4HB in different biomedical applications.[8] In fact, P4HB is the only PHA that has been approved by the FDA (2007) for biomedical uses. In addition to MonoMax® (i.e., a long term bioresorbable suture), TephaFLEX, BioFiber, Phasix, and GalaFLEX are other commercial P4HB based materials that are employed in medical devices such as abdominal wall closure materials, tendon repair scaffolds, hernia repair meshes, and reconstructive surgery materials.[6,9–11]

P4HB sutures and implants, in general, have advantages derived from the gradual loss of mechanical properties and the gradual release of degradation products into the blood that is in contrast with the behavior of the firstly employed polyglycolide materials.[12]

Commercial P4HB is obtained using fermentation processes. Chemical synthesis is disfavored because of the low molecular weight samples (i.e., around 5000 g/mol) that have been attained in most of the studied processes.[13,14] Formation of γ-butyrolactone rings is kinetically favored with respect to the polymer chain extension and consequently, ring-opening polymerization is only feasible under highly expensive high-pressure processes, which lead to moderate molecular weight around 50,000 g/mol [14]. The biosynthesis of P4HB is rather complex since typical bacteria (e.g., *Ralstonia eutropha* that was the first one employed) also incorporate 3-hydroxybutyrate units despite employing nutrient media based only on 4-hydroxybutyrate and γ-butyrolactone.[15] Currently, the P4HB homopolymer is mainly obtained from engineered *E. coli* K12[16] since this transgenic microorganism can produce the P4HB homopolymer even from inexpensive carbon sources such as glucose or lactose.

P4HB is a semicrystalline polymer able to crystallize as single lamellar crystals and defined by an orthorhombic structure (a = 0.775 nm, b = 0.477 nm, and c (fiber axis) = 1.199 nm) as deduced from electron and X-ray diffraction patterns.[17–19] This structure is defined by an antiparallel arrangement of molecular chains that adopt a slightly distorted all-trans conformation.

Monofilament P4HB threads are submitted to extensive annealing processes under mechanical stress and temperature before commercialization. This treatment has repercussions on the melting behavior due to the reorganization of constitutive crystals. Thus, the melting temperature becomes close to 72 °C after annealing, a value that contrasts with the temperature of 58 °C determined for melt crystallized samples.[20,21] Stretching of P4HB leads to a significant increase of its rigidity while flexibility is maintained. This is a distinctive feature with respect to those of other common biodegradable polyesters such as polyglycolide and polylactide,[6] which become brittle under stress and consequently cannot be submitted to similar processes of alignment. Therefore, P4HB can display a particular microstructure that should be characterized by a high orientation of molecular chains along the stretching direction and a compact stacking of constitutive lamellae.

Microstructure and crystalline morphology of materials are crucial factors that influence their degradability. It is well known that degradation proceeds through the amorphous regions and consequently the specific arrangement of spherulites (melt crystallized samples) and lamellar stacks (oriented and annealed fibers) are meaningful. Degradation conditions (e.g., pH of hydrolytic media or the presence of enzymes) affect the microstructure on the material and may lead to distinctive morphological features as a consequence of preferential attack to the surface or the bulk, and in this case on interlamellar stacks or interfibrillar domains.[22] An assessment of the effect of degradation on the microstructure of stretched P4HB fibers was the main goal of the work reported here due to the peculiar and highly oriented molecular arrangement that can be attained with this high molecular weight and flexible polymer. Results should be interesting to progress on the comprehension of the relationships between crystalline morphology and degradability.

4.1.2 MATERIALS AND METHODS

Commercially available sutures of P4HB (Monomax® USP 1) were kindly supplied by B. Braun Surgical S.A.U. The weight and number average molecular

weights of Monomax® samples were 215,000 and 68,000 g/mol, as determined by GPC.

Pseudomonas cepacia and *Rhizopus oryzae* enzymes with a specific activity of 40.0 and 55.7 U/mg solid, respectively, were obtained from Sigma-Aldrich (Madrid, Spain). All reagents, citric acid, phosphoric acid, chloride acid, boric acid, sodium hydroxide, sodium azide, and chloroform ($CHCl_3$) were supplied by Fisher Chemical (Hampton, NH, USA).

4.1.2.1 Hydrolytic and Enzymatic Degradation

In vitro, hydrolytic degradation studies were directly carried out with commercial sutures (USP 1) with 1 cm long fragments. For the sake of completeness, melt pressed films (5 bars, 60 °C) with dimensions of 1 cm × 1 cm × 150 μm were also evaluated. Assays were carried out at 37 and 55 °C at different pH values of 3, 7, and 10 using the Universal buffer (citrate-phosphate-borate/HCl) solution.[23] This was prepared by mixing 20 mL of the stock solution with *x* mL of 0.1 M HCl and distilled water up to 100 mL. The stock solution (1 L) contained 100 mL of citric acid, 100 mL of phosphoric acid, 3.54 g of boric acid, and 343 mL of 1 M NaOH. Therefore, the buffers of pH 3, pH 7, and pH 10 values were obtained by mixing 20 mL of the stock solution and 56.9, 32.9, and 18.1 mL of 0.1 M HCl, respectively. Samples were kept under orbital shaking in bottles filled with 50 mL of the degradation medium and sodium azide (0.03-wt%) to prevent microbial growth for selected exposure times. The samples were then thoroughly rinsed with distilled water, dried to constant weight at reduced pressure, and stored over P_4O_{10} before analysis. Weight retention was evaluated during degradation as well as the changes in molecular weight. Degradation studies were performed in triplicate and the given data correspond to the average values.

Enzymatic degradation studies were performed with both sutures and melt pressed films having the above-indicated geometry. All samples were exposed to 1 mL of phosphate-buffered saline (PBS) (pH 7.4) containing the determined enzyme alongside with sodium azide (0.03 % *w*/*v*). These solutions were

renewed every 48 h to prevent enzymatic activity loss. Samples were kept at 37 °C in an orbital shaker at 80 rpm. Samples were taken from the media at determined times, washed three times with Milli-Q water, and dried in an oven at 37 °C for 24 h to determine the dry weight. All the experiments were conducted in triplicate. The degraded samples were carbon coated and observed in SEM with an accelerating voltage of 15 kV.

4.1.2.2 Measurements

The molecular weight was estimated by size exclusion chromatography (GPC) using a liquid chromatograph (Shimadzu, model LC-8A, Tokyo, Japan) equipped with an Empower computer program (Waters, Milford, MA, USA). A PL HFIP gel column (Polymer Lab) and a refractive index detector (Shimadzu RID-10A, Tokyo, Japan) were employed. The polymer was dissolved and eluted in 1,1,1,3,3,3-hexafluoroisopropanol (HFIP) containing CF_3COONa (0.05 M) at a flow rate of 0.5 mL/min (injected volume 100 μL, sample concentration 2.0 mg/mL). The number and weight average molecular weights were calculated using polymethyl methacrylate standards.

^{1}H-NMR spectra were acquired with a Bruker NMR Ascend 400 spectrometer (Bilerica, MA, USA) operating at 400 MHz. Chemical shifts were calibrated using tetramethylsilane as an internal standard. Deuterated chloroform was used as a solvent.

Calorimetric data were obtained by differential scanning calorimetry with a TA Instruments Q100 series (NewCasttle, DE, USA) equipped with a refrigerated cooling system (RCS) operating at temperatures from −50 to 150 °C. Calibration was performed with indium. Experiments based on heating runs at 10 °C/min were conducted under a flow of dry nitrogen with a sample weight of approximately 5 mg.

WAXD and SAXS data were obtained at the NCD beamline (BL11) of the ALBA synchrotron facility (Cerdanyola del Vallès, Barcelona, Spain), by using a wavelength of 0.100 nm. A WAXD LX255-HS detector from Rayonix and an ImXPAD S1400 photon-counting detector were employed. Polymer samples

were confined between Kapton films. WAXD and SAXS diffraction patterns were calibrated with Cr_2O_3 and silver behenate (AgBh), respectively. The correlation function and the corresponding parameters were calculated with the CORFUNC software for Fibre Diffraction/Non-Crystalline Diffraction provided by the Collaborative Computational Project 13.

The calculations of the parameters such as L or the angle that forms the lamellae with the fibre axis in the SAXS patterns have been carried out by means of Python-based software developed by the authors. It calculates the distance from the direct beam position to the center of a 2D elliptical Gaussian function fitted in a user-defined ROI. If the center of the Gaussian falls outside the ROI, then an azimuthal integrational[24] is done in the ROI to fit a 1D Gaussian. This distance in pixels is converted to q vector units by means of a calibration file that was generated from a well-known standard, (i.e., silver behenate (AgBh)). As the SAXS patterns have some symmetry, the calculation is replicated to its specular reflection on equatorial or meridional axes depending on the case. Finally, an average of the calculated values is shown as a result. Analogously, a calculation for the angles is done.

Scanning electron micrographs were taken using Phenom XL Desktop SEM equipment (Waltham, MA, USA). Degraded films were mounted on a double-sided adhesive carbon disc and were sputter-coated with a thin layer of carbon to prevent sample charging problems using a K950X Turbo Evaporator (West Sussex, UK). All samples were observed at an accelerating voltage of 10 kV.

4.1.2.3 Statistical Analyses

Values were averaged and graphically represented together with their respective standard deviations. Statistical analysis was performed by the one-way ANOVA test to compare the means of all groups, and then Tukey's test was applied to determine a statistically significant difference between the two groups. The test confidence level was set at 95% ($p < 0.05$).

4.1.3 RESULTS AND DISCUSSION

4.1.3.1 Hydrolytic and Enzymatic Degradation of P4HB Sutures

Hydrolytic degradation of commercial P4HB sutures was evaluated through weight loss and molecular weight measurements using media of three different pH values (i.e., acidic, neutral, and basic) and two temperatures (i.e., 37 and 55 °C that are associated with physiological conditions and the higher available temperature before starting fusion, respectively).

Weight loss (W_l) of the specimens was determined through Equation 1 where W_d is the sample weight after degradation and W_0 is the initial sample weight:

$$W_l = 100 \times (W_0 - W_d)/W_o \quad (1)$$

Figure 4.1.1a reveals that scarce soluble fragments were produced during degradation since a loss of only 2.1–1.8% was achieved after 27 days of exposure to the media at 55 °C.

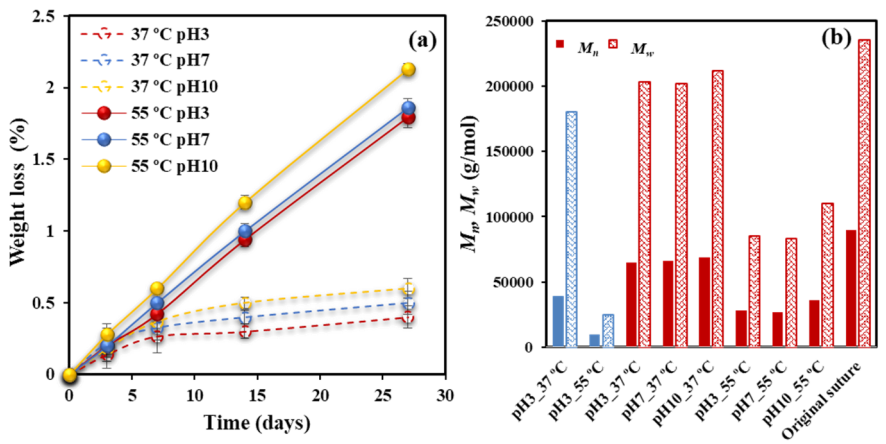

Figure 4.1.1. (**a**) Weight loss versus exposure time for P4HB sutures exposed to hydrolytic media of pH values of 3, 7, and 10 at temperatures of 55 °C (solid lines) and 37 °C (dashed lines). (**b**) M_n (full bars) and M_w (weave bars) molecular weights of the initial suture and after exposure for 27 days to the indicated media. For the sake of completeness, the results obtained from a melt pressed film are also shown (blue bars).

A slightly higher loss was detected for experiments performed at the pH 10 basic medium since fragments having the neutralized carboxylate terminal groups coming from P4HB degradation should have a higher water solubility than those ending with carboxylic acid groups. Exposure to the 37 °C medium caused a minimum weight loss (0.6–0.4%), mainly associated with the first days and which probably corresponded to the solubilization of minor additives as typical colorant molecules.

Therefore, evidence of degradation was only found through GPC measurements. M_n and M_w data after 27 days of exposure to the indicated media and temperature are depicted in **Figure 4.1.1b** for the studied sutures and a representative film was exposed to pH 3. Three points merit attention: (a) Degradation is highly significant at 55 °C, decreasing, for example, M_w from 235,000 g/mol to a minimum value of 83,000 g/mol. On the contrary, a scarce variation was found for samples degraded at 37 °C. (b) The pH of the medium has a moderate influence on degradability, which specifically becomes slightly enhanced in the acidic condition. This feature confirms the above-indicated association between weight loss and solubility. Note that the reaction may also be base-catalyzed, although the given results pointed out an apparent acid-catalysis. (c) Degradability is highly dependent on the crystallinity and morphology of exposed samples. Note the high variation between M_w values of annealed sutures and melt pressed films after exposure to pH 3 media at 55 °C (i.e., 83,000 g/mol with respect to 25,000 g/mol). Even a remarkable difference is found at 37 °C (i.e., 200,000 g/mol with respect to 180,000 g/mol).

Degradation in the presence of two different lipases that are able to promote hydrolysis of the ester bonds of P4HB has been evaluated. Results are quite different from those attained with the hydrolytic degradation due to the high efficacy of the enzymatic attack and also to its characteristic erosion mechanism that contrasts with the bulk process associated with the hydrolytic process. **Figure 4.1.2a** shows the evolution of weight loss during exposure to both enzymatic media and an aqueous medium at 37 °C and pH 7 used as a control. *Rhizopus oryzae* seems more effective than *Pseudomonas cepacia* enzyme,

but both lead to a significant weight loss (i.e., 9–10%) that is higher than observed for the control. The enzymatic attack should produce small fragments probably as a consequence of a stepwise chain scission from the terminal groups that contrasts with the random bond cleavage expected from the bulk degradation.

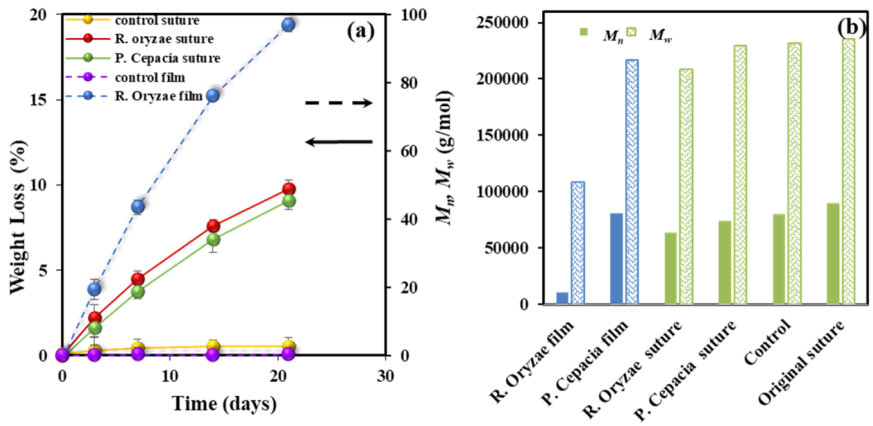

Figure 4.1.2. (**a**) Weight loss versus exposure time for P4HB sutures exposed to the indicated enzymatic media. Results are also plotted for the control and a melt pressed film (right vertical axis, dashed arrow) exposed to the *Rhizopus oryzae* medium for 21 days. (**b**) M_n (full bars) and M_w (weave bars) molecular weights of the initial suture, the control, and sutures after exposure for 21 days to the indicated enzymatic media. For the sake of completeness, the results obtained from a melt pressed film are also depicted (blue bars).

Figure 4.1.2a also displays the results attained for a melt pressed film, which reveals again the decisive influence of crystallinity and the annealed morphology on degradability. **Figure 4.1.2b** shows the impact of enzymatic degradation on the molecular weight, which is summarized as follows: (a) A progressive decrease of molecular weight with the exposure time is observed for both enzymatic media. (b) Hydrolytic degradation seems negligible under low-temperature conditions. (c) The enzymatic attack is more effective than hydrolysis at high temperatures (e.g., M_n values of 64,000 and 28,000 g/mol were determined after 21 days of exposure to the *Rhizopus oryzae* medium and to the aqueous pH 3 medium at 55 °C after 27 days, respectively). (d) The enzymatic attack is less effective on the annealed and highly crystalline sutures

than on the melt pressed films, demonstrating again the difficulty of enzymes to erode the constitutive crystals and a limited activity towards amorphous regions, including folding lamellar surfaces.

4.1.3.2 Influence of Degradation on Thermal Properties

Sutures are submitted to a set of thermal and stretching treatment processes in order to improve their mechanical performance. This treatment has a significant influence on crystallinity but also on morphological features, such as the thickness of the constitutive lamellae. As described in the preceding section, crystallinity plays a determinant role in the degradability of samples, but it is also evident that thermal properties will be affected, as well as the variation of crystalline morphological parameters during degradation processes.

Figure 4.1.3a shows the significant difference in the melting behavior between conventional melt pressed films and annealed sutures. Note that fusion is characterized by a predominant peak and a shoulder at a lower temperature (e.g., 49.7 and 58.2 °C for the film and 61.9 and 72.0 °C for the suture, heating rate of 10 °C/min), which reflects the existence of two populations of lamellar crystals with different thicknesses. The shoulder temperature strongly depends on crystallization and annealing processes since it is related to the less perfect formed crystals that are susceptible to reorganization processes. Therefore, molecular folds in these thinner lamellae underwent a slight reordering that led to an increase of the lamellar crystalline thickness. A simple melt crystallization leads to lamellae that are worse (i.e., lower thickness and more irregular folding surface) than those attained after annealing. Both shoulder and main melting peak logically appear at lower temperatures for the melt crystallized samples. It merits also attention to the low value of the main melting peak, which indicates a limited reordering process of folds that precludes get the highly organized lamellae derived from annealing (i.e., 58.2 °C with respect to 72 °C). Note also that the expected maximum melting temperature is reported to be 79.9 °C[20] as estimated from the Hoffman-Weeks extrapolation[25] for an infinite dimension of P4HB crystals.

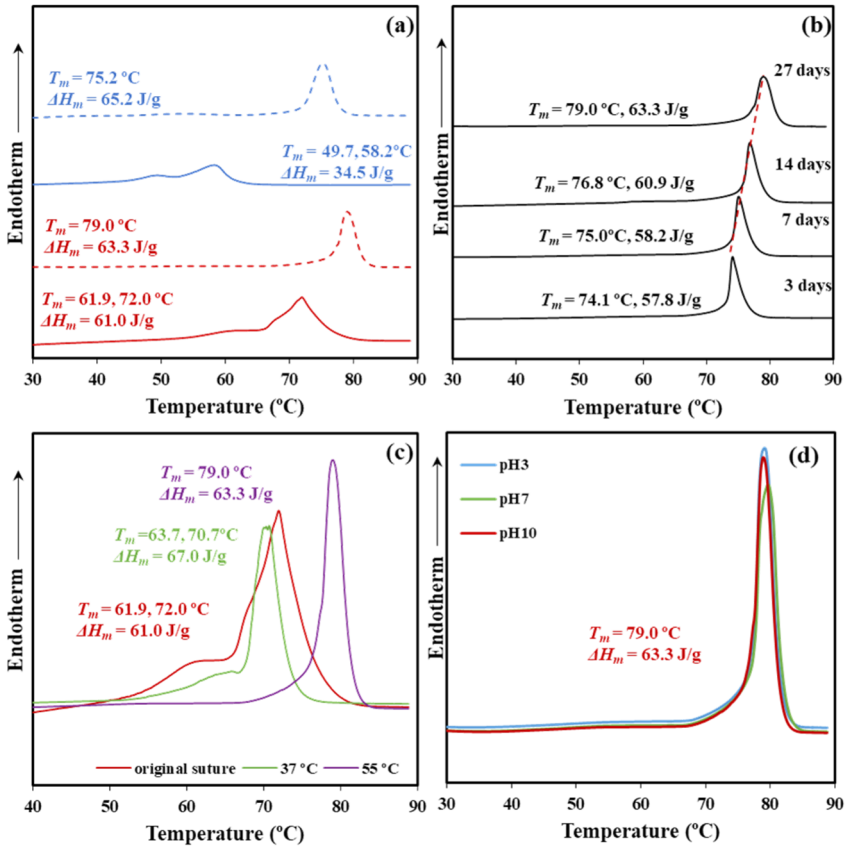

Figure 4.1.3. (**a**) DSC heating scans (10 °C/min) corresponding to a melt pressed film (blue) and the commercial suture (red) before exposure (solid line) and after exposure (dashed line) for 27 days to a pH 10 hydrolytic medium at 55 °C. (**b**) DSC heating runs of commercial sutures exposed for the indicated days to a pH 10 medium at 55 °C. (**c**) DSC heating runs of commercial sutures exposed at a pH 10 medium for 27 days and temperatures of 37 and 55 °C. For the sake of completeness, the curve for the commercial suture is also drawn. (**d**) DSC heating runs of commercial sutures exposed at pH 3, pH 7, and pH 10 media for 27 days and 55 °C.

Figure 4.1.3a also depicts the melting behavior of samples exposed to aggressive hydrolytic conditions (i.e., pH 10, temperature of 55 °C, and 27 days of exposure). Both types of samples, film, and suture, shows the disappearance of the shoulder and a clear increase of the melting peak temperature. Degradation affects the folding surface, facilitates the reordering process, and leads to improved lamellae with a higher melting point. Note the difference around 7 °C that indicates the greater facility of annealed samples to render

practically perfect crystals and that in this case a maximum melting temperature (79.0 °C) close to the equilibrium temperature was attained. Note also that molecular weight measurements showed only a moderate decrease during degradation, which means that thermal behavior is still associated with polymeric samples. Moreover, crystalline phases are those less susceptible to degradation and therefore should show lower changes in their associated properties (i.e., melting point).

The influence of the degradation time on the melting point is displayed in **Figure 4.1.3b** for the high temperature and the less pH aggressive conditions. A progressive increase of the melting point with the exposure time is detected (i.e., from 74.1 to 79.0 °C for three and 27 days, respectively), as well as an increase of the melting enthalpy (i.e., from 57.8 to 63.3 J/g). The observation demonstrates that the crystalline lamellar thickness increases during degradation probably because of some chain breakages in the amorphous lamellar folding surfaces.

The increased chain mobility in the lamellar surface may favor the molecular reordering that leads to an increased crystalline lamellar thickness. In addition, an annealing effect caused, by the exposure to a degradation medium at 55 °C, may be discarded since the observed dependence with long exposure times is not well justified. A highlight also the fact that any stress that could favor annealing was not applied during degradation. Chain mobility is increased at 55 °C and the reordering process that took place after the chain breakage should be enhanced. Degradation performed at 37 °C showed reasonably a less significant change.

Figure 4.1.3c compares the DSC curves of sutures exposed at pH 10 for 27 days at 37 and 55 °C. The sample exposed to the low temperature showed minor changes with respect to the initial suture that mainly affected the low-temperature shoulder related to crystals more susceptible to reorganization (i.e., the temperature increased from 61.9 to 63.7 °C). In this case, the molecular weight decrease was low and the observed impact on thermal properties was limited to the preliminary phase concerning the less perfect crystals.

The impact of the pH of the medium on thermal properties was relatively scarce and the same kind of crystals seems to be attained at 55 °C after 27 days of exposure (**Figure 4.1.3d**). These correspond to the best reorganization that could be obtained from the initial commercial suture. **Figure 4.1.3d** confirms that temperature has a great influence on the degradation of the less perfect crystals since the peak shoulder completely disappeared. **Table 4.1.1** summarizes the calorimetric data attained with representative samples.

Table 4.1.1. Melting peak temperatures and enthalpies of P4HB sutures degraded at the indicated pH values, temperatures, and exposure times.

Samples	T_m (°C)	ΔH_m (J/g)
pH10 27d 37 °C	63.7, 70.7	67.0
pH3 27d 55 °C	79.0	63.3
pH7 27d 55 °C	79.0	63.3
pH10 3d 55 °C	74.1	57.8
pH10 7d 55 °C	75.0	58.2
pH10 14d 55 °C	76.8	60.9
pH10 27d 55 °C	79.0	63.3

Thermal properties were scarcely affected by the enzymatic degradation. Thus, DSC curves for the control (hydrolytic medium without enzyme) and the two selected enzymatic media were practically identical (**Figure 4.1.4**, **Table 4.1.2**). The result agrees with an enzymatic surface erosion of the suture with significant loss of material that contrasts with the indicated bulk hydrolytic degradation mechanism.

Table 4.1.2. Melting peak temperatures and enthalpies of P4HB sutures exposed at 37 °C to the indicated enzymatic degradation medium and exposure time.

Enzymes	Time (days)	T_m (°C)	ΔH_m (J/g)
Control	21	72.1	68.9
P. cepacia	3	71.4	67.3
P. cepacia	21	71.6	68.0
R. oryzae	3	71.5	68.1
R. oryzae	21	71.7	68.7

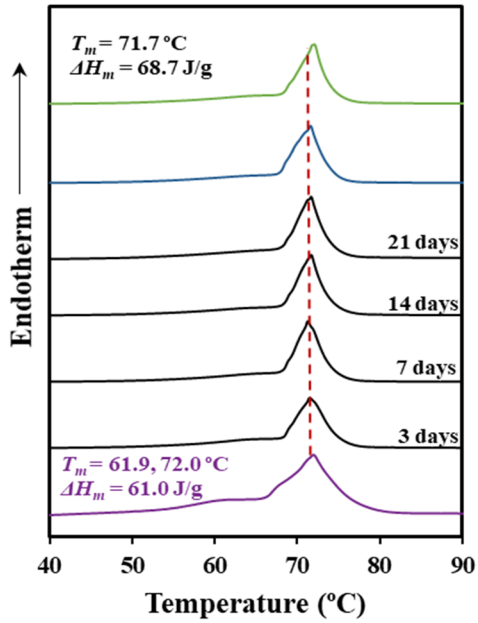

Figure 4.1.4. DSC heating scans (10 °C/min) corresponding to the initial suture (purple line), the suture exposed to a *Rhizopus oryzae* medium at 37 °C for the indicated days (black lines), the suture exposed to a *Pseudomonas cepacia* medium at 37 °C for 21 days (blue line), and the control (green line) (pH 7.4 medium for 21 days and 37 °C).

Figure 4.1.5 shows SEM micrographs that revealed an enzymatic attack that only affected the monofilament surface in a time-dependent manner. Therefore, the DSC traces only reflect the impact of the hydrolytic degradation that as discussed before, mainly concerns the peak shoulder that decreased in intensity and moved from 61.9 to 64.3 °C.

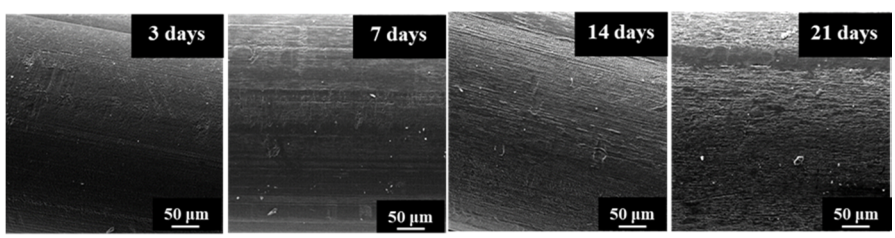

Figure 4.1.5. SEM micrographs showing the progressive surface erosion of P4HB sutures exposed to the *Rhizopus oryzae* medium at 37 °C for 3, 7, 14, and 21 days.

4.1.3.3 Changes on Lamellar Microstructure during Degradation

The degradation behavior of highly annealed sutures is significantly different than observed for melt pressed films as a consequence of the different internal morphology. Stacking of oriented microfibrils with a lamellar organization and disordered spherulitic growth up to the collision are the specific morphologic trends of sutures and films, respectively. The impact of such morphologies led to a lower degradability of annealed samples due to their higher crystallinity. Furthermore, during degradation both crystallinity and melting temperature increased, although the effect was less significant for the annealed sample due to its scarce marge of improvement.

All studied P4HB samples displayed clear SAXS reflections that were analysed to improve the comprehension of differences related to the supramolecular order since specific data concerning the geometrical parameters of constitutive lamellar structures could be easily derived.

Specifically, the study was performed from an isotropic integration of the oriented suture patterns or analyzing directly the disordered rings of film samples. In both cases, the normalized one-dimensional correlation function[26] was employed:

$$\gamma(r) = \int_0^\infty q^2 I(q) \cos(qr) dq / \int_0^\infty q^2 I(q) dq \qquad (2)$$

where $I(q)$ is the intensity of the SAXS peak at each value of the scattering vector ($q = [4\pi \sin \theta/\lambda] = 2\pi/d$, with θ and d being the Bragg angle and the Bragg spacing, respectively). It is assumed that the lamellar stack is constituted by a high number of lamellae that had an infinite lateral size so the stack can be reduced to a one-dimensional two-phase structure that satisfies the Bragg condition.

Limited experimental collection of SAXS data was solved by extrapolation for low and high q values through the Vonk model[27] and Porod's law, respectively.

Analysis of the correlation function allows determining: (1) The long period, L_γ; (2) the crystallinity within the lamellar stacks, X_c^{SAXS}; (3) the crystalline lamellar thickness, l_c, and the amorphous layer thickness, l_a. In this way, L_γ corresponds to the r value of the first maximum of the correlation function; l_a has been assigned to the r value for the intersection of the LRAT (linear regression in the autocorrelation triangle) with the ordinate equal to the first minimum of the correlation function; l_c corresponds to L_γ, l_a; and X_c^{SAXS} is calculated as l_c/L_γ. The lower thickness of the two-phase lamellar model has been assigned to the amorphous layer thickness although the correlation function cannot distinguish the thickness associated with each phase.

Figure 4.1.6 illustrates representative correlation functions that allow comparing and inferring a distinct evolution of films and sutures during the hydrolytic degradation. Thus, the progression of film degradation led to a shift of the correlation function to higher distances and also to more pronounced peaks. Therefore, L_γ increased from 8.60 to 9.80 nm when the temperature of the hydrolytic medium increased from 37 to 55 °C, a change that was a consequence of the increase of the lamellar crystalline thickness (i.e., l_c increased from 6.91 to 7.32 nm). Moreover, an increase was also observed for the amorphous layer thickness (i.e., from 1.69 to 2.48 nm) leading to a practically constant crystallinity of the lamellar stack (i.e., 80 ± 1%). The amorphous phase seems to be less dense due to the increasing thickness probably caused by the chain breakage. The increase in the electronic contrast between crystalline and amorphous phases is observed through the more pronounced profile of the correlation function.

Figure 4.1.6b displays by contrast that the correlation profile becomes smoother when degradation increases, a feature that cannot be well explained at this stage, and a more accurate evaluation of the microstructure of the biphasic systems is required. Nevertheless, a slight shift of the correlation function to the increasing distances is clear. Specifically, L_γ and l_c increased from 10.30 and 8.31 nm to 10.90 and 8.80 nm, respectively when the temperature of the degradation medium increased from 37 to 55 °C. Underlined here that

changes are moderate due to the high initial thickness of the annealed lamellae as previously deduced from the closeness between the experimental melting temperature and the theoretical value deduced from the equilibrium melting temperature. Furthermore, the crystallinity of the lamellar stack remained equal to 80.7%.

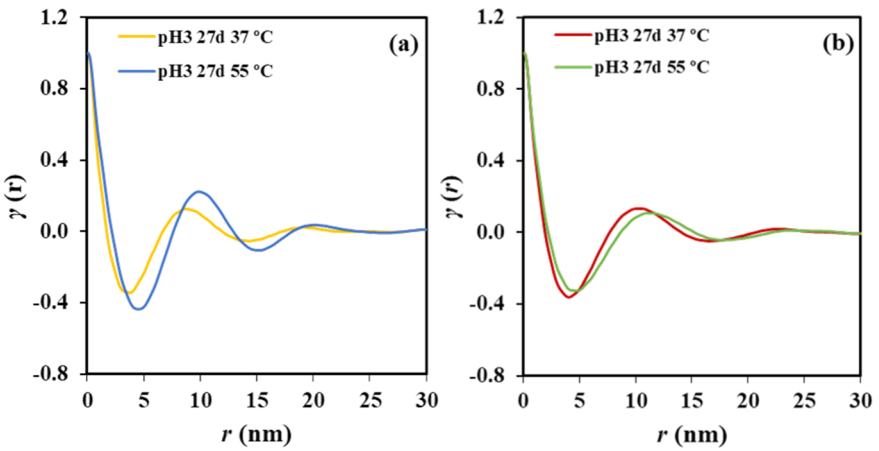

Figure 4.1.6. (**a**) Correlation function of the SAXS peak determined for the P4HB film exposed to a pH 3 medium at 37 and 55 °C for 27 days. (**b**) Correlation function of the SAXS peak determined for the P4HB suture exposed to a pH 3 medium at 37 and 55 °C for 27 days.

In addition to the L_γ value, which is associated with the most probable distance between the centers of gravity of two adjacent crystals, a long period determined from twice the value of the first minimum of the correlation function, L_γ^m, is also useful. This is interpreted as the most probable distance between the centers of gravity of a crystal and its adjacent amorphous layer. A discrepancy between both values indicates a broad distribution of the layer widths of the major component,[28] which in this case corresponds to the crystal phase.

Table 4.1.3 summarizes the morphological parameters determined for representative degraded film and suture samples. The following trends can be indicated: (a) Discrepancy between L_γ and $2\times L_\gamma^m$ is decreasing as the degradation process becomes more significant. This feature can be explained

considering the lamellar reordering process that, for example, lead to a decrease of the population of thinner crystals in film samples, and consequently to a narrow distribution. Note, for example, that differences around ~1 and ~0.6 nm are determined for degradations performed at 37 and 55 °C. (b) Annealed samples showed a greater discrepancy than films (e.g., ~1 and ~2.1 nm for films and sutures, respectively). This feature seems strange since a narrow distribution is expected for the thicker annealed lamellae of sutures.

Table 4.1.3. Morphological parameters of films and sutures exposed to degradation at the indicated media.

Sample	L_γ (nm)	l_c (nm)	l_α (nm)	L_γ^m (nm)
Film pH3 27d 37 °C	8.60	6.91	1.69	3.8
Film pH10 27d 37 °C	8.50	6.88	1.62	3.2
Film pH3 27d 55 °C	9.80	7.32	2.48	4.6
Film pH10 27d 55 °C	9.6	7.62	1.98	4.1
Suture pH3 27d 37 °C	10.30	8.31	1.99	4.1
Suture pH10 27d 37 °C	9.80	7.91	1.89	4.0
Suture pH3 27d 55 °C	10.90	8.80	2.10	4.8
Suture pH10 27d 55 °C	10.70	8.66	2.04	4.3
Film *R. Oryzae* 14 days 37 °C	9.60	7.25	2.35	4.3
Film *P. Cepacia* 14 days 37 °C	9.50	7.72	1.78	3.9
Suture *R. Oryzae* 14 days 37 °C	10.50	8.56	1.94	4.1
Suture *P. Cepacia* 14 days 37 °C	10.40	8.33	2.07	4.1

The SAXS pattern displayed in **Figure 4.1.7a** for a sample exposed to a very little aggressive degradation condition (therefore similar to that observed with the initial suture) reveals that the thermal annealing process at which the commercial sutures were submitted led to a peculiar morphology where two different types of lamellar stacks exist. These differences come up from the distinct lamellar organization in the skin and the core of sutures. This phenomenon is of a different nature than that caused by a simple crystallization process, where usually populations of lamellae with different thicknesses and organizations of folding surfaces are derived. The observations justify the above indicated broad lamellar distribution found in sutures.

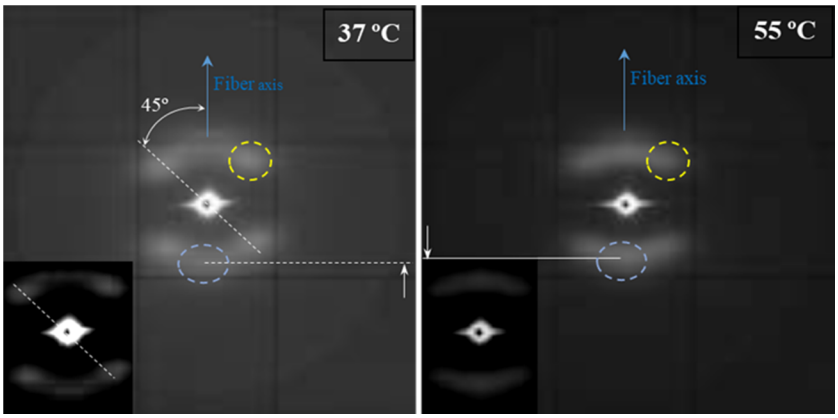

Figure 4.1.7. The SAXS patterns of an annealed suture submitted to low (i.e., pH 10, 37 °C, 27 days) (**a**) and high (i.e., pH 3, 55 °C, 27 days) (**b**) degradation processes. Insets show low contrast exposures of the corresponding patterns. Meridional and off meridional reflections are indicated by the blue and yellow dashed circles, respectively. Solid and dashed white lines highlight the different positions of meridional reflections.

The SAXS pattern is characterized by four off meridional spots and two meridional arches (**Figure 4.1.7a**). The first ones are indicative of the stacking of breadth lamellar crystals tilted with respect to the fiber direction and logically arranged with cylindrical symmetry. The characteristic spacing of these stacks is 14.0 nm. The second ones have a higher spacing (i.e., 14.1 nm) and correspond to lamellar crystals with a lower lateral extension (longer and diffuse reflection) and perpendicularly oriented to the fiber axis. The nanostructure of the core material as compared to the shell material appears rougher and more imperfect. The external part of sutures is submitted to a higher temperature than the core and suffers higher shear stress. In this way, a shift between molecular chains along the annealing direction of lamellae, as well as an increase of the lamellar thickness is produced. Therefore, tilted lamellar surfaces, which moreover appeared at an angle of 45° that corresponds to the maximum shear, are generated.

The microstructure of sutures changed during hydrolytic degradation as can be deduced from the SAXS pattern (**Figure 4.1.7b**) of the sample exposed to the more aggressive conditions (i.e., pH3, 55 °C, and 27 days). Differences concerning the meridional spots associated with the more imperfect crystals are

placed in the core. Thus, the interlamellar spacing slightly increased (from 14.1 to 14.8 nm) as the reflections slightly moved to the center of the pattern. Furthermore, the intensity of these spots increased suggesting a higher electronic contrast between crystalline and amorphous layers. In this way, degradation mainly affected the more defective crystals, causing some molecular breakages on their folding surface. A slight reordering was produced leading to the observed increase of the crystalline lamellar thickness, while simultaneously the amorphous layer became less compact and more disordered.

Molecular chains in the crystalline lamellae remained aligned with the longitudinal direction of sutures, even those crystals with tilted surfaces. All observed reflections in WAXD patterns (**Figure 4.1.8**) were in agreement with the published orthorhombic unit cell of P4HB.[16,17] Specifically, (110) and (020) reflections at 0.388 and 0.406 nm appeared as very small arcs in the equator.

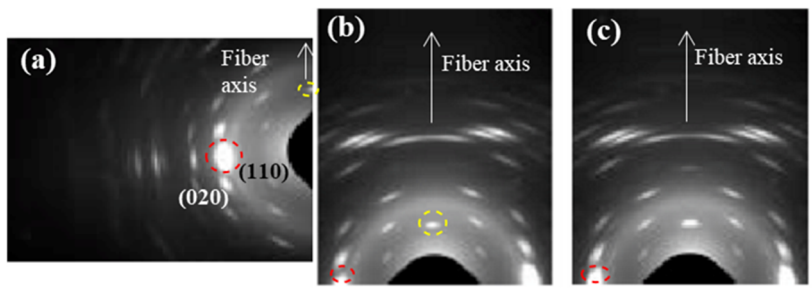

Figure 4.1.8. WAXD patterns of an annealed suture submitted to low (i.e., pH 10, 37 °C, 27 days) (**a**,**b**) and high (i.e., pH 3, 55 °C, 27 days) (**c**) degradation processes. Only a region of the reciprocal space is registered due to the specific configuration of the beamline that allows recording simultaneously SAXS and WAXD patterns. (**a**,**b**) Patterns were obtained from different orientations of the suture in the holder in order to get information of both equatorial (**a**) and meridional (**b**) reflections. Common meridional and equatorial reflections are indicated by the dashed yellow and red circles.

The scheme of **Figure 4.1.9** illustrates the deduced microstructure of the annealed fiber and the consequences of the hydrolytic attack. The lamellar thickness remained unaltered for the more perfect tilted crystals and even slight densification was detected for their stretched folds, since the intensity of the corresponding spots seemed to decrease. This deduction is in agreement with the previously indicated contradictory results determined from the analysis of

the correlation function. The crystalline structure remained unchanged, as well as the degree of orientation of crystals since no change was detected in the WAXD patterns as displayed in **Figure 4.1.8c**.

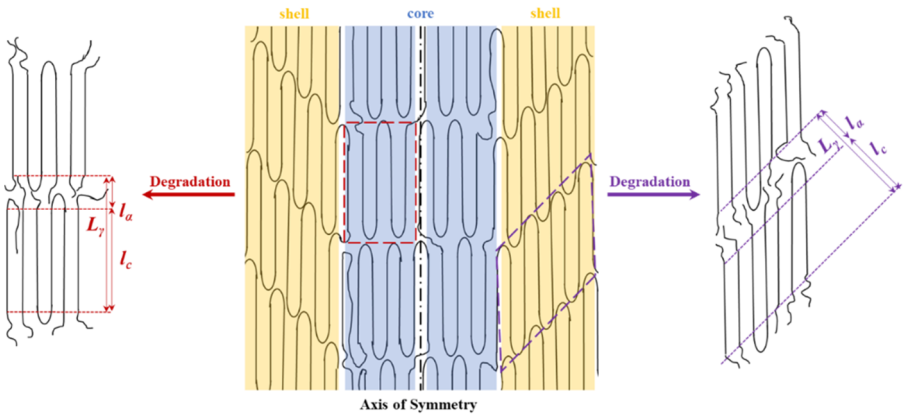

Figure 4.1.9. Scheme showing the structure of annealed fibers characterized by the presence of two types of lamellar crystals that are part of the shell and the core before and after being submitted to hydrolytic degradation.

Intensification of the meridional spot and its shift to the center of the pattern shows a correlation with the degradation degree, as can be inferred from the gradual evolution (see blue spot) presented in **Figure 4.1.10** for representative conditions.

Despite the fact that enzymatic degradation was effective as deduced from a weight loss of 8–9% after 21 days of exposure to both assayed media (**Figure 4.1.2a**), the impact on the microstructure of the remaining material should be minimum as reflected by the scarce change on the molecular weight (**Figure 4.1.2b**) and the melting point (**Figure 4.1.4** and **Table 4.1.2**). This is corroborated through analysis of SAXS patterns (**Figure 4.1.11**), since no changes were detected between samples exposed to the less (i.e., *Pseudomonas cepacia*) and the more (i.e., *Rhizopus oryzae*) aggressive media for 14 days. Thus, L_γ, l_c, l_a, and L_γ^m parameters remained practically constant and equal to 10.40–10.50, 8.33–8.56, 2.07–1.94, and 4.1 nm (**Table 4.1.3**), respectively. Note again the high discrepancy between L_γ and $2\times L_\gamma^m$ values as expected from the existence of two well-differentiated types of lamellae.

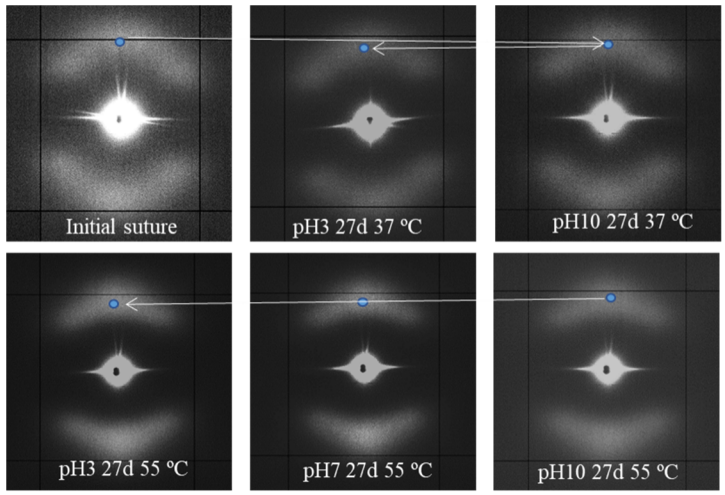

Figure 4.1.10. SAXS patterns of the initial suture and those exposed to the indicated hydrolytic conditions.

Figure 4.1.11 also shows the different susceptibility to the enzymatic attack of P4HB films constituted by spherulitic morphologies. In this case, a clear increase of lamellar spacing was detected (**Table 4.1.3**), as well as on the electronic contrast. Logically, differences came from the different degradability of films and sutures, with the weight loss of the former being for example around (75–95%).

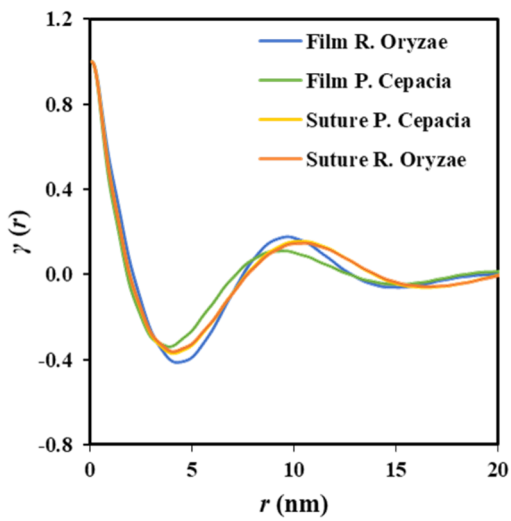

Figure 4.1.11. Correlation function of the SAXS peak determined for P4HB films and sutures exposed to *Pseudomonas cepacia* and *Rhizopus oryzae* media at 37 °C for 14 days.

SAXS patterns of the less and more degraded sutures were again highly similar, considering both the position (angle and distance) of the observed spots and the relative intensity between meridional and off-meridional reflections (**Figure 4.1.12**).

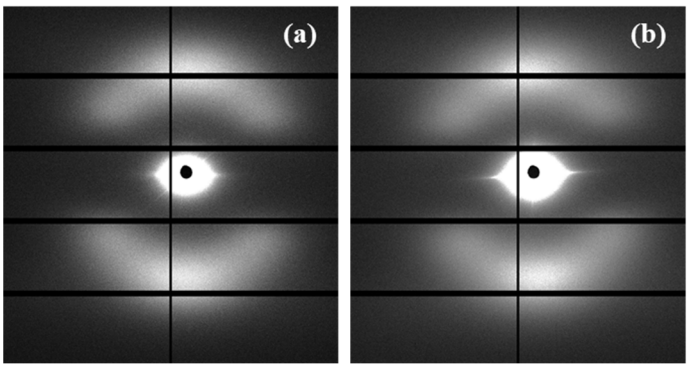

Figure 4.1.12. SAXS patterns of suture exposed to *Pseudomonas cepacia* (**a**) and *Rhizopus oryzae* (**b**) media at 37 °C for 14 days.

In conclusion, there are no evidences of the observed morphological change that occurs at an advanced stage of hydrolytic degradation. These results are fully consistent with an enzymatic surface attack that led to an erosion of the suture (see **Figure 4.1.5)** and did not change the internal microstructure of the remaining material.

4.1.3.4 Changes on Lamelar Microstructure of Degraded Samples during Heating

The evolution of SAXS patterns during heating processes can give relevant information concerning the microstructure of sutures as detected, for example, with segmented glycolide based copolymers. These exhibited differentiated behaviors depending on the degradation treatment.[20] Annealed P4HB sutures showed fewer changes during heating due to the high perfection of crystals, the more reduced presence of intralamellar amorphous regions, and the lack of any evidence related to the presence of regularly distributed interfibrilar amorphous regions. These should be originated from disordered regions placed on lateral sides of lamellae arranged in a fibrillar way and should lead to patterns with equatorial reflections.

Figure 4.1.13 compares the temperature evolution of patterns of representative samples hydrolytically degraded at 37 and 55 °C, with the previously indicated differences being highlighted.

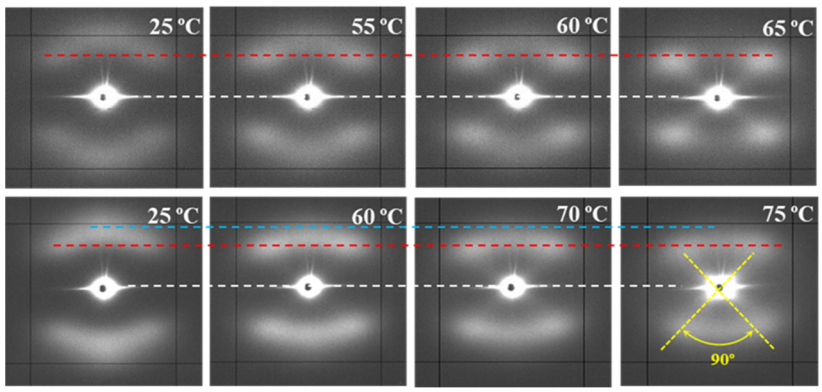

Figure 4.1.13. SAXS patterns of P4HB sutures exposed to hydrolytic media of pH 10, at 37 °C (top row) and pH 3, at 55 °C (bottom row) for 27 days. Patterns were recorded at the indicated temperatures during a heating run performed at 10 °C/min. Dashed lines are used as references for the position of the center of the pattern (white), off-meridional spots (red), and meridional spots (blue).

The following features can be indicated: (a) Lamellae that constitute the core of the suture are more imperfect and therefore initiates melting at lower temperatures than the tilted ones. A continuous decrease in their intensity is detected when the temperature approaches the melting of the suture, while the intensity of tilted lamellae remained practically constant. It is interesting to point out that the suture degraded at 37 °C and heated to 55 °C still demonstrates weaker meridional spots, allowing to discard that a thermal annealing process could intensify the meridional spots in the case of degradation performed at 55 °C. (b) Meridional reflections can still be envisaged at temperatures very close to the fusion of the suture for the more degraded sample, while they practically disappeared for the samples exposed to the 37 °C medium. (c) Lamellar spacings increase with temperature for both tilted and non-tilted lamellae, although the effect is clearer for the last ones (**Table 4.1.4**). (d) Tilted surfaces have always the same orientation with respect to the meridian (i.e., ± 45°).

Table 4.1.4. Spacings of the reflections observed in SAXS patterns recorded at different temperatures during heating of hydrolytically degraded samples (pH 10, 27 days) at 37 °C and (pH 3, 27 days) 55 °C.

Degradation Temperature (°C)	Temperature (°C)	$L_{meridional}$ [a] (nm)	$L_{off\text{-}meridional}$ [a] (nm)
37	25	14.1	14.0
37	55	14.9	14.3
37	60	15.9	14.9
37	65	16.1	15.3
55	25	14.8	14.6
55	60	16.9	16.0
55	70	18.5	16.4
55	75	20.8	17.4

[a] Spacings directly measured on the pattern are always slightly higher than L_γ values evaluated with the correlation function.

4.1.4 CONCLUSIONS

Stretched P4HB commercial sutures were characterized by two different types of lamellar stacks. These were originated by the different shear stress that experimented with the shell and the core of the fibers during processing. Therefore, the stacks placed in the shell were constituted by the thicker lamellae having tilted surfaces as a consequence of the slippage of molecular chains. The inner stacks were constituted by more imperfect lamellae having surfaces perpendicularly oriented to the fiber axis. SAXS patterns revealed the interlamellar spacings but did not show any evidence concerning the possible existence of interfibrillar amorphous regions.

Different degrees of degradation could be achieved by exposure to hydrolytic media by modifying pH, temperature, and time. Significant chain breakages were found from GPC measurements, but weight losses were practically depreciable even under the most aggressive conditions. Microstructural changes were found dependent on the progress of degradation and distinctly affected the lamellar stacks. More significant changes were observed for the inner lamellar that experimented with a higher increase of both crystalline and amorphous lamellar thicknesses. Hence, the chain breakages occurred in the amorphous regions of a more disordered surface and allowed a

certain reorganization of the chains which increased the crystalline region. On the contrary, enzymatic degradation only caused a surface erosion with loss of surface material and had a scarce influence on the microstructure.

Both hydrolytic and enzymatic degradation was different for melt crystallized films. In this case, the microstructure was characterized by spherulites constituted by thinner lamellae with a relatively narrow distribution. The progress of degradation caused a significant thickening that affected the thermal properties.

Heating of stretched sutures revealed again differences according to the different degrees of degradation experimented by the distinct types of lamellar stacks. Thus, a slight thickening was detected for both types of lamellae as a consequence of the typical temperature reordering process, but with the melting of lamellae placed in the fiber core being faster.

4.1.5 REFERENCES

(1) Hirko, M. K.; Lin, P. H.; Greisler, H. P.; Chu, C. C. Biological Properties of Suture Materials. In *Wound closure biomaterials and devices*; CRC Press: Boca Raton, FL, USA, 1996; pp 237–287.

(2) Ray, J.; Doddi, N.; Regula, D.; Williams, J.; Melveger, A. Polydioxanone (PDS), a Novel Monofilament Synthetic Absorbable Suture. *Surgery, Gynecol. Obstet.* **1981**, *153* (4), 497–507.

(3) Odermatt, E. K.; Funk, L.; Bargon, R.; Martin, D. P.; Rizk, S.; Williams, S. F. MonoMax Suture: A New Long-Term Absorbable Monofilament Suture Made from Poly-4-Hydroxybutyrate. *Int. J. Polym. Sci.* **2012**, *2012*, 1–12. https://doi.org/10.1155/2012/216137.

(4) Martin, D. P.; Williams, S. F. Medical Applications of Poly-4-Hydroxybutyrate: A Strong Flexible Absorbable Biomaterial. *Biochem. Eng. J.* **2003**, *16* (2), 97–105. https://doi.org/10.1016/S1369-703X(03)00040-8.

(5) Utsunomia, C.; Ren, Q.; Zinn, M. Poly (4-Hydroxybutyrate): Current State and Perspectives. *Front. Bioeng. iotechnology* **2020**, *8* (April), 1–18. https://doi.org/10.3389/fbioe.2020.00257.

(6) Williams, S. F.; Rizk, S.; Martin, D. P. Poly-4-Hydroxybutyrate (P4HB): A New Generation of Resorbable Medical Devices for Tissue Repair and Regeneration. *Biomed. Eng. (NY).* **2013**, *58* (5), 439–452. https://doi.org/10.1515/bmt-2013-0009.

(7) Rodriguez-Contreras, A. Recent Advances in the Use of Polyhydroyalkanoates in Biomedicine. *Bioengineering* **2019**, *6* (3), 1–14. https://doi.org/10.3390/bioengineering6030082.

(8) Zafar, M. S.; Ullah, R.; Qamar, Z.; Fareed, M. A.; Amin, F.; Khurshid, Z.; Sefat, F. *Properties of Dental Biomaterials*; Elsevier Ltd: Amsterdam, The Netherlands, 2019. https://doi.org/10.1016/b978-0-08-102476-8.00002-5.

(9) Brigham, C. J.; Sinskey, A. J. Applications of Polyhydroxyalkanoates in the Medical Industry. *Int. J. Biotechnol. Wellness Ind.* **2012**, *1* (1), 53–60. https://doi.org/10.6000/1927-3037.2012.01.01.03.

(10) Tornier, announces launch of BioFiber® Surgical Mesh for tendon repair at arthroscopic surgery conference https://www.businesswire.com/news/home/20110414005940/en/Tornier-Announces-Launch-BioFiber®-Surgical-Mesh-Tendon (accessed Jul 2, 2020).

(11) Deeken, C. R.; Matthews, B. D. Characterization of the Mechanical Strength, Resorption Properties, and Histologic Characteristics of a Fully Absorbable Material (Poly-4-Hydroxybutyrate-PHASIX Mesh) in a Porcine Model of Hernia Repair. *ISRN Surg* **2013**, *2013*, 1–12. https://doi.org/10.1155/2013/238067.

(12) Böstman, O. M. Absorbable Implants for the Fixation of Fractures. *J. Bone Jt. Surg.* **1991**, *73* (1), 148–153.

(13) Hori, Y.; Yamaguchi, A.; Hagiwara, T. Chemical Synthesis of High Molecular Weight Poly(3-Hydroxybutyrate-Co-4-Hydroxybutyrate). *Polymer (Guildf).* **1995**, *36* (24), 4703–4705. https://doi.org/10.1016/0032-3861(95)96838-Y.

(14) Moore, T.; Adhikari, R.; Gunatillake, P. Chemosynthesis of Bioresorbable Poly(γ-Butyrolactone) by Ring-Opening Polymerisation: A Review.

Biomaterials **2005**, *26* (18), 3771–3782. https://doi.org/10.1016/j.biomaterials.2004.10.002.

(15) Doi, Y.; Segawa, A.; Kunioka, M. Biosynthesis and Characterization of Poly(3-Hydroxybutyrate-Co-4-Hydroxybutyrate) in Alcaligenes Eutrophus. *Int. J. Biol. Macromol.* **1990**, *12* (2), 106–111. https://doi.org/10.1016/0141-8130(90)90061-E.

(16) Huisman, G. W.; Skraly, F. Biological Systems for Manufacture of Polyhydroxyalkanoate Polymers Containing 4-Hydroxyacids. US 6,316,262, 2001.

(17) Mitomo, H.; Kobayashi, S.; Morishita, N.; Doi, Y. Structural Changes and Properties of Poly(3HB-Co-4HB). *Polym. Prepr.* **1995**, *44*, 3156.

(18) Su, F.; Iwata, T.; Sudesh, K.; Doi, Y. Electron and X-Ray Diffraction Study on Poly(4-Hydroxybutyrate). *Polymer (Guildf).* **2001**, *42* (21), 8915–8918. https://doi.org/10.1016/S0032-3861(01)00412-8.

(19) Su, F.; Iwata, T.; Tanaka, F.; Doi, Y. Crystal Structure and Enzymatic Degradation of Poly(4-Hydroxybutyrate). *Macromolecules* **2003**, *36* (17), 6401–6409. https://doi.org/10.1021/ma034546s.

(20) Keridou, I.; del Valle, L. J.; Funk, L.; Turon, P.; Yousef, I.; Franco, L.; Puiggalí, J. Isothermal Crystallization Kinetics of Poly(4-Hydroxybutyrate) Biopolymer. *Polym. Morphol. Princ. Charact. Process.* **2019**, *12* (2488), 1–20. https://doi.org/10.3390/ma12152488.

(21) Keridou, I.; Del Valle, L. J.; Funk, L.; Turon, P.; Franco, L.; Puiggalí, J. Non-Isothermal Crystallization Kinetics of Poly(4-Hydroxybutyrate) Biopolymer. *Molecules* **2019**, *24* (15), 1–24. https://doi.org/10.3390/molecules24152840.

(22) Márquez, Y.; Martínez, J.; Turon, P.; Franco, L.; Puiggalí, J. Influence of PH on Morphology and Structure during Hydrolytic Degradation of the Segmented GL-b-[GL-Co-TMC-Co-CL]-b-GL Copolymer. *Fibers* **2015**, *3* (3), 348–372. https://doi.org/10.3390/fib3030348.

(23) Teorell, T.; Stenhagen, E. Universal Buffer over the PH Range 2.0 to 12.0. *Biochem Z* **1938**, *299*, 416–419.

(24) Kieffer, J.; Wright, J. P. PyFAI: A Python Library for High Performance Azimuthal Integration on GPU. *Powder Diffr.* **2013**, *28* (SUPPL.2), 339–350. https://doi.org/10.1017/S0885715613000924.

(25) Hoffman, J. D.; Weeks, J. J. Melting Process and the Equilibrium Melting Temperature of Polychlorotrifluoroethylene. *J. Res. Natl. Bur. Stand. Sect. A Phys. Chem.* **1962**, *66A* (1), 13. https://doi.org/10.6028/jres.066a.003.

(26) Vonk, C. G.; Kortleve, G. X-Ray Small-Angle Scattering of Bulk Polyethylene - II. Analyses of the Scattering Curve. *Kolloid-Zeitschrift Zeitschrift für Polym.* **1967**, *220* (1), 19–24. https://doi.org/10.1007/BF02086052.

(27) Vonk, C. G. A General Computer Program for the Processing of Small-Angle X-Ray Scattering Data. *J. Appl. Crystallogr.* **1975**, *8*, 340–341.

(28) Hsiao, B. S.; Wang, Z. G.; Yeh, F.; Gao, Y.; Sheth, K. C. Time-Resolved X-Ray Studies of Structure Development in Poly(Butylene Terephthalate) during Isothermal Crystallization. *Polymer (Guildf).* **1999**, *40* (12), 3515–3523. https://doi.org/10.1016/S0032-3861(98)00573-4.

4.2 HYDROLYTIC AND ENZYMATIC DEGRADATION OF BIOBASED POLY-4-HYDROXYBUTYRATE FILMS. SELECTIVE ETCHING OF SPHERULITES.

4.2.1 INTRODUCTION

Poly-4-hydroxybutyrate (P4HB) is a biodegradable polyester widely employed in biomedical applications due to its biocompatibility and unique properties. Specifically, P4HB is considered for developing long-term sutures, abdominal wall closure materials, reconstructive surgery materials, scaffolds, heart valves, and vascular grafts among other uses.[1–8]

P4HB, like other poly(hydroxyalkanoates) can be produced in high yield from microorganisms (e.g. *Escherichia coli*) in response to nutrient defective conditions.[9] P4HB mainly degrades by surface erosion giving rise to 4-hydroxybutyrate as the main product. This is a common metabolite of the human body and therefore minimum adverse reactions in soft tissues (e.g., abdominal wall and muscles) are derived after implantation. Microbial P4HB has a very high molecular weight ($M_n \sim 10^6$ g/mol) and a remarkable elastomeric character at room and body temperatures. P4HB can be stretched 10 times its original length before breaking. Other advantages of P4HB correspond to its solubility in organic polar solvents and low melting temperature that facilitates its processing if it is not compromised by the high molecular weight.[10]

Despite the above-indicated properties of P4HB, scarce works have been performed on the study of physical properties, crystalline structure, morphology, and crystallization processes. This feature contrasts with the exhaustive information concerning related polyesters (e.g., polyglycolide and poly(ε-caprolactone), which are the most similar ω-hydroxy acid derivatives, constituted also by an even number of carbon atoms in the main chain) or even to other biodegradable polyesters, such as polylactide and poly(3-hydroxybutyrate) (P3HB), which differ on the presence of methyl

side groups. The peculiar characteristics of P4HB have enhanced the interest in their copolymers. Thus, poly (3-hydroxybutyrate-co-4-hydroxybutyrate) (P(3HB-co-4HB)) is a widely employed bacterial copolyester where the presence of 4-hydroxybutyrate units is fundamental to reduce the stiffness of the P3HB homopolymer.[11,12] Chemical synthesis has also been employed to develop copolyesters based on 4-hydroxybutyrate units.[13]

X-ray fiber diffraction data and single-crystal electron diffraction patterns pointed out that P4HB crystallizes according to an orthorhombic unit cell with space group $P2_12_12_1$ and parameters: a = 0.775 nm, b = 0.479 nm, and c (fibre axis) = 1.194 nm.[14,15] Diffraction data and energy calculations [15] indicated that P4HB molecules crystallized according to a slight distortion of an all-trans conformation. Molecular deformation under uniaxial stretching has been simulated, being suggested that crystalline regions played a fundamental role in the stretching deformation.[16]

Concerning the crystalline morphologies, it should be pointed out that lozenge-shaped multi-terrace crystals can be obtained from crystallization in dilute ethanol solutions at 80 ºC. Growth planes corresponded to {110} planes and the ratio between the two diagonal axes is close to 3:5.[15]

Enzymatic degradation of such single crystals was studied by turbidity assays in lipase medium from *Pseudomonas sp.* and an extracellular PHB depolymerase from *Pseudomonas stutzeri* YM1006.[15] Morphological observations indicated that enzymatic attack took place from the crystal edges since both molecular weight and lamellar thickness remained unchanged. This feature suggested that chain-folding regions on the lamellar surface were unaltered. Nevertheless, evidence that enzymatic degradation had also occurred at the folded chain region of single-crystal surfaces have been found for P(3HB-co-4HB) copolymers.[17]

P4HB crystallized from the melt and also from chloroform solutions as negative ringed spherulites.[18,19] Rings were distinguished by highly zigzag irregularities and had different widths depending on birefringence (i.e., the

dark and non-birefringent rings were the narrowest). Analysis of thin spherulites obtained by the solvent casting by infrared microspectroscopy was not conclusive about molecular orientation differences in dark and bright rings[18]. Therefore, reported experimental data were not useful to discern between the two typical explanations formulated, to elucidate the ringed morphology of spherulites. Namely, a continuous twisting of constitutive lamellae[20] or a rhythmic growth derived from the presence of depletion zones in the growth front.[21]

Partial degradation of P4HB films in a lipase from *Pseudomonas sp.* medium (24 h at 37 °C) revealed the apparition of spherulites without a defined texture, while experiments performed with stretched films showed the apparition of shish-kebab morphologies, both features as a consequence of a faster erosion of amorphous regions and the cropping out of crystal regions.[15]

The main goal of the present work is to insist on the study of degradation of melt pressed films considering different media and conditions. Specifically, the evaluation of the impact of degradation on crystalline and amorphous regions will be considered. The expected preferential attack on the amorphous phase appears as a relevant feature that can be employed to highlight spherulitic characteristics when surface erosion is favored.

4.2.2 EXPERIMENTAL SECTION

4.2.2.1 Materials

Commercially available samples of P4HB (MonoMax®, USP 1) were kindly supplied by B. Braun Surgical S.A.U. The weight and number average molecular weights of these samples were 215,000 and 68,000 g/mol, respectively, as determined by GPC. *Pseudomonas cepacia* and *Rhizopus oryzae* enzymes with a specific activity of 40.0 and 55.7 U/mg solid, respectively, were obtained from Sigma-Aldrich (Spain). All reagents, chloride acid (HCl), and chloroform ($CHCl_3$) were provided from Fisher Chemical (U.S).

4.2.2.2 Hydrolytic Degradation

In vitro, hydrolytic degradation studies were performed at 37 ºC and 55 ºC to simulate human body conditions and compost media. Studies were performed with films with dimensions of 1 cm × 1 cm × 150 µm, which. These films were obtained by melt pressing (5 bar) at a temperature of 60 ºC, and subsequent spontaneous cooling to room temperature where they remained for 5 min. *In vitro*, hydrolytic degradation studies were performed at 37 ºC and 55 ºC to simulate human body conditions and compost media. Studies were performed with films with dimensions of 1 cm × 1 cm × 150 µm, which were pressed (5 bar) and melted at a temperature of 60 ºC. Assays were carried out at the two indicated temperatures in different pH values of 3, 7, and 10 using the Universal buffer (citrate-phosphate-borate/HCl) solution.[22] This buffer was prepared by mixing 20 mL of the stock solution with *x* mL of 0.1 M HCl and distilled water up to 100 mL. The stock solution (1 L) contained 100 mL of citric acid, 100 mL of phosphoric acid, 3.54 g of boric acid, and 343 mL of 1M NaOH. Therefore, the buffers of pH 3, pH 7, and pH 10 values were obtained by mixing 20 mL of the stock solution and 56.9, 32.9, and 18.1 mL of 0.1 M HCl, respectively. Samples were kept under orbital shaking in bottles filled with 50 mL of the degradation medium and sodium azide (0.03 wt-%) to prevent microbial growth for selected exposure times. The samples were then thoroughly rinsed with distilled water, dried to constant weight under vacuum, and stored over P_4O_{10} before analysis. Weight retention was evaluated during degradation as well as the changes in molecular weight. Degradation studies were performed in triplicated and the given data corresponded to the average values.

4.2.2.3 Enzymatic Degradation

Enzymatic degradation studies were performed at 37 ºC with melt pressed films having the above-indicated dimensions. Indeed, according to Boesel et al. the bacterial synthesis of P4HB usually leads up to very high molecular weight (M_n ~ 10^6 g/mol), however, the MonoMax® suture (commercialized product)

which was used to prepare the films is derived from poly-4-hydroxybutyrate homopolymer, which is produced by Tepha, Inc. (Lexington, MA, USA). Tepha, Inc. produces P4HB using a proprietary transgenic fermentation process utilizing a genetically engineered *Escherichia coli* K12 microorganism that incorporates new biosynthetic pathways to produce the homopolymer. The advantage of this fermentation approach is the control of the molecular weight because the varied activities of specific pathway enzymes within the cells are dependent on the molecular weight. Studies were carried out in media containing lipases from *Pseudomonas cepacia* (0.1 mg/mL) and *Rhizopus oryzae* (0.072 mg/mL). All samples were exposed to 1 mL of phosphate-buffered saline (PBS) (pH 7.4) containing the determined enzyme alongside with sodium azide (0.03% w/v). These solutions were renewed every 48 h to prevent enzymatic activity loss. Samples were kept at 37 °C in an orbital shaker at 80 rpm. Samples were taken from the media at determined times, washed three times with Milli-Q water, and dried in an oven at 37 °C for 24 h to determine the dry weight. All the experiments were conducted in triplicate. The degraded samples were carbon coated and observed in SEM with an accelerating voltage of 15 kV.

4.2.2.4 Measurements

Weight loss (W_l) of the specimens was determined through **Equation 1** where W_d is the sample weight after degradation and W_0 is the initial simple weight, i.e., before exposure to the degradation medium:

$$W_l = 100 \times (W_0 - W_d) / W_o \quad \textbf{(1)}$$

Molecular weight was estimated by size exclusion chromatography (GPC) using a liquid chromatograph (Shimadzu, model LC-8A) equipped with an Empower computer program (Waters). A PL HFIP gel column (Polymer Lab) and a refractive index detector (Shimadzu RID-10A) were employed. The polymer was dissolved and eluted in 1,1,1,3,3,3-hexafluoroisopropanol (HFIP) containing CF_3COONa (0.05 M) at a flow rate of 0.5 mL/min (injected volume

100 µL, sample concentration 2.0 mg/mL). The number and weight average molecular weights were calculated using polymethyl methacrylate standards.

^{1}H-NMR spectra were acquired with a Bruker NMR Ascend 400 spectrometer operating at 400 MHz. Chemical shifts were calibrated using tetramethylsilane as an internal standard. Deuterated chloroform was used as the solvent.

Calorimetric data were obtained by differential scanning calorimetry with a TA Instruments Q100 series equipped with a refrigerated cooling system (RCS) operating at temperatures from -50 ºC to 150 ºC. Calibration was performed with indium. Experiments based on heating runs at 10ºC/min were conducted under a flow of dry nitrogen with a sample weight of approximately 5 mg.

WAXD and SAXS data were obtained at the NCD beamline (BL11) of the ALBA synchrotron facility (Cerdanyola del Vallès, Barcelona, Spain), by using a wavelength of 0.100 nm. A WAXD LX255-HS detector from Rayonix and an ImXPAD S1400 photon counting detector was employed. Polymer samples were confined between Kapton films. WAXD and SAXS diffraction patterns were calibrated with Cr_2O_3 and silver behenate (AgBh), respectively. The correlation function and the corresponding parameters were calculated with the CORFUNC software for Fibre Diffraction/Non-Crystalline Diffraction provided by the Collaborative Computational Project 13. Deconvolution of WAXD peaks was performed using the PeakFit 4.0 software.

4.2.2.5 Spherulite Cropping Out by Enzymatic Degradation

Spherulites were grown from homogeneous thin films prepared by evaporation of dilute solutions of the polymer in $CHCl_3$ (0.01 g/mL). The films were dried in a vacuum until a constant weight was achieved. The prepared thin films were exposed to both *Pseudomonas cepacia* (0.1 mg/mL) and *Rhizopus oryzae* (0.072 mg/mL) enzymatic media during different exposure times. Samples were subsequently washed three times with Milli-Q water and dried in an oven at 37 °C for 24 h to determine the dry weight.

Bright-field and polarized optical micrographs were taken with a Zeiss Axioskop 40 Pol light polarizing microscope. A first-order red tint plate was employed to determine the sign of spherulitic birefringence under crossed polarizers.

Scanning electron micrographs were taken using Phenom XL Desktop SEM equipment. Degraded films were mounted on a double-sided adhesive carbon disc and were sputter-coated with a thin layer of carbon to prevent sample charging problems using a K950X Turbo Evaporator. All samples were observed at an accelerating voltage of 15 kV.

4.2.2.6 Statistical Analysis

Values were averaged and graphically represented together with their respective standard deviations. Statistical analysis was performed by one-way ANOVA test to compare the means of all groups, and then Tukey's test was applied to determine a statistically significant difference between the two groups. The test confidence level was set at 95% ($p < 0.05$).

4.2.3 RESULTS AND DISCUSSION

4.2.3.1 Hydrolytic Degradation of P4HB Films

Hydrolytic degradation of P4HB is a bulk process that is influenced by the pH of the medium and obviously by temperature. The evolution of weight loss and molecular weight have been evaluated at representative pH values of 3, 7 (close to physiological), and 10 and temperatures of 37 ºC (physiological) and 55 ºC (maximum allowed value before starting the melting process). **Figure 4.2.1a** shows that the degradation at 37 ºC is not significant when only the weight loss is considered. Note that, only a small weight loss that reaches a value lower than 0.2% can be detected during the 3 first days of exposure and that probably corresponds to additives, like typical colorants and very small fragments that have been incorporated into the commercial sample. The behavior is different at 55 ºC where a loss of material around 2.1% can be determined for the pH 10 medium suggesting a very small degradation process.

Results were again not significant at the other two pH values (i.e., around 0.6% after 3 days of exposure at pH 3 and around 0.7% after 21 days at pH 7). It is evident, as well-reported, that hydrolytic degradation of P4HB is a slow process that leads to few small and soluble fragments. These are the only ones that can be detected through simple weight loss measurements and become originated from a depolymerization process, which seems not favored. Logically, solubilization of these small fragments having carboxylate end groups can only be significant at basic pH media.

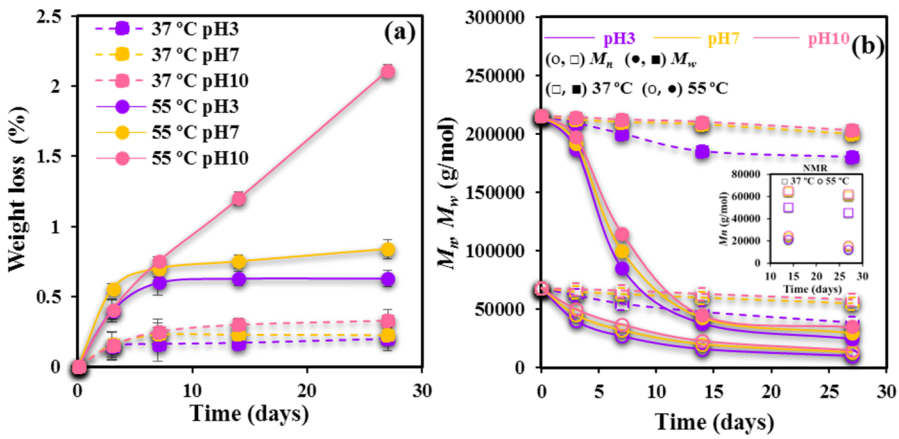

Figure 4.2.1. (**a**) Weight loss percentage versus exposure time to the hydrolytic degradation media at pH values of 3, 7, and 10 and temperatures at 37 ºC (dashed lines) and 55 ºC (solid lines). (**b**) M_n (o, □) and M_w (●, ■) molecular weights determined from GPC during degradation at the indicated pH values and temperatures. For the sake of completeness M_n values estimated from NMR spectra are also incorporated and specifically shown in the inset.

Nevertheless, GPC measurements allowed confirming that degradation is relatively significant at 55 ºC and even at 37 ºC since a reduction of molecular weight is detected (**Figure 4.2.1b**). In this case, the more aggressive medium corresponds to the acidic pH, demonstrating the contradictory conclusions that could be derived if only the weight loss of material is taken into account. Random chain scissions seem to be the preferential degradation mechanism and consequently, small soluble fragments are produced in agreement with weight

loss measurements. An important conclusion is that a preferential attack over the amorphous domains in polymer films cannot be easily detected by simple morphological observations, due to both a bulk erosion and scarce production of soluble fragments.

NMR spectra allowed estimating also the number average molecular weight of exposed samples to hydrolytic degradation media. In this case, measurements have the advantage of being independent of the solution molecular chain conformation and the appropriate selection of the GPC calibration standard, although some imprecision is expected for samples with high molecular weight (e.g., M_n higher than 10,000 g/mol). **Figure 4.2.2** displays a typical spectrum of a representative sample, where in addition to the proton signals of the three CH_2 groups of the main chain repeat unit at 4.08 ppm (OCH_2, t), 2.35 ppm (CH_2CO, t), and 1.94 ppm (OCH_2CH_2, m), small signals associated to terminal groups can be observed.

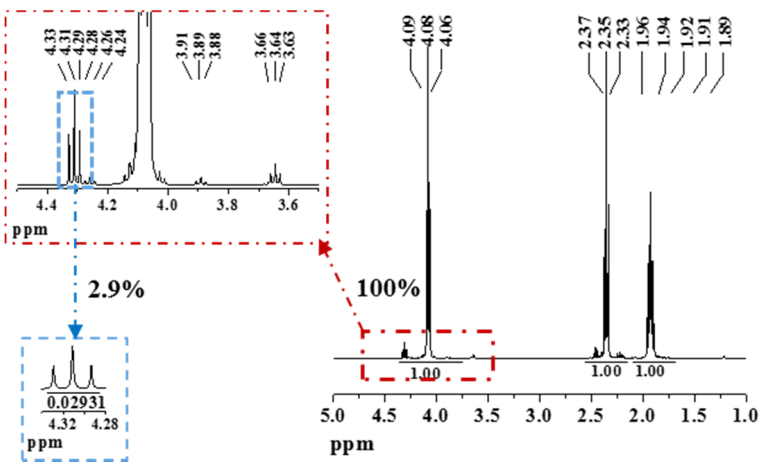

Figure 4.2.2. ^{1}H-NMR spectra of a P4HB melted film exposed to a pH 3 solution at 55 ºC for 27 days. Insets show the presence of terminal groups.

Thus, M_n could also be estimated taking into account the intensity ratio between signals at 4.08 ppm and 4.29 ppm (CH_2OH, t):

$$M_n \text{ (g/mol)} = 86 * I_{4.08}/I_{4.29} + 87 + 103 \qquad (2)$$

where 86, 87, and 103 are the molecular weights of the repeat unit, the hydroxyl terminal group, and the carboxyl-terminal group, respectively.

NMR results indicate a molecular weight dependence with medium pH that is in full agreement with that observed from GPC measurements, although values are usually higher. Only data corresponding to the lower molecular weights (i.e., degradation at 37 ºC and 55 ºC during 14 and 27 days) are plotted in **Figure 4.2.1b** and summarized in **Table 4.2.1**.

Table 4.2.1. Number average molecular weights determined from GPC and NMR techniques.

Mn **(x 10^3 g/mol)**							
Temperature	**pH**		**Time (days)**				
			0	**3**	**7**	**14**	**27**
37 ºC	3	GPC	68	62	55	48	39
		NMR	-	-	-	50	45
	7	GPC	68	65	63	60	55
		NMR	-	-	-	64	60
	10	GPC	68	67	66	63	58
		NMR	-	-	-	65	62
55 ºC	3	GPC	68	40	27	16	10
		NMR	-	-	-	21	12
	7	GPC	68	45	32	20	13
		NMR	-	-	-	23	15
	10	GPC	68	50	37	23	15
		NMR	-	-	-	25	16

4.2.3.2 Enzymatic Degradation of P4HB Films

Degradation in lipase media was more efficient, as can be detected in the SEM micrographs taken after 27 days of exposure. Assays were performed using *Pseudomonas cepacia* and *Rhizopus oryzae* enzymes, where different susceptibility of P4HB films towards the indicated enzymes is clear. It should be pointed out that the surface of films is more eroded using *Rhizopus oryzae*, a feature that evidences the capacity to finely tune the degradation by the selection of the appropriate enzymes. The surface of films used as a control was practically not affected due to the scarce hydrolytic degradation at 37 ºC.

Micrographs depict also the presence of crystals produced from degradation products that evidenced the problems associated with their low solubility (**Figure 4.2.3**).

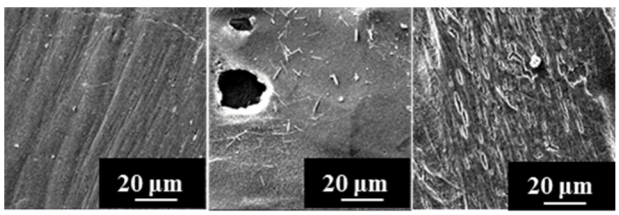

Figure 4.2.3. SEM micrographs of P4HB films after being submitted to enzymatic degradation in a *Pseudomonas cepacia* (middle) and *Rhizopus oryzae* (right) media at 37 ºC for 21 days. A micrograph corresponding to a control (left) (degradation without enzyme in a pH 7.4 medium at 37 ºC) is also depicted for comparative purposes.

In contrast with results attained using hydrolytic media, **Figure 4.2.4a** demonstrates the highly significant weight loss of exposed samples (e.g., 25% and 40% after 7 days of exposure to *Pseudomonas cepacia* and *Rhizopus oryzae* media, respectively). A practically complete degradation (i.e., 95%) was even produced after only 21 days of exposure to the most aggressive medium. These high weight losses were observed despite that the solubility problems remain and that the erosion is a surface process instead of a bulk degradation. Results suggest that a selective erosion of amorphous regions can be achieved through the appropriate selection of an enzyme and exposure time.

Figure 4.2.4b compares the GPC molecular weights of samples exposed to both enzymatic media and the control (pH 7.4 aqueous medium). In this case, differences between hydrolytic and enzymatic degradation are not so noticeable as those deduced from the weight loss measurements. It is evident that degraded fragments are retained in the bulk-eroded sample and probably a different chain scission mechanism exists (i.e., random chain scission for the hydrolytic process and depolymerization or successive removal of monomer units for the enzymatic one). Molecular weight results were again in agreement with a preferential degradation on the *Rhizopus oryzae* medium.

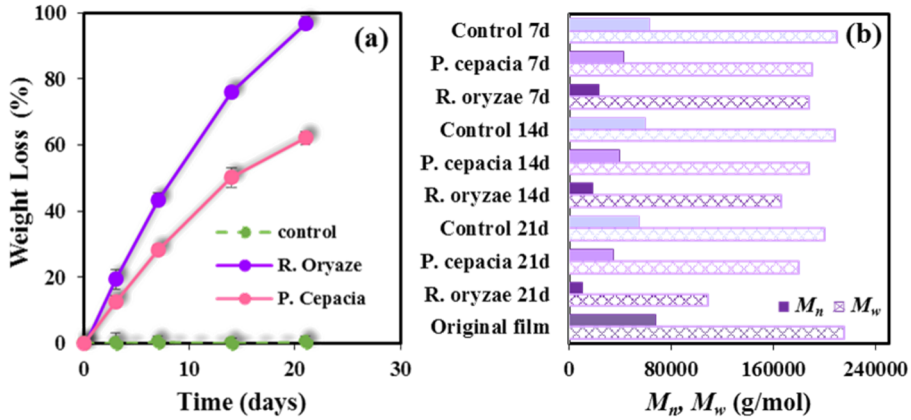

Figure 4.2.4. (a) Weight loss percentage versus exposure time to enzymatic media containing lipases from *Pseudomonas cepacia* (0.1 mg/mL) and *Rhizopus oryzae* (0.072 mg/mL) at 37 ºC. (b) M_n (■) and M_w (☒) molecular weights determined from GPC during degradation at the indicated enzymatic media and temperature.

4.2.3.3 Thermal Properties of Hydrolytically and Enzymatically P4HB Degraded Samples

The fusion of the P4HB homopolymer is characterized by a double melting peak, as shown in the left inset of **Figure 4.2.5a**. This complex fusion has been associated with the existence of two lamellar populations with different thicknesses since no polymorphic forms have been described for P4HB[18]. Temperatures of the melting peaks are susceptible to thermal annealing processes since clear differences have been reported[18] between melt crystallized sample and annealed sutures. Specifically, the temperature of the lower (T_{m1}) and the main (T_{m2}) melting peak can be increased from 58 ºC to 72 ºC and from 50 ºC to 62 ºC, respectively.

P4HB films exposed to hydrolytic degradation showed a significant change in thermal properties (i.e., T_{m1}, T_{m2}, and melting enthalpy) as summarized in **Table 4.2.2**. Interpretation of the observed changes is difficult since annealing effects derived from exposure to different temperatures, times and media may play a significant role and mask those effects attributed to the potential degradation of molecular chains.

Table 4.2.2. Melting peak temperatures and enthalpies of P4HB samples hydrolytically degraded at different pH values, temperatures, and exposure times.

pH	*T* (ºC)	Time (days)	T_{m1}[a] (ºC)	T_{m2} (ºC)	ΔH_m[b] (J/g)
3	37	3	54.4	61.5	50.1
3	37	7	55.2	61.8	54.4
3	37	14	55.9	62.1	55.4
3	37	27	58.8	64.1	59.7
3	55	3	47.7	71.5	54.7
3	55	7	47.8	73.4	58.0
3	55	14	50.1	75.8	61.5
3	55	27	50.7	75.9	70.6
7	37	3	53.8	61.1	49.1
7	37	7	54.5	61.8	49.6
7	37	14	56.0	62.1	54.8
7	37	27	59.0	63.8	59.3
7	55	3	47.9	71.4	54.2
7	55	7	47.9	73.5	58.9
7	55	14	49.2	75.1	60.1
7	55	27	51.4	75.8	69.1
10	37	3	53.2	59.5	50.1
10	37	7	54.7	60.5	51.2
10	37	14	55.8	61.8	54.0
10	37	27	58.9	63.6	58.5
10	55	3	47.9	71.5	54.0
10	55	7	48.0	73.3	59.3
10	55	14	48.7	74.6	60.3
10	55	27	53.5	75.2	65.2

[a)] Peaks of samples coming from 55 ºC are very broad and have small intensity. Probably correspond to highly defective crystals of distinct nature than those detected for samples exposed to 37 ºC. Peak temperatures are written in italics to point out this feature.

[b)] Enthalpies corresponding to the main peak for degradations performed at 55 ºC and the global value for the shoulder and the main peak for degradations performed at 37 ºC.

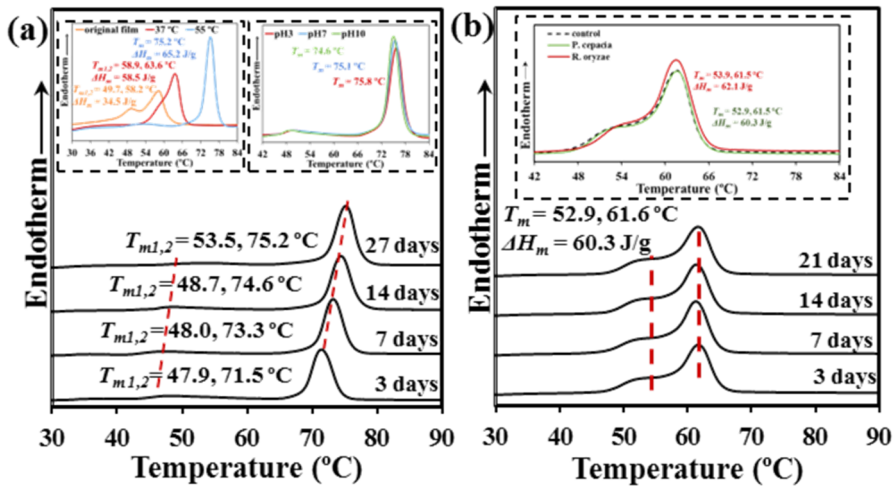

Figure 4.2.5. (a) DSC heating runs of P4HB hydrolytically degraded films after 3, 7, 14, and 27 days at 55 ºC and pH 10. Insets show the comparison between films degraded at 37 ºC and 55 ºC after 27 days of exposure at a pH 10 medium (left) and films degraded by exposure for 14 days to pH 3, pH 7, and pH10 media at 55 ºC (right). For the sake of comparison, the DSC trace of the initial melt pressed sample is shown in the left inset. (b) DSC heating runs of P4HB enzymatically degraded films in a *Pseudomonas cepacia* medium after 21 days at 37 ºC. The inset shows, for the sake of completeness, the DSC curves of samples exposed for 21 days to both enzymatic media and the comparison with the control.

Nevertheless, experimental data allow us to perform the following conclusions:

- Thermal annealing caused a significant increase in the melting temperatures as shown in the left inset of **Figure 4.2.5a** that compares the DSC traces of the initial sample and films exposed for 27 days to a pH 10 representative media at 37 ºC and 55 ºC. According to **Table 4.2.2**, T_{m1} increased from 49.7 ºC (initial film and 25 ºC) to 53.2-59.0 ºC after exposure to the media at 37 ºC, and T_{m2} increased from 58.2 ºC (initial film at 25 ºC) to 59.5-63.3 ºC and 71.4-75.9 ºC for media at 37 ºC and 55 ºC, respectively. Samples hydrolyzed at 55 ºC showed a broad and low intense T_{m1} peak that was produced as a consequence of some residual crystallization during the subsequent drying at room temperature. It is obvious that the initial thinner crystals were melted and recrystallized in the degradation media at 55 ºC. Note also that in

these media, films could reach a T_{m2} temperature higher than the annealed commercial sutures. An effect caused by degradation could, in addition, be considered. Namely, degradation of crystalline regions should proceed through the amorphous lamellar folding surfaces giving rise to a significant decrease in the molecular weight as detected at 55 ºC and an increase of the lamellar core thickness and even on the thickness of the amorphous lamellar surface layer.

Melting enthalpy was also clearly influenced by the lamellar reordering process induced by temperature and probably to a minor degree by degradation as discussed in the following points. Thus, the enthalpy of the initial sample (34.5 J/g) increased to 49.1-59.7 ºC and 54.7-70.6 ºC after exposure to media at 37 ºC and 55 ºC, respectively. Note that the observed changes cannot be attributed to degradation and solubilization of amorphous domains as could be deduced by the minimum weight losses indicated in **Figure 4.2.1**.

- For a given degradation assay melting peak temperatures and melting enthalpy gradually increased with the exposure time. **Figure 4.2.5a** illustrates the evolution of the melting peak for a sample exposed to a pH 10 medium at 55 ºC. In this case, the melting temperature regularly increased from 71.5 ºC to 75.2 ºC as the degradation time increased from 3 to 27 days. In the same way, the melting enthalpy slightly increased from 54.0 J/g to 65.2 J/g. Results indicate a significant increase in the crystallinity of the sample during exposure, as reflected by the variation of enthalpy. A crystallization process may occur as a consequence of both the decrease of molecular weight and time-dependent annealing since as indicated the solubilization of amorphous domains is discarded. A regular increase in the lamellar thickness that justifies the observed change in the melting temperature can also be inferred. Change in thermal properties was logically more significant at the higher temperature and for example, the melting enthalpy of samples exposed to the pH 3 medium at 37 ºC and 55 ºC varied from

54.7 J/g to 70.9 J/g (i.e., 16.2 J/g) and from 50.1 J/g to 59.7 J/g (i.e., 9.6 J/g), respectively.

- The pH of the medium had a slight influence on thermal properties but as a general trend, it was observed that both melting peak temperature and melting enthalpy slightly increased whit the decrease of the pH value (**Table 4.2.2** and right inset of **Figure 4.2.5.a**). Thus, samples exposed for 27 days at 37 ºC showed a T_{m2} increase from 63.6 ºC to 64.1 ºC and a melting enthalpy increase from 58.5 J/g to 59.7 J/g when pH decreased from 10 to 3. Similar changes were observed at 55 ºC and specifically, the temperature increased from 75.2 ºC to 75.9 ºC and the enthalpy from 65.2 J/g to 70.6 J/g. This trend correlates with the observed higher degradation in acidic media.

Figure 4.2.5b shows the evolution of DSC heating runs of samples exposed, for increasing times, to the less aggressive *Pseudomonas cepacia* enzymatic medium. The behavior became similar to that found for the control (i.e., an aqueous medium without enzyme and pH 7.4) and demonstrated that this enzymatic degradation has a very small effect on the crystalline regions. A slight shift of the main melting peak (T_{m2}) and the associated shoulder (T_{m1}) can be detected as the exposure time increased (**Table 4.2.3**), but this evolution appears in full agreement with the data corresponding to the hydrolytic degradation. The inset of **Figure 4.2.5b** compares the DSC heating runs of samples exposed to *Pseudomonas cepacia* and the *Rhizopus oryzae* media for the maximum studied exposure of 21 days. In this situation, small differences can be detected and demonstrated that the higher attack of *Rhizopus oryzae* to the amorphous regions leading to a significant weight loss and a small increase in crystallinity (i.e., higher melting enthalpy) with respect to the samples coming from the *Pseudomonas cepacia* medium. It can also be indicated the shift of the T_{m1} shoulder to higher temperatures, a feature that may suggest that the amorphous folding surfaces of the thinner lamellae were more susceptible to the enzymatic attack.

Table 4.2.3. Melting peak temperatures and enthalpies of P4HB samples enzymatically degraded at a pH of 7.4, 37 ºC and different exposure times.

Enzyme	Time (days)	T_{m1}, T_{m2} (ºC)	ΔH_m[a)] (J/g)
Pseudomonas cepacia	3	52.6, 61.7	54.7
Pseudomonas cepacia	7	52.7, 61.3	56.8
Pseudomonas cepacia	14	52.9, 61.5	56.9
Pseudomonas cepacia	21	53.4, 61.7	57.0
Rhizopus oryzae	3	53.6, 61.6	56.4
Rhizopus oryzae	7	53.5, 61.3	57.5
Rhizopus oryzae	14	54.3, 61.5	59.1
Rhizopus oryzae	21	54.2, 61.5	59.9

a) Global enthalpy corresponding to the shoulder and the main peak.

4.2.3.4 Influence of Hydrolytic and Enzymatic Degradation on the P4HB Lamellar Thickness

In order to complement the DSC observations, small-angle X-ray scattering (SAXS) patterns were also considered to analyse the change in the lamellar morphologies during exposure to the different media and temperatures.

The analysis was performed through the use of the normalized correlation function:

$$\gamma(r) = \int_0^\infty q^2 I(q) \cos(qr)\, dq \;\Big/\; \int_0^\infty q^2 I(q)\, dq \qquad (3)$$

where $I(q)$ is the intensity of the SAXS peak at each value of the scattering vector ($q = [4\pi/\lambda] \sin \theta = 2\pi/d$, with θ and d being the Bragg angle and the Bragg spacing, respectively).

Long period, L_γ, amorphous layer thickness, l_a, and crystalline lamellar thickness, l_c, can be determined by the normalized one-dimensional correlation function[23] and applying the Vonk's model[24] and Porod's law to perform extrapolations to low and high q values.

Figure 4.2.6a illustrates 1D-SAXS profiles and the corresponding correlation functions of samples degraded during 27 days at 37 ºC. Differences are significant with respect to the original film and agree with the previously indicated thermal annealing effect. Nevertheless, correlation functions were

practically identical, despite the change of the pH of the medium. Data summarized in **Table 4.2.4** indicated L_γ, l_c and l_a values of 8.50-8.60, 6.80-6.91, and 1.62-1.70, which means random changes of the three parameters that are lower than 0.12 nm and that have no physical meaning.

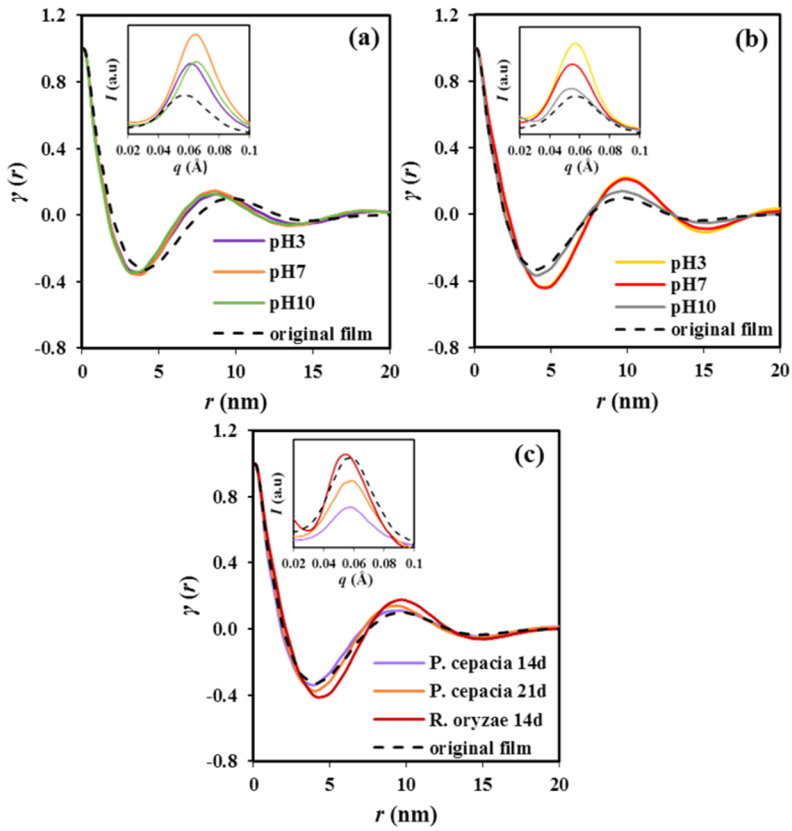

Figure 4.2.6. SAXS correlation functions of P4HB films exposed for 27 days to an aqueous medium of pH 3, pH 7, and pH 10 at 37 ºC (**a**) and 55 ºC (**b**). Correlation function during enzymatic degradation exposed to two different lipases: *Pseudomonas cepacia* and *Rhizopus oryzae* (**c**) after 14 and 21 days. Insets show in all cases the corresponding 1D-SAXS profiles.

Clearer differences were observed with the previous data when degradation was performed at 55 ºC since L_γ increased significantly to 9.60-9.80 nm and l_c increased to 7.29-7.62 nm (**Figure 4.2.6b**). Note that this evolution is in agreement with the discussed DSC observations that suggested an increase in the lamellar spacing as degradation and annealing temperature

were increased. Lamellar parameters of samples degraded at 55 ºC in different pH values were relatively similar but evidenced a significant increase of l_a from 1.98 nm to 2.48-2.51 nm when pH was lowered. The advance of degradation seems to affect the lamellar folding surfaces, with the corresponding thickness increase being associated with the breakage of chains in the irregular folds and the production of less compact layers. Note also the increase of l_a when samples degraded at 37 ºC and 55 ºC is compared. The shape of the correlation functions also varied and specifically showed that minima and maxima were sharper as the degradation progressed. This feature is a consequence of a greater difference between the electronic densities of amorphous and crystalline layers as could be justified from the loosely packing of broken folds.

The change of the correlation function during enzymatic degradation in different media is also shown in **Figure 4.2.6c** and **Table 4.2.4**. Yet again, more degraded samples showed sharper maxima and minima and increased L_γ and l_a values. Note for example that the enzymatic degradation for only 14 days (pH 7.4, 37 ºC) in the *Rhizopus oryzae* medium becomes similar to the hydrolytic degradation for 27 days in a pH 3 medium at 55 ºC. This feature suggests that the observed morphological changes were not only a direct consequence of lamellar reordering processes induced by temperature and that degradation played also a highly significant role.

Despite the observed changes in the l_c and l_a values, it should be pointed out that the crystallinity of the lamellar stacks (i.e., $\chi^{SAXS} = l_c / l_\gamma$) is relatively constant and specifically varies between 0.75 and 0.81 without any specific trend (**Table 4.2.3**). The morphology of lamellae changed during annealing and degradation but the corresponding crystallinity does not change significatively in contrast with the global crystallinity of the sample that is affected by the attack, solubilization, or recrystallization of the amorphous domains.

Table 4.2.4. Lamellar morphological parameters of P4HB samples after being exposed to different degradation media.

Medium	pH	T (ºC)	Time (days)	L_γ (nm)	l_c (nm)	l_a (nm)	χ^{SAXS}
Original film	-	-	-	8.80	7.10	1.70	0.81
Hydrolytic	3	37	27	8.60	6.91	1.69	0.80
Hydrolytic	7	37	27	8.50	6.80	1.70	0.80
Hydrolytic	10	37	27	8.50	6.88	1.62	0.81
Hydrolytic	3	55	27	9.8	7.32	2.48	0.75
Hydrolytic	7	55	27	9.8	7.29	2.51	0.74
Hydrolytic	10	55	27	9.6	7.62	1.98	0.79
Pseudomonas cepacia	7.4	37	14	9.5	7.72	1.78	0.81
Pseudomonas cepacia	7.4	37	21	9.3	7.32	1.98	0.79
Rhizopus oryzae	7.4	37	14	9.6	7.25	2.35	0.76

4.2.3.5 Revealing P4HB Spherulitic Morphologies by Enzymatic Degradation of Thin Films

Thin films of P4HB (thickness lower than 10 μm) were prepared as exposed in the materials and methods section. Films were placed to the same enzymatic media, considering the two previously evaluated lipases in order to visualize the morphology of crystalline spherulites developed on the surface of films. The activity of enzymes was however increased (i.e., from 4 to 40 U/mL for both *Pseudomonas cepacia* and *Rhizopus oryzae*) to get sufficiently eroded surfaces within a reasonable time of exposure (i.e., maximum 3 hours).

Figures 4.2.7a and **4.2.7b** show bright field and polarized optical micrographs of the P4HB film initial surface. The bright-field image allows detecting the presence of multiple bumps in the film surface, which can be related to the spherulites as clearly observed in the corresponding micrograph taken under polarizers. The observed spherulites had a variable size with diameters ranging between 20 and 40 μm and a banded texture with a spacing between rings close to 5 μm. A negative birefringence was always detected (see inset of **Figure 4.2.7b**) as characteristic of aliphatic polyesters and as reported for melt crystallized P4HB.

The origin of banded spherulites is a matter motif of controversial with different explanations being postulated. Thus, the development of interlamellar

screw dislocations or the presence of polymorphic structures has been in some cases indicated.

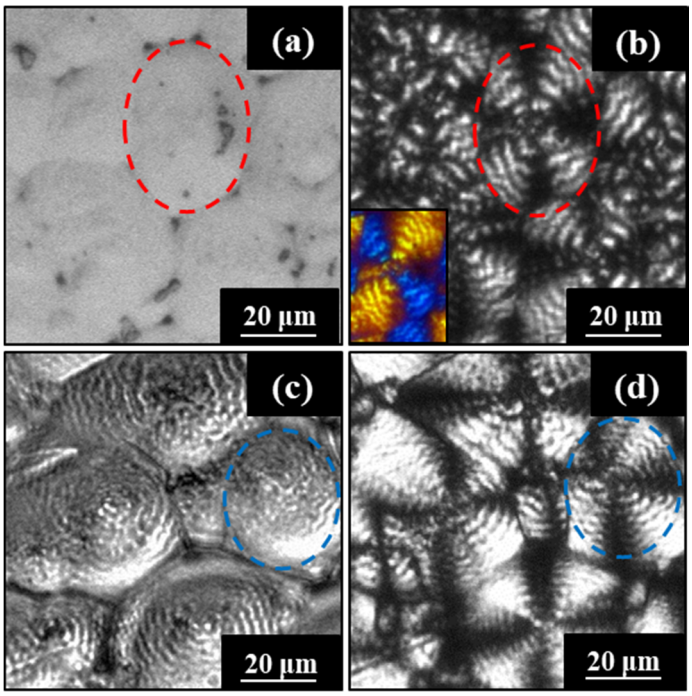

Figure 4.2.7. Optical micrographs showing P4HB thin films before (**a, b**) and after being exposed to a *Pseudomonas cepacia* (0.1 mg/mL) medium at 37 ºC (**c, d**) for 3 days. Images were taken without (**a, c**) and with polarizers (**b, d**) for the indicated days. Red and blue dashed ellipsoids point out spherulites before and after being exposed to the degradation medium.

An interesting explanation was also given considering the effects of rhythmic growth caused by the periodic presence of depletion zones in the crystal growth front.[25] A diffusion rate of the melted polymer, lower than the rate at which chains are consumed to form the crystalline lamellae, leads to these depletion zones. Films having concentric-ringed textures and an alternate disposition of ridges and valleys (i.e., the depletion zones) have been observed in polymers like isotactic polystyrene.[26,27] Moreover, ringed textures constituted by flat on lamellar crystals were characteristic of some solution crystallized thin films and explained in some cases by the rhythmic model (e.g., poly(bisphenol A hexane ether)[28] and poly(ε-caprolactone).[25]

Nevertheless, the most generalized interpretation considers a continuous twisting of constitutive lamellae along the spherulite radius. Imbalanced stresses at the two lamellar folding surfaces have been postulated as the main reason to induce a regular lamellar twisting.[29] Imbalances can be a consequence of the presence of chiral units (e.g., poly(3-hydroxybutyrate)[30] and isotactic poly(1-butene)[31]), chain tilt with respect to the lamellar surface (e.g., polyethylene[32,33]), asymmetric repeat units (e.g., ω-hydroxy acid derivatives like polypivalolactone[34]) and differences on the folding units (e.g., nylon 6,6[35] and poly(vinylidene fluoride),[36] which lead in this case to a lamellar scrolling). Lamellar twisting can also be deduced from SEM micrographs of melt crystallized spherulites after chemical etching[37] (e.g., polyethylene[38]) where cooperative C-shaped lamellar edges (or inverted C-shaped edges depending on the handle sense of lamellae) can be observed surrounding rings constituted by flat-on crystals with low birefringence. The peculiar shape of lamellar edges has been associated with the intersection of the twisting lamellae and the spherulite surface.[39]

In previous work, FTIR microspectroscopic experiments were performed with a solution of P4HB crystallized spherulites which displayed a ridged texture in POM observations[19]. FTIR results showed a spherulitic sectorization when chemical images were obtained from the integration of highly specific infrared peaks. Thus, only a few bonds had a sufficiently different geometrical orientation to render a typical Maltese cross under polarizers. Chemical mapping was unable to show a ringed texture derived from a change of the orientation of selected chemical bonds along the spherulitic radius as could be expected for a twisted lamellar morphology. However, experimental limitations concerning a resolution limit that is very close to the interring spacing could not be discarded. Therefore, direct microscopy images obtained after selective removal of the amorphous regions were considered ideal to support the lamellar twisting in P4HB spherulites. **Figure 4.2.7c** reveals as the banded texture is defined after an appropriate exposure to enzymatic degradation media. Note

that the bright field image showing the cropped out spherulites is fully consistent with the corresponding POM image (**Figure 4.2.7d**).

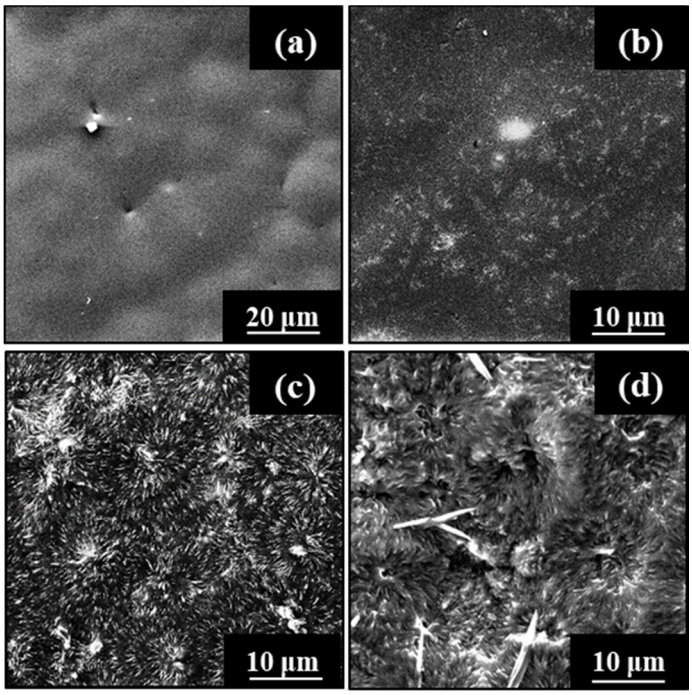

Figure 4.2.8. SEM micrographs showing P4HB thin films before (**a**) and after being exposed to a *Pseudomonas cepacia* (1 mg/mL) medium at 37 ºC for 1 (**b**), 2 (**c**), and 3 (**d**) days.

Controlling the exposure time and selecting the appropriate enzyme allows highlighting the spherulite morphology with high detail precision. Thus, SEM micrographs in **Figure 4.2.8** show the evolution of the initial sample, where bumps with diameters between 20-30 µm could be detected during exposure for 1, 2, and 3 days to the *Pseudomonas cepacia* enzymatic medium. The progressive erosion of the amorphous regions enables the identification of the banded structure, which began to be cropped after only 1 day (**Figure 4.2.8b**) and allows distinguishing the presence of edge lamellae at 2 days (**Figure 4.2.8c**). After that, images became unclear due to the presence of big crystals involving molecules produced during degradation (**Figure 4.2.8d**), nevertheless, erosion has increased.

The sequence of degraded spherulites in the *Rhizopus oryzae* medium is shown in **Figure 4.2.9**. In this case, degradation advanced faster as it can be deduced by the comparison of images taken after 1 day (i.e., **Figures 4.2.8b** and **4.2.9a**) when by-products of degradation caused fewer interferences in the visual aspect of the spherulites.

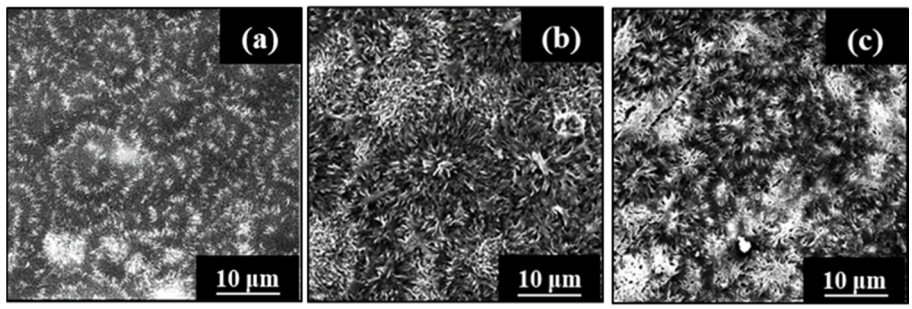

Figure 4.2.9. SEM micrographs showing P4HB thin films after being exposed to a *Rhizopus oryzae* (0.72 mg/mL) medium at 37 ºC for 1 (**a**), 2 (**b**), and 3 days (**c**).

The performed assays indicated that the *Rhizopus oryzae* medium was the adequate one to visualize the spherulitic morphology and that after 3 days of exposure the crystalline texture of the spherulite was delimitated. **Figure 4.2.10a** depicts a degraded spherulite where rings formed by cooperative C-shaped lamellar edges are highlighted. The magnification in **Figure 4.2.10b** enables the distinction of the main features of the two kinds of bands: those mainly constituted by edge-on lamellae and those based on flat-on lamellae. Besides that, an abrupt lamellar twist seems to be produced, but similar effects have been reported for other systems indicating that lamellae curve smoothly despite the optical illusion.[40]

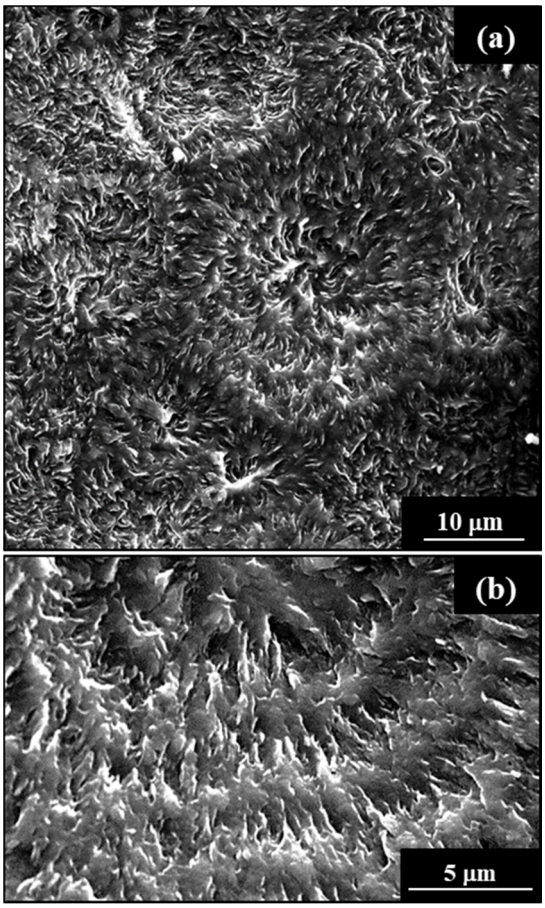

Figure 4.2.10. SEM micrographs showing the details at different magnifications of a highlighted P4HB spherulite after exposure of a thin film to a *Pseudomonas cepacia* (1 mg/mL) medium for 3 days at 37 ºC.

4.2.4 CONCLUSIONS

Hydrolytic and enzymatic degradation of P4HB proceeds by following different mechanisms. Bulk degradation and random chain scissions are characteristic of samples exposed to hydrolytic media, whereas surface erosion and depolymerization are characteristic of samples exposed to enzymatic media. Hydrolytic degradation rate can be controlled through the pH of the medium, being specifically enhanced in acidic media, and more significantly by increasing the temperature. Solubilization of degraded fragments is significant in the enzymatic degradation due to its mechanism based on the successive removal of monomer units. Degradation processes are affected predominantly to the amorphous regions, causing an increase in the degree of crystallinity as determined by DSC. Furthermore, the amorphous folds on the lamellar surface were more susceptible to degradation, leading to a slight change in the lamellar morphology. An increase in the lamellar width has been inferred through DSC data by considering the increase in the melting temperature, and more directly by the analysis of SAXS correlation functions. The surface attack, high solubilization, and high degradation rate (when appropriate enzymes with high activity are selected) are characteristics that enhance the interest in the enzymatic process to crop out the morphologies of constitutive spherulites. In the present work, the enzymatic degradation has been successfully employed to show directly the structure of P4HB banded spherulites once the amorphous regions were selectively removed. SEM micrographs pointed out an alternate disposition of edge-on and flat-of lamellae and supported the theories based on a lamellar twisting.

4.2.5 REFERENCES

(1) Martin, D. P.; Williams, S. F. Medical Applications of Poly-4-Hydroxybutyrate: A Strong Flexible Absorbable Biomaterial. *Biochem. Eng. J.* **2003**, *16* (2), 97–105. https://doi.org/10.1016/S1369-703X(03)00040-8.

(2) Le Meur, S.; Zinn, M.; Egli, T.; Thöny-Meyer, L.; Ren, Q. Poly(4-Hydroxybutyrate) (P4HB) Production in Recombinant Escherichia Coli: P4HB Synthesis Is Uncoupled with Cell Growth. *Microb. Cell Fact.* **2013**, *12* (1), 123. https://doi.org/10.1186/1475-2859-12-123.

(3) Odermatt, E. K.; Funk, L.; Bargon, R.; Martin, D. P.; Rizk, S.; Williams, S. F. MonoMax Suture: A New Long-Term Absorbable Monofilament Suture Made from Poly-4-Hydroxybutyrate. *Int. J. Polym. Sci.* **2012**, *2012*, 1–12. https://doi.org/10.1155/2012/216137.

(4) Tornier, announces launch of BioFiber® Surgical Mesh for tendon repair at arthroscopic surgery conference https://www.businesswire.com/news/home/20110414005940/en/Tornier-Announces-Launch-BioFiber®-Surgical-Mesh-Tendon (accessed Jul 2, 2020).

(5) Deeken, C. R.; Matthews, B. D. Characterization of the Mechanical Strength, Resorption Properties, and Histologic Characteristics of a Fully Absorbable Material (Poly-4-Hydroxybutyrate-PHASIX Mesh) in a Porcine Model of Hernia Repair. *ISRN Surg* **2013**, *2013*, 1–12. https://doi.org/10.1155/2013/238067.

(6) Williams, S. F.; Rizk, S.; Martin, D. P. Poly-4-Hydroxybutyrate (P4HB): A New Generation of Resorbable Medical Devices for Tissue Repair and Regeneration. *Biomed. Eng. (NY).* **2013**, *58* (5), 439–452. https://doi.org/10.1515/bmt-2013-0009.

(7) Martin, D. P.; Badhwar, A.; Shah, D. V.; Rizk, S.; Eldridge, S. N.; Gagne, D. H.; Ganatra, A.; Darois, R. E.; Williams, S. F.; Tai, H. C.; et al. Characterization of Poly-4-Hydroxybutyrate Mesh for Hernia Repair Applications. *J. Surg. Res.* **2013**, *184* (2), 766–773. https://doi.org/10.1016/j.jss.2013.03.044.

(8) Mendelson, K.; Aikawa, E.; Mettler, B. A.; Sales, V.; Martin, D.; Mayer, J. E.; Schoen, F. J. Healing and Remodeling of Bioengineered Pulmonary Artery Patches Implanted in Sheep. *Cardiovasc. Pathol.* **2007**, *16* (5), 277–282. https://doi.org/10.1016/j.carpath.2007.03.008.

(9) Ackermann, J. uwe; Müller, S.; Lösche, A.; Bley, T.; Babel, W. Methylobacterium Rhodesianum Cells Tend to Double the DNA Content under Growth Limitations and Accumulate PHB. *J. Biotechnol.* **1995**, *39* (1), 9–20. https://doi.org/10.1016/0168-1656(94)00138-3.

(10) Boesel, L. F.; Meur, S. Le; Thöny-Meyer, L.; Ren, Q. The Effect of Molecular Weight on the Material Properties of Biosynthesized Poly(4-Hydroxybutyrate). *Int. J. Biol. Macromol.* **2014**, *71*, 124–130. https://doi.org/10.1016/j.ijbiomac.2014.04.015.

(11) Park, D. H.; Kim, B. S. Production of Poly(3-Hydroxybutyrate) and Poly(3-Hydroxybutyrate-Co-4-Hydroxybutyrate) by Ralstonia Eutropha

from Soybean Oil. *N. Biotechnol.* **2011**, *28* (6), 719–724. https://doi.org/10.1016/j.nbt.2011.01.007.

(12) Zhang, L.; Shi, Z. Y.; Wu, Q.; Chen, G. Q. Microbial Production of 4-Hydroxybutyrate, Poly-4-Hydroxybutyrate, and Poly(3-Hydroxybutyrate-Co-4-Hydroxybutyrate) by Recombinant Microorganisms. *Appl. Microbiol. Biotechnol.* **2009**, *84* (5), 909–916. https://doi.org/10.1007/s00253-009-2023-7.

(13) Martínez-Palau, M.; Franco, L.; Ramis, X.; Puiggalí, J. Poly[(4-Hydroxybutyric Acid)-Alt-(Glycolic Acid)]: Synthesis by Thermal Polycondensation of Metal Salts of 4-Chlorobutyric Acid Carboxymethyl Ester. *Macromol. Chem. Phys.* **2006**, *207* (1), 90–103. https://doi.org/10.1002/macp.200500260.

(14) Su, F.; Iwata, T.; Sudesh, K.; Doi, Y. Electron and X-Ray Diffraction Study on Poly(4-Hydroxybutyrate). *Polymer (Guildf).* **2001**, *42* (21), 8915–8918. https://doi.org/10.1016/S0032-3861(01)00412-8.

(15) Su, F.; Iwata, T.; Tanaka, F.; Doi, Y. Crystal Structure and Enzymatic Degradation of Poly(4-Hydroxybutyrate). *Macromolecules* **2003**, *36* (17), 6401–6409. https://doi.org/10.1021/ma034546s.

(16) Tanaka, F.; Doi, Y.; Iwata, T. The Deformation of the Chain Molecules and Crystallites in Poly([R]-3-Hydroxybutyrate) and Poly(4-Hydroxybutyrate) under Tensile Stress. *Polym. Degrad. Stab.* **2004**, *85* (2), 893–901. https://doi.org/10.1016/j.polymdegradstab.2004.04.006.

(17) Hsieh, W. C.; Mitomo, H.; Kasuya, K. I.; Komoto, T. Enzymatic Degradation and Aminolysis of Microbial Poly(3-Hydroxybutyrate-Co-4-Hydroxybutyrate) Single Crystals. *J. Polym. Environ.* **2006**, *14* (1), 79–87. https://doi.org/10.1007/s10924-005-8710-2.

(18) Keridou, I.; del Valle, L. J.; Funk, L.; Turon, P.; Yousef, I.; Franco, L.; Puiggalí, J. Isothermal Crystallization Kinetics of Poly(4-Hydroxybutyrate) Biopolymer. *Polym. Morphol. Princ. Charact. Process.* **2019**, *12* (2488), 1–20. https://doi.org/10.3390/ma12152488.

(19) Keridou, I.; Del Valle, L. J.; Funk, L.; Turon, P.; Franco, L.; Puiggalí, J. Non-Isothermal Crystallization Kinetics of Poly(4-Hydroxybutyrate) Biopolymer. *Molecules* **2019**, *24* (15), 1–24. https://doi.org/10.3390/molecules24152840.

(20) Barham, P. J.; Keller, A.; Otun, E. L.; Holmes, P. A. Crystallization and Morphology of a Bacterial Thermoplastic: Poly-3-Hydroxybutyrate. *J. Mater. Sci.* **1984**, *19* (9), 2781–2794. https://doi.org/10.1007/BF01026954.

(21) Kyu, T.; Chiu, H. W.; Guenthner, A. J.; Okabe, Y.; Saito, H.; Inoue, T. Rhythmic Growth of Target and Spiral Spherulites of Crystalline Polymer Blends. *Phys. Rev. Lett.* **1999**, *83* (14), 2749–2752. https://doi.org/10.1103/PhysRevLett.83.2749.

(22) Teorell, T.; Stenhagen, E. Universal Buffer over the PH Range 2.0 to 12.0. *Biochem Z* **1938**, *299*, 416–419.

(23) Vonk, C. G.; Kortleve, G. X-Ray Small-Angle Scattering of Bulk Polyethylene. *Kolloid Z Z Polym* **1967**, *220*, 19–24.

(24) Vonk, C. G. A General Computer Program for the Processing of Small-Angle X-Ray Scattering Data. *J. Appl. Crystallogr.* **1975**, *8*, 340–341.
(25) Wang, Z.; Alfonso, G. C.; Hu, Z.; Zhang, J.; He, T. Rhythmic Growth-Induced Ring-Banded Spherulites with Radial Periodic Variation of Thicknesses Grown from Poly(ε-Caprolactone) Solution with Constant Concentration. *Macromolecules* **2008**, *41* (20), 7584–7595. https://doi.org/10.1021/ma8005697.
(26) Duan, Y.; Jiang, Y.; Jiang, S.; Li, L.; Yan, S. Depletion-Induced Nonbirefringent Banding in Thin Isotactic Polystyrene Thin Films. *Macromolecules* **2004**, *37*, 9283–9286.
(27) Duan, Y.; Zhang, Y.; Yan, S.; Schultz, J. M. In Situ AFM Study of the Growth of Banded Hedritic Structures in Thin Films of Isotactic Polystyrene. *Polymer (Guildf).* **2005**, *46* (21), 9015–9021. https://doi.org/10.1016/j.polymer.2005.07.024.
(28) Wang, Y.; Chan, C. M.; Li, L.; Ng, K. M. Concentric-Ringed Structures in Polymer Thin Films. *Langmuir* **2006**, *22* (17), 7384–7390. https://doi.org/10.1021/la060863r.
(29) Lotz, B.; Cheng, S. Z. D. A Critical Assessment of Unbalanced Surface Stresses as the Mechanical Origin of Twisting and Scrolling of Polymer Crystals. *Polymer (Guildf).* **2005**, *46* (3), 577–610. https://doi.org/10.1016/j.polymer.2004.07.042.
(30) Saracovan, I.; Cox, J. K.; Revol, J. F.; Manley, R. S. J.; Brown, G. R. Optically Active Polyethers. 3. on the Relationship between Main-Chain Chirality and the Lamellar Morphology of Solution-Grown Single Crystals. *Macromolecules* **1999**, *32* (3), 717–725. https://doi.org/10.1021/ma971874h.
(31) Lotz, B.; Thierry, A. Spherulite Morphology of Form III Isotactic Poly(1-Butene). *Macromolecules* **2003**, *36* (2), 286–290. https://doi.org/10.1021/ma021452u.
(32) Keith, H. D.; Padden, F. J. Banding in Polyethylene and Other Spherulites. *Macromolecules* **1996**, *29* (24), 7776–7786. https://doi.org/10.1021/ma960634j.
(33) Meille, S. V.; Konishi, T.; Geil, P. H. Morphology of Polypivalolactone: A Polymer with a Direction. *Polymer (Guildf).* **1984**, *25* (6), 773–777. https://doi.org/10.1016/0032-3861(84)90005-3.
(34) Keith, H. D.; Padden, F. J. Twisting Orientation and the Role of Transient States in Polymer Crystallization. *Polymer (Guildf).* **1984**, *25* (1), 28–42. https://doi.org/10.1016/0032-3861(84)90264-7.
(35) Cai, W.; Li, C. Y.; Li, L.; Lotz, B.; Keating, M.; Marks, D. Submicrometer Scroll/Tubular Lamellar Crystals of Nylon 6,6. *Adv. Mater.* **2004**, *16* (7), 600–605. https://doi.org/10.1002/adma.200305634.
(36) Lotz, B.; Thierry, A.; Schneider, S. Molecular Origin of the Scroll-like Morphology of Lamellae in Gamma PVF2 Spherulites. *Comptes Rendus Chim.* **1998**, *1* (10), 609–614.
(37) Bassett, D. C.; Olley, R. H. On the Lamellar Morphology of Isotactic Polypropylene Spherulites. *Polymer (Guildf).* **1984**, *25* (7), 935–943.

https://doi.org/10.1016/0032-3861(84)90076-4.
(38) Murthy, S. S. N.; Sobhanadri, J. Study of Some Polyurethane Elastomers Using Electrical Methods. *J. Appl. Polym. Sci.* **1994**, *54* (10), 1499–1506. https://doi.org/10.1002/app.1994.070541014.
(39) Xu, J.; Ye, H.; Zhang, S.; Guo, B. Organization of Twisting Lamellar Crystals in Birefringent Banded Polymer Spherulites: A Mini-Review. *Crystals* **2017**, *7* (8). https://doi.org/10.3390/cryst7080241.
(40) Lustiger, A.; Lotz, B.; Duff, T. S. The Morphology of the Spherulitic Surface in Polyethylene. *J. Polym. Sci. Part B Polym. Phys.* **1989**, *27* (3), 561–579. https://doi.org/10.1002/polb.1989.090270306.

5. PREPARATION OF POLY-4-HYDROXYBUTYRATE SCAFFOLDS BY MEANS OF ELECTROSPINNING.

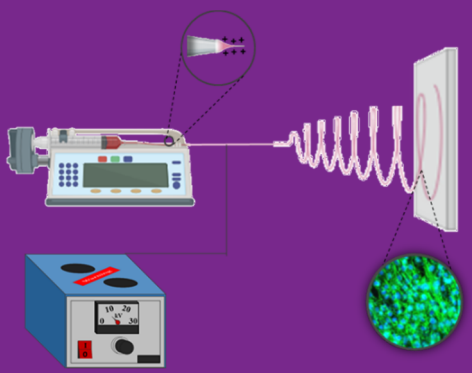

Electrospun scaffolds of the biodegradable and biocompatible poly-4-hydroxybutyrate (P4HB) polyester have been prepared using horizontal and vertical set-up configurations of electro-spinning. Specifically, it has been evaluated the influence of solvent, polymer concentration, and processing parameters, such as applied voltage, flow rate, and needle tip-collector distance. Scaffolds obtained under the most favorable conditions were characterized in terms of crystallinity, lamellar supramolecular order, thermal (including calorimetric and thermogravimetric data), mechanical and surface properties. Results pointed out significant differences with respect to commercial sutures (based in P4HB, e.g., MonoMax®) and demonstrated that electrospun scaffolds were constituted by crystalline microfibers with a tangled distribution that leads to both high modulus and elasticity. Furthermore, new scaffolds had thermal stability and a rough surface that led to a hydrophobic character. Scaffolds could also be successfully loaded during the electrospinning process with a peptide analog to the fibroblast growth factor (e.g., CYRSRKYSSWYVALKRC), giving rise to fully biocompatible samples with a clear acceleration in wound healing.

5.1 ELECTROSPUN SCAFFOLDS FOR WOUND HEALING APPLICATIONS FROM POLY-4-HYDROXYBUTYRATE: A BIOBASED AND BIODEGRADABLE LINEAR POLYMER WITH HIGH ELASTOMERIC PROPERTIES

5.1.1 INTRODUCTION

Poly-4-hydroxybutyrate (P4HB) is a biodegradable polyester belonging to the polyhydroxyalkanoates family (PHA), which can be obtained with a high yield from microorganisms (e.g., *Escherichia coli* K12)[1] in response to physiological stress conditions. Limitation of nutrients is probably the main mechanism to induce the production of P4HB, as it is also reported for another poly(hydroxyalkanoates)[2] P4HB has exceptional mechanical properties considering its high elongation at break, which is not comparable with related linear polyesters with an even number of carbon atoms in the main chain of the repeat unit. These are derived from the condensation of ω-hydroxy acids or ring-opening polymerization of glycolide and lactones and correspond to poly(glycolic acid) or polyglycolide and poly(6-hydroxyhexanoic acid) or poly(ε-caprolactone) (i.e., polymers with two and six carbon atoms instead of the four atoms of P4HB).

P4HB is hydrolyzed in the body under the action of water and enzymes to 4-hydroxybutyric acid, which is found within a variety of tissues of mammalians (e.g., brain, heart, kidney, liver, lung, muscles). The monomer can be quickly metabolized in the body, with a reported half-life time close to 30 minutes.[3]

Nowadays P4HB has wide biomedical applications due to its biocompatibility, biodegradability, and mechanical properties. TephaFLEX®, MonoMax®, BioFiber™, Phasix™, and GalaFLEX are commercial trademarks of P4HB based materials used in medical devices, such as abdominal wall closure materials, long-term bioresorbable sutures, tendon repair scaffolds, hernia repair meshes, and reconstructive surgery materials.[1,4–8]

Porous scaffolds constituted by knitted P4HB monofilament fibers (diameter close to 40 μm) provided a durable mechanical reinforcement of soft tissue, according to both *in vitro* and *in vivo* assays[9]. A 50% of its initial strength could be retained over 12 weeks after implantation and the device could be fully resorbed within 12 to 18 months.

Electrospinning is currently one of the most popular processes for preparing nonwoven micro- and nanofibers arranged into porous scaffolds.[9–11] This process uses electrostatic forces (10–100 kV) to stretch drops of a polymer dilute solution from a needle tip to a collector. Applications in the biomedical field are extensive[12–14] due to a combination of factors that include economic feasibility, easiness of preparation, and high versatility. Incorporation of drugs into electrospun scaffolds can also be easily performed, with minimum changes being usually required from the optimized processing conditions determined for building the polymer matrix. The repercussions on the final fiber geometry are usually low even when several drugs are incorporated to provide multifunctional properties.[15]

Electrospinning has been widely applied for the preparation of scaffolds based on poly(hydroxyalkanoates), such as poly(3-hydroxybutyrate) (P3HB) and poly(3-hydroxyvalerate).[16,17] Thus, properties of the rigid P3HB can be improved after being electrospun due to the decrease in its degree of crystallinity. In addition, an increase in the biodegradation rate and an improvement of interactions with tissue cells were also observed.[16] Copolymers of 3HB and 4HB have also been satisfactorily electrospun,[18] but surprisingly no specific study has been performed with the related and linear P4HB homopolymer.

The FGF-2 protein is a powerful pluripotent Fibroblast Growth Factor (FGF) that is also relevant for being the first angiogenic protein obtained from a tumor.[19] This protein prevents cell depletion by differentiation and apoptosis, and it is implicated in wound healing and angiogenesis processes.[20] FGF-P is a synthetic analogue that can also bind to the fibroblast growth factor receptor. This mimetic polypeptide is based on a 15-amino acid region with the order:

CYRSRKYSSWYVALKRC that is also present in the natural FGF-2 protein. On the other hand, FGF-P has the advantage, with respect to other growth factors, to cause a minimum inflammation or vascular leakage. Furthermore, it enhances the formation of new blood vessels in angiogenesis and improves bone growth.[21]

The main goals of the present work focus on the evaluation of the polymer solution conditions, processing parameters, and optimal experimental set-up configurations to produce suitable P4HB scaffolds by electrospinning. Furthermore, the conditions for loading the FGF-P growth factor into a representative electrospun scaffold will also be determined to assess its wound healing effect.

5.1.2 EXPERIMENTAL SECTION

5.1.2.1 Materials

Commercially available samples of P4HB (MonoMax®) were kindly supplied by B. Braun Surgical S.A.U. The weight and number average molecular weights of P4HB samples were 215,000 and 68,000 g/mol, as determined by GPC.[22] The synthetic FGF-P peptide had a purity of 93%, a molecular weight of 2,170 g/mol, and was purchased from GenScript (Piscataway, NJ, USA). Saos-2 cells (ATCC® HTB-85™, epithelial cells derived from human osteosarcoma) and NRK-49F cells (ATCC® CRL-1570™, fibroblast cells derived from rat kidney, *Rattus norvegicus*) both of growth adherent were purchased from ATCC (American Type Culture Collection, Manassas, VA, USA).

5.1.2.2 Preparation of–Neat and FGF-P Loaded Electrospun Scaffolds

Electrospinning was carried out in a non-conductor cabinet. Polymer solutions were loaded in a 10 mL BD Discardit (Becton Dickson Co., Franklin Lakes, NJ, USA) plastic syringe for delivery through a blunt-tipped (i.e., without bevel) 23 G needle (inner diameter 0.64 mm). The prepared solutions were

delivered via a single KDS100 infusion syringe pump (KD Scientific, USA) to control the flow rate (from 1 to 5 mL h^{-1}). Electrospun fibers were deposited to both a flat and a rotatory collector placed at different distances (10–25 cm) from the needle tip, which was vertically and horizontally oriented, respectively (**Figure 5.1.1**). A high voltage supply (Gamma High Voltage Research, ES30−5W) was applied to the selected collector. All electrospinning experiments were carried out at room temperature.

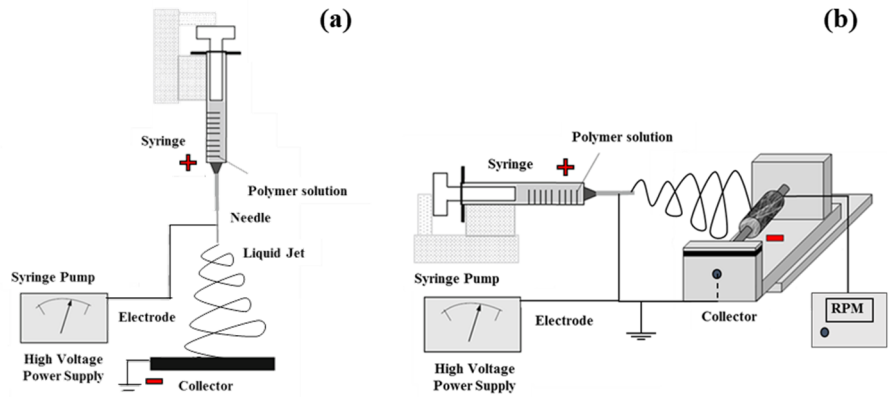

Figure 5.1.1. Schematic diagrams of the employed electrospinning equipment: (**a**) Vertical disposition with a planar collector surface, (**b**) Horizontal disposition with a rotating cylinder collector.

Neat and FGF-P loaded electrospun fibers were prepared using optimized parameters (i.e., collector distance, voltage, and flow rate) and dissolution conditions (i.e., solvent and concentrations of polymer and polymer/polypeptide).

Fiber morphology was firstly surveyed by optical microscopy using a Zeiss Axioskop 40 optical microscope equipped with a Zeiss AxioCam MRC5 digital camera. The accurate morphologic analysis was carried out by scanning electron microscopy (SEM) using Phenom XL Desktop SEM equipment. Fibrous mats, which were cut in 1 cm × 1 cm samples, were mounted on a double-sided adhesive carbon disc and were sputter-coated with a thin layer of carbon to prevent sample charging problems using a K950X Turbo Evaporator. All samples were observed at an accelerating voltage of 15 kV. Diameters of

electrospun microfibers were measured with the SmartTiff software from Carl Zeiss SMT, Ltd.

5.1.2.3 Measurements of Physical Properties of Electrospun Scaffolds

Calorimetric data were obtained by differential scanning calorimetry with a TA Instruments Q100 series equipped with a refrigerated cooling system (RCS) operating at temperatures from -80 ºC to 400 ºC. Calibration was performed with indium. Experiments were conducted under a flow of dry nitrogen with a sample weight of approximately 5 mg. Calorimetric data were obtained from runs performed at a heating rate of 10 ºC/min.

The thermal stability of the P4HB samples was studied by thermogravimetric analysis (TGA) at a heating rate of 10 ºC/min (sample weight *ca.* 5 mg) with a Q50 thermogravimetric analyzer of TA Instruments and under a flow of dry nitrogen. Test temperatures ranged from 30 to 600 ºC.

WAXD and SAXS patterns were taken simultaneously employing the 16 bits-CCD Rayonix LX255-HS and 20 bits-single photon counter Dectris Pilatus 3s 1M detectors respectively. The experiment was performed at the NCD-SWEET beamline (BL11) of the ALBA synchrotron facility (Cerdanyola del Vallès, Barcelona, Spain), by using a photon wavelength of 0.100 nm. Polymer samples were confined between Kapton films. WAXD and SAXS diffraction patterns were calibrated with Cr_2O_3 and silver behenate (AgBh), respectively. The correlation function and the corresponding parameters were calculated with the CORFUNC software for Fibre Diffraction/Non-Crystalline Diffraction provided by the Collaborative Computational Project 13. Deconvolution of WAXD peaks was performed using the PeakFit 4.0 software.

Contact angle (CA) measurements were conducted using the sessile drop method. 0.5 µL of milliQ water drops were deposited onto the surface of the electrospun mats, which were cut into rectangular pieces (3 cm x 1 cm) and fixed on a holder, and recorded after stabilization with the equipment OCA 15EC (DataPhysics Instruments GmbH, Filderstadt). The SCA20 software was

used to measure the CA, which is shown here as the average of at least 40 measures for each condition.

Mechanical properties were determined with a Zwick Z2.5/TN1S (Zwick/Roell; Ulm, Germany) testing machine in stress-strain tests carried out at a deformation rate of 10 mm/min. The load cell capacity was 100 N. Mechanical parameters were evaluated by means of the testXpert software of Zwick. In the case of the elastic modulus calculation, force values were delimited to the lineal part of the representation. Measurements were performed on rectangular samples of 3 cm × 0.4 cm and a width of 0.40 mm that were cut from the collected electrospun scaffolds. The mechanical parameters were averaged from a minimum of six measurements for each polymer sample.

5.1.2.4 Cell Adhesion and Proliferation Assays

Studies were performed with fibroblast NRK cells and epithelial Saos-2 cells. In all cases, cells were cultured in Dulbecco's Modified Eagle Medium (DMEM) with 4500 mg/L of glucose, 110 mg/L of sodium pyruvate, and 2 mM of L-glutamine) supplemented with 10% fetal bovine serum (FBS), 50 U/mL penicillin, 50 mg/mL streptomycin and L-glutamine 2 mM at 37 ºC in a 10% humidified atmosphere of 5% CO_2 and 95% air. Culture media were changed every two days. For sub-culture, cell monolayers were rinsed with PBS and detached by incubating them with 0.25% trypsin/EDTA for 2-5 min at 37 ºC. The incubation was stopped by suspending in 5 mL of fresh medium and the cell concentration was determined by counting with Neubauer camera and using 4% trypan blue as dye vital.

Square pieces of neat and FGF-P loaded electrospun scaffolds (1 cm x 1 cm x 0.40 mm) were placed and fixed in each well of a 24-well culture plate with a small drop of silicone (Silbione® MED ADH 4300 RTV, Bluestar Silicones France SAS, Lyon, France). This plate was then sterilized by UV-radiation in a laminar flux cabinet for 15 min. For cell adhesion assays, aliquots of 50–100 µL containing 5×10^4 cells were seeded onto the scaffold samples in each well and incubated for 24 h (adhesion assay). For cell proliferation assays, the same

aliquot volume but containing a lower cell concentration than that for adhesion experiments (i.e., 2×10^4 cells) was seeded and incubated for 96 h.

Adhesion and proliferation in the samples were evaluated to obtained quantitative data by the MTT method.[23] The procedure is based on a simple modification of the ISO10993–5:2009 standard test, which describes the appropriate methodology to assess *in vitro* cytotoxicity of medical devices. This test is designed to determine the *in vitro* biological response of mammalian cells using appropriate biological parameters. According to this ISO standard, devices fall into one of three categories based on expected contact with the patient: (a) Limited (≤24 h), (b) Prolonged (>24 h and ≤30 days), and (c) Permanent (>30 days). In our case, the assay was performed according to the limited and prolonged categories. The viability results were averaged after doing four replicates. Samples with adhered and grown cells were fixed with 2.5 w/v-% formaldehyde at 4°C overnight. They were subsequently dehydrated and processed for observation of cell morphology using fluorescence microscopy, where the nucleus and actin cytoskeleton was stained with Hoescht and phalloidin, respectively.

5.1.2.5 *In vitro* Wound Healing Activity of FGF-P

An *in-vitro* wound healing migration assay was employed to evaluate the effect of FGF-P peptide-loaded in the electrospun because FGF-P enhances proliferation and cell migration. Confluent monolayers of fibroblast NRK cells were obtained after 48 h of culture in 1 mL of DMEM medium containing 10^5 cells seeded in each well (24-well plate). Subsequently, a scratch (a linear defect to mimic a wound) was made in the monolayers with a sterilized propylene tip (diameter of 0.2 mm) and the layer was rinsed with PBS to remove cells damaged during scratch formation. Then, 1 mL of medium was added to each well, together with a square piece of the FGF-P loaded electrospun scaffolds (1 cm x 1 cm x 0.40 mm) (five samples for each assay). Unloaded scaffolds were used as controls. The rate of healing was monitored using an inverted light microscope and taking micrographs every 24 h at the same

magnification. The free area between cells was determined by fitting it to a rectangular geometry. The evolution of healing over time (*WC, wound healing*) was determined as:

$$WH\ (\%) = (A_0 - A_t) / A_0 \times 100 \quad (1)$$

where A_t and A_0 correspond to the areas evaluated at times t and 0, respectively. The micrographs were stitched successfully, so as to depict the evolution of the wound closure, by using the grid/collection stitching plugin available through ImageJ Fiji.[24]

5.1.2.6 Statistical Analysis

Values were averaged and graphically represented together with their respective standard deviations. Statistical analysis was performed by one-way ANOVA test to compare the means of all groups, and then Tukey's test was applied to determine a statistically significant difference between the two groups. The test confidence level was set at 95% ($p < 0.05$).

5.1.3 Results and Discussion

5.1.3.1 Electrospinning of P4HB Solutions

Electrospinning is a complex process where different forces are involved (e.g., fluid dynamics, electric force, Coulomb repulsion force, surface tension, and gravity). The influence of gravity can be varied through the experimental set-up, therefore in this work, both vertical and horizontal configurations are considered (**Figure 5.1.1**). Theoretically, gravity can increase the effect of the applied electrical field and contribute to rendering thin fibers with a wide diameter size distribution.[25]

The type of selected collector has also a great repercussion on the disposition of fibers in the electrospun scaffold. In this case, we have chosen a static plane collector for the vertical set-up and a rotatory collector, which should favor the alignment of fibers, for the horizontal disposition.

The selection of an appropriate solvent for a polymer with a determined chemical structure and the molecular weight is fundamental to success in the production of micro/nanofibers electrospun.[26] However, the correlation between solubility and spinnability is nevertheless problematic since in some cases it may be preferable to select a worse solvent to avoid the formation of irregularities such as droplets and beads.[27] Thus, to test conditions using a set of solvents with relatively close solubility parameters (both typical Hildebrand[28] and Hansen[29] parameters can be considered) is fundamental.

The predicted solubility parameter of P4HB becomes higher than that determined for P3HB, which is the related and most common studied PHA, due to the different contribution of CH, CH_3, and CH_2 groups (57, 437, and 272 $MPa^{1/2}$ mL/mol, respectively). Therefore, values of 10.3 H and 9.3 H can be estimated for P4HB and P3HB, respectively, considering densities of 1.25 g/mL (P4HB) and 1.21 g/mL (P3HB). Abundant studies can be found concerning P3HB solubility[30] and electrospinnability,[31,32] which could be an adequate basis for selecting appropriate conditions for P4HB. The high molecular weight of P3HB produced by microbial biosynthesis was found problematic in some cases due to the high viscosity attained in determining solvents. For example, acetone (dry) showed some advantages with respect to chloroform (stabilized with amylene) as a consequence of rendering a lower solution viscosity. However, chloroform is in general preferred due to its closer solubility parameter with that estimated for P3HB (i.e., 9.24-9.29 H and 9.78-10.02 H are determined for chloroform and acetone, respectively).[31] Nevertheless, some problems concerning the use of chloroform have been reported, being these mainly related to its low dielectric constant and boiling point, which could lead to a fast polymer crystallization, needle obstruction and noncontinuous processing. Addition of a small percentage of solvents with lower volatility, such as dimethylformamide, may be interesting to solve the mentioned difficulties.

In the present work, chloroform, chloroform/acetone mixture in a 2:1 *v*/*v* ratio, dichloromethane (DCM), tetrahydrofurane (THF), and 1,1,1,3,3,3-

hexafluoroisopropanol (HIFP) have been selected as potential solvents. Hildebrand and Hansen solubility parameters of these solvents are summarized in **Table 5.1.1**. Reported dispersive, polar, and hydrogen bond parameters for P3HB are 7.77, 3.27, and 4,79 $(cal/mL)^{1/2}$,[33] each value being intermediate between those reported in the Table. Note that acetone, dichloromethane, and HFIP are the most appropriate considering the dispersive, polar, and hydrogen bond contributions, respectively.

Table 5.1.1. Hildebrand and Hansen parameters of the assayed solvents.[29,32]

Solvent	Hildebrand parameter $(cal/mL)^{1/2}$	Hansen parameters[a] D-P-H $(cal/mL)^{1/2}$
Chloroform	9.21	8.70-1.52-2.79
Dichloromethane	9.93	8.31-3.57-3.47
Acetone	9.77	7.58-5.08-3.42
Chloroform/ Acetone 2:1	9.40	8.31-2.69-3.00
Tetrahydrofurane	9.52	8.21-2.79-3.91
1,1,1,3,3,3-Hexafluoroisopropanol	8.74	8.41-2.20-7.19

[a] Dispersive, polar, and hydrogen bonding contributions are indicated by D, P, H, respectively.

The main study for the optimization of processing parameters (needle tip, collector distance, flow rate, applied voltage, and polymer concentration) was performed with chloroform. These parameters were the initial starting conditions for the study of the other solvents, with them being subsequently modified according to morphological observations by optical microscopy. Note that the maximum difference between Hildebrand parameters of the polymer and each solvent was less than 1.8 $(cal/mL)^{1/2}$, which is the maximum allowed value.

Electrospinning experiments were planned to work with dissolutions having high polymer concentration and great flow rate in order to minimize the deposition time required to get a consistent scaffold. In general, high voltages were required due to the high viscosity of concentrated solutions and the high polymer molecular weight.

The vertical set-up configuration had as the main limitation the trend to produce drops in the collector due to incomplete evaporation of the solvent in the fluid jet. **Figures 5.1.2a** and **5.1.2b** show typical disks attained after solvent evaporation (chloroform) in the plate collector. Our observations indicated that these drops could be avoided by decreasing the flow rate and also by increasing the applied voltage, which strengthens the fluid jet. Additionally, note the reduction of the disk diameter according to the indicated decrease and increase of the flow rate and voltage, respectively.

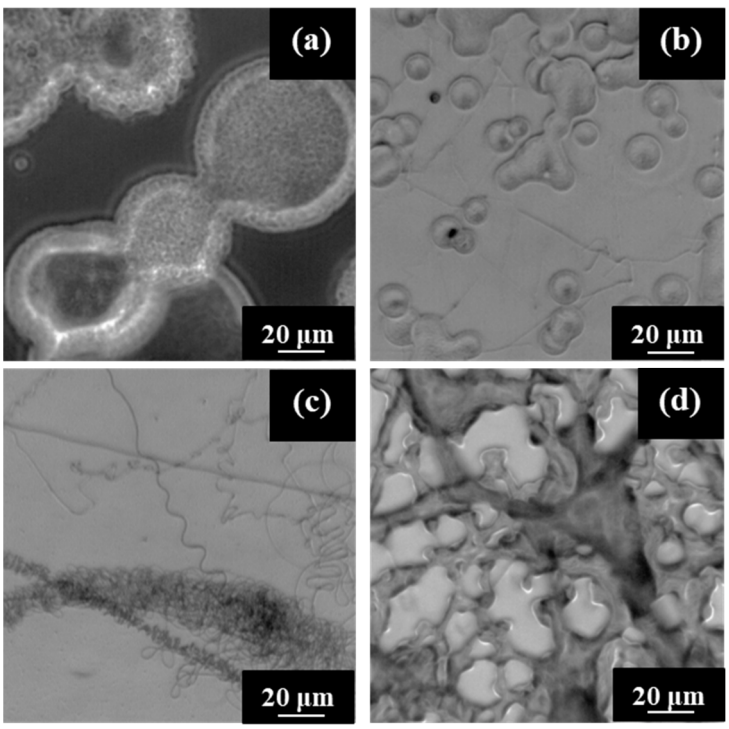

Figure 5.1.2. Optical micrographs showing typical defects attained with vertical electrospinning: (**a, b**) Disk morphologies, (**c**) wavy fiber agglomerates and (d) irregular planar fibers with solvent retention. Specific conditions: (**a**) 5 *w*/*v*-% in chloroform, 15 cm, 25 kV, 5 mL/h; (**b**) 8 *w*/*v*-% in chloroform, 16.5 cm, 40 kV, 2 mL/h; (**c**) 0.5 *w*/*v*-% in HFIP, 16.5 cm, 70 kV, 9 mL/h and (**d**) 15 *w*/*v*-% in HFIP, 16.5 cm, 70 kV, 2 mL/h.

The behavior of chloroform, dichloromethane, chloroform/acetone mixtures, and THF was similar with specific differences that will then be explained. HFIP is a polar solvent with strong hydrogen bonding properties

(i.e., the Hansen hydrogen bonding parameter becomes 7.19 $(cal/mL)^{1/2}$) that enables it to dissolve hydrogen-bond acceptors as P4HB despite the existing high discrepancy between Hildebrand solubility parameters (i.e., 1.56 $(cal/mL)^{1/2}$). In that event, the main problems concern the buckling instability of the fluid jet during deposition, which leads to circles, figures-of-eight, wavy fibers, and meanders. **Figure 5.1.2c** depicts that nanosized fibers could be obtained from highly diluted solution, but even using a relatively high flow rate the formed wavy fibers had a clear trend to form aggregates. Finally, high polymer concentrations lead to deficient solvent evaporation and a meander appearance (**Figure 5.1.2d**).

Comparison of optical micrographs shown in **Figures 5.1.3a** and **5.1.3b** illustrates as a general trend that an increment on the solvent flow rate (e.g., from 0.5 mL/h to 1.5 mL/h) required a higher voltage (e.g., 50 kV with respect to 70 kV) and a drastic decrease on the polymer concentration (e.g., from 15 *w/v*-% to 9 *w/v*-%) in order to avoid drop formation and obtain homogeneous and continuous fibers.

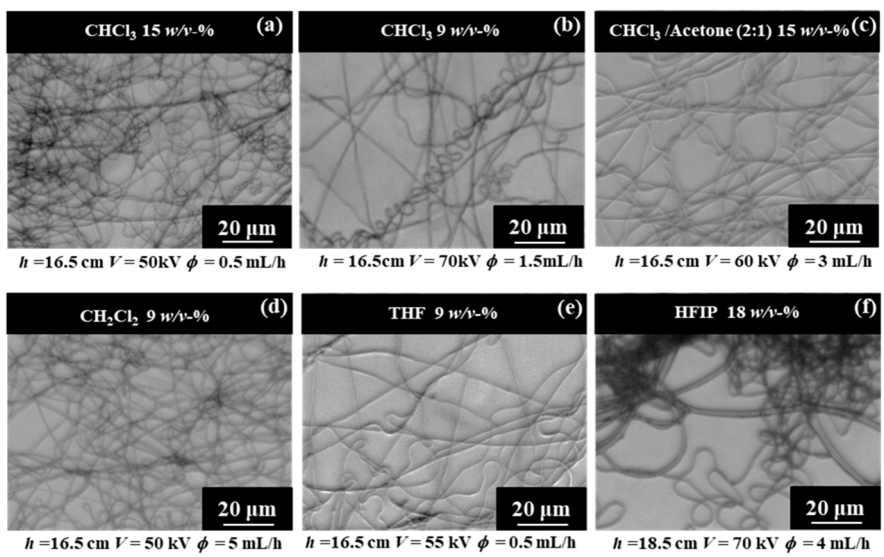

Figure 5.1.3. Optical micrographs showing electrospun fibers obtained with a vertical set up and the indicated solvent, polymer concentration, flow rate, voltage, and collector distance.

The given example corresponds to chloroform, but similar conclusions were deduced for the other studied solvents. **Figure 5.1.3c** shows that the addition of acetone to chloroform allowed working with a very high polymer concentration (e.g., 15 *w*/*v*-%) and even a lower voltage (60 kV) and higher flow rate (3 mL/h) while keeping the same needle-collector distance (16.5 cm). The change of chloroform (**Figure 5.1.3b**) by dichloromethane (**Figure 5.1.3d**) had also some advantages since the flow rate could be higher (5 mL/h with respect to 1.5 mL/h) whereas the voltage could be lower (50 kV respecting to 70 kV) when concentration and collector distance were maintained at the same values. THF was a highly problematic solvent since processing conditions were highly limited and for example, the flow rate should be as lower as 0.5 mL/h for a concentration of 9 *w*/*v*-% (**Figure 5.1.3e**). Finally, and despite the above-indicated problems, a high concentration (18 *w*/*v*-%) and moderate flow rate (4 mL/h) was possible when HFIP was selected (**Figure 5.1.3f**). Note, however, the increase in the collector distance (up to 18.5 cm and the fact that fiber agglomeration could still be observed.

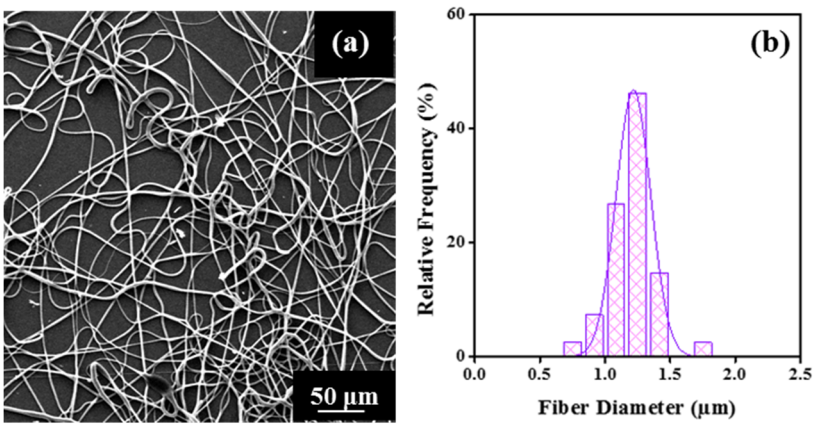

Figure 5.1.4. (**a**) Scanning electron micrograph of electrospun P4HB fibers prepared with a vertical set up from chloroform at a polymer concentration of 9 *w*/*v*-%, flow rate of 1.5 mL/h, voltage of 70 kV, and tip-collector distance of 16.5 cm. (**b**) Diameter distribution of the electrospun fibers obtained from the above-indicated conditions.

SEM micrographs of the sample preparation obtained from chloroform with 9 *w*/*v*-% concentration showed the formation of continuous microfibers with a relatively narrow distribution (1.3 ± 0.5 μm) and a smooth surface (**Figure 5.1.4**). Higher diameters were attained with the chloroform/acetone solvent mixture and dichloromethane as expected from the increased flow rate.

The horizontal set-up showed clear advantages since solvent dropping was clearly avoided and consequently, the voltage could be reduced to more conventional values (i.e., 30 kV). In addition, a high polymer concentration could be used allowing to decrease the collection time and to get fibers with high diameter if necessary. The main limitations corresponded, in this event, to bead formation as shown in **Figure 5.1.5a** for a chloroform solution. Note that the increase of the polymer concentration from 17 *w*/*v*-% to 19 *w*/*v*-% allowed to avoid completely the formation of beads as clearly observed in the SEM micrographs of **Figure 5.1.6**. Continuous fibers with a smooth surface, a preferred orientation (see yellow arrow), and a relatively low diameter distribution (i.e., 7 ± 1.2 μm) were attained. This kind of fibers could also be obtained with the other assayed solvents using similar conditions as shown in **Figure 5.1.5c** for fibers coming from the electrospinning of HFIP solutions. Underline that, the high polymer concentration (i.e., 18-19 *w*/*v*-%) rendered fibers with diameters in the micron scale that was considered appropriate for further biological studies.

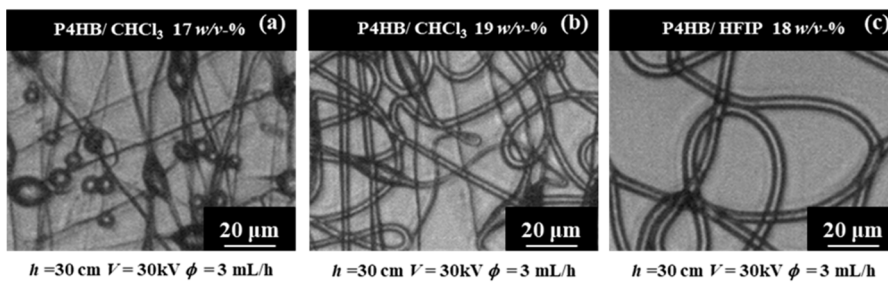

Figure 5.1.5. Optical micrographs of electrospun P4HB fibers prepared with a horizontal set up and a rotatory collector from the indicated solvent, polymer concentration, flow rate, voltage, and tip-collector distance.

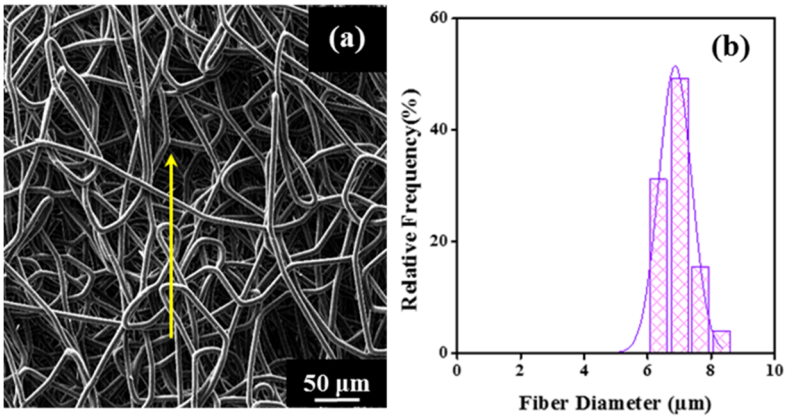

Figure 5.1.6. (**a**) SEM micrograph of electrospun P4HB fibers prepared from chloroform (19 *w*/*v*-%, 3 mL/h, 30 kV, 30 cm) by using horizontal electrospinning set-up. (**b**) Diameter distribution of electrospun fibers obtained from the above-indicated conditions.

5.1.3.2 Electrospinning of P4HB Solutions Containing the FGF-P Growth Factor

Horizontal electrospinning was selected to get FGF-P loaded scaffolds due to the possibility to work with higher polymer concentrations and get 3D scaffolds in a suitable period. Furthermore, a fiber diameter in micrometric scales was considered the most appropriate to encapsulate the selected growth factor. The main problem was derived from the insolubility of FGF-P in chloroform. Nevertheless, this solvent was chosen instead of HFIP due to its lower capability to induce polyester and polypeptide degradation and more important its lower retention in the processed fibers. FGF-P could be dissolved in dimethylsulfoxide (DMSO) and consequently the electrospun solution was performed by using a 98:2 mixture of P4HB dissolved in chloroform at the 12.9 wt-% concentration and FGF-P dissolved in DMSO at a concentration of 0.9 wt-%. Therefore, the final solvent mixtures had 11.3 wt-% of P4HB and 0.001 wt-% FGF-P, respectively. P4HB scaffolds were consequently loaded with a 0.01 wt-% of FGF-P.

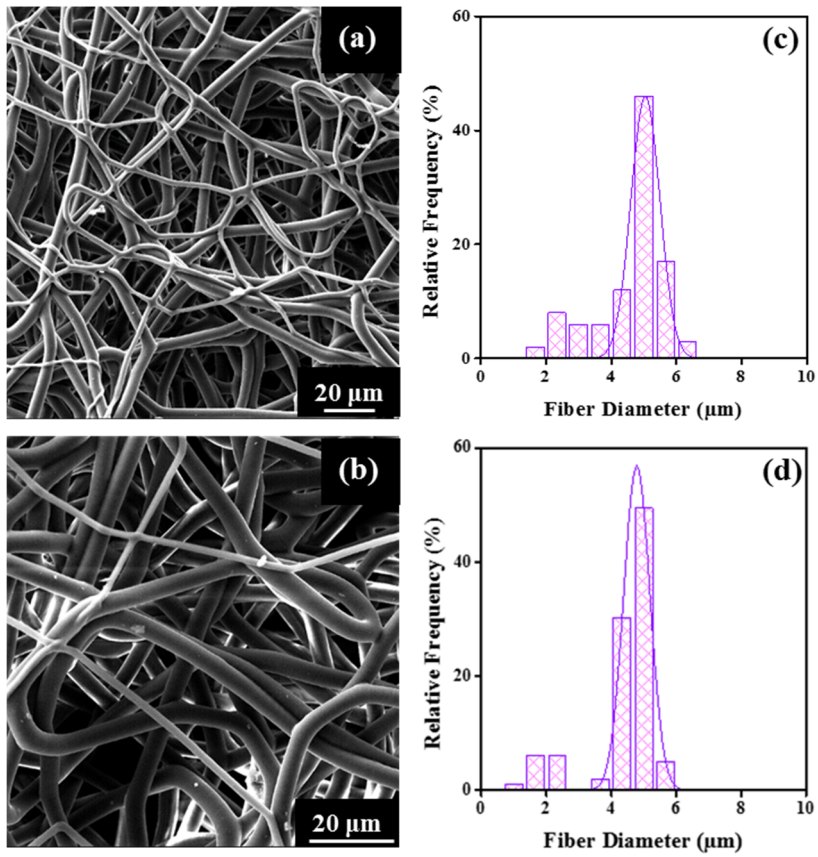

Figure 5.1.7. SEM micrographs of electrospun P4HB fibers without (**a**) and with the FGF-P growth factor (**b**). Fibers were obtained with a horizontal setup and using a $CHCl_3$+DMSO solvent mixture under the optimized conditions. The corresponding diameter size distributions are shown in (**c**) and (**d**).

The influence of DMSO on the electrospinning process was evaluated using P4HB as a control. **Figure 5.1.7** revealed that desirable fiber characteristics (continuity, regularity, and absence of defects) were still observed without any modification of the above-determined set of parameters. The main change was the reduction of the average fiber diameter (i.e., from 6.9 ± 0.02 µm for the $CHCl_3$ solution to 5.0 ± 0.05 µm for the $CHCl_3$+DMSO solution with or without FGF-P added), which could be explained by considering the increase of solution conductivity when the more polar DMSO solvent was added. Additionally, note its higher Hildebrand parameter (12.9 $(cal/mL)^{1/2}$)

and its higher polar (8.07 (cal/mL)$^{1/2}$) and hydrogen bonding (4.99 (cal/mL)$^{1/2}$) Hansen contributions with respect to $CHCl_3$. Morphologies of unloaded and FGF-P loaded electrospun P4HB fibers were practically identical (**Figures 5.1.7a** and **5.17b**). SEM micrographs of loaded fibers revealed a smooth surface without any possible surface defect attributable to the incorporated growth factor.

5.1.3.3 Characterization of Neat and FGF-P Loaded P4HB Electrospun Scaffolds

Electrospun scaffolds of P4HB were rather crystalline, as observed from the corresponding DSC heating runs (**Figure 5.1.8**). A complex double melting peak was observed as a consequence of the reported lamellar reordering process of P4HB that took place during the heating run and where the thinner lamellae became thicker.[22,34] At any rate, the thermal behavior of the different scaffolds was different from that observed for processed commercial sutures, which showed higher melting enthalpies and temperatures (**Figure 5.1.8a**). Even the high temperature melting peak of sutures is complex as a consequence of a careful and specific procedure to process them. This consists of performing a series of heating and stretching steps carried out in order to improve the mechanical properties of the final product and that lead to a non-usual high melting temperature (i.e., the peak can be observed around 72 ºC). By contrast, the behavior of a melt crystallized film is completely different to that of the initial suture and becomes characterized by a minor peak around 50 ºC and the main peak at 58 ºC, which corresponds to the reordered lamellae.[22]

Scaffolds coming from $CHCl_3$ solution (**Figure 5.1.8b**) showed two practically overlapped peaks around 56-58 ºC that suggest greater thermodynamic stability of the thin lamellae that hinders the reordering process. The two peaks appeared well-differentiated (i.e., 54.3 ºC and 59.8 ºC) and the intensity of the first one was higher when the scaffold was prepared from the $CHCl_3$: DMSO mixture (**Figure 5.1.8c**). Minor differences in the fiber morphology (bear in mind that the diameter decreased from 6.9 to 5 μm when

DMSO was added to the $CHCl_3$ solution) seem to slightly influence thermal properties. **Figure 5.1.8d** shows that scarce differences in the melting behavior could be observed when the low amount of the growth factor was incorporated onto the scaffold.

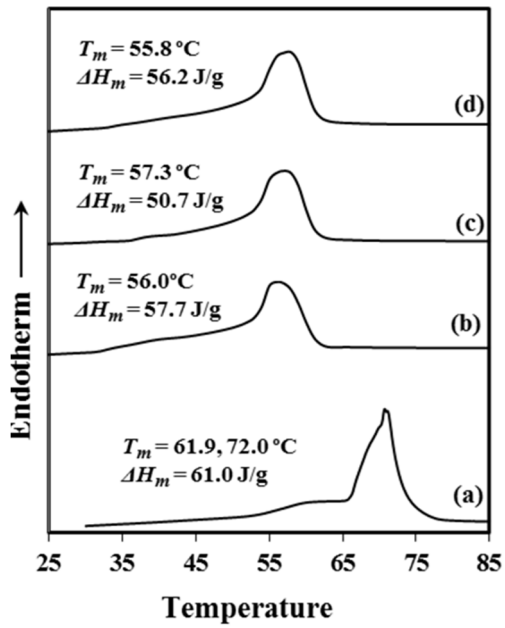

Figure 5.1.8. DSC first heating runs of the commercial suture (**a**), P4HB electrospun scaffolds from $CHCl_3$ (**b**), $CHCl_3$/DMSO solvent mixture(**c**), and $CHCl_3$/DMSO solvent mixture containing FGF-P (**d**).

Enthalpy values demonstrated also that P4HB was able to crystallize during the electrospinning process since a decrease of only 5% was detected with respect to the value found for the commercial suture (i.e., 57.7 J/g with respect to 61 J/g). Crystallinity slightly depended on the electrospinning conditions and the enthalpy decreased for example to 53.3 J/g (i.e., around 12%) when the $CHCl_3$: DMSO mixture was employed. The presence of the growth factor did not significantly influence the final crystallinity.

WAXD patterns (**Figure 5.1.9**) of electrospun scaffolds revealed also their crystalline character and the existence of a single crystalline form. The observed Bragg peaks appeared at 0.406 and 0.388 nm and corresponded to the (110) and

(200) reflections of the reported orthorhombic structure of P4HB (a = 0.775 nm, b = 0.477 nm, and c (fiber axis) = 1.199 nm).[35] The diffraction pattern also shows a significant and broad halo centered at 0.421 nm that is indicative of the amorphous content.

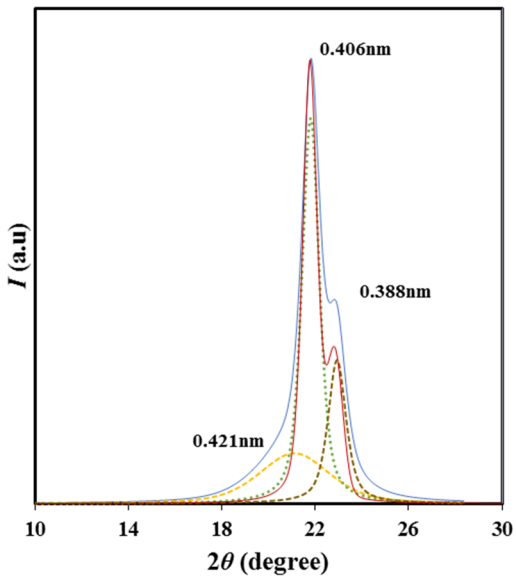

Figure 5.1.9. WAXD profile and deconvoluted peaks of P4HB electrospun scaffolds.

SAXS diffraction patterns of electrospun samples revealed also the crystalline order and the existence of supramolecular structure. The corresponding lamellar parameters being possible to determine (i.e., long period, L_p, amorphous layer thickness, l_a, and crystalline lamellar thickness, l_c) and crystallinity (i.e., crystallinity within the lamellar stacks, $X_c^{SAXS} = l_c/L_p$) were determined by the normalized one-dimensional correlation function,[36] $\gamma(r)$:

$$\gamma(r) = \int_0^\infty q^2 I(q)\cos(qr)dq \Big/ \int_0^\infty q^2 I(q)dq \qquad (2)$$

where $I(q)$ is the intensity at each value of the scattering vector (q = [4π/λ] sin θ), r the real space distance, λ the wavelength, and θ the Bragg angle.

Figure 5.1.10 compares both SAXS peaks and correlation functions obtained from the representative loaded electrospun scaffold and the commercial P4HB suture.

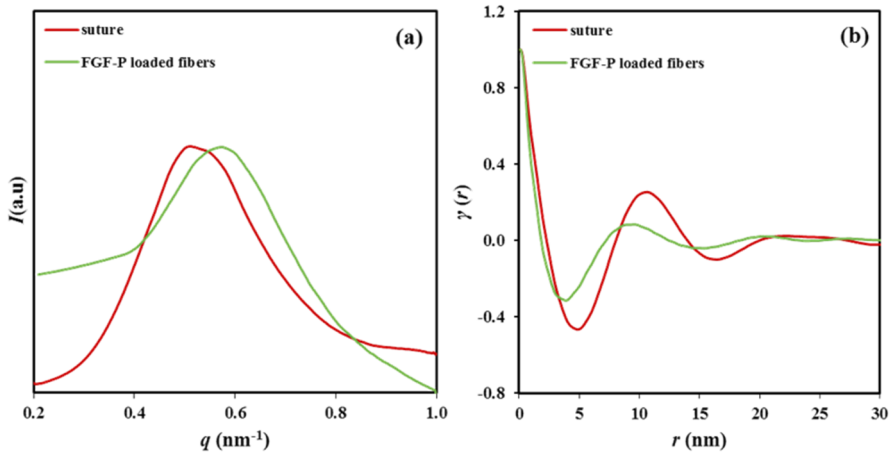

Figure 5.1.10. (**a**) SAXS profiles and (**b**) correlation functions of the commercial P4HB suture (red line) and the FGF-P loaded electrospun scaffold (green line).

Three points should be emphasized: (a) Lamellar long period was significantly lower for the electrospun sample (i.e., 8.9 nm with respect to 10.5 nm), which is a consequence of the fact that fibers were obtained at room temperature whereas the sutures were submitted as indicated to different thermal treatments that lead to reordering processes with the subsequent increase of the lamellar thickness. (b) Maximum and minimum peaks of the correlation function were better defined for the commercial suture, which means a higher electronic contrast between amorphous and crystalline phases. (c) Crystalline lamellar thickness was similar for both samples (i.e., 7.2 nm and 7.9 nm for the scaffold and the suture, respectively), whereas the amorphous lamellar thickness was rather different (i.e., 1.7 nm and 2.6 nm for the scaffold and the suture, respectively). In this way, the folding surface was more compact in the electrospun fibers in agreement with the indicated lower electronic contrast. Crystallinity in the lamellar stacks was therefore slightly higher for the electrospun fibers (i.e., 80.9% with respect to 75%)

Electrospun scaffolds showed good mechanical properties as a consequence of their compact and tangled fibrous structure, the relatively high crystallinity of the processed polymer, and especially the above indicated elastic nature of P4HB. **Figure 5.1.11** displays typical stress-strain curves, which are characterized by the first region of high modulus and non-plastic deformation and a second region with a low slope and high plastic deformations (i.e., even higher than 600%).

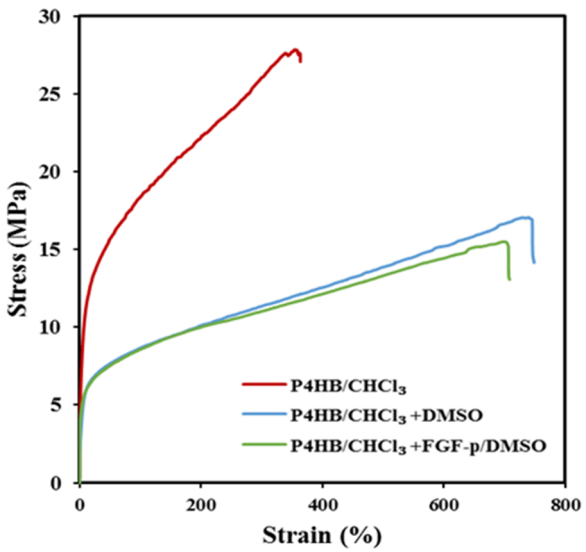

Figure 5.1.11. Stress-strain curves of selected P4HB electrospun scaffolds.

Scaffolds processed under different conditions showed a variation in properties that are mainly dependent on the final diameter. Thus, fibers of 6.9 μm coming from chloroform showed greater resistance and low deformation than those with 5 μm coming from the $CHCl_3$: DMSO mixture (i.e., 28 MPa and 360% with respect to 17 MPa and 750%). Elastic moduli of the first elastic region were comparable (i.e., around 4 MPa), but significant differences were detected between the limit strengths (i.e., 12 and 6 MPa). The incorporation of the reduced amount of the FGF-P growth factor had only a slight influence on the plastic deformation that led to a slight decrease of the maximum stress (i.e., 15 MPa with respect to 17 MPa) and the maximum deformation (i.e., 725% respect to 750%) as shown also in **Figure 5.1.11**.

Electrospun scaffolds had thermal stability up to temperatures more than 150 ºC higher than the melting temperature of P4HB as shown in the representative TGA curves of **Figure 5.1.12**. Polymer degradation seemed to follow a single decomposition step as observed in the corresponding DTGA curves. Therefore, the stability of scaffolds was similar independently of the processing conditions (i.e., melt of electrospinning) and the incorporation of the growth factor.

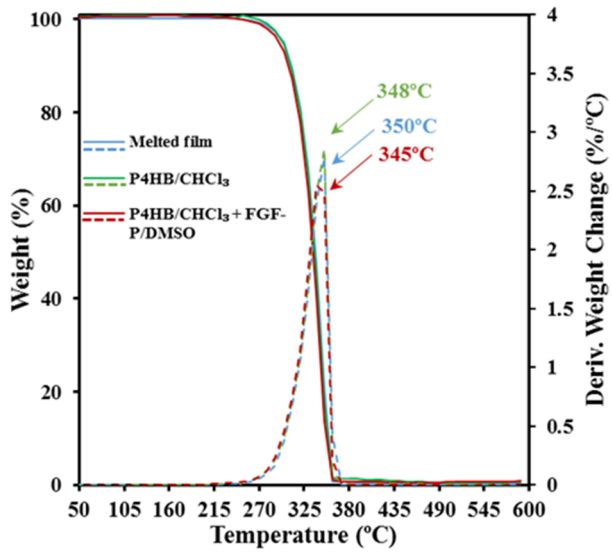

Figure 5.1.12. TGA (solid lines) and DTGA (dashed lines) curves of the indicated P4HB samples. Note that the curve of the melted film overlaps the curves of the electrospun nanofibers.

Surface characteristics are a primordial property of materials when they should be employed for tissue engineering applications. Overall, it is assumed that serum-treated hydrophilic surfaces support significantly greater cell attachment, cell spreading, and cytoskeletal organization relative to hydrophobic surfaces.[37] Contact angle measurements of the prepared scaffolds displayed a slight hydrophobicity with angles around 105º (**Figure 5.1.13**). These values were higher than detected for the original suture (85º) and even for a smooth melt casting film (73º). Probably, the increase in the surface roughness of the scaffolds[38] and the higher contribution of air pockets[39] were

the reason for the observed increase in the hydrophobicity. Angles slightly decreased by the reduction of the microfiber diameter as observed when scaffolds from $CHCl_3$ and $CHCl_3$ + DMSO are compared. Most significantly, a clear angle shift towards a more hydrophobic value (121º) was detected when the peptide growth factor was loaded.

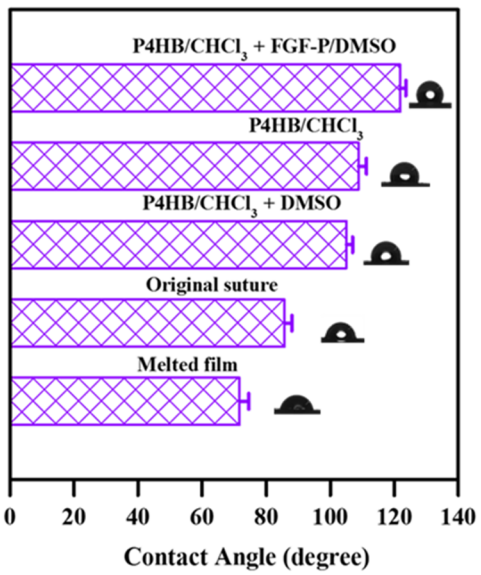

Figure 5.1.13. Contact angle measurements of P4HB electrospun scaffolds in distilled water and comparison with the original suture. Illustration of liquid droplets for all samples.

5.1.3.4 *In vitro* Wound Healing Activity.

The in-vitro wound-healing assay, also known as the scratch assay is a helpful alternative to animal models where complete wound-closure research can be performed. The in-vitro wound healing assay studies the proliferation and migration of cells. Specifically, the assay measures at the microscopic scale the rate at which cells, in a cell monolayer, migrate to fill a cell-free gap homemade by a scratch.[40] Initially, primary cultures of epithelial and endothelial cells were used in this assay. However, the cell lines derived from embryo, normal, and tumor tissues are frequently used for getting better control of culture cell growth.[41,42] For example, MC-3T3 cells (fibroblasts derived from mouse embryo),[43] HUVEC cells (normal endothelial cells isolated from a

human umbilical vein),[44] HaCaT cells (cell line that is a spontaneously transformed aneuploidy immortal keratinocyte cell line from adult human skin),[45] HEK-293 cells (epithelial cells isolated from human embryonic kidney, immortal cells that contain adenovirus and forms tumors in nude mice),[46] and others line cells derived from tumor: 769-P cells (human renal carcinoma cell line),[40] Py4-1 cells (hemangioendothelioma cells),[47] MCF-7 cells (epithelial mammary carcinoma cells),[48] etc. Note that the main requisite of the cells used in this assay is the capability to render a 2D-growth with the formation of a cell monolayer or a cell sheet.[42]

The activity of FGF-P for wound healing was demonstrated *in-vitro* by evaluating the growth of Saos-2 epithelial-like and NRK fibroblasts-like cells. The FGF-P was tested at doses of 0.0003, 0.002, 0.003, and 0.02 mg/mL, to this end the synthetic factor was diluted from a stock of 1 mg/mL (prepared in PBS) in 1 mL of culture medium. **Figure 5.1.14a** shows that both cell types grow in a dose-dependent manner with an increase in the number of cells when they were stimulated with FGF-P. The increased cell growth is shown normalized according to the control that corresponds to a nil FGF-P dose. However, growth was significantly higher in NRK fibroblasts. This result was expected since the synthetic factor FGF-P was designed based on FGF-2, which binds naturally to its receptor (FGFR1) in fibroblasts and stimulates the proliferation, migration, and cell differentiation.[21,49] Recently, it has been described that osteoblasts are stimulated with FGF-2 during their transition and differentiation to osteoclast.[50] Therefore, it can be justified that Saos-2 cells of bone origin showed an increase in their cell population in response to the FGF-P stimulus. Namely, Saos-2 cells were not refractory to the influence of FGF-P despite giving rise to a lower response than that found for NRK fibroblasts.

Figure 5.1.14b shows the time-course during the culture of the NRK fibroblasts exposed to different doses of FGF-P. Initially, the lower doses (0.0003 and 0.002 mg/mL) seem to be more stimulating for proliferation (e.g., second and third day of culture), while the higher doses (0.003 and 0.02 mg/mL) could be responsible for negative regulation of the receptor through

the typical mechanisms of regulation of membrane receptors, such as internalization and degradation.[49,51,52] However, in prolonged culture times (fourth and fifth day of culture) it is observed that high doses (such as 0.003 and 0.02 mg / mL) were more stimulatory for cell growth. In addition, at the above-mentioned times of culture, it seems that both doses achieve a similar cellular response as a saturation effect. For this reason, the dose of 0.003 mg/mL was selected as the loading dose in the P4HB fiber matrix.

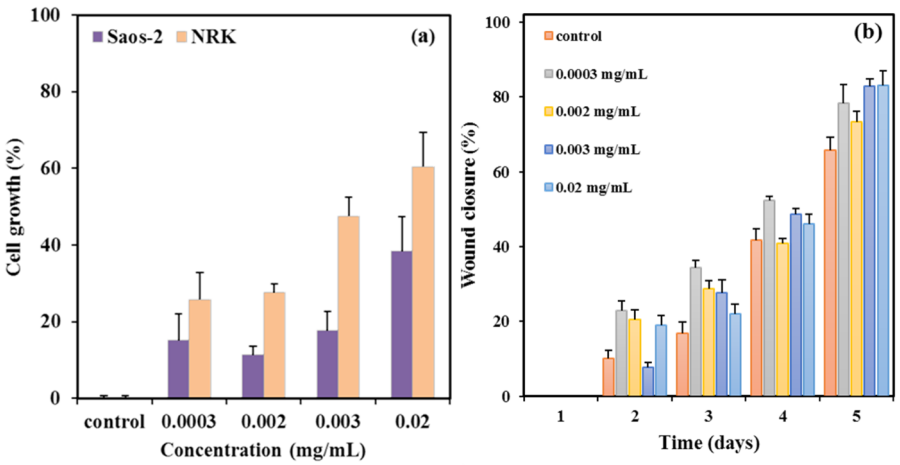

Figure 5.1.14. (**a**) Dose-response effect of the synthetic factor FGF-P on cell proliferation (96 hours). *In vitro* evolution of wound healing during culture time and different doses of FGF-P (**b**).

In-vitro biocompatibility of P4HB electrospun scaffolds with the indicated FGF-P load was determined by adhesion and proliferation assays using NRK cells (**Figure 5.1.15**). Fibroblasts were specifically selected since their adhesion to material surfaces implied focal joint points instead of the wide extension of the cell membrane that is characteristic of the epithelial cells. **Figure 5.1.15a** shows that the adhesion after 24 h of the NRK cells on the fiber scaffolds (3D growth) was greater than on the 2D surface of the well. The improved adhesion of the NRK cells in the fiber scaffold is due to the micrometric diameter of the fibers and the more hydrophilic character (i.e., with respect to the control) of the scaffold. However, at 96 hours of culture (i.e., the proliferation event) a lower percentage of the number of cells was observed in the scaffolds loaded

with FGF-P and an increase of about 20% was observed in the well (**Figure 5.1.15b**). This result can be explained by indicating that the FGF-P diffuses from the matrix to the medium and therefore the entire population of cells contained in the well becomes stimulated.

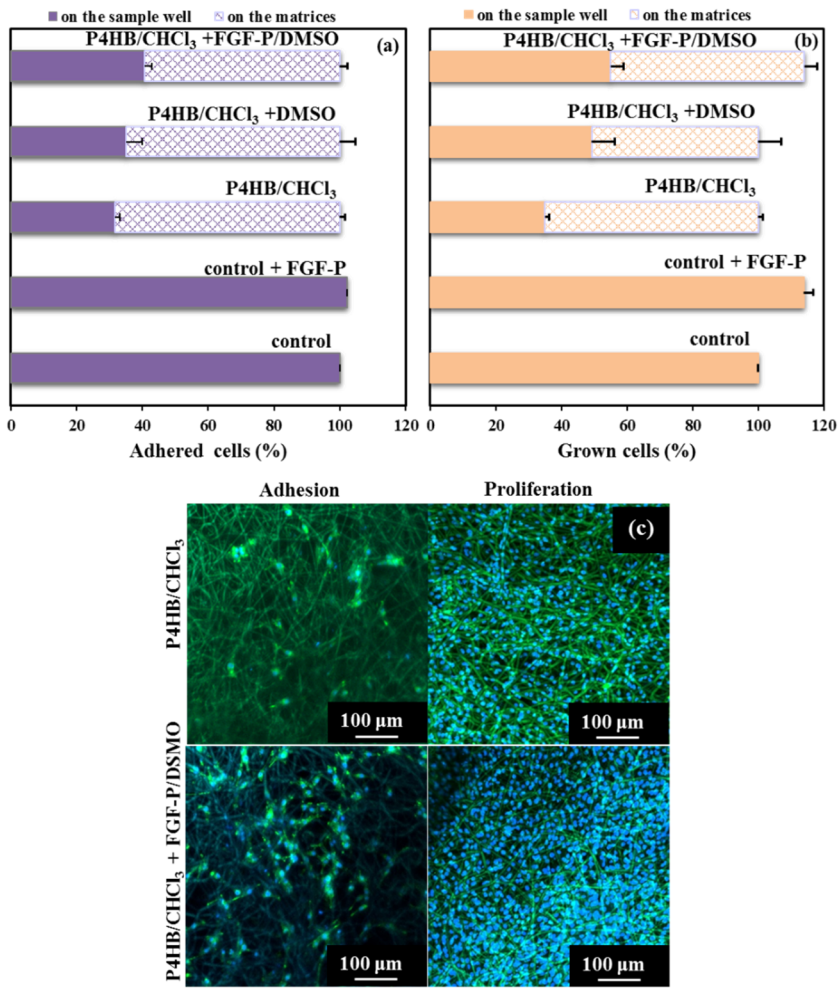

Figure 5.1.15. Adhesion (**a**) and proliferation (**b**) of fibroblast-like NRK cells on the different samples of the P4HB electrospun scaffolds. (**c**) Fluorescence microscopy images showing the adhesion and proliferation of NRK cells in P4HB electrospun scaffolds with and without the FGF-P load.

Finally, the fluorescence microscopy images (**Figure 5.1.15c**) illustrate the high biocompatibility of loaded scaffolds compared to neat scaffolds. It could

be concluded that the fiber matrices are suitable supports for both adhesion and proliferation of cells, and do not have cytotoxic effects for the cells growing in the matrices.

The results of the study of *in vitro* wound healing in the presence of electrospun scaffolds loaded with FGF-P are shown in **Figure 5.1.16**. We consider that this test is the gold standard to demonstrate the applicability of these scaffolds. Thus, it allows verifying that the incorporated FGF-P is conveniently released from the matrices into the medium and that it can stimulate cell proliferation.

Figure 5.1.16a depicts the light microscopy images corresponding to the scratch healing process in the presence of the P4HB electrospun scaffold loaded with the synthetic factor FGF-P and the respective controls. The scratch can be observed up to the third day of culture in the control conditions (growth in culture medium) and the growth conditions of the cells in the presence of the unloaded electrospun scaffolds (e.g., P4HB-$CHCl_3$ and P4HB-$CHCl_3$ + DMSO). On the other hand, the P4HB electrospun loaded with FGF-P as well as the control + FGF-P (culture medium supplemented with FGF-P) showed a clear imprint of the wound until only the second day of culture, namely the presence of FGF-P accelerates scratch healing. The mechanism of the process simply corresponds to the increase in the cell number caused by the presence of the growth factor FGF-P. Finally, it can be observed that after the fifth day of culture, the morphological scratch healing occurs in all the conditions studied.

The quantitative data (**Figure 5.1.16b**) on the growth of NRK fibroblasts during wound closure demonstrate a linear increase for the control and the two non-loaded electrospun scaffolds (i.e., P4HB/$CHCl_3$ and P4HB/$CHCl_3$ + DMSO). Scratch healing in the control supplemented with FGF-P initially occurred according to a linear NRK growth, but an exponential change was observed between the fifth and sixth day of culture.

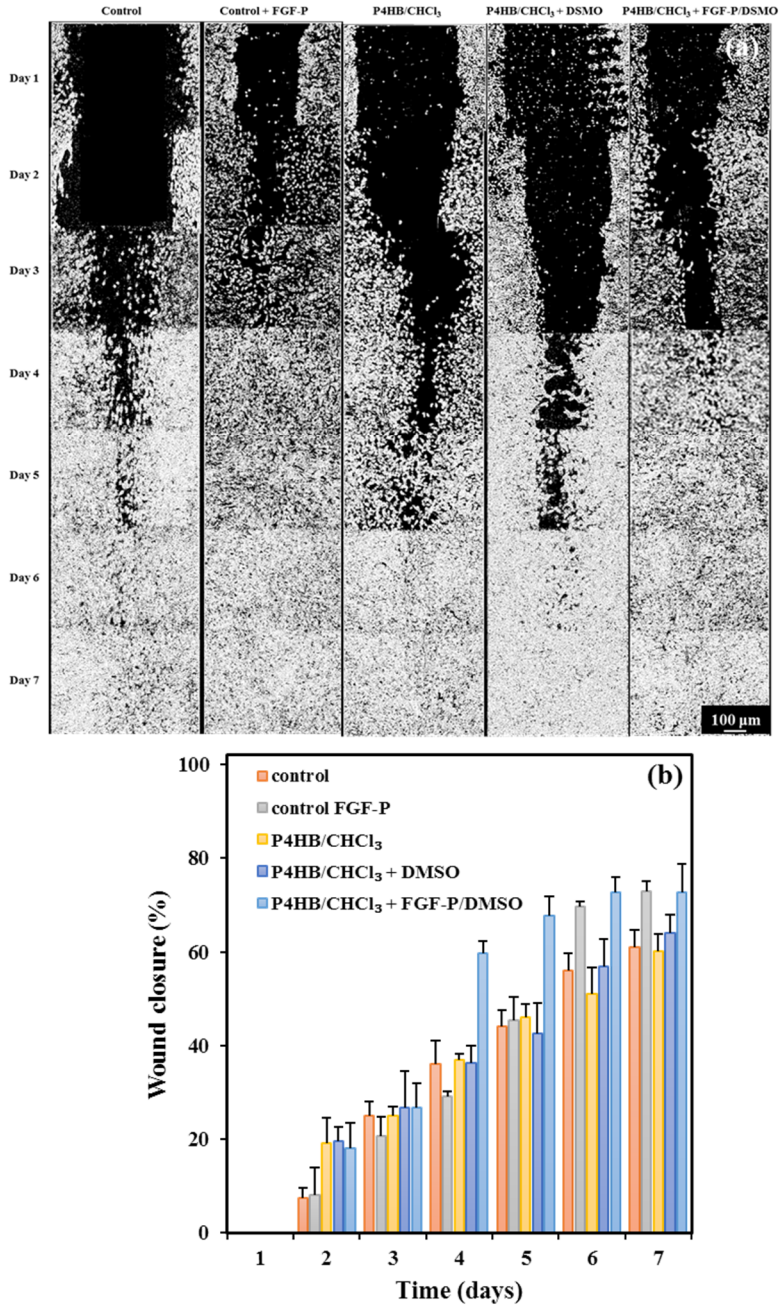

Figure 5.1.16. Optical microscopy images of the *in vitro* wound healing evolution in the presence of the different P4HB electrospun matrices (**a**). Quantification of the cellular colonization of the scratch during the time evolution of the *in vitro* wound healing assay (**b**).

However, the scratch healing in the presence of the electrospun scaffold loaded with FGF-P was the fastest condition since the exponential growth was observed between the third and fourth day of culture. These quantitative data are consistent with the qualitative description based on the light microscopy images. In this sense, it can be concluded that the progressive release of FGF-P from the electrospun scaffold favors the stimulation of the growth of NRK fibroblasts in comparison to its application as a bolus in cell culture.

5.1.4 CONCLUSIONS

Electrospun scaffolds of P4HB were successfully obtained from different solvents after cautious optimization of polymer concentration and electrospinning parameters. Drop formation, fiber agglomeration, and solvent retention were the main observed problems. In general terms, chloroform resulted in the most appropriate solvent to get continuous, uniform, and smooth microfibers. The equipment with a horizontal set-up configuration was appropriate to solve drop formation problems while allowing it to work with high flow rates and polymer concentrations.

The processing under the optimized conditions led to semi-crystalline microfibers (i.e., diameters around 7 μm) with lower lamellar thickness and melting point than the commercial suture submitted to extensive thermal and stretching treatments. Electrospun scaffolds showed excellent mechanical properties with Young modulus, maximum strength, and elongation values of 4 MPa, 28 MPa, and 360%, respectively, and surfaces with higher hydrophobic character than initial sutures due to an increase in the roughness.

The FGF-P peptide growth factor was successfully loaded into the P4HB scaffolds by the modification of the electrospinning solvent. The required addition of a small DMSO percentage led to a slight decrease in the fiber diameter and a change in the scaffold properties. Specifically, the maximum strength decreased and the elongation at break (i.e., from 360% to 730%) increased. Loaded samples showed good biocompatibility, a slight hydrophobicity, and a clear wound healing effect when the amount of incorporated FGF-P was 0.01 wt-%. Finally, the new fiber scaffold may have promising biomedical applications in tissue engineering and reparative medicine by reducing the time required for wound closure.

5.1.5 REFERENCES

(1) Martin, D. P.; Williams, S. F. Medical Applications of Poly-4-Hydroxybutyrate: A Strong Flexible Absorbable Biomaterial. *Biochem. Eng. J.* **2003**, *16* (2), 97–105. https://doi.org/10.1016/S1369-703X(03)00040-8.

(2) Ackermann, J. uwe; Müller, S.; Lösche, A.; Bley, T.; Babel, W. Methylobacterium Rhodesianum Cells Tend to Double the DNA Content under Growth Limitations and Accumulate PHB. *J. Biotechnol.* **1995**, *39* (1), 9–20. https://doi.org/10.1016/0168-1656(94)00138-3.

(3) Ferrara, S.; Zotti, S.; Tedeschi, L.; Frison, G.; Castagna, F.; Gallimberti, L.; Gessa, G.; Palatini, P. Pharmacokinetics of Gamma hydroxybutyric Acid in Alcohol Dependent Patients after Single and Repeated Oral Doses. *Br. J. Clin. Pharmacol.* **1992**, *34* (3), 231–235. https://doi.org/10.1111/j.1365-2125.1992.tb04129.x.

(4) P4HB made TephaFLEX is our breakthrough Technology https://www.tepha.com/technology/overview/ (accessed Apr 17, 2020).

(5) Odermatt, E. K.; Funk, L.; Bargon, R.; Martin, D. P.; Rizk, S.; Williams, S. F. MonoMax Suture: A New Long-Term Absorbable Monofilament Suture Made from Poly-4-Hydroxybutyrate. *Int. J. Polym. Sci.* **2012**, *2012*, 1–12. https://doi.org/10.1155/2012/216137.

(6) Tornier, announces launch of BioFiber® Surgical Mesh for tendon repair at arthroscopic surgery conference https://www.businesswire.com/news/home/20110414005940/en/Tornier-Announces-Launch-BioFiber®-Surgical-Mesh-Tendon (accessed Jul 2, 2020).

(7) Deeken, C. R.; Matthews, B. D. Characterization of the Mechanical Strength, Resorption Properties, and Histologic Characteristics of a Fully Absorbable Material (Poly-4-Hydroxybutyrate—PHASIX Mesh) in a Porcine Model of Hernia Repair. *ISRN Surg.* **2013**, *2013*, 1–12. https://doi.org/10.1155/2013/238067.

(8) Williams, S. F.; Rizk, S.; Martin, D. P. Poly-4-Hydroxybutyrate (P4HB): A New Generation of Resorbable Medical Devices for Tissue Repair and Regeneration. *Biomed. Eng. (NY).* **2013**, *58* (5), 439–452. https://doi.org/10.1515/bmt-2013-0009.

(9) Reneker, D. H.; Chun, I. Nanometre Diameter Fibres of Polymer, Produced by Electrospinning. *Nanotechnology* **1996**, *7* (3), 216–223. https://doi.org/10.1088/0957-4484/7/3/009.

(10) Li, D.; Xia, Y. Electrospinning of Nanofibers: Reinventing the Wheel? *Adv. Mater.* **2004**, *16* (14), 1151–1170. https://doi.org/10.1002/adma.200400719.

(11) Deitzel, J. M.; Kleinmeyer, J.; Harris, D.; Tan, N. C. B. The Effect of Processing Variables on the Morphology of Electrospun Nanofibers and Textiles. *Polymer (Guildf).* **2001**, *42*, 261–272.

(12) Yang, G.; Li, X.; He, Y.; Ma, J.; Ni, G.; Zhou, S. From Nano to Micro to Macro: Electrospun Hierarchically Structured Polymeric Fibers for Biomedical Applications. *Prog. Polym. Sci.* **2018**, *81*, 80–113. https://doi.org/10.1016/j.progpolymsci.2017.12.003.

(13) Li, L.; Zhou, G.; Wang, Y.; Yang, G.; Ding, S.; Zhou, S. Controlled Dual Delivery of BMP-2 and Dexamethasone by Nanoparticle-Embedded Electrospun Nanofibers for the Efficient Repair of Critical-Sized Rat Calvarial Defect. *Biomaterials* **2015**, *37*, 218–229. https://doi.org/10.1016/j.biomaterials.2014.10.015.

(14) Yang, G.; Wang, J.; Wang, Y.; Li, L.; Guo, X.; Zhou, S. An Implantable Active-Targeting Micelle-in-Nanofiber Device for Efficient and Safe Cancer Therapy. *ACS Nano* **2015**, *9* (2), 1161–1174. https://doi.org/10.1021/nn504573u.

(15) Llorens, E.; Del Valle, L. J.; Puiggalí, J. Multifunctional Ternary Drug-Loaded Electrospun Scaffolds. *J. Appl. Polym. Sci.* **2016**, *133* (8), 1–16. https://doi.org/10.1002/app.42751.

(16) Martin, D. P.; Badhwar, A.; Shah, D. V.; Rizk, S.; Eldridge, S. N.; Gagne, D. H.; Ganatra, A.; Darois, R. E.; Williams, S. F.; Tai, H. C.; et al. Characterization of Poly-4-Hydroxybutyrate Mesh for Hernia Repair Applications. *J. Surg. Res.* **2013**, *184* (2), 766–773. https://doi.org/10.1016/j.jss.2013.03.044.

(17) Sanhueza, C.; Acevedo, F.; Rocha, S.; Villegas, P.; Seeger, M.; Navia, R. Polyhydroxyalkanoates as Biomaterial for Electrospun Scaffolds. *Int. J. Biol. Macromol.* **2019**, *124*, 102–110. https://doi.org/10.1016/j.ijbiomac.2018.11.068.

(18) Volova, T.; Goncharov, D.; Sukovatyi, A.; Shabanov, A.; Nikolaeva, E.; Shishatskaya, E. Electrospinning of Polyhydroxyalkanoate Fibrous Scaffolds: Effects on Electrospinning Parameters on Structure and Properties. *J. Biomater. Sci. Polym. Ed.* **2014**, *25* (4), 370–393. https://doi.org/10.1080/09205063.2013.862400.

(19) Shing, Y.; Folkman, J.; Sullivan, R.; Butterfield, C.; Murray, J.; Klagsbrun, M. Heparin Affinity: Purification of a Tumor-Derived Capillary Endothelial Cell Growth Factor. *Science (80-.).* **1984**, *223* (4642), 1296–1299. https://doi.org/10.1126/science.6199844.

(20) Goldfarb, M. Functions of Fibroblast Growth Factors in Vertebrate Development. *Cytokine Growth Factor Rev.* **1996**, *7* (4), 311–325. https://doi.org/10.1016/S1359-6101(96)00039-1.

(21) Casey-Sawicki, K.; Zhang, M.; Kim, S.; Zhang, A.; Zhang, S. B.; Zhang, Z.; Singh, R.; Yang, S.; Swarts, S.; Vidyasagar, S.; et al. A Basic Fibroblast Growth Factor Analog for Protection and Mitigation against Acute Radiation Syndromes. *Health Phys.* **2014**, *106* (6), 704–712. https://doi.org/10.1097/HP.0000000000000095.

(22) Keridou, I.; del Valle, L. J.; Funk, L.; Turon, P.; Yousef, I.; Franco, L.; Puiggalí, J. Isothermal Crystallization Kinetics of Poly(4-Hydroxybutyrate) Biopolymer. *Polym. Morphol. Princ. Charact.*

Process. **2019**, *12* (2488), 1–20. https://doi.org/10.3390/ma12152488.

(23) Llorens, E.; Del Valle, L. J.; Díaz, A.; Casas, M. T.; Puiggalí, J. Polylactide Nanofibers Loaded with Vitamin B6 and Polyphenols as Bioactive Platform for Tissue Engineering. *Macromol. Res.* **2013**, *21* (7), 775–787. https://doi.org/10.1007/s13233-013-1090-x.

(24) Preibisch, S.; Saalfeld, S.; Tomancak, P. Globally Optimal Stitching of Tiled 3D Microscopic Image Acquisitions. *Bioinformatics* **2009**, *25* (11), 1463–1465. https://doi.org/10.1093/bioinformatics/btp184.

(25) Yang, C.; Jia, Z.; Xu, Z.; Wang, K.; Guan, Z.; Wang, L. Comparisons of Fibers Properties between Vertical and Horizontal Type Electrospinning Systems. *Annu. Rep. - Conf. Electr. Insul. Dielectr. Phenomena, CEIDP* **2009**, 204–207. https://doi.org/10.1109/CEIDP.2009.5377758.

(26) McKee, M. G.; Elkins, C. L.; Long, T. E. Influence of Self-Complementary Hydrogen Bonding on Solution Rheology/Electrospinning Relationships. *Polymer (Guildf).* **2004**, *45* (26), 8705–8715. https://doi.org/10.1016/j.polymer.2004.10.049.

(27) Luo, C. J.; Nangrejo, M.; Edirisinghe, M. A Novel Method of Selecting Solvents for Polymer Electrospinning. *Polymer (Guildf).* **2010**, *51* (7), 1654–1662. https://doi.org/10.1016/j.polymer.2010.01.031.

(28) Van Krevelen, D. W.; Nijenhuis, K. T. *Cohesive Properties and Solubility*, 4th ed.; Elsevier B.V: Amsterdam, The Netherlands, 2009. https://doi.org/10.1016/b978-0-444-82877-4.50014-7.

(29) Hansen, C. M. *The Three Dimensional Solubility Parameter and Solvent Diffusion Coefficient. Their Importance in Surface Coating Formulation*; Danish Tecnhical Press: Copenhagen, 1967.

(30) Terada, M.; Marchessault, R. H. Determination of Solubility Parameters for Poly(3-Hydroxyalkanoates). *Int. J. Biol. Macromol.* **1999**, *25* (1–3), 207–215. https://doi.org/10.1016/S0141-8130(99)00036-7.

(31) Correia, D. M.; Ribeiro, C.; Ferreira, J. C. C.; Botelho, G.; Ribelles, J. L. G.; Lanceros-Mendez, S.; Sencadas, V. Influence of Electrospinning Parameters on Poly(Hydroxybutyrate) Electrospun Membranes Fiber Size and Distribution. *Polym. Eng. Sci.* **2013**, *54* (7), 1608–1617. https://doi.org/10.1002/pen.23704.

(32) Hansen, C. M. *Hansen Solubility Parameters: A User's Handbook: Second Edition*; CRC Press: Boca Raton, FL, USA, 2007. https://doi.org/10.1201/9781420006834.

(33) Jacquel, N.; Lo, C.-W.; Wu, H.-S.; Wang, S. S. Solubility of Polyhydroxyalkanoates by Experiment and Thermodynamic Correlations. *AIChE J.* **2007**, *53* (10), 2704–2714. https://doi.org/DOI 10.1002/aic.11274.

(34) Alamo, R.; Mandelkern, L. Origins of Endothermic Peaks in

Differential Scanning Calorimetry. *J. Polym. Sci. Part B Polym. Phys.* **1986**, *24* (9), 2087–2105. https://doi.org/10.1002/polb.1986.090240914.

(35) Su, F.; Iwata, T.; Sudesh, K.; Doi, Y. Electron and X-Ray Diffraction Study on Poly(4-Hydroxybutyrate). *Polymer (Guildf).* **2001**, *42* (21), 8915–8918. https://doi.org/10.1016/S0032-3861(01)00412-8.

(36) Vonk, C. G.; Kortleve, G. X-Ray Small-Angle Scattering of Bulk Polyethylene - II. Analyses of the Scattering Curve. *Kolloid-Zeitschrift Zeitschrift für Polym.* **1967**, *220* (1), 19–24. https://doi.org/10.1007/BF02086052.

(37) Webb, K.; Hlady, V.; Tresco, P. A. Relative Importance of Surface Wettability and Charged Functional Groups on NIH 3T3 Fibroblast Attachment, Spreading, and Cytoskeletal Organization. *J. Biomed. Mater. Res.* **1998**, *41* (3), 422–430. https://doi.org/10.1002/(SICI)1097-4636(19980905)41:3<422::AID-JBM12>3.0.CO;2-K.

(38) Wenzel, R. N. Resistance of Solid Surfaces to Wetting by Water. *Ind. Eng. Chem.* **1936**, *28* (8), 988–994. https://doi.org/10.1021/ie50320a024.

(39) Cassie, B. D.; Baxter, S. Wettability of Porous Surfaces. *Trans. Faraday Soc.* **1944**, No. 5, 546–551.

(40) Bobadilla, A. V. P.; Arévalo, J.; Sarró, E.; Byrne, H. M.; Maini, P. K.; Carraro, T.; Balocco, S.; Meseguer, A.; Alarcón, T. In Vitro Cell Migration Quantification Method for Scratch Assays. *J. R. Soc. Interface* **2019**, *16* (151). https://doi.org/10.1098/rsif.2018.0709.

(41) Liang, C. C.; Park, A. Y.; Guan, J. L. In Vitro Scratch Assay: A Convenient and Inexpensive Method for Analysis of Cell Migration in Vitro. *Nat. Protoc.* **2007**, *2* (2), 329–333. https://doi.org/10.1038/nprot.2007.30.

(42) Jonkman, J. E. N.; Cathcart, J. A.; Xu, F.; Bartolini, M. E.; Amon, J. E.; Stevens, K. M.; Colarusso, P. Cell Adhesion & Migration An Introduction to the Wound Healing Assay Using Livecell Microscopy An Introduction to the Wound Healing Assay Using Livecell Microscopy. *Cell Adhes. Migr.* **2014**, *8* (5), 440–451. https://doi.org/10.4161/cam.36224.

(43) Lipton, A.; Klinger, I.; Paul, D.; Holley, R. W. Migration of Mouse 3T3 Fibroblasts in Response to a Serum Factor. *Proc. Natl. Acad. Sci. U. S. A.* **1971**, *68* (11), 2799–2801. https://doi.org/10.1073/pnas.68.11.2799.

(44) Yue, P. Y. K.; Leung, E. P. Y.; Mak, N. K.; Wong, R. N. S. A Simplified Method for Quantifying Cell Migration/Wound Healing in 96-Well Plates. *J. Biomol. Screen.* **2010**, *15* (4), 427–433. https://doi.org/10.1177/1087057110361772.

(45) Liarte, S.; Bernabé-García, Á.; Armero-Barranco, D.; Nicolás, F. J. Microscopy Based Methods for the Assessment of Epithelial Cell Migration during in Vitro Wound Healing. *J. Vis. Exp.* **2018**, *2018*

(131), 1–7. https://doi.org/10.3791/56799.

(46) Tanno, B.; Sesti, F.; Cesi, V.; Bossi, G.; Ferrari-Amorotti, G.; Bussolari, R.; Tirindelli, D.; Calabretta, B.; Raschellà, G. Expression of Slug Is Regulated by C-Myb and Is Required for Invasion and Bone Marrow Homing of Cancer Cells of Different Origin. *J. Biol. Chem.* **2010**, *285* (38), 29434–29445. https://doi.org/10.1074/jbc.M109.089045.

(47) Gebäck, T.; Schulz, M. M. P.; Koumoutsakos, P.; Detmar, M. TScratch: A Novel and Simple Software Tool for Automated Analysis of Monolayer Wound Healing Assays. *Biotechniques* **2009**, *46* (4), 265–274. https://doi.org/10.2144/000113083.

(48) Razak, N. A.; Abu, N.; Ho, W. Y.; Zamberi, N. R.; Tan, S. W.; Alitheen, N. B.; Long, K.; Yeap, S. K. Cytotoxicity of Eupatorin in MCF-7 and MDA-MB-231 Human Breast Cancer Cells via Cell Cycle Arrest, Anti-Angiogenesis and Induction of Apoptosis. *Sci. Rep.* **2019**, *9* (1), 1–12. https://doi.org/10.1038/s41598-018-37796-w.

(49) Eswarakumar, V. P.; Lax, I.; Schlessinger, J. Cellular Signaling by Fibroblast Growth Factor Receptors. *Cytokine Growth Factor Rev.* **2005**, *16* (2 SPEC. ISS.), 139–149. https://doi.org/10.1016/j.cytogfr.2005.01.001.

(50) Teven, C. M.; Farina, E. M.; Rivas, J.; Reid, R. R. Fibroblast Growth Factor (FGF) Signaling in Development and Skeletal Diseases. *Genes Dis.* **2014**, *1* (2), 199–213. https://doi.org/10.1016/j.gendis.2014.09.005.

(51) Ornitz, D. M.; Itoh, N. Protein Family Review: Fibroblast Growth Factors. *Genome Biol.* **2001**, *2* (3), reviews3005.1-3005.12.

(52) Ornitz, D. M.; Itoh, N. The Fibroblast Growth Factor Signaling Pathway. *Wiley Interdiscip. Rev. Dev. Biol.* **2015**, *4* (3), 215–266. https://doi.org/10.1002/wdev.176.

6. PREPARATION OF BIOBASED BLENDS.

The preparation of blends constituted by two different polymers is an interesting approach to get new polymers with enhanced properties. Thus, the resulting materials can find more extensive applications.

This chapter covers the study of two types of blends. First, the mixture of two biodegradable polyesters widely used in biomedical applications: polyglycolide (PGA) and poly-ε-caprolactone (PCL), and second the mixture of one polyester, polylactide (PLA) and a polyamide that can be derived from biomass, polyamide 6,10 (PA610).

Specifically, the vertical set-up configuration of the electrospinning technique has been applied to produce electrospun nanofibers of PGA/PCL. Electrospun scaffolds constituted by different mixtures of hydrophilic PGA and hydrophobic PCL were prepared. Generally, it has been evaluated the influence of solvent, polymer concentration, and processing parameters, such as applied voltage, flow rate, and needle tip-collector distance.

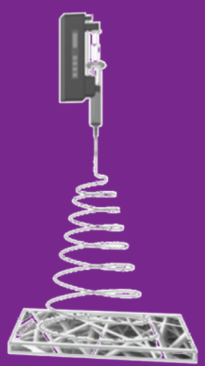

Electrospinning conditions have been selected to get homogeneous and continuous fibers with diameters in the nano/micrometric range. These conditions were also applied to load the different scaffolds with curcumin (CUR) and polyhexamethylene biguanide (PHMB) as hydrophobic and hydrophilic bactericide compounds, respectively. Physicochemical characterization of both unloaded and loaded scaffolds was performed and involved FTIR and ^{1}H NMR spectroscopies, morphological observations by scanning electron microscopy, the study of thermal properties through calorimetry and thermogravimetric analysis, and evaluation of surface characteristics through contact angle measurements. The release behavior of the loaded scaffolds was evaluated in two different media. Results pointed out

a well-differentiated behavior where the delivery of CUR and even PHMB were highly dependent on the PGA/PCL ratio, the capability of the medium to swell the polymer matrix, and the diffusion of the selected solvent into the electrospun fibers. All samples showed a bactericide effect in both hydrophilic cell culture and hydrophobic agar media.

In the case of PLA/PA, blends with different ratios of PLA and PA610 have been prepared by melt-mixing using a Brabender mixer equipment. Previously, a rheologically modified polylactide (PLA_{REx}) was obtained through reactive extrusion using a multifunctional epoxide agent.

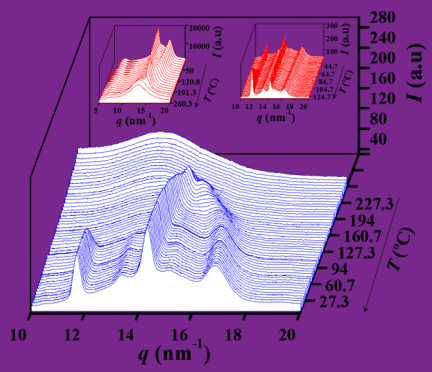

It was expected that unreacted epoxy groups of PLA_{REx} were able to improve the compatibility between the two polymers. SEM observations revealed a logical dependence of the morphology of immiscible phases with composition, and more interestingly a co-continuity at relatively low PA content (around 50%) was detected. This result contrasts with previous observations performed with non-modified PLA.

Confined PA domains increased with the PA content and hardly crystallized at the typical crystallization temperature of the pure PA (195 °C). Synchrotron X-ray diffraction studies indicated that a PA crystallization at a lower temperature close to 120 °C was enhanced and led to a pseudohexagonal γ phase that differs from the characteristic layered structure of PA610. SAXS data revealed also that well-differentiated lamellar entities could be assigned at both immiscible polymer phases. Clear differences were observed in the spherulitic morphologies attained under isothermal melt crystallization experiments. Results indicated that the texture of PLA_{REx} spherulites was modified by the presence of PA. Compatibilization of PA molecules on the crystal lamellar boundaries of PLA_{REx} led to an enhancement of the lamellar twisting frequency. Optical microscopy results also indicated that the crystal growth rate of PLA_{REx} increased by the incorporation of PA, but in contrast, this harmed the nucleation process

6.1 SCAFFOLDS WITH TUNABLE PROPERTIES CONSTITUTED BY ELECTROSPUN NANOFIBERS OF POLYGLYCOLIDE AND POLY-ε-CAPROLACTONE

6.1.1 INTRODUCTION

Polyglycolide (PGA) and poly-ε-caprolactone (PCL) are currently two of the most employed biodegradable and bioresorbable polymers.[1,2] Tissue engineering, orthopedic devices, and drug delivery systems are representative examples where such polymers are extensively used. PGA has significant issues (e.g., relatively high insolubility, rapid degradation, and significant local production of glycolic acid) which limit in some cases their application.[2] Nevertheless, the use of PGA-based materials is extensive as bioabsorbable surgical sutures[3] and scaffolds for tissue regeneration.[4–7] PCL is characterized by easy processability, low tensile strength, and high elongation at breakage, which confers good elastic properties and suitability for tissue engineering applications. This polymer becomes therefore attractive for the preparation of scaffolds based on electrospun micro/nanofibers.[8–10] The repeat units of PGA and PCL differ on the number of methylene groups (i.e., one and five, respectively) (**Figure 6.1.1**), a feature that leads to distinct chain flexibility, surface hydrophobicity, and mechanical and thermal properties. For example, the melting points of PCL and PGA are 59–64 and 220–225 ºC, respectively, namely a difference of more than 150 ºC.[11] In this way, materials with tuned properties could hypothetically be obtained by a simple blending of different ratios of PGA and PCL if samples were miscible, which is not the usual case. Nevertheless, simple composition changes can give rise to highly differentiated drug delivery systems as previously observed when two hydrophobic polymers like polylactide and PCL were employed.[12] Scaffolds based on PGA/PCL mixtures have recently merited attention from different points of view, for example, the evaluation of physical and mechanical properties of electrospun fibers,[13] preparation of scaffolds with aligned fibers for neural

applications[14], and in vitro degradation studies.[15]

Electrospinning is one of the most versatile processes for preparing nonwoven nanofibers that could be arranged into porous scaffolds.[16–18] This process uses electrostatic forces (10–100 kV) to stretch drops of a polymer dilute solution from a needle tip to a collector. Nowadays, extensive works concern the fabrication of polymer fibers via electrospinning and their use in different biomedical applications (e.g., drug delivery, tissue engineering, and diagnostics).[19–21]

Electrospinning is a fast technique and allows easy preparation of polymer mixtures if a common solvent is found. Furthermore, domains corresponding to the different polymers should be small due to the nanometric dimensions of the produced fibers and consequently, intimate contact between PGA and PCL molecules may be possible.

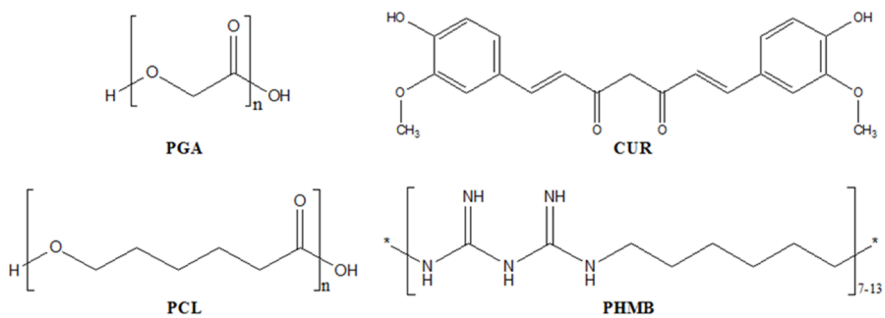

Figure 6.1.1. Chemical structures of polyglycolide (PGA), poly-ε-caprolactone, curcumin (CUR), and polyhexamethylene biguanide (PHMB).

Incorporation of drugs into electrospun scaffolds is also an easy process since only minor modifications on the processing parameters are required, being also minimal the repercussion on the final geometry due to the usually low amount of loaded drug that is necessary to get a significant pharmacologic effect. The incorporation of several drugs can provide materials with multifunctional properties.[22] In this work the use of a typical bactericide agent (i.e., polyhexamethylene biguanide (PHMB)) and an anticancerigen drug (i.e., curcumin (CUR)), which in addition has a

bacteriostatic effect, was assayed in order to provide a high added value to the new scaffolds.

PHMB is a mixture of cationic oligomers having an average of 7–13 biguanide groups spaced by flexible hexamethylene segments (**Figure 6.1.1**). The high number of biguanide groups leads to high effectiveness against microorganisms, although chemical characterization is difficult due to the high dispersion of oligomer sizes.[23] CUR is a molecule constituted by two phenol groups connected by α, β-unsaturated carbonyl groups (**Figure 6.1.1**). These diketones can form stable enols and are readily deprotonated to form enolates. Curcumin seems to have beneficial effects on various diseases, including multiple myeloma, pancreatic cancer, myelodysplastic syndromes, colon cancer, psoriasis, and Alzheimer's disease.[24,25] CUR is also a pleiotropic molecule capable of interacting with molecular targets involved in inflammation. It has also been recently evaluated as having a bactericide effect since it can produce a membrane leakage of both Gram-negative and Gram-positive bacteria.[26]

The main goal of this work is the preparation and characterization of electrospun scaffolds with tuned properties in function of their PGA/PCL ratio. To this end electrospun scaffolds constituted by PGA/PCL ratios of 100/0, 80/20, 65/35, 50/50, 35/65, and 0/100 have been considered, optimizing in each case the processing conditions. Special attention is paid to demonstrate the different release behavior that can be attained by a simple modification of composition, a less complex alternative than that derived from the use of other processes like coaxial electrospinning.[27]

6.1.2 EXPERIIMENTAL SECTION

6.1.2.1 Materials

Curcumin (CUR), polycaprolactone (M_w: 45,000 g/mol) polyglycolide (PGA) (M_w: 180,000 g/mol) and solvents were purchased from Sigma-Aldrich. Cosmocil® (polyhexamethylene biguanide hydrochloride, PHMB) was kindly provided by B. Braun Surgical, S.A.U. The microbial culture was prepared with

reagents and labware from Scharlab. *Escherichia Coli* and *Staphylococcus aureus* bacteria strains were obtained from the Spanish Collection of Type Culture (CECT, Valencia, Spain).

6.1.2.2 Preparation of Fibers by Electrospinning

Electrospun fibers were collected on a target placed at different distances (10–25 cm) from the needle tip (inside diameter 0.84 mm). The voltage was varied between 10 and 30 kV and applied to the target using a high-voltage supply (Gamma High Voltage Research, ES30-5W). Polymer solutions were delivered via a single KDS100 infusion syringe pump (KD Scientific, USA) to control the flow rate (from 1 to 5 mL/h). All electrospinning experiments were carried out at room temperature. Unloaded and drug-loaded electrospun fibers were prepared using optimized parameters (i.e., collector distance, voltage, and flow rate) and solvent conditions (i.e., polymer and drug concentrations). Samples will be named indicating only the PGA weight percentage (e.g., PGA/PCL-100 and PGA/PCL-35 correspond to PGA only and a mixture with 35% PGA and 65% PCL, respectively. CUR and PHMB content of the electrospinning solution was 1 *w*/*v*-% and 3 *w*/*v*-%, respectively. For comparative purposes, PGA/PCL-50 samples only loaded with CUR (1 *w*/*v*-%) or PHMB (3 *w*/*v*-%) were also prepared. The number of loaded drugs was determined by absorbance measurements as explained below.

6.1.2.3 Measurements

Infrared absorption spectra were recorded in the 4000–600 cm^{-1} range with a Fourier Transform FTIR 4100 Jasco spectrometer equipped with a Specac model MKII Golden Gate attenuated total reflection (ATR) cell.

^1H NMR spectra were recorded with a Bruker AMX-300 spectrometer operating at 300.1 MHz. Chemical shifts were calibrated using tetramethylsilane as the internal standard and $CDCl_3$ ($\delta(^1H)$ = 7.26 ppm) and deuterated DMSO ($\delta(^1H)$ = 2.50 ppm) as solvents.

Calorimetric data were obtained by differential scanning calorimetry with a TA Instruments Q100 series with T_{zero} technology and equipped with a

refrigerated cooling system (RCS). Experiments were conducted under a flow of dry nitrogen with a sample weight of approximately 5 mg and at heating and cooling rates of 20 °C min^{-1} and 10 °C min^{-1}, respectively. Calibration was performed with indium.

Thermal degradation was studied at a heating rate of 10 °C min^{-1} with around 5 mg samples in a Q50 thermogravimetric analyzer (TGA) of TA Instruments and under a flow of dry nitrogen. Test temperatures ranged from 50 to 600 °C.

Contact angles (CA) were measured at room temperature with sessile drops using an OCA-15 plus Contact Angle Microscope (Dataphysics, USA) and SCA20 software. Contact angle values of the right and left sides of distilled water drops were measured and averaged. Measurements were performed 10 s after the drop (5 μL) was deposited on the sample surface. All CA data were an average of six measurements on different surface locations.

Detailed inspection of texture and morphology of electrospun samples was conducted by scanning electron microscopy using a Focused Ion Beam Zeiss Neon 40 instrument (Carl Zeiss, Germany). Carbon coating was accomplished by using a Mitek K950 Sputter Coater fitted with a k150× film thickness monitor. Samples were visualized at an accelerating voltage of 5 kV. The diameter of electrospun fibers was measured with SmartTiff software from Carl Zeiss SMT Ltd.

6.1.2.4 Release Experiments

Controlled release measurements were performed with 1 cm × 1 cm square pieces of the different loaded scaffolds. The thickness was always close to 700 μm. These pieces were incubated at 37 °C in an orbital shaker at 80 rpm in tubes of 10 mL for 1 day. Phosphate-buffered saline (PBS) and a 3:7 *v*/*v* mixture of PBS and ethanol were employed as release media. Drug concentration was evaluated by UV absorbance measurements using a Shimadzu 3600 spectrometer. Calibration curves were obtained by plotting the absorbance measured at 428 and 326 nm versus CUR and PHMB

concentrations, respectively. Samples were withdrawn from the release medium at predetermined time intervals. The volume was kept constant by the addition of fresh medium. All drug release tests were carried out using three replicates and the results obtained were averaged.

6.1.2.5 Antimicrobial Test

E. coli and *S. aureus* bacteria were selected to evaluate the antimicrobial effect of PHMB and CUR loaded electrospun fibers. The bacteria were previously grown aerobically to exponential phase in broth culture (5 g/L beef extract, 5 g/L NaCl, 10 g/L tryptone, pH 7.2).

Growth experiments were performed on a 24-well culture plate. All drug (CUR, PHMB, or both) loaded scaffolds (1 cm x 1 cm and thickness close to 700 μm) were placed into the plate as well as an unloaded sample that was used as a control. Then, 2 mL of broth culture containing 10^3 colony forming units (CFU) was added to the samples. Cultures were incubated at 37 °C and agitated at 80 rpm. Aliquots of 100 μL were taken at predetermined time intervals for absorbance measurement at 595 nm in a microplate reader (every 2 h for 8 h, and after 22, 24, and 48 h from the starting time). Thus, turbidity was directly related to the relative bacterial growth by considering the maximum growth attained in the absence of any polymeric matrix (control). Experiments were performed in quadruplicate and the results averaged.

In order to perform a qualitative evaluation, the drug (CUR, PHMB, or both) loaded pieces and a commercial gentamicin dose (10 μg), which was used as a control, were placed onto an agar diffusion plate and seeded separately with 10^4 CFU/mL of each bacterium. The culture medium was prepared with 37 g Brain Heart Infusion broth, 10g Bacto™ Agar in 1 L of Milli-Q water, and sterilized in an autoclave at 121 ºC for 15 min. Plates were filled with 15 mL of medium and left to rest at room temperature to allow solidification of the medium. Inhibition halo images were taken after incubation of samples with bacteria at 37 ºC for 24 h.

6.1.3 RESULTS AND DISCUSSION

6.1.3.1 Electrospinning of PGA/PCL Mixtures

PCL is soluble in a wide variety of organic solvents and therefore the preparation of electrospun micro/nanofibers with continuous morphology and uniform distribution has been successfully described for a high variety of solvents (e.g., acetone/chloroform 33% *v*/*v* or ethanol/chloroform 33% *v*/*v* mixtures). On the contrary, PGA is scarcely soluble and consequently, electrospinning is practically limited to the use of 1,1,1,3,3,3,-hexafluoroisopropanol (HFIP). Therefore, all experiments were performed employing HFIP in order to have the most similar conditions for all selected blends. Sharifi and collaborators[13] demonstrated that this solvent was appropriate to get scaffolds from PGA/PCL mixtures up to a 50% content of PGA.

Electrospinning parameters were optimized to get fibers with an average diameter close to 1 μm in order to avoid an instantaneous drug release caused by the presence of nanofibers with a very small cross-section.

It is well known that fiber diameter is strongly influenced by polymer concentration which was, therefore, kept practically constant and high (i.e., 8 wt-%) for all PGA/PCL blends. Experimental conditions were also optimized for each polymer blend to avoid typical problems like bead formation and to obtain a similar diameter distribution. The selection process was complex since multiple parameters had to be taken under consideration and a clear optimization strategy did not exist. Nevertheless, an iterative study was carried out considering the variation of the voltage for intermediate values of the flow rate and the collector distance. Next steps corresponded to the evaluation of the effect of the flow rate and finally of the collector distance, readjusting the selected voltage after each study. Note that the study was carried out for the different blends and the selection of parameters was also performed trying to minimize differences between the final electrospun fibers.

The selection of the spinning voltage (V) was essential to ensure a stable, conical liquid jet which minimized bead formation and guaranteed again a diameter over a minimum value. The flow rate was also important to get sufficiently high diameters while complete solvent evaporation was assured. These requirements are favored at high and low rates, respectively. The distance between the collector and the syringe tip (h) was varied in order to get the minimum value and avoid typical problems of coalescence derived from non-completed solvent evaporation. Note that the surface tension and the solution viscosity, which usually have a strong influence on fiber morphology, could not be modified since the solvent and polymer concentration was not changed.

All selected PGA/PCL mixtures could finally be electrospun using the same parameters as summarized in **Table 6.1.1**.

Table 6.1.1. Selected electrospinning parameters for the preparation of the scaffolds derived from different PGA/PCL mixtures.

Sample	Voltage (kV)	Flow (mL/h)	Distance (cm)	Diameter[a)] (nm)	Diameter[b)] (nm)
PGA/PCL-0	15	3	19	155 ± 1	306 ± 7
PGA/PCL-35	20	3	10	749 ± 26	536 ± 17
PGA/PCL-50	20	3	10	784 ± 23	567 ± 30
PGA/PCL-65	20	3	10	904 ± 42	740 ± 19
PGA/PCL-80	20	3	10	1190 ± 30	852 ± 19
PGA/PCL-100	20	3	10	1532 ± 33	1267 ± 39

[a)]Unloaded samples; [b)] Samples loaded with both PHMB and CUR.

The deduced parameters were slightly different from those reported in the previous work of Aghdam et al.[13] (i.e., 17 kV, 10 cm, and 2 mL/h for voltage, distance, and flow rate, respectively) since we were interested to get fibers with greater diameters as previously indicated. Comparatively, we increased the flow rate as well as the polymer concentration in the electrospun solution (i.e., from 2 to 3 mL/h and from 6% to 8%, respectively). The PCL homopolymer sample required special conditions due to its lower molecular weight (M_n: 45,000 g/mol). Note for example that a concentration of 6% was necessary for the electrospinning of high molecular weight (M_n: 80,000 g/mol) PCL samples[13]. Therefore, polymer concentration was increased from 8 wt-% to 18 wt-% to

get a solution with a sufficiently high viscosity. At the same time, the applied voltage was decreased from 20 kV to 15 kV and the collector distance was increased from 10 cm to 19 cm. Scanning electron micrographs of the electrospun samples (**Figure 6.1.2**) demonstrated that continuous and straight fibers with a smooth surface could be obtained in all cases.

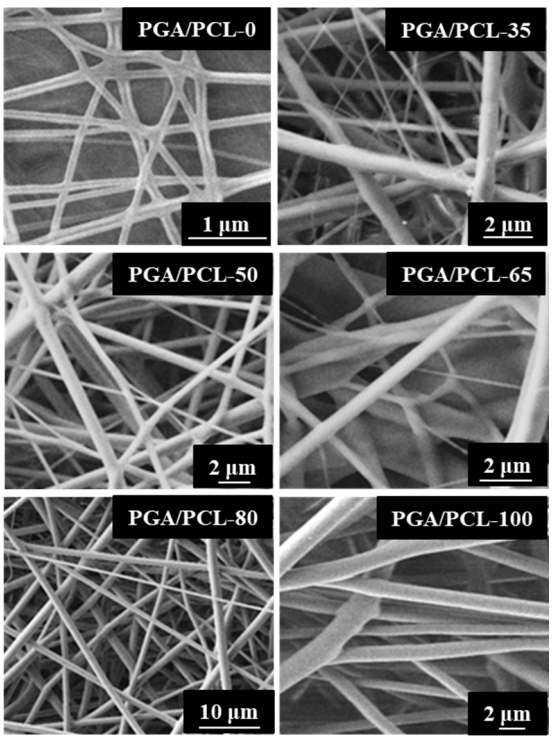

Figure 6.1.2. SEM micrographs of PGA/PCL-x electrospun fibers prepared under the optimized conditions.

Representative histograms of the diameter distributions for the different electrospun samples are given in **Figure 6.1.3**. Morphology of PGA/PCL-0 (i.e., the PCL homopolymer) electrospun fibers was different since the average diameter remained in the nanoscale (155 nm) despite the great changes on the electrospun parameters that were applied to increase the diameter. The changes were only successful in producing continuous and homogeneous fibers but had not a significant effect on the final diameter size. Micrographs of scaffolds obtained from the selected PGA/PCL blends showed also the presence of a

small proportion of thin fibers (i.e., less than 10% for PGA/PCL-35). This could be attributed to PCL rich fibers, being less abundant as the PGA composition in the electrospun solution increased. Note for example the differences between the PGA/PCL-35 and PGA/PCL-80 samples (**Figure 6.1.3**).

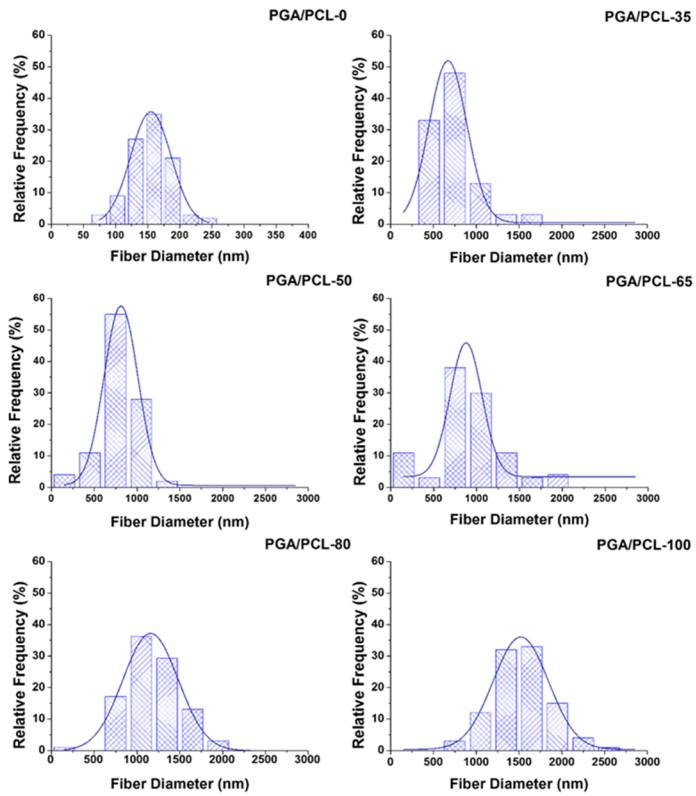

Figure 6.1.3. Frequency distribution of the fiber diameter and Gaussian functions of PGA/PCL-x fibers prepared under the optimized conditions.

The presence of the small population of thin fibers may suggest the occurrence of minor phase separation during the electrospinning process (e.g., just before ejection from the drop). The PGA/PCL-20 sample was discarded from further studies since nanofibers were highly predominant and consequently, the derived scaffolds were not useful for establishing a simple study on the drug release and composition dependence (i.e., without a significant influence of the fiber diameter). Histograms corresponding to the

high diameter population showed always a Gaussian distribution with an average diameter that progressively increased (i.e., from 750 to 1500 nm) as the PGA content in the electrospun solution did. This feature is significant since it suggests that PCL is also incorporated in the coarse fibers.

6.1.3.2 Basic Characterization of PGA/PCL-x Scaffolds

FTIR spectra of the electrospun samples showed logically the characteristic bands of each homopolymer as displayed in **Figure 6.1.4** for the representative PGA/PCL-50 sample.

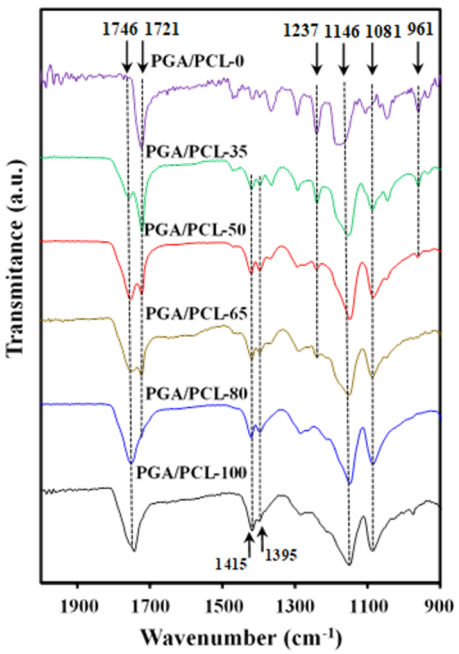

Figure 6.1.4. FTIR spectra (2000-900 cm^{-1}) of PGA/PCL-*x* electrospun fibers.

This point is observed through the presence of carbonyl bands at 1746 cm^{-1} and 1721 cm^{-1} that corresponds to PGA and PCL, respectively. Note that the intensity of these bands changed according to the final composition. The 1500-1300 cm^{-1} region is also significant since the multiple peaks observed for PCL became progressively simplified in such a way that only two peaks corresponding to crystalline PGA (at 1415 cm^{-1}) and amorphous PGA (at 1395 cm^{-1}) could be detected when the PCL content decreased. Similar conclusions

could be obtained from the disappearance of PCL bands at 1237 cm^{-1} and 961 cm^{-1} or the appearance of PGA bands at 1081 cm^{-1} when the PGA content increased. The analysis of the C-O region (at ≈ 1145 cm^{-1}) was more complex due to the overlapping of characteristic bands of both polymers.

The composition of prepared scaffolds was determined from ^1H NMR spectra where signals corresponding to glycolic acid (4.95 ppm) and ε-caprolactone (4.17, 2.45, 1.74-1.67, and 1.44-1.42 ppm) units appeared well-differentiated (**Figure 6.1.5**).

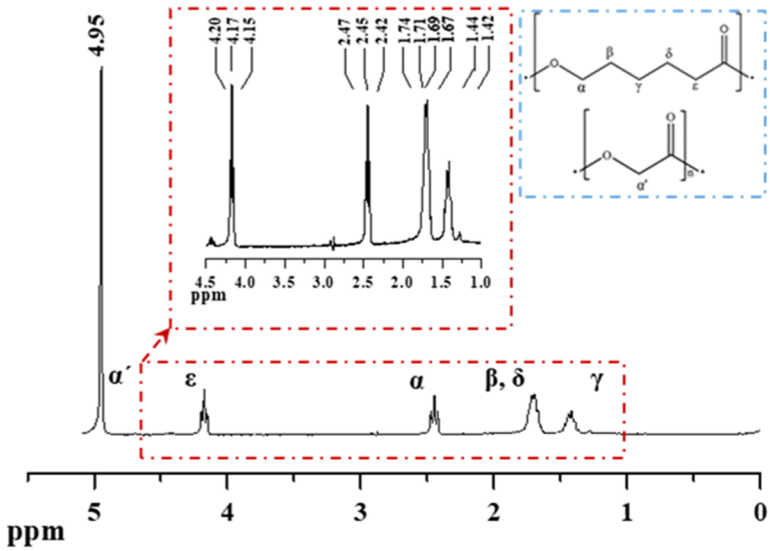

Figure 6.1.5. ^1H NMR spectrum of the representative PGA/PCL-35 electrospun sample. The selected spectrum corresponds to the sampling spot with the farthest composition from the theoretical one.

The glycolic acid content (GA wt-%) was evaluated through the areas of signals observed at 4.95 and 4.17 ppm, which correspond to $O(CH_2)$ protons of glycolyl and ε-caproyl units, respectively:

$$GA\ w\text{-}t\% = [A_{4.95} \times 58 / (A_{4.95} \times 58 + A_{4.17} \times 114)] \times 100 \quad (1)$$

where 58 and 114 correspond to the molecular weight of glycolyl and ε-caproyl units, respectively.

Logically, the global composition of the scaffold should agree with the feed polymer ratio in the electrospun solution, but it is not clear that a homogeneous and regular fiber deposition was achieved. Therefore, an analysis was performed by sampling each electrospun scaffold and taking data from five points regularly spaced along the diagonal of 5 cm × 5 cm square piece. Thus, GA wt-% of 80 ± 2, 66 ± 3, 50 ± 4 and 34 ± 3 were determined for PGA/PCL-80, PGA/PCL-65, PGA/PCL-50, PGA/PCL-35 samples, respectively.

Figure 6.1.6 shows the typical protocol performed for the calorimetric study of the different scaffolds. This consists of a first heating scan of the electrospun sample to detect crystallinity of the processed sample, a cooling scan to determine the crystallization behavior after erasing thermal history by keeping the sample 10 ºC above fusion, a second heating scan to determine the behavior of the melt crystallized sample, and finally, a third heating scan of a sample quenched from the melt at the maximum cooling rate allowed by the equipment (50 ºC min^{-1}).

Specifically, traces for PGA/PCL-50, as a representative scaffold due to its intermediate composition, are shown in **Figure 6.1.6**. The corresponding data for all studied samples are summarized in **Tables 6.1.1** and **6.1.2**. Well-differentiated melting and crystallization peaks that can be associated with each homopolymer can be detected for the PGA/PCL-50 sample at 55.7 ºC and 221.4 ºC (for fusion) and 29.3 and 185.7 ºC (for crystallization). Melting temperatures are in full agreement with those reported[11] (59-64 ºC and 220-225 ºC) for the two homopolymers, indicating that well-differentiated crystalline phases were developed, even for the electrospun processed sample.

For other compositions, the behavior was similar with logical variations of peak temperatures that move in a wider range (e.g., 40 ºC- 57 ºC and 12 ºC- 31 ºC for the fusion and crystallization of PCL, respectively). The DSC heating trace of the PGA/PCL-50 electrospun sample (**Figure 6.1.6** and **Table 6.1.2**) shows two significant features concerning PCL and PGA domains that deserve attention:

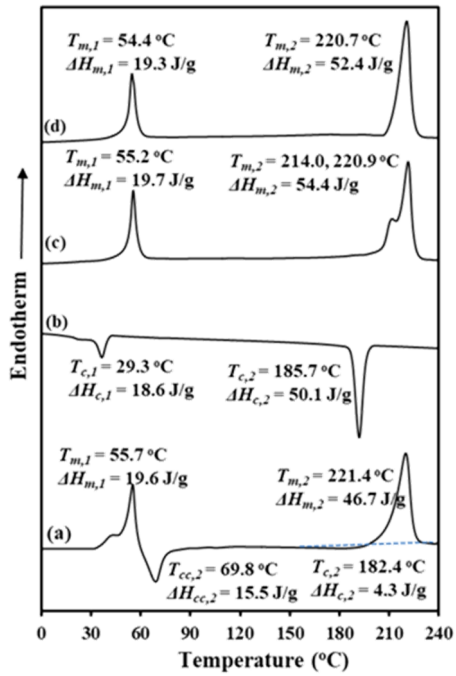

Figure 6.1.6. DSC traces showing the typical protocol followed for the PGA/PCL-50 electrospun sample: (**a**) Heating scan of the initial sample, (**b**) Cooling scan from the melt state, (**c**) Heating scan of the melt crystallized sample, and (**d**) Heating scan of a melt quenched sample.

PCL is crystallized easily during electrospinning probably as a consequence of the high orientation achieved, especially for the narrow fibers enriched on PCL. Two melting peaks were detected (**Figure 6.1.6a**, **Table 6.1.2**) suggesting the existence of two lamellar populations, with the narrower ones being sufficiently stable to prevent its reordering process during heating. The degree of crystallinity was close to 38% taking into account a PCL content of 50 wt-% and the reported enthalpy for a 100% crystalline sample (136 J/g).[28] Note that a single peak (55 °C) corresponding to reordered lamella having a lower crystallinity (i.e., close to 26%) was observed for melt crystallized (**Figure 6.1.6c**) and quenched (**Figure 6.1.6d**) samples. Therefore, crystallization of PCL was in such cases hindered for the previously formed PGA crystalline domains, which is not the case of samples prepared by electrospinning. The crystallization peak of PCL was very low during the cooling scan from the melt

state (**Figure 6.1.6b**), being this feature a clear demonstration that when the PCL remains at the lowest temperature is crystallized slowly before performing the subsequent heating scan. Similar behavior can be deduced from the melt quenched sample, justifying the similar crystallinity that was achieved.

Table 6.1.2. Calorimetric data derived from the first heating scan of PCL/PGA-*x* electrospun samples.

Samples[a)]	$T_{m,1}$ (ºC)	$\Delta H_{m,1}$ (Jg^{-1})	χ_{PCL} (%)	T_{cc} (ºC)	ΔH_{cc} (Jg^{-1})	T_{hc} (ºC)	ΔH_{hc} (Jg^{-1})
PGA/PCL-0	57.5	84.8	62	-	-	-	-
PGA/PCL-35	40.1, 56.9	42.6	48	67.5	3.6	182.5	1.7
PGA/PCL-50	43.2, 55.7	26.3	38	69.8	15.5	182.4	4.3
PGA/PCL-65	39.1, 49.2	12.5	26	62.2	17.5	179.2	8.3
PGA/PCL-80	40.4, 48.9	7.1	26	60.0	13.0	178.4	10.5
PGA/PCL-100	-	-	-	57.3	1.5	128.0	16.1

Samples	$T_{m,2}$ (ºC)	$\Delta H_{m,2}$ (Jg^{-1})	χ_{PGA}[b)] (%)	χ_{PGA}[c)] (%)
PGA/PCL-0	-	-	-	-
PGA/PCL-35	220.4	18.2	37	26
PGA/PCL-50	221.4	38.7	55	27
PGA/PCL-65	219.5	52.0	57	29
PGA/PCL-80	220.3	57.5	51	30
PGA/PCL-100	220.0	67.8	49	33

[a)] Subscripts 1 and 2 refer to PCL and PGA, respectively. T_{cc} and ΔH_{cc} indicate the temperature and enthalpy of the cold crystallization peak. T_{hc} and ΔH_{hc} indicate the temperature and enthalpy of the hot crystallization peak; [b)] Crystallinity of the PGA phase determined from the melting enthalpy and the PGA content; [c)] Crystallinity of the PGA phase determined from the melting enthalpy, the PGA content, and the substraction of cold and hot crystallization enthalpies.

The electrospinning process has also allowed the crystallization of PGA, but the degree of crystallinity (39% when the reported value of 139 J/g for a 100% crystalline sample[29] was considered, as well as a PGA content of 50 wt-% and the enthalpy of exothermic peaks subtracted) was lower than the obtained one from melt crystallized or melt quenched samples. Both were close to 68% since PGA was able to crystallize under the maximum cooling rate allowed by the equipment. Note also that the electrospun sample showed a clear

cold exothermic crystallization peak at 69.8 ºC and even a very small hot crystallization peak at 215 ºC. The melting enthalpy and the final crystallinity (achieved during the heating process) became similar to those determined for the melt crystallized samples. A single melting peak close to 221 ºC was observed for the electrospun sample, being indicative of a lamellar reorganization during heating. Note that a double melting peak was only detected for the melt crystallized sample at the slow rate of 10 ºC min^{-1} since in this case thinner and stable lamellae were formed and a peak at 214 ºC corresponding to the non-reordered crystals could be detected.

Calorimetric data of the different electrospun samples are compared in **Table 6.1.3**, making it clear that melting enthalpies of PCL and PGA domains logically decreased and increased, respectively with the PGA content. More interestingly, the PGA cold crystallization peak for fibers with a PGA content lower than 80% was enhanced when the PCL content increased, indicating a greater difficulty to get crystalline PGA domains during electrospinning. It is clear that PCL was well-mixed inside the fibers and hindered PGA crystallization during the electrospinning process. Note also that the cold crystallization temperature increased for higher PCL contents demonstrating again the greater difficulty of PGA to crystallize from the mixed-phase. A contrary effect was observed for the PGA cold crystallization peak of samples with a high PGA content (i.e., ≥ 80 wt-%) since in this case, electrospinning was able to render highly ordered PGA domains.

Table 6.1.3. Calorimetric data from the first cooling scan and second heating scan of PGA/PCL-*x* electrospun samples.

Samples[a)]	$T_{c,1}$ (ºC)	$\Delta H_{c,1}$ (Jg^{-1})	$T_{c,2}$ (ºC)	$\Delta H_{c,2}$ (Jg^{-1})	$T_{m,1}$ (ºC)	$\Delta H_{m,1}$ (Jg^{-1})	$T_{m,2}$ (ºC)	$\Delta H_{m,2}$ (Jg^{-1})
PGA/PCL-0	31.5	65.9	-	-	56.1	69.6	-	-
PGA/PCL-35	30.2	40.0	187.5	25.7	55.4	44.8	211.3, 220.1	24.4
PGA/PCL-50	29.3	18.6	185.7	48.1	55.2	19.7	214.0, 220.9	50.4
PGA/PCL-65	13.3	12.7	185.9	53.5	53.3	13.1	211.0, 220.6	51.5
PGA/PCL-80	12.0	8.6	185.6	59.3	53.2	9.1	210.3, 220.6	53.5
PGA/PCL-100	-	-	187.0	68.1	-	-	212.0, 220.4	67.1

[a)] Subscripts 1 and 2 refer to PCL and PGA, respectively.

The final crystallinity of PCL domains was relatively high (26-62%) for all samples as well as that of PGA domains after thermal treatment of samples (i.e., 37-57%) (cold and hot crystallization processes). These values were also in agreement with those determined from melt crystallized samples (**Table 6.1.3**). Nevertheless, the crystallinity of PGA domains of electrospun samples before thermal recrystallization processes showed moderate values (i.e., 26-33%) and a regular increase with the PGA content.

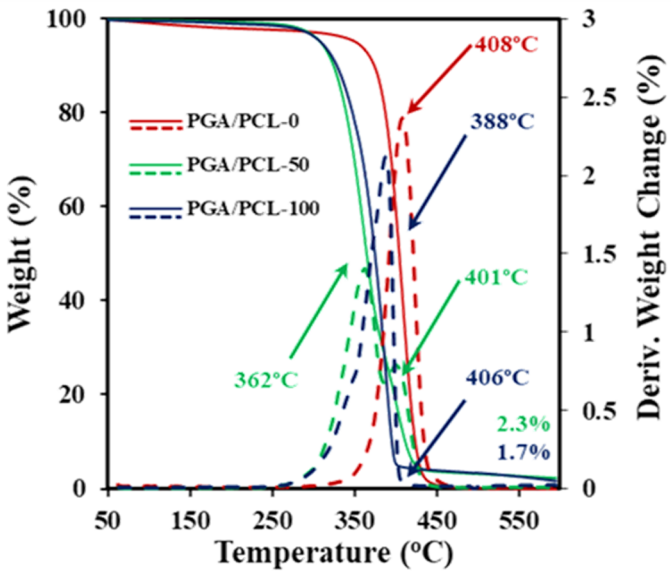

Figure 6.1.7. TGA (solid lines) and DTGA (dashed lines) curves of PGA-PCL-100 (blue), PGA/PCL-50 (green), and PGA/PCL-0 (red) electrospun scaffolds.

Thermogravimetric analysis (**Figure 6.1.7**) shows that the behavior of the electrospun blends is not exactly defined by a simple combination of TGA curves of the corresponding homopolymers. Note that the degradation of PCL is characterized by a single DTGA peak at 408 ºC (for a heating rate of 10 ºC min^{-1}) without char yield, while degradation of PGA is complex with a predominant peak at 388 ºC, a shoulder at a lower temperature (345 ºC) and a significant char yield (1.7 wt-%). DTGA curves of blends, as shown for the representative PGA/PCL-50 sample, were also complex and revealed two main peaks with a variable intensity depending on composition. The first one appeared at an intermediate position to those detected for the two

decomposition steps of PGA (i.e., 362 ºC), while the second one appeared at a significantly lower temperature (388 ºC) than the one found for PCL. This observation indicates that the degradation of the PCL component was accelerated by the decomposition products of the most unstable PGA component.

Note that PGA/PCL-50 was practically degraded (remaining weight of 12%) before achieving the temperature of the DTGA peak of PCL. Nevertheless, degradation gave rise to a significant char yield, even higher than the one determined for the PGA homopolymer.

X-ray diffraction patterns of the electrospun samples showed the characteristic reflections of both homopolymers. Thus, three Bragg peaks at 0.416, 0.403 and 0.373 nm, which correspond to the (110), (111) and (200) reflections of the orthorhombic unit cell (a = 0.747 nm, b = 0.498 nm, c (fiber axis) = 1.705 nm) of poly(ε-caprolactone),[30,31] were determined for the PGA/PCL-0 sample (**Figure 6.1.8a**). PGA/PCL-100 showed two main peaks at 0.399 and 0.309 nm that correspond to the (110) and (020) reflections of the orthorhombic unit cell of polyglycolide (**Figure 6.1.8c**) (a = 0.522 nm, b = 0.619 nm, c (fiber axis) = 0.702 nm).[32] In addition, a clear amorphous halo centered around 0.455-0.446 nm was always observed, making it possible to determine the degree of crystallinity of all samples by the deconvolution of the WAXD patterns.

Results pointed out that PCL is crystallized more easily than PGA during electrospinning (i.e., degree of crystallinities of 86% and 49% for PCL and PGA, respectively), a feature that could be related with the higher molecular orientation that could be attained when the diameter of the electrospun fibers decreased. Diffraction profiles of the different blends showed always a global crystallinity higher than the determined one for the PGA sample. Results demonstrated the capability of PCL to crystallize, even in the presence of PGA, and pointed out a clear phase separation of the two copolymers during the electrospinning process. Deconvolution confirmed the DSC results which indicated that final crystallinity can be attributed mainly to the PCL phase. Thus,

the representative PGA/PCL-50 had a final crystallinity of 68%, with 47% and 21% being the values deduced for PCL and PGA domains respectively.

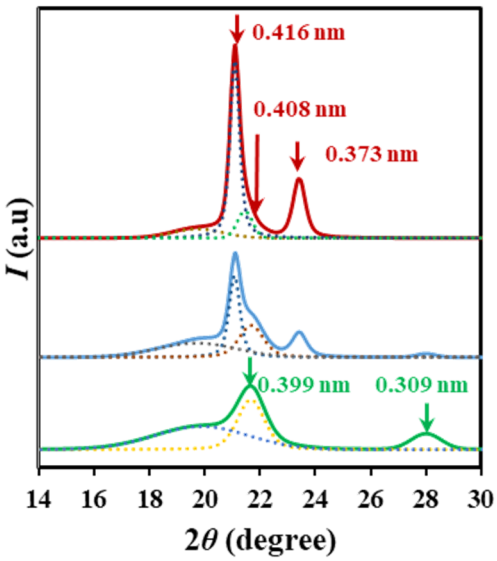

Figure 6.1.8. X-ray diffraction profiles with the corresponding deconvolution of PGA/PCL-0 (red), PGA/PCL-50 (blue), and PGA/PCL-100 (green) electrospun samples.

The increase of the PGA content in the electrospun scaffolds lead logically to an increase of the hydrophilicity of the samples as revealed by contact angle measurements (**Figure 6.1.9**).

Scaffolds of the PCL homopolymer were highly hydrophobic, with the contact angle being close to 130º. The hydrophobic surface was kept up to a PGA content of 65 wt-%, but a monotonous decrease of the contact angle was detected as the PGA content increased (i.e., from 130º to 114º). Note that the influence of the PGA content could be slightly counterbalanced by the increase of the surface roughness. Specifically, the increase of the fiber diameter size should lead to a more hydrophobic surface according to the Wenzel equation.[33] The importance of the surface effect is evident when data reported for scaffolds made up of fibers with smaller diameters[13] are considered (e.g., the contact angle of PCL decreased from 130 º to 118º when diameters decreased from 155 nm

to 86 nm). The scaffold with a PGA content of 80 wt-% became completely hydrophilic, with the contact angle being similar to that determined from the corresponding homopolymers (i.e., < 5º). In summary, physical properties (e.g., hydrophobic/hydrophilic surface characteristics) of the new scaffolds could be tuned by changing the polymer composition, making it possible to have a fine control at high/moderate PCL content (i.e., ≥ 35 wt-%).

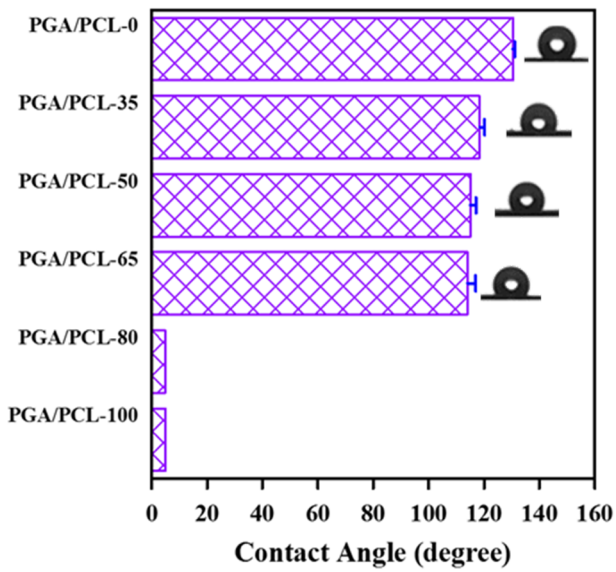

Figure 6.1.9. Contact angle measurements of PGA/PCL-*x* electrospun scaffolds in distilled water.

6.1.3.3 CUR and PHMB Loaded PGA/PCL-*x* Electrospun Scaffolds

Electrospinning parameters could be maintained when both CUR and PHMB compounds were incorporated in the HFIP solution of the corresponding polymer mixture. Continuous fibers were always obtained and in general, a small decrease of the fiber diameters (**Table 6.1.1**) concerning those determined for the unloaded samples was detected. Probably the most important effect was the increase of the conductivity of the electrospinning solutions as a consequence of the presence of the cationic PHMB compound. In any case, the reduction of diameter was scarce and lower than 30%. An

increase of the diameter was only detected for the PGA/PCL-0 homopolymer, but it should be pointed out that in this case the concentration of the polymer was well differentiated from all the other samples. Incorporation of PHMB had a higher effect on the reduction of diameter as could be deduced from the values of 749, 537, 587 and 636 nm determined for the PGA/PCL-50 unloaded sample and that loaded with PHMB+CUR, PHMB, and CUR, respectively. **Figure 6.1.10** shows that the texture of the fibers was always smooth and that the presence of crystals corresponding to each loaded compound could not be detected.

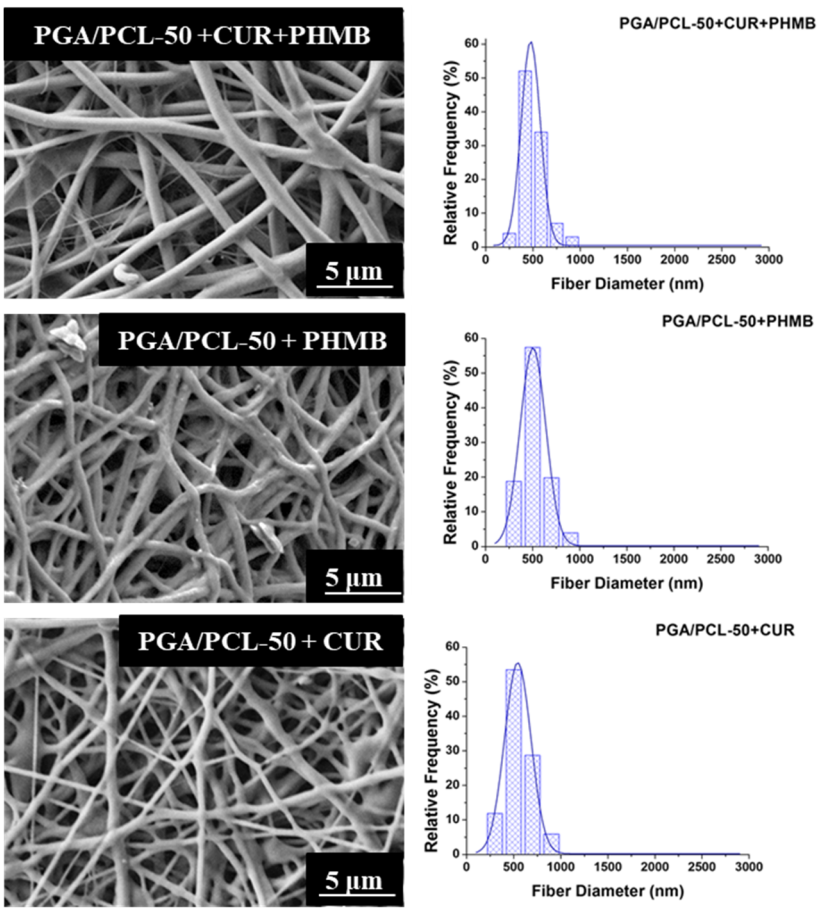

Figure 6.1.10. SEM micrographs of drug-loaded PGA/PCL-50 electrospun scaffolds and frequency distribution of the corresponding fiber diameters.

The appearance of fibers changed after exposure to an aqueous release medium (i.e., PBS/ethanol mixture) since the presence of pores and longitudinal striations were evident (**Figure 6.1.11**). This feature could be related to an initial swelling, the delivery of soluble compounds, and a final shrinkage after drying. The diameter size decreased after exposure to the indicated medium by approximately 10-15% (e.g., the diameter of PGA/PCL-50 loaded with PHMB+CUR decreased from 537 to 475 nm).

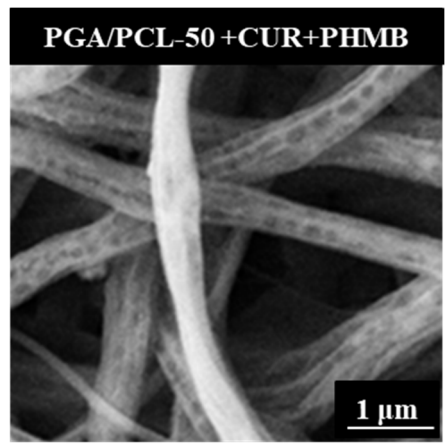

Figure 6.1.11. SEM micrograph of a dried PGA/PCL-50 electrospun scaffold loaded with CUR and PHMB after exposure for 1 day to a PBS/ethanol medium.

The presence of domains associated with CUR or PHMB crystals could be discarded considering both X-ray diffraction patterns and DSC heating scans (not shown) since characteristic reflections or melting peaks were not detected. Thus, the crystallization of the drugs during the electrospinning process seems to be prevented in agreement with the absence of crystals deduced from morphological observations. This feature is important since the activity of the added compounds should be higher in the amorphous state. On the other hand, the influence of the drugs on calorimetric parameters (e.g., crystallization and melting temperatures and the corresponding enthalpies) were not as highly significant as expected when drugs were not incorporated into the crystalline domains of PGA and PCL.

The incorporation of CUR and PHMB had a strong influence on the thermal stability of the prepared scaffolds as shown in **Figure 6.1.12** for the PGA/PCL-50 representative sample. The most important feature is a clear thermal destabilization, with the onset degradation temperature being decreased by at least 40 ºC. The DTGA profiles changed also remarkably and a great decrease in the degradation peak temperature associated with the first decomposition step was observed. Thus, values of 262-263 ºC and 303 ºC were determined for the samples loaded with CUR and PHMB, respectively, in contrast with the temperature of 362 ºC detected for the unloaded sample. The weight loss associated with this step was close to 35% for both loaded samples, a value that was higher than the amount of incorporated drug, and this points out an accelerated degradation of the most unstable PGA homopolymer. The degradation process may be logically enhanced by the decomposition products of CUR and PHMB, which were reported to appear at lower temperatures than the onset of PGA decomposition. Specifically, the most negative effect was observed for PHMB, in which degradation was reported to start at 230 ºC,[34] although the more significant decomposition steps occur at 364 ºC and 473 ºC.[35] The degradation of CUR is characterized by two steps that corresponded to single processes with degradation peaks at 292 ºC (mass loss of 33.8%) and 486 ºC (mass loss of 66.2%).[36]

DTGA profiles of loaded electrospun PGA/PCL samples showed also a second and predominant degradation peak at temperatures close to that observed in the unloaded samples. This peak appears at a slightly higher temperature (i.e., 407 ºC with respect to 401 ºC) for the CUR loaded sample or at a lower temperature when PHMB was incorporated (e.g., see the complex peak near 390 ºC). In addition, these samples showed an additional decomposition step at 450 ºC that could be linked with the observed one for PHMB.[35] Degradation was also characterized by an increase of the char yield (i.e., from 2% to 6%, 10%, or 14% when CUR, PHMB, or both compounds were respectively incorporated).

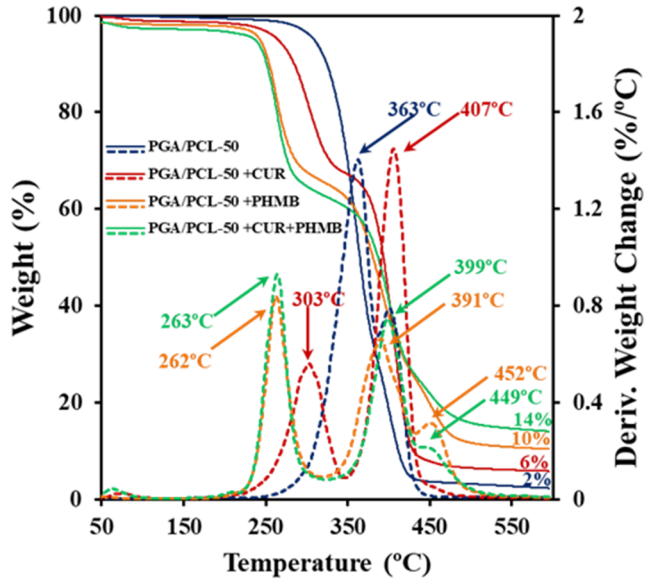

Figure 6.1.12. TGA (solid lines) and DTGA (dashed lines) curves of unloaded and drug-loaded PGA/PCL-50 electrospun scaffolds.

6.1.3.4 CUR and PHMB release from PGA/PCL-*x* Electrospun Scaffolds

PGA/PCL electrospun scaffolds showed a well-differentiated release behavior in function of their composition, the hydrophilicity of the drug, and the selected release medium. However, in all cases, the release occurred according to two different steps: a fast delivery of molecules that were probably located near or on the high surface area of micro/nanofibers, and a subsequent slow delivery that should involve the diffusion of molecules through the polymer matrix to the release medium. This process is usually described by a two-step kinetic model that follows Higuchi[37] and first-order[38] (2) equations for 0-60% and 40-100% of the release, respectively.[39]

Time evolution of CUR release percentages during exposition to an aqueous PBS medium is displayed in **Figure 6.1.13a** for all studied compositions. Plots revealed a typical initial fast release that covers the 100 min and a subsequent slow release that reaches a saturation level and hence achievement of equilibrium. Saturation level diminished significantly by

increasing the PCL ratio (i.e., from 65% to 5%), demonstrating the capability to tune the release behavior by a simple modification of the ratio between two of the most employed biodegradable polyesters. Logically the hydrophobic CUR had a higher affinity with the polymer matrix when it was enriched on the more hydrophobic PCL component. A relatively good linear dependence was found between the CUR saturation level (y) and the PGA wt-% (x) (i.e., $y = 0.56\ x + 12$, $r = 0.98$). The slopes of the release curves at the beginning also indicated an increase in the release rate with the PGA content.

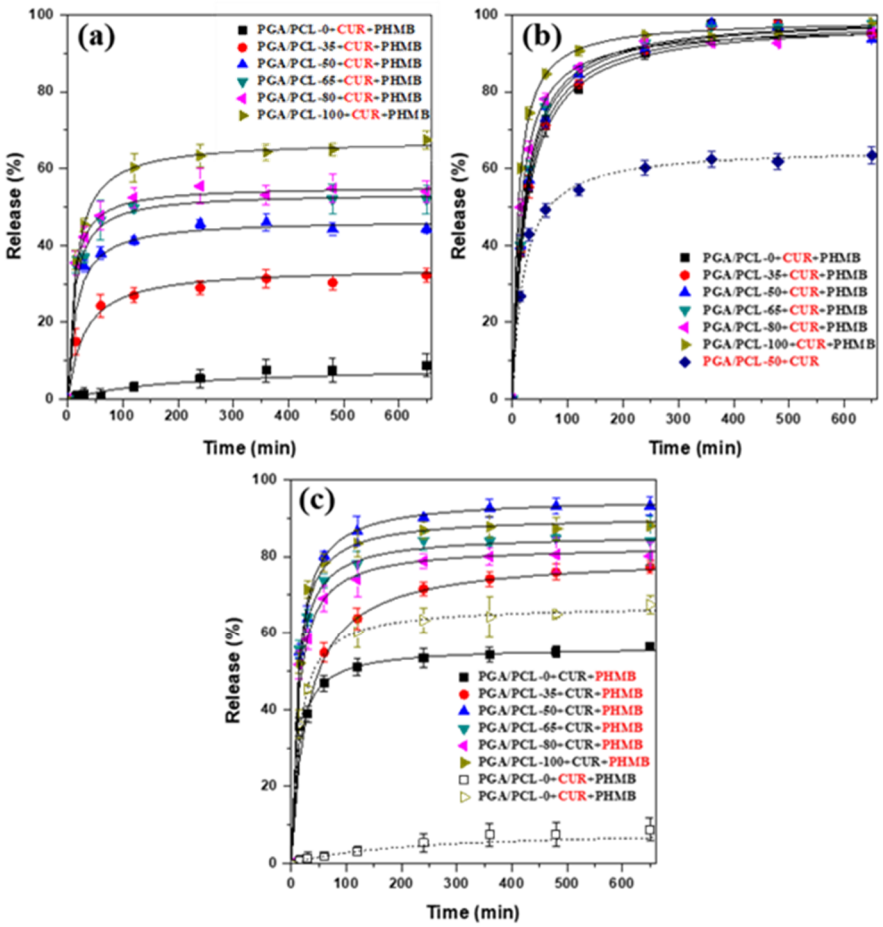

Figure 6.1.13. (**a**, **b**) Cumulative CUR and (**c**) PHMB release profiles of the indicated electrospun samples in a PBS (**a**, **c**) and PBS/ethanol (7:3 *v*/*v*) medium (**b**). For comparison purposes, cumulative CUR release profiles in a PBS medium are also plotted in (**c**).

The addition of ethanol to the release medium facilitated the delivery of both CUR and PHMB since this solvent enhanced the swelling of fibers and also increased the solubility of both compounds. This effect is illustrated in **Figure 6.1.13b** where the differences between the saturation levels were minimized (i.e., release percentages varied between 98 and 92% after an exposure of 650 min). Nevertheless, the above-indicated trend concerning the release rate was clear at short exposure times. Thus, release percentages decreased from 75% to 55% after 25 min of exposure when the PGA wt-% decreased. The presence of PHMB enhanced also the delivery of CUR as illustrated in **Figure 6.1.13b** for PGA/PCL-50 loaded only with CUR (see the dashed line). Note that in this case, the saturation level decreased up to 60%, although it remains higher than observed for the PBS medium. This point gives a second argument to explain differences in the release and emphasizes the importance of increasing the hydrophilicity of the fiber (as expected by the incorporation of PHMB) to favor the release in an aqueous media as will be discussed below for PHMB.

The release of PHMB in PBS (**Figure 6.1.13c**) also showed the achievement of a saturation level, which was higher than the one observed for CUR (i.e., see dashed lines for a direct comparison). This feature can be well justified considering the higher solubility of PHMB in the aqueous medium due to its higher hydrophilic character and the lower capability of the polymer matrix to retain the bactericide component. In general, the observed trend is that the saturation level increased with the PGA content, which is in contradiction with a higher affinity of the drug with the matrix. Note that the release should be higher by increasing the hydrophobic PCL ratio. Therefore, in this case, results strongly support the hypothesis that the delivery mainly depends on the ability of the solvent to penetrate inside the fiber, which is logically higher when the PGA content increases, but must also depend on other factors such as crystallinity and diameter size.

Thus, a bad linear dependence was found between the PHMB saturation level (y) and the PGA wt-% (x) (i.e., $y = 0.29\,x + 62.8$, $r = 0.77$).The regression

coefficient increased to 0.94 when the release of the more amorphous PGA/PCL-50 sample was not considered (y = 0.31 x + 58.9), a feature that supports the different diffusion of solvent inside the polymeric matrices.

6.1.3.5 Antibacterial Activity of PGA/PCL-*x* Electrospun Scaffolds

The antimicrobial effect of PHMB and CUR loaded matrices was evaluated quantitatively by considering the growth curves of Gram-negative (*E. coli*) and Gram-positive (*S. aureus*) bacteria, (**Figures 6.1.14a** and **6.1.14b**, respectively). The unloaded matrix was highly susceptible to bacterial infection and biofilm formation, with a latency phase that extended for 6 h and that was followed by an exponential growth (log) phase. Bacterial growth was completely inhibited for all samples loaded with PHMB. The only remarkable difference was the higher time required for the PGA/PCL-0 sample to attain a 0% relative growth of the less susceptible *E. coli* bacterium (**Figure 6.1.14a**).

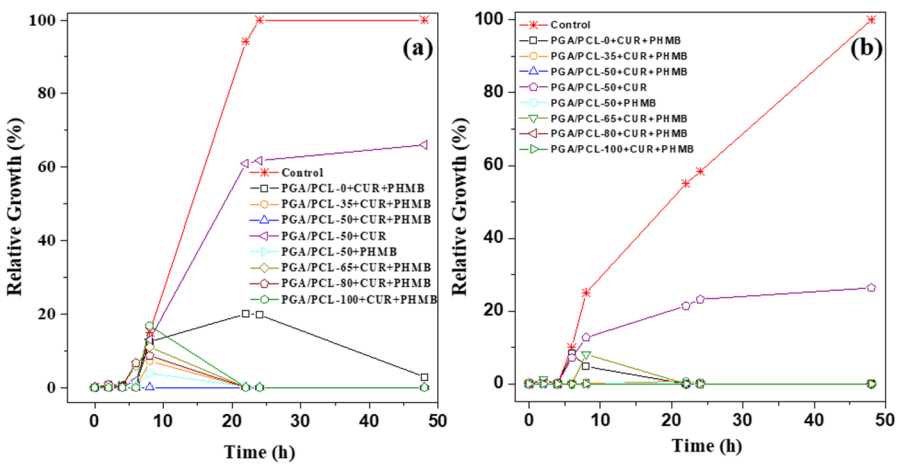

Figure 6.1.14. Growth curves of *E. coli* (**a**) and *S. aureus* (**b**) in the indicated drug-loaded electrospun scaffolds and the unloaded one used as a control.

This result seems coherent considering the lower observed release of both loaded drugs from this more hydrophobic composition. A total inhibition was not attained when samples were only loaded with CUR, for example, the detected decrease of bacterial growth was close to 35% and 73% for *E. coli* and

S. aureus, respectively, for the PGA/PCL-50 sample. CUR has a lower bactericide effect than PHMB and its release was also lower as explained before. The bactericidal effect was qualitatively corroborated by agar tests, i.e., measuring the inhibition halos around scaffold pieces (**Figure 6.1.15**). This method may be problematic to evaluate the bactericidal effect caused by hydrophilic drugs such as PHMB since their release in the hydrophobic agar medium may be difficult. Results (**Figure 6.1.15**) point out that inhibition halos were significant for all loaded samples, regardless of the type of bacteria, and even when only CUR was loaded. Note that no inhibition halo was observed for the unloaded PGA/PCL-50 sample, which can be considered as the negative control.

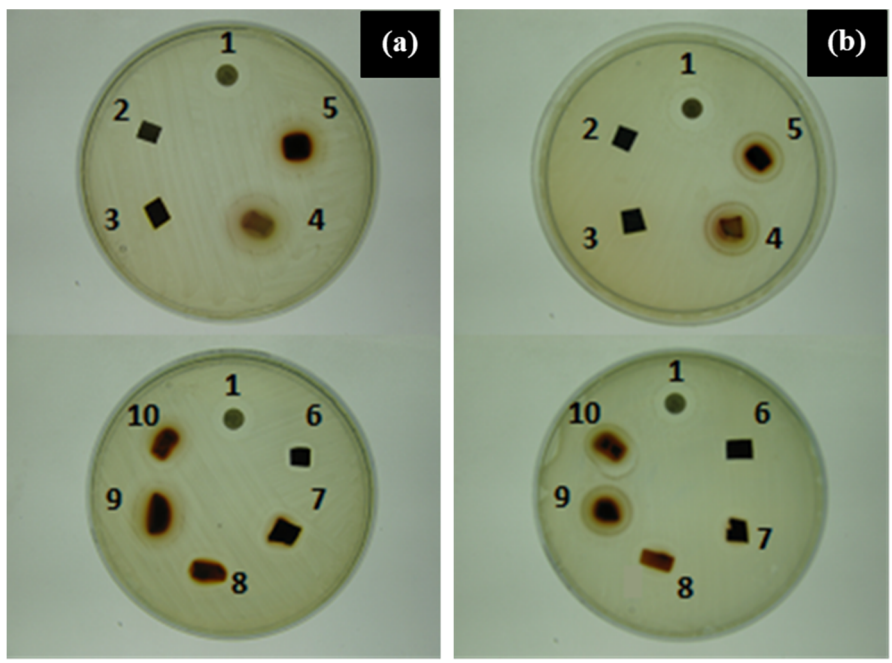

Figure 6.1.15. Images showing inhibition halos on agar plates seeded with *E. coli* (**a**) and *S. aureus* (**b**) that were caused by 1. Gentamicin control, 2. PGA/PCL-50, 3. PGA/PCL-50 +PHMB, 4. PGA/PCL-50 + CUR, 5. PGA/PCL-50 +CUR+PHMB, 6. PGA/PCL-0 + CUR + PHMB, 7. PGA/PCL-35 + CUR + PHMB, 8. PGA/PCL-65 +CUR + PHMB, 9. PGA/PCL-80 + CUR + PHMB and 10. PGA/PCL-100 + CUR + PHMB samples.

6.1.4 CONCLUSIONS

Electrospinning of HFIP solutions of PGA and PCL homopolymer mixtures becomes a simple method to obtain materials with tuned properties in terms of hydrophilic/hydrophobic character and drug delivery behavior. Furthermore, the system is interesting since it involves two of the most applied biodegradable polyesters in the biomedical field. Electrospinning parameters can be well suited to get, homogeneous and continuous fibers in the nano/micrometer diameter range, even when pharmacologically active compounds (i.e., CUR and PHMB) were loaded. Crystallinity and in general thermal properties of new scaffolds were dependent on the PGA/PCL ratio, where the samples with an intermediate composition were logically more amorphous. The selected CUR and PHMB compounds could be effectively loaded into electrospun fibers, while their crystallization was possible to be avoided. The incorporation of CUR and PHMB had a remarkable effect on the thermal stability of the loaded scaffolds, with the addition of the cationic PHMB being more problematic.

A well-differentiated CUR release in PBS medium was observed depending on the PGA/PCL ratio. In all cases, the release achieved a saturation level that decreased with the increase of the content of the hydrophobic PCL component. The release of PHMB was also dependent on the composition and more specifically increased when diffusion of the medium into the polymer matrix was favored by the increase of sample hydrophilicity and the decrease of crystallinity. In the same way, the release of CUR was enhanced when scaffolds were also loaded with the hydrophilic PHMB.

All scaffolds loaded with CUR and PHMB showed a bactericide effect independently of employing a hydrophilic or a hydrophobic culture medium. Nevertheless, CUR loaded samples had lower activity than PHMB loaded ones.

6.1.5 REFERENCES

(1) Martina, M.; Hutmacher, D. W. Biodegradable Polymers Applied in Tissue Engineering Research: A Review. *Polym. Int.* **2007**, *56* (2), 145–157. https://doi.org/10.1002/pi.2108.

(2) Ulery, B. D.; Nair, L. S.; Laurencin, C. T. Biomedical Applications of Biodegradable Polymers. *J. Polym. Sci. Part B Polym. Phys.* **2011**, *49* (12), 832–864. https://doi.org/10.1002/polb.22259.

(3) Chu, C. C.; Von Fraunhofer, J. A.; Greisler, H. P. *Wound Closure Biomaterials and Devices*; CRC Press, 1997.

(4) Knecht, S.; Erggelet, C.; Endres, M.; Sittinger, M.; Kaps, C.; Stüssi, E. Mechanical Testing of Fixation Techniques for Scaffold-Based Tissue-Engineered Grafts. *J. Biomed. Mater. Res. part B Appl. Biomaterilas* **2007**, *83* (1), 50–57. https://doi.org/10.1002/jbmb.

(5) Dunne, N.; Jack, V.; O'Hara, R.; Farrar, D.; Buchanan, F. Performance of Calcium Deficient Hydroxyapatite–Polyglycolic Acid Composites: An in Vitro Study. *J. Mater. Sci. Mater. Med.* **2010**, *21* (8), 2263–2270. https://doi.org/10.1007/s10856-010-4021-9.

(6) Mahmoudifar, N.; Doran, P. M. Chondrogenic Differentiation of Human Adipose-Derived Stem Cells in Polyglycolic Acid Mesh Scaffolds under Dynamic Culture Conditions. *Biomaterials* **2010**, *31* (14), 3858–3867. https://doi.org/10.1016/j.biomaterials.2010.01.090.

(7) Erggelet, C.; Neumann, K.; Endres, M.; Haberstroh, K.; Sittinger, M.; Kaps, C. Regeneration of Ovine Articular Cartilage Defects by Cell-Free Polymer-Based Implants. *Biomaterials* **2007**, *28* (36), 5570–5580. https://doi.org/10.1016/j.biomaterials.2007.09.005.

(8) Li, W. J.; Cooper, J. A.; Mauck, R. L.; Tuan, R. S. Fabrication and Characterization of Six Electrospun Poly(α-Hydroxy Ester)-Based Fibrous Scaffolds for Tissue Engineering Applications. *Acta Biomater.* **2006**, *2* (4), 377–385. https://doi.org/10.1016/j.actbio.2006.02.005.

(9) Luciani, A.; Coccoli, V.; Orsi, S.; Ambrosio, L.; Netti, P. A. PCL Microspheres Based Functional Scaffolds by Bottom-up Approach with Predefined Microstructural Properties and Release Profiles. *Biomaterials* **2008**, *29* (36), 4800–4807. https://doi.org/10.1016/j.biomaterials.2008.09.007.

(10) Chung, S.; Ingle, N. P.; Montero, G. A.; Kim, S. H.; King, M. W. Bioresorbable Elastomeric Vascular Tissue Engineering Scaffolds via Melt Spinning and Electrospinning. *Acta Biomater.* **2010**, *6* (6), 1958–1967. https://doi.org/10.1016/j.actbio.2009.12.007.

(11) Platt, D. K. *Biodegradable Polymers Market Report*; Smithers Rapra Limited: Shropshire, United Kingdom, 2006.

(12) Del Valle, L. J.; Camps, R.; Díaz, A.; Franco, L.; Rodríguez-Galán, A.;

Puiggalí, J. Electrospinning of Polylactide and Polycaprolactone Mixtures for Preparation of Materials with Tunable Drug Release Properties. *J. Polym. Res.* **2011**, *18*, 1903–1917. https://doi.org/10.1007/s10965-011-9597-3.

(13) Aghdam, R. M.; Najarian, S.; Shakhesi, S.; Khanlari, S.; Shaabani, K.; Sharifi, S. Investigating the Effect of PGA on Physical and Mechanical Properties of Electrospun PCL/PGA Blend Nanofibers. *J. Appl. Polym. Sci.* **2011**, *124*, 123–131. https://doi.org/10.1002/app.

(14) Paskiabi, F. A.; Mirzaei, E.; Amani, A.; Shokrgozar, M. A.; Saber, R.; Faridi-Majidi, R. Optimizing Parameters on Alignment of PCL/PGA Nanofibrous Scaffold: An Artificial Neural Networks Approach. *Int. J. Biol. Macromol.* **2015**, *81*, 1089–1097. https://doi.org/10.1016/j.ijbiomac.2014.10.040.

(15) Jonnalagadda, J. B.; Rivero, I. V.; Warzywoda, J. In-Vitro Degradation Characteristics of Poly(e-Caprolactone)/Poly(Glycolic Acid) Scaffolds Fabricated via Solid-State Cryomilling. *J. Biomater. Appl.* **2015**, *30* (4), 472–483. https://doi.org/10.1177/0885328215592853.

(16) Reneker, D. H.; Chun, I. Nanometre Diameter Fibres of Polymer, Produced by Electrospinning. *Nanotechnology* **1996**, *7* (3), 216–223. https://doi.org/10.1088/0957-4484/7/3/009.

(17) Li, D.; Xia, Y. Electrospinning of Nanofibers: Reinventing the Wheel? *Adv. Mater.* **2004**, *16* (14), 1151–1170. https://doi.org/10.1002/adma.200400719.

(18) Deitzel, J. M.; Kleinmeyer, J.; Harris, D.; Tan, N. C. B. The Effect of Processing Variables on the Morphology of Electrospun Nanofibers and Textiles. *Polymer (Guildf).* **2001**, *42*, 261–272.

(19) Yang, G.; Li, X.; He, Y.; Ma, J.; Ni, G.; Zhou, S. From Nano to Micro to Macro: Electrospun Hierarchically Structured Polymeric Fibers for Biomedical Applications. *Prog. Polym. Sci.* **2018**, *81*, 80–113. https://doi.org/10.1016/j.progpolymsci.2017.12.003.

(20) Li, L.; Zhou, G.; Wang, Y.; Yang, G.; Ding, S.; Zhou, S. Controlled Dual Delivery of BMP-2 and Dexamethasone by Nanoparticle-Embedded Electrospun Nanofibers for the Efficient Repair of Critical-Sized Rat Calvarial Defect. *Biomaterials* **2015**, *37*, 218–229. https://doi.org/10.1016/j.biomaterials.2014.10.015.

(21) Yang, G.; Wang, J.; Wang, Y.; Li, L.; Guo, X.; Zhou, S. An Implantable Active-Targeting Micelle-in-Nanofiber Device for Efficient and Safe Cancer Therapy. *ACS Nano* **2015**, *9* (2), 1161–1174. https://doi.org/10.1021/nn504573u.

(22) Llorens, E.; Del Valle, L. J.; Puiggalí, J. Multifunctional Ternary Drug-Loaded Electrospun Scaffolds. *J. Appl. Polym. Sci.* **2016**, *133* (8), 1–16. https://doi.org/10.1002/app.42751.

(23) Kaehn, K. Polihexanide: A Safe and Highly Effective Biocide. *Skin Pharmacol. Physiol.* **2010**, *23* (SUPPL. 1), 7–16. https://doi.org/10.1159/000318237.

(24) Hatcher, H.; Planalp, R.; Cho, J.; Torti, F. M.; Torti, S. V. Curcumin: From Ancient Medicine to Current Clinical Trials. *Cell. Mol. Life Sci.* **2008**, *65* (11), 1631–1652. https://doi.org/10.1007/s00018-008-7452-4.

(25) Jiao, Y.; Wilkinson IV, J.; Di, X.; Wang, W.; Hatcher, H.; Kock, N. D.; D'Agostino, R.; Knovich, M. A.; Torti, F. M.; Torti, S. V. Curcumin, a Cancer Chemopreventive and Chemotherapeutic Agent, Is a Biologically Active Iron Chelator. *Blood* **2009**, *113* (2), 462–469. https://doi.org/10.1182/blood-2008-05-155952.

(26) Tyagi, P.; Singh, M.; Kumari, H.; Kumari, A.; Mukhopadhyay, K. Bactericidal Activity of Curcumin I Is Associated with Damaging of Bacterial Membrane. *PLoS One* **2015**, *10* (3), 1–15. https://doi.org/10.1371/journal.pone.0121313.

(27) Llorens, E.; Ibañez, H.; Del Valle, L. J.; Puiggalí, J. Biocompatibility and Drug Release Behavior of Scaffolds Prepared by Coaxial Electrospinning of Poly(Butylene Succinate) and Polyethylene Glycol. *Mater. Sci. Eng. C* **2015**, *49*, 472–484. https://doi.org/10.1016/j.msec.2015.01.039.

(28) Crescenzi, V.; Manzini, G.; Calzolari, G.; Borri, C. Thermodynamics of Fusion of Poly-β-Propiolactone and Poly-⌾-Caprolactone. Comparative Analysis of the Melting of Aliphatic Polylactone and Polyester Chains. *Eur. Polym. J.* **1972**, *8* (3), 449–463. https://doi.org/10.1016/0014-3057(72)90109-7.

(29) Cohn, D.; Younes, H.; Marom, G. Amorphous and Crystalline Morphologies in Glycolic Acid and Lactic Acid Polymers. *Polymer (Guildf).* **1987**, *28* (12), 2018–2022. https://doi.org/10.1016/0032-3861(87)90035-8.

(30) Chatani, Y.; Okita, Y.; Tadokoro, H.; Yamashita, Y. Structural Studies of Polyesters. III. Crystal Structure of Poly-ε-Caprolactone. *Polym. J.* **1970**, *1* (5), 555–562.

(31) Iwata, T.; Doi, Y. Morphology and Enzymatic Degradation of Poly(ε-Caprolactone) Single Crystals: Does a Polymer Single Crystal Consist of Micro-Crystals? *Polym. Int.* **2002**, *51* (10), 852–858. https://doi.org/10.1002/pi.858.

(32) Suehiro, K.; Chatani, Y.; Tadokoro, H. Structural Studies of Polyesters. VI. Disordered Crystal Structure (Form II) of Poly(β-Propiolactone). *Polym. J.* **1975**, *7* (3), 352–358. https://doi.org/10.1295/polymj.7.352.

(33) Wenzel, R. N. Resistance of Solid Surfaces to Wetting by Water. *Ind. Eng. Chem.* **1936**, *28* (8), 988–994. https://doi.org/10.1021/ie50320a024.

(34) East, G. C.; McIntyre, J. E.; Shao, J. Polybiguanides: Synthesis and Characterization of Polybiguanides Containing Hexamethylene Groups. *Polymer (Guildf).* **1997**, *38* (15), 3973–3984. https://doi.org/10.1016/S0032-3861(96)00969-X.

(35) de Paula, G. F.; Netto, G. I.; Mattoso, L. H. C. Physical and Chemical Characterization of Poly(Hexamethylene Biguanide) Hydrochloride. *Polymers (Basel).* **2011**, *3* (2), 928–941. https://doi.org/10.3390/polym3020928.

(36) Chen, Z.; Xia, Y.; Liao, S.; Huang, Y.; Li, Y.; He, Y.; Tong, Z.; Li, B. Thermal Degradation Kinetics Study of Curcumin with Nonlinear Methods. *Food Chem.* **2014**, *155*, 81–86. https://doi.org/10.1016/j.foodchem.2014.01.034.

(37) Higuchi, T. Mechanism of Sustained-action Medication. Theoretical Analysis of Rate of Release of Solid Drugs Dispersed in Solid Matrices. *J. Pharm. Sci.* **1963**, *52* (12), 1145–1149. https://doi.org/10.1002/jps.2600521210.

(38) Wagner, J. G. Interpretation of Percent Dissolved-time Plots Derived from in Vitro Testing of Conventional Tablets and Capsules. *J. Pharm. Sci.* **1969**, *58* (10), 1253–1257. https://doi.org/10.1002/jps.2600581021.

(39) Baker, R. W. *Controlled Release of Biologically Active Agent*; John Wiley & Sons: New York, USA, 1987.

(40) Stoclet, G.; Seguela, R.; Lefebvre, J. M. Morphology, Thermal Behavior and Mechanical Properties of Binary Blends of Compatible Biosourced Polymers: Polylactide/Polyamide11. *Polymer (Guildf).* **2011**, *52* (6), 1417–1425. https://doi.org/10.1016/j.polymer.2011.02.002.

6.2 Biphasic Polylactide/polyamide 6,10 Blends: Influence of Composition on Polyamide Structure and Polyester Crystallization.

6.2.1 Introduction

Nowadays, environmental concerns associated with plastics and the limitation of fossil fuel resources have greatly oriented academic and industrial attention for developing polymer blends from renewable resources. Among the large family of bio-based blends, melt blending polylactide (PLA) with polyamides (PA) has attracted attention in recent years with an intent to counteract the well-known PLA drawbacks.[1–5] Indeed, PA is a good candidate since its exhibits outstanding physical and mechanical properties, excellent processability, and can be derived from biomass. Recently, some authors also extended the concept of developing in situ microfibrillated composites to PLA/PA blends using both conventional industrially scalable melt-processing techniques[6–8] and additive manufacturing process[9] to tailor PLA mechanical properties.

In the melted state, it has been well reported that PLA exhibits a lower melt viscosity and elasticity than PA in the typical shear rate range associated with conventional melt-processing techniques.[1,5,7,10,11] For low PA contents (< 50 wt-%), the well-known inherent immiscibility between polymers coupled with the abovementioned melt properties lead to the creation of coarse droplet-matrix morphologies exhibiting poor interfacial adhesion.[3,5,10] Larger PA contents (≥ 50 wt-%) need to be added in order to change the morphology to a co-continuous one to enhance PLA heat resistance, ductility, and toughness.[2,4,10,12]

However, one of the ongoing challenges remains in the manufacturing of PLA/PA bioblends rich in PLA to take advantage of its renewable resource-based origin and its competitive price as compared to PAs. In this context, detailed studies reported copolymerization[10–15] and the use of nanoparticles[2,3,16]

as an intent to enhance the interfacial adhesion between both polymers and to shift the onset of co-continuity to lower PA contents, respectively. Nevertheless, the use of organic solvents, the excessive reaction times coupled with the occurrence of undesirable reactions (i.e., crosslinking), and the use of nanometric-sized powders reduce the attractiveness of these preparation routes for industrial implementation.

Considering the need for an industrial approach, the modification of the PLA rheological properties through reactive extrusion using a styrene-acrylic multifunctional epoxide reactive agent (referred to as SAmfE) seems to be an approach of choice to provide a solution against the above-mentioned shortcomings.[5,9,10] That is, the initial enhancement of the PLA melt viscosity and elasticity before blending with PA has been reported much more efficient for yielding a finer and more homogeneous PA microstructure with improved interfacial adhesion than one-step reactive processing where all components are introduced simultaneously.[10] Additionally, in this approach, Walha *et al.*[10] also concluded that the unreacted epoxy groups bore by the modified PLA (referred to as PLA_{REx}) are likely to react with the amine chain ends of PA, hence improving the compatibility of PLA_{REx}/PA blends.

Being an environmentally friendly and cost-effective process, the reactive blending of PLA and PA in a two-step process could be a good way to counteract two of the main PLA drawbacks: its poor melt strength and its inherent brittleness.

However, the authors are surprised by the lack of in-depth researches on another major PLA weakness: how effective is the disperse phase of semi-crystalline PA in promoting PLA crystallization? And, if so, is the PA polymorphism affected by the blend formulation? To the best of the author's knowledge, Kakroodi *et al.*[6] reported the only detailed study regarding the enhancement of the PLA crystallization kinetics by in situ PA6 microfibrillation under both atmospheric and high pressures. However, no information is given on the PA crystalline structure. In this context, the present work aims at providing more information regarding the crystallization behavior of immiscible

PLA/PA blends as a function of the PA content. Specifically, PLA_{REx}/ PA610 blends covering the 10-50 wt-% PA610 composition range were manufactured through reactive blending. It is noteworthy that PLA melt properties were initially enhanced by adding 0.6 wt-% of SAmfE prior to PA addition. A two-step reactive process was selected to be able to control initially the enhancement of the PLA melt properties. PA610 was selected for its predominant bio-based content (≥ 60%) and its glass transition temperature similar to that of PLA (T_g ≈ 60ºC). Varying the PA content allows us to generate different blend morphologies. Both, the morphological and crystallization behavior under dynamic and isothermal conditions at atmospheric pressure were studied to evaluate a potential nucleation effect of PA on the crystallization of PLA. Moreover, the influence of the presence of melted PLA phase on the final crystalline structure of the PA was studied.

6.2.2 EXPERIMENTAL SECTION

6.2.2.1 Materials

A commercial PLA grade (Ingeo PLA 4032D, D-lactic content ≈ 2%, MFI (210 °C, 2.16 kg) =6.4 ±0.3 g/10 min, T_m = 168.5 ºC) was supplied by Natureworks LLC (Belgium). SAmfE agent, namely Joncryl-ADR-4400F®, was kindly supplied by BASF (Ludwigshafen, Germany) with an epoxy equivalent weight of 485 $g.mol^{-1}$ and a functionality of about 14. Renewable sourced polyamide 610 was purchased from DuPont (Midland, USA) under the trade name Zytel® RS LC3060 NC010 (T_m = 222ºC). A sterically hindered phenolic primary antioxidant (Irganox 1010) and a hydrolytically stable organo-phosphite secondary antioxidant (Irgafos 168) were kindly supplied by BASF (Barcelona, Spain).

6.2.2.2 Processing and Bioblends Manufacturing

A two-step process was used to manufacture PLA_{REx}/PA blends. Initially, pre-dried PLA was melt compounded with 0.6 wt-% of SAmfE to tailor PLA melt properties, as already described elsewhere.[5,17] The manufactured material,

referred to as PLA_{REx} was water-cooled and pelletized. Since SAmfE is a multifunctional epoxy-functionalized reactive agent, several PLA chains can be chemically bonded to one SAmfE molecule through the reaction between the epoxide groups and the carboxyl or hydroxyl functional end groups of the polyester. However, the architectural modifications achieved are not trivial and would be a mixture of several types of nonuniform structures in molecular weight, in architecture, and in number of branch per macromolecules, as shown in.[17,18]

The obtained pellets were melt blended with PA610 using a Brabender batch mixer (Brabender Plastic-corder W50EHT, Brabender GmbH¬Co., Duisburg, Germany) under a N_2 blanket to manufacture five PLA_{REx}/PA bioblends covering the 10-50 wt-% PA composition range. A screw speed of 50 rpm, a residence time of 12 min, and a barrel temperature of 235 °C were used. Prior to processing, PLA_{REx} and PA were vacuum-dried at 80 °C overnight. Thermal degradations were counteracted by adding 0.5 wt-% of an Irganox 1010-Irgafos 168 blend (1:2 by weight). The nominal PLA_{REx}/PA ratios were 90/10, 80/20, 70/30, 60/40, and 50/50 wt/wt. Plates with a nominal thickness of 0.6 mm were compression molded using a IQAP LAPPL-15 hot plate press. For comparison purposes, PLA_{REx} and PA were manufactured using the same procedure.

6.2.2.3 Morphology Observation of Blends

Scanning electron microscopy (SEM, JEOL, JSM-7001F, Japan) observations were carried out at 2 kV on the cryogenically fractured surface of compression-molded samples. Prior to observations, PLA_{REx} was selectively extracted to highlight the dispersion of the PA phase. Samples were immersed in a water-methanol solution (1:2 by volume) containing 0.025 $mol.L^{-1}$ of NaOH for 7 days at 23°C. After an extensive drying step, samples were sputter-coated with a thin platinum-palladium layer. The weight-average diameter, $\overline{d_w}$, of the near-spherical PA droplet is measured by means of image processing

software (Image J, USA) from a representative surface area of 108 μm², according to the following equation.

$$\overline{d_w} = \frac{\sum n_i d_i^2}{\sum n_i d_i} \quad (1)$$

where *n* is the number of particles having diameter *d*.

6.2.2.4 Differential Scanning Calorimetry (DSC)

A modulated DSC Q2000 instrument (TA Instrument) was used to perform DSC experiments under a dry N_2 atmosphere. Standard aluminum pans were used to seal 5-6 mg of each sample, which were then subjected to a classical heating/cooling/heating procedure from 20 to 250 ºC at 10 ºC·min^{-1}.

From the cooling scans, the degree of crystallinity (X_c) was calculated as follows:

$$X_c(\%) = \frac{\Delta H_c}{\Delta H_m^0 * \varphi} * 100 \quad (2)$$

where ϕ is the weight fraction of the polymer considered and ΔH_m^0 the melting enthalpy for a 100% crystalline PLA (93.6 J·g^{-1})[19] or PA610 (197 J·g^{-1}),[20] respectively.

6.2.2.5 Structural Studies

The real-time variable temperature synchrotron studies were carried out on beamline BL11-NCD-SWEET at ALBA (Cerdanyola del Vallès, Barcelona, Spain) by using a wavelength of 0.100 nm and a WAXD LX255-HS detector from Rayonix. Polymer samples were confined between Kapton films and then held on a Linkam hot stage with temperature control within ± 0.1 °C. WAXD profiles were acquired during heating and cooling runs in time frames of 20 s and rates of 10 °C/min. WAXD diffraction patterns were calibrated by means of a geometrical calibration process of a well-known sample (standard Cr_2O_3). Diffraction profiles were normalized to the beam intensity and corrected considering the empty sample background.

SAXS data were obtained using a 20 bits-single photon counter Dectris Pilatus 3s 1M detector and silver behenate (AgBh) was employed for calibration.

The correlation function and the corresponding parameters were calculated with the CORFUNC program for Fibre Diffraction/Non-Crystalline Diffraction provided by the Collaborative Computational Project 13.

Characteristic lamellar parameters (i.e., long period, L_p, amorphous layer thickness, l_a, and crystalline lamellar thickness, l_c) and crystallinity (i.e., crystallinity within the lamellar stacks, $X_c^{SAXS} = l_c/L_p$) were determined by the normalized one-dimensional correlation function[21], $\gamma(r)$:

$$\gamma(r) = \int_0^\infty q^2 I(q)\cos(qr)dq \; / \; \int_0^\infty q^2 I(q)dq \qquad (3)$$

where $I(q)$ is the intensity at each value of the scattering vector ($q = [4\pi/\lambda] \sin\theta$), r the real space distance, λ the wavelength and θ the Bragg angle.

SAXS data were collected within a limited angular range, with the application of Vonk's model[22] and Porod's law to perform extrapolations to low and high q values. Deconvolution of WAXD peaks was performed using the PeakFit 4.0 program.

6.2.2.6 Optical Microscopy Crystallization Studies

Samples for optical microscopy observations were prepared from small sections of melted films of molded samples. These thin sections were subsequently pressed between two cover slides, inserted in a hot stage, heated 10 degrees above the melting temperature of the PA for 3 min and quickly cooled to the selected isothermal crystallization temperature. A Zeiss Axioscop 40 Pol light polarizing microscope (Carl Zeiss, Göttingen, Germany) was employed to measure the spherulite growth rate. The temperature was controlled with a Linkam temperature control system having a THMS 600 heating and freezing stage connected to an LNP 94 liquid nitrogen cooling system (Linkam Scientific, Tadworth, UK). A Zeiss AxiosCam MRC5 digital camera (Carl Zeiss, Göttingen, Germany) was employed to get micrographs at appropriate time intervals. The sign of spherulite birefringence was determined by inserting a first-order red tint plate between crossed polarizers.

6.2.3 RESULTS AND DISCUSSION

6.2.3.1 Morphologies of PLA/PA Blends

Figure 6.2.1 shows the PA phase morphologies of the cryogenically fractured surface of PLA_{REx}/PA blends after surface etching. For blends in the composition range 90-70 wt-% of PLA_{REx}, the morphology consists of submicronic and near-spherical PA droplets homogeneously dispersed in the PLA_{REx} matrix. As reported in **Figure 6.2.1**, the gradual growth of the weight-average PA droplet diameter was measured as the concentration of the PA phase increases to 30 wt-% due to the well-reported coalescence process between PA domains during melt blending. When the PA content increased to 40 wt-%, both submicronic near-spherical droplets and micronic elliptical PA domains coexisted. Finally, a mixture of co-continuous and submicronic near-spherical particles is observed when the PA content was further increased to 50 wt-%.

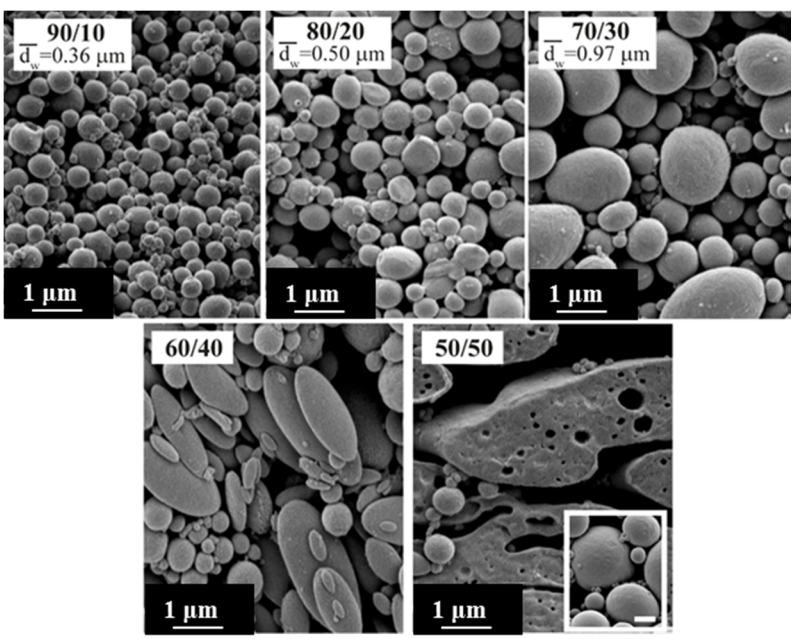

Figure 6.2.1. SEM micrographs of the cryofractured surface of the PLA_{REx}/PA blends after surface etching. The inset in the micrograph 50/50 represents the microstructure obtained for a PLA-based sample with 50 wt-% of PA and manufactured using similar processing conditions.

Considering immiscible polymer systems, it has been well reported that blend composition is one of the major factors governing the final morphology. However, rheological (viscosity and elasticity ratio) and interfacial properties (interfacial tension) between the melted disperse and continuous phases may also greatly influence the morphology evolution.[4,7,23–25] In this context, an unmodified PLA/PA 50/50 wt-% blend was manufactured using the above-described melt processing conditions. The sample was cryogenically fractured; the PLA phase was selectively etched, and the obtained morphology is shown in the inset of **Figure 6.2.1** for comparison purposes. As compared to the PLA_{REx}-based blend, PLA/PA 50/50 wt-% exhibits a coarse drop-matrix morphology. These observations are in line with our previous study[5] and confirm that the initial enhancement of the PLA melt properties through reactive extrusion before blending with PA is a cost-effective and industrially scalable method to shift the onset of co-continuity towards lower PA content in immiscible PLA_{REx}/PA blends.

6.2.3.2 Calorimetric Data on PLA/PA Blends

PLA crystallization remains one of the major PLA drawbacks of its large-scale commercialization. In order to investigate the effectiveness of the PA domains to promote PLA crystallization, the thermal behavior of PLA_{REx}, PA, and their blends were investigated using DSC measurements. The controlled cooling scans at 10 °C·min^{-1} from the melt are shown in **Figure 6.2.2**.

Table 6.2.1 reports the main thermal parameters. From the melt, no crystallization peak was observed in the DSC cooling scan of PLA_{REx}. This behavior was largely expected and ascribed to the slow crystallization kinetics of PLA resin.[26] In contrast, changes in the thermal behavior of the neat matrix was observed when PLA_{REx} was melt blended with PA. That is, irrespective of the blend composition, an exothermic process took place in the range T = 92-98 °C. This transition was ascribed to the crystallization process of the PLA_{REx}, which gradually shifted to slightly higher temperatures with increasing the PA content in the blend. Additionally, a gradual increase in the achievable PLA_{REx}

X_c was recorded for the 60/40 and 50/50 blends (c.f., **Table 6.2.1**). All these observations are in line with previous works and were attributed to the nucleating effect of PA domains, promoting PLA heterogeneous crystallization.[1,27,28]

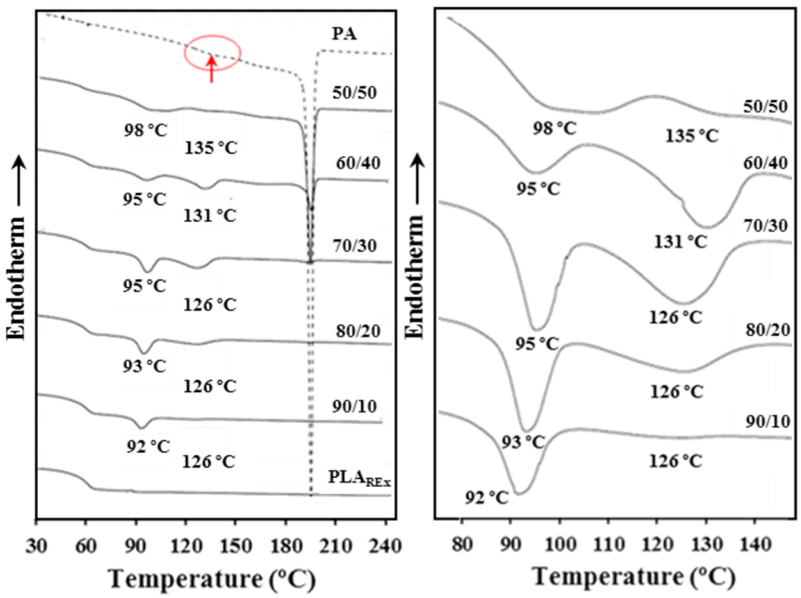

Figure 6.2.2. DSC cooling runs at 10 °C·min^{-1} of PLA$_{REx}$, PA610, and their blends: (**a**) DSC traces over the whole temperature range, (**b**) enlargement of the temperature range 75-150°C for the blends.

In parallel to this nucleating effect, the well-defined PA bulk crystallization around 195 °C experimented with drastic changes when PA610 was melt blended with PLAREx. As can be seen in **Figure 6.2.2**, the PA bulk crystallization was completely suppressed in the 90/10 blend. However, a weak crystallization peak emerged around 126 °C. In **Table 6.2.1**, it can be equally observed that the degree of crystallinity of the PA dispersed phase drastically decreased as compared to the pure PA. Regarding the blends in the PA composition range 20-50 wt-%, the DSC cooling traces show two crystallization events with different degrees of supercooling, *i.e.,* a first crystallization peak centered around the bulk temperature (T_{c1} = 195 °C) and a second peak (T_{c2}) at lowered temperatures (c.f., **Figure 6.2.2** and **Table 6.2.1**). Interestingly, it can

be observed that the relative intensity of the low-temperature peak (T_{c2}) decreased at the expense of the high-temperature peak (T_{c1} = 195 ºC) with increasing the PA content from 30 to 50 wt-%. For the 60/40 and 50/50 blends, X_c of PA is lower than in the pure component (c.f., **Table 6.2.1**), suggesting that the crystallization of PA610 was restrained in the presence of PLA_{Rex}.

Table 6.2.1. Crystallization temperature (T_c) and degree of crystallinity (X_c) determined from the controlled cooling scans.

	Cooling (10 ºC·min^{-1})				
	PLA		PA		
Samples	T_c (ºC)	X_c (%)	T_{c1} (ºC)	T_{c2} (ºC)	X_c (%)
PLA_{REx}	-	0	-	-	-
PA	-	-	195	-	49
90/10	92	4	-	126	2
80/20	93	n/a	194	126	n/a
70/30	95	n/a	194	126	n/a
60/40	95	5	195	131	25
50/50	98	12	194	135	44

n/a: not available because the crystallization process of both polymers overlaps.

In this context, the crystallization features can be correlated with the blend morphology displayed in **Figure 6.2.1**. When the PA exhibits a co-continuous structure (i.e., 50/50) or a coarse and poorly distributed morphology (i.e., 60/40), most of the PA domains crystallize around the bulk temperature (T_{c1} = 195ºC). However, when a larger content of smaller and more homogeneously dispersed PA droplets are obtained (70/30, 80/20, and 90/10 blends), the bulk crystallization is almost suppressed and a larger fraction crystallizes at lower temperatures.

A depression in the PA crystallization temperature has already been reported in immiscible polymer blends with dispersed submicronic PA6 or PA11 droplets and was ascribed to the so-called fractionated crystallization phenomenon in the confined domains.[1,29–32] That is, crystallization of semi-crystalline polymers commonly occurs through heterogeneous nucleating impurities, acting as substrates for nucleation. Nevertheless, when a semi-crystalline polymer is highly dispersed in a large fraction of submicronic droplets, an increasing probability of obtaining heterogeneity-free droplets is

expected. This lack of active nuclei within the impurity-free droplets obliges the polymer chains to nucleate on their own, inducing a transition from heterogeneous to homogeneous nucleation. A higher degree of supercooling is therefore needed to allow macromolecular chains to self-nucleate, hence shifting crystallization to lower temperatures. In the present case, since PA droplets are dispersed in a non-nucleating viscoelastic medium, the crystallization peak at low temperatures is likely to be related to the homogeneous nucleation of PA610 droplets wherein all heterogeneities have been excluded. Nonetheless, all the blends exhibit the characteristic thermal behavior of immiscible blends and the fractioned PA crystallization process corroborated the submicronic PA droplet morphology previously observed in the 90/10, 80/20, and 70/30 blends.

6.2.3.3 PA610 Crystalline Structures

The confined crystallization phenomena in immiscible polymer blends with dispersed submicrometric PA droplets has been largely reported, nonetheless, information regarding the PA polymorphism developed in such process are scarce. Accordingly, dynamic measurements during cooling from the melt state were performed and for the sake of completeness subsequent heating run was in some cases recorded.

In general, the structure of commercial aliphatic polyamides is based on the stack of sheets composed of hydrogen-bonded molecular chains with practically all trans molecular conformation.[33,34] At room temperature the corresponding X-ray fiber diffraction pattern of such crystalline structure (i.e., the so-named α-form) is characterized by the presence of two strong equatorial reflections associated with intrasheet and intersheet spacings (near 0.440 and 0.380 nm, respectively). Chains with a high number of methylene groups can also crystallize according to a pseudohexagonal packing (defined by one or two close equatorial reflections in the 0.420–0.400 nm range).[35] In this case, hydrogen bonds seem to be also established along a single direction that becomes outside the sheet, a plane defined by the methylene groups (i.e., amide

groups rotate approximately 60º and form intersheet bonds, analogous with the previously described structure). Thermal induced structural transitions are also a common characteristic of PAs and thus the two intense reflections of the α-form gradually merge into a single peak indicative of a new pseudohexagonal arrangement at the named Brill temperature. This transition seems reversible but shows a hysteresis effect since it usually takes place at a lower temperature during cooling. Understanding of Brill transition is problematic and different interpretations have been postulated.[36–39] These consider increased mobility of methylene groups that lead to a pseudohexagonal packing or the disruption of the initial hydrogen bonds pattern to form new interactions randomly distributed along with three planar directions at 120°. Polymorphic forms have a great influence on mechanical properties, with the γ-form being generally accepted as more ductile than the α-form, while this leads to both a higher Young modulus and a higher tensile strength as reported for nylon 6.[40,41]

Figure 6.2.3a shows the WAXD patterns of pure nylon 6,10 during a cooling run (10 ºC/min) from the melt state. The three-dimensional profiles showed that the sample started to crystallize in a pseudohexagonal form (q = 14.6 nm^{-1} and d = 0.430 nm) at a temperature of 195. ºC, but then a typical Brill transition can be detected in such a way that the two typical reflections of an α-form were found at room temperature (d = 0.376 and 0.442 nm). It should be pointed out that a very small reflection at d = 0.410 nm appeared when the temperature was close to 140 ºC. Calorimetric data showed also a very small exothermic peak around this temperature (see red ellipsoid and arrow in **Figure 6.2.2a**), which may be associated with the formation of γ-form structure, although it is remarkable that this kind of calorimetric evidence has never been described for nylon 6 10.

The subsequent heating of the melt crystallized sample (**Figure 6.2.3b**) showed the disappearance of the minority phase and the merge of the two α-phase reflections to a new pseudohexagonal form at a similar temperature determined in the previous crystallization run.

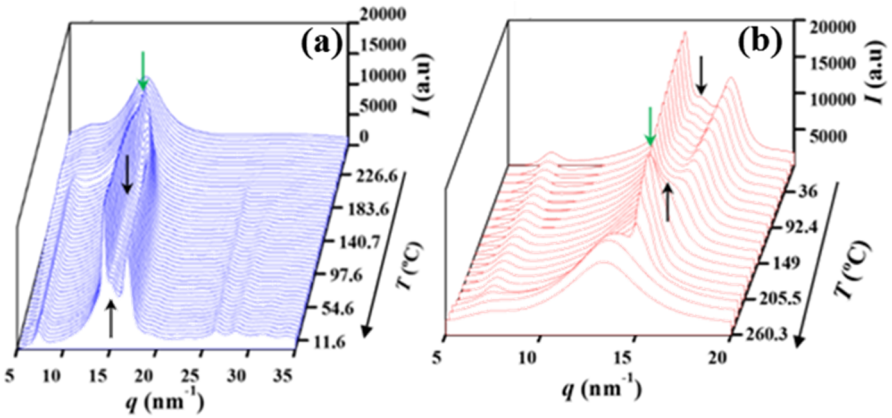

Figure 6.2.3. Three-dimensional representation of WAXD profiles of a PA610 sample cooled from the melt (**a**) and subsequently heated (**b**). Black arrows indicate the presence of a small reflection indicative of pseudohexagonal structure that appeared or disappeared around 160-120 ºC. Green arrows pointed out the pseudohexagonal Brill structure that is achieved at high temperatures in both cooling and heating runs.

PA610 polymorphism was previously described by Ramesh[42] through conventional X-ray diffraction patterns taken with samples crystallized at selected specific temperatures and submitted to cooling runs. The given results demonstrated that nylon 6,10 crystallized according to a typical α form or a not fully understood pseudohexagonal form by slow and fast cooling from the melt state, respectively. Ramesh also reported that the crystalline structure obtained by isothermal crystallization from the melt state was dependent on the selected temperature.[42] Thus, PA610 crystallized at temperatures below 160 ºC in a pseudohexagonal form that progressively derived to an α-form on cooling following the named Brill transition. However, at higher temperatures (e.g., 210 ºC), nylon 6,10 crystallized according to a high-temperature α-form (i.e., two relatively close spacings around 0.429 and 0.415 nm). When this sample was cooled rendered the typical low-temperature α-form together with a minority phase (small peak around 0.425-0.412 nm), which was not associated with the γ-form. Jones *et al.*[43] also reported the existence of the hexagonal γ-phase along with the triclinic α phase in sedimented mats of solution-grown single crystals of PA610.

Cooling runs of PLA_{REx}/PA 50:50 blend showed a crystallization in the Brill pseudohexagonal form and then the transition towards the α-form (**Figure 6.2.4a**). More significant is the reflection associated with the γ-form, which appeared at a temperature close to 160 ºC. The relative intensity of this peak with respect to those associated with the α-form increased clearly and supported the weak evidence detected for the pure PA. At temperatures close to 100 ºC characteristic reflections of the α-form of polylactide appeared with a surprisingly high intensity since it is well known the difficulty of PLA to crystallize from the melt state. Specifically, reflections at 0.540 and 0.473 nm, which correspond to the (200) + (110) and (203) reflections of the α-form of polylactide were observed.[44,45]

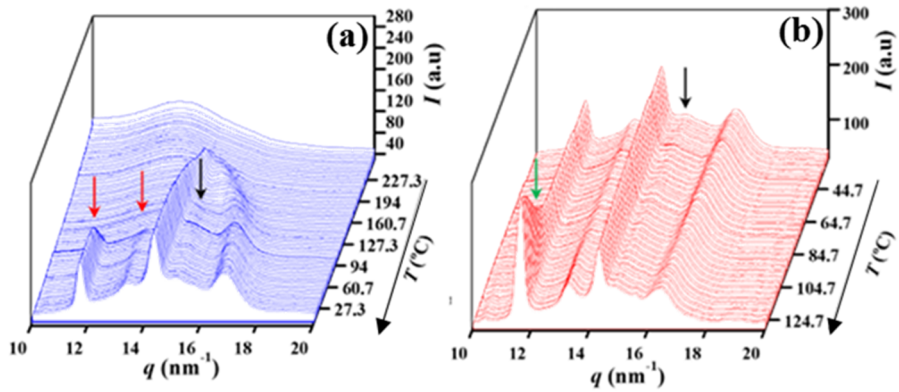

Figure 6.2.4. Three-dimensional representation of WAXD profiles of the PLA/PA 50:50 cooled blend from the melt (**a**) and subsequently heated (**b**). Black arrows indicate the presence of the minority γ-form structure and red arrows the reflections associated with PLA. Note the increase of the most intense PLA reflection during the heating run due to the cold crystallization process (green arrow).

The increase in the PLA_{REx} content in the blends led to a decrease in the capacity of PA to crystallize at high temperature, but not hindered the crystallization of the γ-form that took place again at 160 ºC (e.g., **Figure 6.2.5a** for the 60:40 blend). Three features should be highlighted: (a) Only the pseudohexagonal Brill structure developed at high temperature could be transformed into the α-form on cooling. Despite the low-temperature γ-form displayed a similar pseudohexagonal arrangement of molecular chains than this

structure, the disposition of hydrogen bonds should be highly different making unfeasible a concerted process of breaking and reforming the hydrogen bonding interactions. Note that these interactions should be established between different chains in the γ- and the α-forms (i.e., intersheet and intrasheet interactions as previously indicated). On this basis, the Brill structure may correspond to well-formed hydrogen bonds between chains that on cooling will constitute the final sheets. This cooling process should involve the ordering of methylene groups and the contraction of the intersheet parameter (i.e., where hydrogen bonds were not established). In this sense, note the high variation of the low-intensity reflection that changed from 0.430 to 0.481 nm. (b) The exothermic DSC peak observed around 126 ºC can unambiguously be associated with the development of the γ-form. (c) The ratio between γ-form and the α-form appears maximum for a blend composition around 70:30 as can be observed from both DSC and synchrotron data (not shown). (d) The intensity of PLA peaks decreased as the ratio of PA in the blend diminished, a feature that indicates an enhancement of PLA_{REx} crystallization caused by the presence of PA. Note in **Figure 6.2.6a** that the sample became practically amorphous after cooling, being envisaged some minor peaks associated with PLA and both forms of PA.

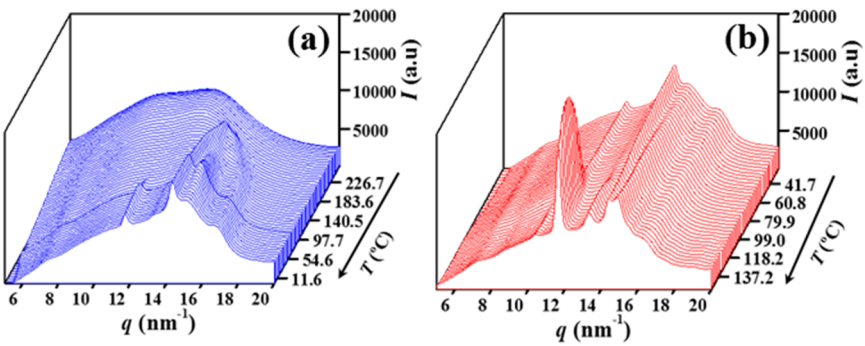

Figure 6.2.5. Three-dimensional representation of WAXD profiles of the PLA_{REx}/PA 60:40 blend cooled from the melt (**a**) and subsequently heated (**b**).

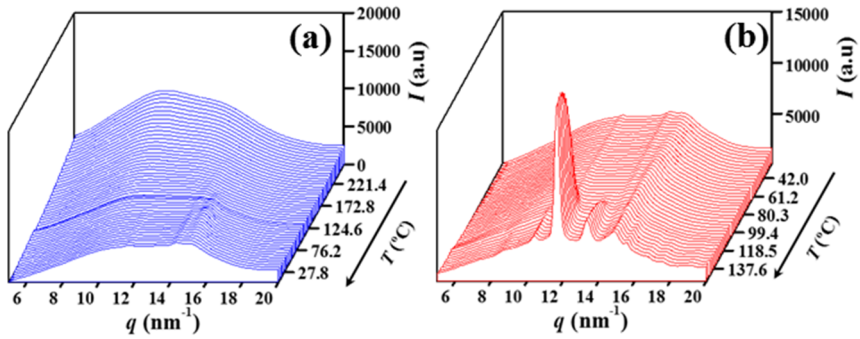

Figure 6.2.6. Three-dimensional representation of WAXD profiles of the PLA_{REx}/PA 80:20 blend cooled from the melt (**a**) and subsequently heated (**b**).

Heating runs of melt crystallized samples clearly showed the cold crystallization process of PLA, which was more significant when the PA content in the blend decreased as can be deduced from the comparison of **Figures 6.2.4b**, **6.2.5b**, and **6.2.6b**. This point agrees with the lower crystallization of PLA_{REx} during the previous cooling, which is a consequence of the decrease of effective PA nuclei. **Figures 6.2.5b** and **6.2.6b** showed also that the intensity of the PA α-form reflections (note especially that around 0.440 nm) decreased during heating. This is an unexpected feature that could be related to the decrease of the PLA_{REx} amorphous halo and that lead to highlight the presence of the γ-form reflection, which intensity remained practically constant.

Experimental evidence indicated that PA influences the crystallization process of PLA_{REx} by facilitating its crystallization. Nevertheless, the crystallization of PA was hindered by the presence of PLA_{REx}, indicating that PA and PLA_{REx} developed separated crystalline phases. SAXS data showed well-differentiated lamellar morphologies associated with each crystalline phase and optical microscopy observation allowed distinguishing the spherulites related to each polymer.

Figure 6.2.7a shows the SAXS profiles of the 50:50 blend taken during the heating process of a melt crystallized sample. It is clear that at the beginning, only a very broad peak corresponding to PA (q = 0.74 nm^{-1}) could be detected and no traces of the presence of PLA could be distinguished despite its high content of nuclei. However, a new peak appeared (named as the first peak attending its lower value q = 0.33 nm^{-1}) at a temperature close to 90ºC, which means that cold crystallization of PLA_{REx} rendered well-differentiated lamellae. The profile obtained before the beginning of the melting process is shown in **Figure 6.2.7b**. This could be effectively deconvoluted in two peaks and consequently, morphological features of PLA_{REx} and PA lamellae were determined.

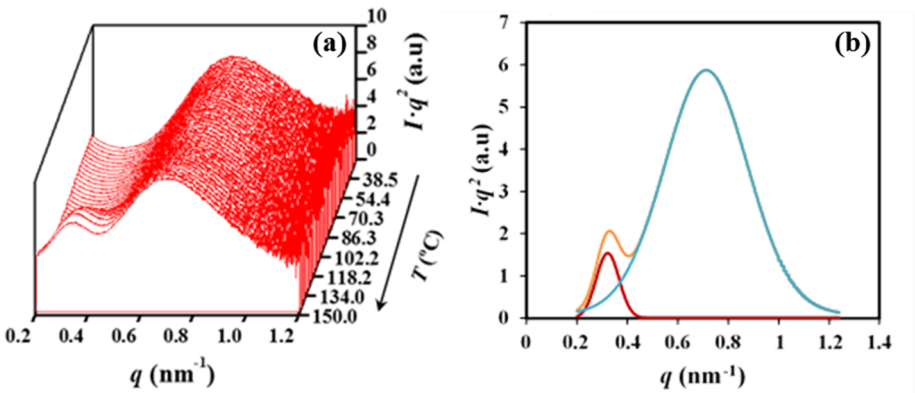

Figure 6.2.7. (**a**) Three-dimensional representation of SAXS profiles of the PLA_{REx}/PA 50:50 blend during the heating process of the melt crystallized sample. (**b**) Deconvolution of the profile obtained after finishing the cold crystallization process of PLA_{REx}.

The selected profile changed drastically according to the blend composition as shown in **Figure 6.2.8a** for the 80:20 blend where the PLA peak became predominant. **Figure 6.2.8b** shows representative correlation functions that reveal the following features: (a) Both PLA_{REx} and PA phases have great electronic contrast between amorphous and crystalline regions, as can be deduced from the well-defined peaks that extend over more than two orders in the correlation function. (b) PA lamellae are thinner than PLA_{REx}

despite that are formed at a significantly lower temperature. Probably, PAs have significant hydrogen bond restrictions that impose a defined lamellar core and folding surface geometry as discussed in detail by Dreyfuss *et al.*.[46] Specifically, for the 50:50 blend, L_p, l_c and l_a values of 8.40, 5.56 and 2.84 nm were determined from the second peak and values of 18.60, 10.82 and 7.78 nm were evaluated from the first peak, respectively. (c) During heating the PA peak becomes slightly narrower and the contrast between amorphous and crystalline regions increased, as well as, the lamellar parameters involving the amorphous layer (i.e., L_p, l_c and l_a values of 7.30, 5.61 and 1.69 nm were determined for the first profile of the 50:50 blend). (d) The PLA lamellar parameters after finishing the cold crystallization process were practically independent on the blend composition (i.e., L_p, l_c, and l_a values of 17.10, 8.72, and 8.38 nm were determined for the first peak of the 80:20 blend).

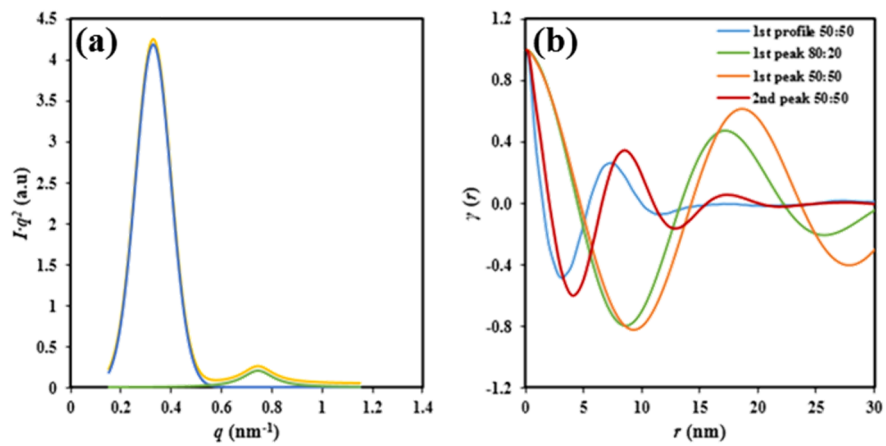

Figure 6.2.8. (**a**) Deconvolution of the SAXS profile obtained after finishing the PLA cold crystallization process of the PLA_{REx}/PA 80:20 blend. (**b**) Representative correlation functions obtained during heating the PLA_{Rex}/PA 50:50 blend that correspond to the first profile (light blue) and the two deconvoluted peaks of the profile obtained after PLA_{REx} cold crystallization (orange and garnet for the first and second peak, respectively). For the sake of completeness, the correlation function of the first deconvoluted peak after PLA cold crystallization is showed (green) for the PLA_{Rex}/PA 80:20 blend.

6.2.3.4 Effect of PA on PLA$_{REx}$ Crystallization

Optical microscopy observations of crystallization assays performed with thin PLA$_{REx}$ films rendered amorphous samples when melted samples were cooled at reasonable rates (e.g., greater than 0.5 ºC/min), as presumable from DSC scans. Nevertheless, the polymer could be isothermally crystallized at different temperatures allowing us to analyze the morphology of the derived spherulites. These could achieve a relatively high size (i.e., diameter close to 360 μm) at 145 ºC, which represents a low supercooling degree (26 ºC since the melting peak of PLA$_{REx}$ was 171 ºC.[5] The size was logically reduced when temperature decreased, and a drastic reduction was observed at 130 ºC (i.e., diameter close to 50 μm). Both induction time and crystallization time up to impingement increased with temperature (e.g., 9 min and 32 min for 130 ºC and 18 min and 173 min for 145 ºC). Therefore, a crystallization temperature of 145 ºC was selected as ideal considering both size and time to evaluate morphology and get the corresponding kinetic data.

Figure 6.2.9a shows a typical PLA$_{REx}$ spherulite obtained at 145 ºC. The birefringence sign is negative and a fine texture which suggests a fibrillar morphology, although an incipient banding could be envisaged (see white arrows). Banded spherulites have usually been explained because of a periodic twisting of crystalline lamellae along the radial growth direction.[47,48] This twisting was postulated to be a consequence of unbalanced surface stresses, which were for example characteristic of chiral polymers like polylactide.[49] The band spacing, which corresponds to the half-pitch of the twisted lamellae, depends on the crystallization temperature since it increases at lower supercooling, probably to a decrease of the unbalanced surface stress and also of the increased lamellar thickness that makes difficult the cooperative twisting of lamellae.

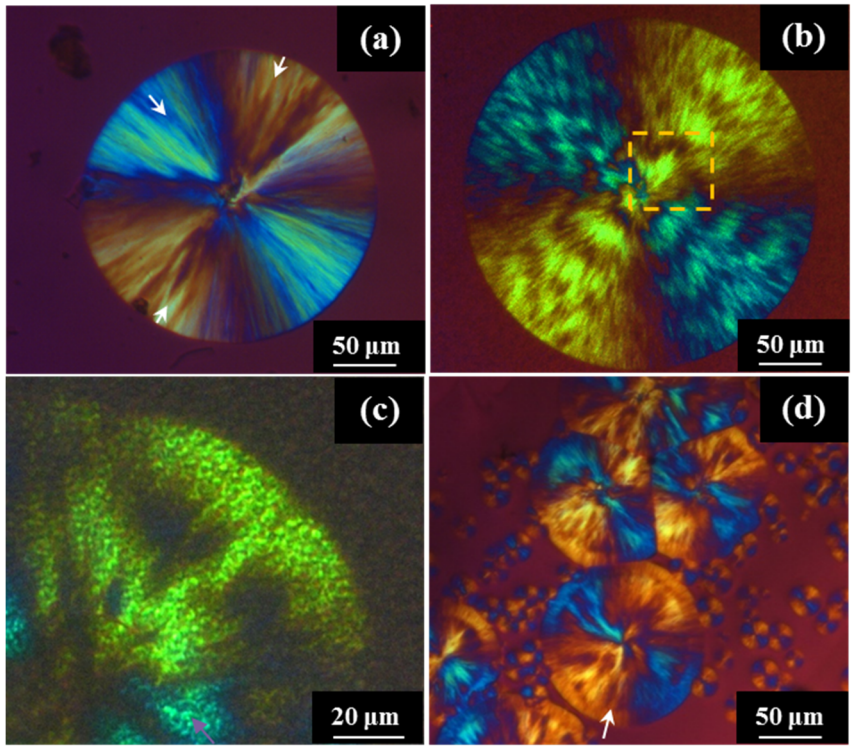

Figure 6.2.9. (**a**) PLA_{REx} and (**b**, **c**) PLA_{REx}/PA 70:30 spherulites isothermally crystallized from the melt at 145 ºC. A magnification of the orange dashed rectangle is displayed in (**c**) in order to reveal the granular texture caused by the presence of small PA spherulites (in this case micrograph was taken before finishing the crystallization). (**d**) Spherulites were obtained from a melted PLA_{REx}/PA 70:30 sample after two isothermal crystallization performed first at 145 ºC and then at 130 ºC. At this last temperature, new smaller spherulites with a different texture to those previously grown appeared (see white arrow).

Polymer blends rendered also negatively birefringent spherulites by isothermal crystallization from the melt, as shown in **Figure 6.2.9b** for the 50:50 blend crystallization performed at 145 ºC. Two features should be pointed out: (a) The banding texture becomes highlighted, and (b) The spherulites have a granular texture since they encompass the previously formed PA spherulites (**Figure 6.2.9c**). PA crystallization took non-isothermally place during the cooling run from the melt to the selected temperature. The corresponding spherulites were very small (diameter less than 30 µm) even if higher temperature isothermal crystallization was assayed. **Figure 6.2.10** reveals the

presence of these PA spherulites when the crystallized sample is heated up to 200 ºC (around 30 degrees above the PLA_{REX} melting temperature) after be cooled to room temperature.

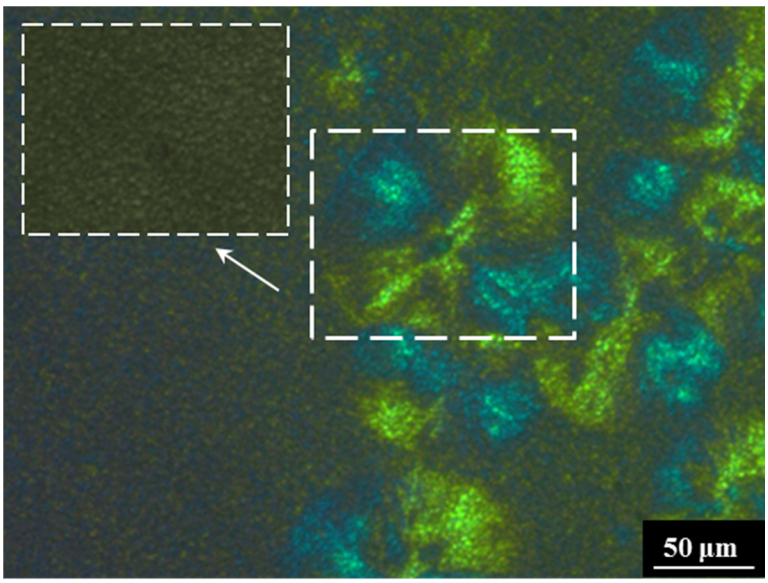

Figure 6.2.10. Spherulites of PLA_{REx}/PA 70:30 isothermally crystallized from the melt at 145 ºC for 42 min and then cooled to room temperature. Insert corresponds to an optical micrograph taken after heating again the sample up to 200 ºC.

The observed banding in the spherulites of PLA_{REx}/PA blends may be a consequence of a small change in the degree of supercooling since DSC data (**Figure 6.2.2**) indicated that PLA crystallization started at a lower supercooling when the PA content increased (e.g., peaks at 98 and 92 ºC for the 50:50 and 90:10 blends). This interpretation appears problematic since a greater band spacing should be expected for the blend with high PA content. Note also the different texture of spherulites (**Figure 6.2.9d**) when crystallization temperature decreased to 130 ºC. The two-step experiment showed a morphological change towards a fibrillar texture exempted of banding evidence in the spherulites grown at 130 ºC concerning those previously crystallized at 145 ºC

Nevertheless, the most significant influence may be derived from the specific presence of PA in the forming spherulites. It has been reported[50,51] that

blending has a high repercussion in the band spacing. Specifically, the increase in the ratio of a second immiscible polymer may increase the unbalanced surface stress on the crystalline lamellae as a consequence of its molecular absorption on the crystal boundaries, and lead to an enhancement of the lamellar twisting frequency.

The next point to be elucidated concerns the influence of the presence of PA on the crystal growth rate and nucleation of PLA_{REx}. To this end, the blend with higher PA content was considered. **Figure 6.2.11** compares the linear evolution of the spherulite radius with the crystallization time for the 50:50 blend and the pure PLA_{REx} sample at a common temperature of 145 ºC. Hardly any differences were observed in the PLA samples and the blend regarding the nucleation time and the crystallization time until the collapse of the spherulites.

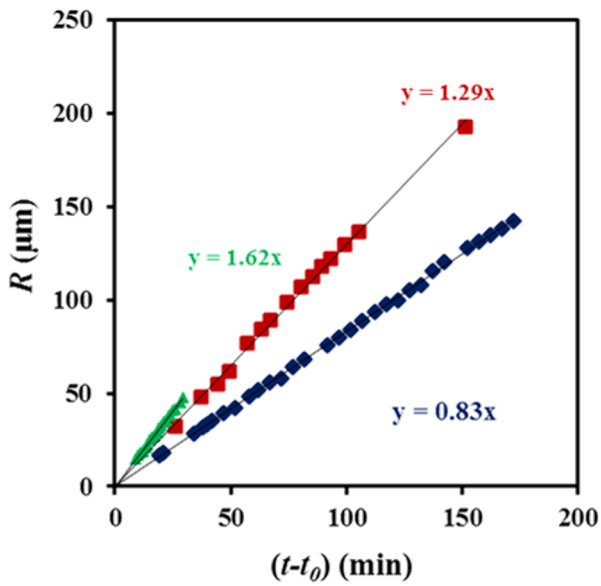

Figure 6.2.11. Variation of the spherulitic radius versus crystallization time after the induction period (t_0) for PLA_{REx} crystallized at 130ºC (▲) and 145 ºC (♦) and PLA_{REx}/PA 70:30 crystallized at 145 ºC (■).

A great difference between the corresponding slopes (i.e., growth rates of 1.29 and 0.83 μm/min) was found, suggesting a higher growth rate for the blended sample. Nevertheless, cautions should be taken into account since the

available space for a growing spherulite in the blended sample is lower due to the presence of previously crystallized PA spherulites. Note that according to the densities of PLA and PA610 (i.e., 1.25 and 1.04 g/mL), the real volume occupied by PLA inside an already grown spherulite should be the global volume divided by 2.2 (i.e., 1+ (1.25/1.04)) if PA is assumed to be incorporated inside. This means that the real ratio corresponding to PLA should be the measured ratio divided by $2.2^{1/3}$. This rough approximation leads to a growth rate of 0.99 μm/min, which is still greater than that determined for pure $PLA_{REx.}$ Figure 5.2.11 also showed the increase of the PLA_{REx} spherulite growth rate when temperatures decreased to 130 ºC (i.e., 1.62 μm/min with respect to 0.83 μm/min).

Figure 6.2.12 shows representative optical micrographs taken during isothermal crystallization at 145 ºC of pure PLA_{REx} and the PLA_{REx}/PA 70:30 blend. Some points can be deduced: (a) Both samples followed practically athermal nucleation since the number of nuclei appears to be constant or slightly increased. Note that only a limited number of new nuclei can be distinguished in the blend (see orange arrows), (b) The size of spherulites is greater for the blend at a similar crystallization time (e.g., Figures 5.2.12c and 5.2.12f for 30-33 min), (c) The density of nuclei is lower for the blend (i.e., 270 nuclei/mm^2 with respect to 50 nuclei/mm^2).

A nucleating effect caused by the previously formed PA spherulites can therefore be discarded and even an antinucleant effect could be deduced. The increase in the crystallization rate of the blend samples can therefore only be associated with a surprising increase of the crystal growth rate which is probably derived from the influence of newly created interfaces. Note that their repercussion on the lamellar twisting has also been observed.

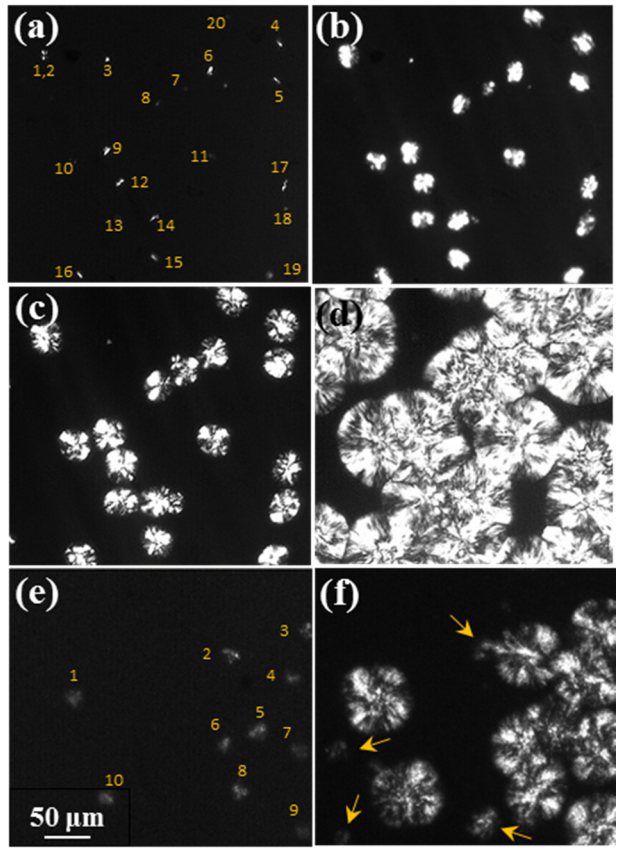

Figure 6.2.12. PLA_{REx} spherulites crystallized at 145 ºC for (**a**) 10 min, (**b**) 20 min, (**c**) 30 min and (**d**) 80 min. PLA_{REx}/PA 70:30 spherulites crystallized from the melt at 145 ºC for (**e**) 12 min and (**f**) 33 min. Yellow arrows point out new spherulites that in each case are appearing as a consequence of thermal nucleation.

6.2.4 CONCLUSIONS

The modification of the PLA melt properties through reactive extrusion prior to mixing with PA allowed to achieve a co-continuous morphology at lower PA content as compared to unmodified PLA/PA blends. The performed studies with blends of PLA_{REx} and PA610 revealed the following meaningful points: (a) Continuity between immiscible phases was detected even at a lower PA content, in contrast with the results attained when non-modified PLA was employed; (b) Confinement of PA610 droplets inside the PLA_{REx} phase hindered the crystallization of the polyamide. This was possible when at a high supercooling degree, a pseudohexagonal γ-form rendered, which was hardly detected in the melt crystallization studies of the pure polyamide; (c) Crystalline lamellae developed in each phase has differentiated morphological parameters and specifically, the polyamide developed thinner crystals probably as a consequence of hydrogen bonding restriction; (d) Amorphous PA chains could interact with the crystalline PLA_{REx} interfaces giving rise to an enhanced lamellar twisting and even an increase of the crystal growth rate, and (e) PA610 lead to an antinucleant effect on the crystallization of PLA_{REx}.

6.2.5 REFERENCES

(1) Stoclet, G.; Seguela, R.; Lefebvre, J. M. Morphology, Thermal Behavior and Mechanical Properties of Binary Blends of Compatible Biosourced Polymers: Polylactide/Polyamide11. *Polymer (Guildf).* **2011**, *52* (6), 1417–1425. https://doi.org/10.1016/j.polymer.2011.02.002.

(2) Nuzzo, A.; Coiai, S.; Carroccio, S. C.; Dintcheva, N. T.; Gambarotti, C.; Filippone, G. Heat-Resistant Fully Bio-Based Nanocomposite Blends Based on Poly(Lactic Acid). *Macromol. Mater. Eng.* **2014**, *299* (1), 31–40. https://doi.org/10.1002/mame.201300051.

(3) Rashmi, B. J.; Prashantha, K.; Lacrampe, M. F.; Krawczak, P. Toughening of Poly(Lactic Acid) without Sacrificing Stiffness and Strength by Melt-Blending with Polyamide 11 and Selective Localization of Halloysite Nanotubes. *Express Polym. Lett.* **2015**, *9* (8), 721–735. https://doi.org/10.3144/expresspolymlett.2015.67.

(4) Heshmati, V.; Zolali, A. M.; Favis, B. D. Morphology Development in Poly (Lactic Acid)/Polyamide11 Biobased Blends: Chain Mobility and Interfacial Interactions. *Polymer (Guildf).* **2017**, *120*, 197–208. https://doi.org/10.1016/j.polymer.2017.05.056.

(5) Cailloux, J.; Abt, T.; García-Masabet, V.; Santana, O.; Sánchez-Soto, M.; Carrasco, F.; Maspoch, M. L. Effect of the Viscosity Ratio on the PLA/PA10.10 Bioblends Morphology and Mechanical Properties. *Express Polym. Lett.* **2018**, *12* (6), 569–582. https://doi.org/10.3144/expresspolymlett.2018.47.

(6) Kakroodi, A. R.; Kazemi, Y.; Nofar, M.; Park, C. B. Tailoring Poly(Lactic Acid) for Packaging Applications via the Production of Fully Bio-Based in Situ Microfibrillar Composite Films. *Chem. Eng. J.* **2017**, *308*, 772–782. https://doi.org/10.1016/j.cej.2016.09.130.

(7) Yousfi, M.; Dadouche, T.; Chomat, D.; Samuel, C.; Soulestin, J.; Lacrampe, M. F.; Krawczak, P. Development of Nanofibrillar Morphologies in Poly(l-Lactide)/Poly(Amide) Blends: Role of the Matrix Elasticity and Identification of the Critical Shear Rate for the Nodular/Fibrillar Transition. *RSC Adv.* **2018**, *8* (39), 22023–22041. https://doi.org/10.1039/c8ra03339k.

(8) García-Masabet, V.; Pérez, O. S.; Cailloux, J.; Abt, T.; Sánchez-Soto, M.; Carrasco, F.; Maspoch, M. L. PLA/PA Bio-Blends: Induced Morphology by Extrusion. *Polymers (Basel).* **2020**, *12* (1), 1–23. https://doi.org/10.3390/polym12010010.

(9) Rasselet, D.; Caro-Bretelle, A. S.; Taguet, A.; Lopez-Cuesta, J. M. Reactive Compatibilization of PLA/PA11 Blends and Their Application in Additive Manufacturing. *Materials (Basel).* **2019**, *12* (3). https://doi.org/10.3390/ma12030485.

(10) Walha, F.; Lamnawar, K.; Maazouz, A.; Jaziri, M. Rheological, Morphological and Mechanical Studies of Sustainably Sourced Polymer Blends Based on Poly(Lactic Acid) and Polyamide 11. *Polymers (Basel).* **2016**, *8* (3). https://doi.org/10.3390/polym8030061.

(11) Gug, J. I.; Sobkowicz, M. J. Improvement of the Mechanical Behavior of Bioplastic Poly(Lactic Acid)/Polyamide Blends by Reactive Compatibilization. *J. Appl. Polym. Sci.* **2016**, *133* (45), 1–12. https://doi.org/10.1002/app.43350.

(12) Patel, R.; Ruehle, D. A.; Dorgan, J. R.; Halley, P.; Martin, D. Biorenewable Blends of Polyamide-11 and Polylactide. *Polym. Eng. Sci.* **2013**, 1–10. https://doi.org/10.1002/pen.

(13) Pai, F. C.; Lai, S. M.; Chu, H. H. Characterization and Properties of Reactive Poly(Lactic Acid)/Polyamide 610 Biomass Blends. *J. Appl. Polym. Sci.* **2013**, *130* (4), 2563–2571. https://doi.org/10.1002/app.39473.

(14) Dong, W.; Cao, X.; Li, Y. High-Performance Biosourced Poly(Lactic Acid)/Polyamide 11 Blends with Controlled Salami Structure. *Polym. Int.* **2014**, *63* (6), 1094–1100. https://doi.org/10.1002/pi.4618.

(15) Zolali, A. M.; Favis, B. D. Compatibilization and Toughening of Co-Continuous Ternary Blends via Partially Wet Droplets at the Interface. *Polymer (Guildf).* **2017**, *114*, 277–288. https://doi.org/10.1016/j.polymer.2017.02.093.

(16) Nuzzo, A.; Bilotti, E.; Peijs, T.; Acierno, D.; Filippone, G. Nanoparticle-Induced Co-Continuity in Immiscible Polymer Blends - A Comparative Study on Bio-Based PLA-PA11 Blends Filled with Organoclay, Sepiolite, and Carbon Nanotubes. *Polymer (Guildf).* **2014**, *55* (19), 4908–4919. https://doi.org/10.1016/j.polymer.2014.07.036.

(17) Cailloux, J.; Santana, O. O.; Maspoch, M. L.; Bou, J. J.; Carrasco, F. Using Viscoelastic Properties to Quantitatively Estimate the Amount of Modified Poly(Lactic Acid) Chains through Reactive Extrusion. *J. Rheol. (N. Y. N. Y).* **2015**, *59* (5), 1191–1227. https://doi.org/10.1122/1.4928071.

(18) Cailloux, J.; Santana, O. O.; Franco-Urquiza, E.; Bou, J. J.; Carrasco, F.; Gámez-Pérez, J.; Maspoch, M. L. Sheets of Branched Poly(Lactic Acid) Obtained by One Step Reactive Extrusion Calendering Process: Melt Rheology Analysis. *Express Polym. Lett.* **2013**, *7* (3), 304–318. https://doi.org/10.3144/expresspolymlett.2013.27.

(19) Cailloux, J.; Raquez, J. M.; Lo Re, G.; Santana, O.; Bonnaud, L.; Dubois, P.; Maspoch, M. L. Melt-Processing of Cellulose Nanofibril/Polylactide Bionanocomposites via a Sustainable Polyethylene Glycol-Based Carrier System. *Carbohydr. Polym.* **2019**, *224* (May), 115188. https://doi.org/10.1016/j.carbpol.2019.115188.

(20) Elzein, T.; Brogly, M.; Schultz, J. Crystallinity Measurements of Polyamides Adsorbed as Thin Films. *Polymer (Guildf).* **2002**, *43* (17), 4811–4822. https://doi.org/10.1016/S0032-3861(02)00239-2.

(21) Vonk, C. G.; Kortleve, G. X-Ray Small-Angle Scattering of Bulk Polyethylene - II. Analyses of the Scattering Curve. *Kolloid-Zeitschrift Zeitschrift für Polym.* **1967**, *220* (1), 19–24. https://doi.org/10.1007/BF02086052.

(22) Vonk, C. G. A General Computer Program for the Processing of Small-

Angle X-Ray Scattering Data. *J. Appl. Crystallogr.* **1975**, *8*, 340–341.

(23) Lee, J. K.; Han, C. D. Evolution of Polymer Blend Morphology during Compounding in an Internal Mixer. *Polymer (Guildf).* **1999**, *40* (23), 6277–6296. https://doi.org/10.1016/S0032-3861(99)00022-1.

(24) Burch, H. E.; Scott, C. E. Effect of Viscosity Ratio on Structure Evolution in Miscible Polymer Blends. *Polymer (Guildf).* **2001**, *42* (17), 7313–7325. https://doi.org/10.1016/S0032-3861(01)00240-3.

(25) Jana, S. C.; Sau, M. Effects of Viscosity Ratio and Composition on Development of Morphology in Chaotic Mixing of Polymers. *Polymer (Guildf).* **2004**, *45* (5), 1665–1678. https://doi.org/10.1016/j.polymer.2003.12.047.

(26) Hakim, R. H.; Cailloux, J.; Santana, O. O.; Bou, J.; Sánchez-Soto, M.; Odent, J.; Raquez, J. M.; Dubois, P.; Carrasco, F.; Maspoch, M. L. PLA/SiO2 Composites: Influence of the Filler Modifications on the Morphology, Crystallization Behavior, and Mechanical Properties. *J. Appl. Polym. Sci.* **2017**, *134* (40), 9–11. https://doi.org/10.1002/app.45367.

(27) Kakroodi, A. R.; Kazemi, Y.; Ding, W. D.; Ameli, A.; Park, C. B. Poly(Lactic Acid)-Based in Situ Microfibrillar Composites with Enhanced Crystallization Kinetics, Mechanical Properties, Rheological Behavior, and Foaming Ability. *Biomacromolecules* **2015**, *16* (12), 3925–3935. https://doi.org/10.1021/acs.biomac.5b01253.

(28) Retolaza, A.; Eguiazábal, J. I.; Nazábal, J. Structure and Mechanical Properties of Polyamide-6,6/Poly(Ethylene Terephthalate) Blends. *Polym. Eng. Sci.* **2004**, *44* (8), 1405–1413. https://doi.org/10.1002/pen.20136.

(29) Tol, R. T.; Mathot, V. B. F.; Groeninckx, G. Confined Crystallization Phenomena in Immiscible Polymer Blends with Dispersed Micro- and Nanometer Sized PA6 Droplets, Part 2: Reactively Compatibilized PS/PA6 and (PPE/PS)/PA6 Blends. *Polymer (Guildf).* **2005**, *46* (2), 383–396. https://doi.org/10.1016/j.polymer.2004.10.070.

(30) Tol, R. T.; Mathot, V. B. F.; Groeninckx, G. Confined Crystallization Phenomena in Immiscible Polymer Blends with Dispersed Micro- and Nanometer Sized PA6 Droplets, Part 1: Uncompatibilized PS/PA6, (PPE/PS)/PA6 and PPE/PA6 Blends. *Polymer (Guildf).* **2005**, *46* (2), 369–382. https://doi.org/10.1016/j.polymer.2004.10.085.

(31) Salmerón Sánchez, M.; Mathot, V.; Poel, G. Vanden; Groeninckx, G.; Bruls, W. Crystallization of Polyamide Confined in Sub-Micrometer Droplets Dispersed in a Molten Polyethylene Matrix. *J. Polym. Sci. Part B Polym. Phys.* **2006**, *44* (5), 815–825. https://doi.org/10.1002/polb.20738.

(32) Sánchez, A.; Rosales, C.; Laredo, E.; Müller, A. J.; Pracella, M. Compatibility Studies in Binary Blends of PA6 and ULDPE-Graft-DEM. *Macromol. Chem. Phys.* **2001**, *202* (11), 2461–2478. https://doi.org/10.1002/1521-3935(20010701)202:11<2461::AID-MACP2461>3.0.CO;2-1.

(33) Kohan, M. I. *Nylon Plastics Handbook*; Hanser Publishers: Munich, Germany, 1995.
(34) Bunn, C. W.; Garner, E. V. The Crystal Structures of Two Polyamides ('Nylons'). *Proc. R. Soc. London. Ser. A. Math. Phys. Sci.* **1947**, *189* (1016), 39–68. https://doi.org/10.1098/rspa.1947.0028.
(35) Owen, A. J.; Kollross, P. A Note on the Crystal Structure of Nylon 12. *Polym.Commun.* **1983**, *24*, 303–306.
(36) Brill, R. Beziehungen Zwischen Wasserstoffbindung Und Einigen Eigenschaften von Polyamiden. *Makromol. Chem.* **1956**, *18*, 294–309.
(37) Wendoloski, J. J.; Gardner, K. H.; Hirschinger, J.; Miura, H.; English, A. D. Molecular Dynamics in Ordered Structures: Computer Simulation and Experimental Results for Nylon 66 Crystals. *Science (80-.).* **1990**, *247* (4941), 431–436. https://doi.org/10.1126/science.247.4941.431.
(38) Wolanov, Y.; Feldman, A. Y.; Harel, H.; Marom, G. Amorphous and Crystalline Phase Interaction during the Brill Transition in Nylon 66. *Express Polym. Lett.* **2009**, *3* (7), 452–457. https://doi.org/10.3144/expresspolymlett.2009.55.
(39) Suzuki, H.; Ishii, S.; Sato, H.; Yamamoto, S.; Morisawa, Y.; Ozaki, Y.; Uchiyama, T.; Otani, C.; Hoshina, H. Brill Transition of Nylon-6 Characterized by Low-Frequency Vibration through Terahertz Absorption Spectroscopy. *Chem. Phys. Lett.* **2013**, *575*, 36–39. https://doi.org/10.1016/j.cplett.2013.05.002.
(40) Ito, M.; Mizuochi, K.; Kanamoto, T. Effects of Crystalline Forms on the Deformation Behaviour of Nylon-6. *Polymer (Guildf).* **1998**, *39* (19), 4593–4598. https://doi.org/10.1016/S0032-3861(97)10132-X.
(41) Penel-Pierron, L.; Séguéla, R.; Lefebvre, J. M.; Miri, V.; Depecker, C.; Jutigny, M.; Pabiot, J. Structural and Mechanical Behavior of Nylon-6 Films. II. Uniaxial and Biaxial Drawing. *J. Polym. Sci. Part B Polym. Phys.* **2001**, *39* (11), 1224–1236. https://doi.org/10.1002/polb.1096.
(42) Ramesh, C. New Crystalline Transitions in Nylons 4,6, 6,10, and 6,12 Using High Temperature x-Ray Diffraction Studies. *Macromolecules* **1999**, *32* (11), 3721–3726. https://doi.org/10.1021/ma981284z.
(43) Jones, N. A.; Atkins, E. D. T.; Hill, M. J.; Cooper, S. J.; Franco, L. Chain-Folded Lamellar Crystals of Aliphatic Polyamides. Investigation of Nylons 4 8, 4 10, 4 12, 6 10, 6 12, 6 18 and 8 12. *Polymer (Guildf).* **1997**, *38* (11), 2689–2699. https://doi.org/10.1016/S0032-3861(97)85603-0.
(44) De Santis, P.; Kovacs, A. J. Molecular Conformation of Poly(S□ lactic Acid). *Biopolymers* **1968**, *6* (3), 299–306. https://doi.org/10.1002/bip.1968.360060305.
(45) Hoogsteen, W.; Postema, A. R.; Pennings, A. J.; Brinke, G. Ten; Zugenmaier, P. Crystal Structure, Conformation, and Morphology of Solution-Spun Poly(L-Lactide) Fibers. *Macromolecules* **1990**, *23* (2), 634–642. https://doi.org/10.1021/ma00204a041.
(46) Dreyfuss, P.; Keller, A. Invariance of the Long Spacing-Crystallization Temperature Dependence of Polyamides Precipitated From Solution. *J. Polym. Sci. Polym. Phys. Ed.* **1973**, *11* (2), 193–200. https://doi.org/

10.1002/pol.1973.180110201.
(47) Keith, H. D.; Padden, F. J. Banding in Polyethylene and Other Spherulites. *Macromolecules* **1996**, *29* (24), 7776–7786. https://doi.org/10.1021/ma960634j.
(48) Keith, H. D.; Chen, W. Y. On the Origins of Giant Screw Dislocations in Polymer Lamellae. *Polymer (Guildf).* **2002**, *43* (23), 6263–6272. https://doi.org/10.1016/S0032-3861(02)00426-3.
(49) Lotz, B.; Cheng, S. Z. D. A Critical Assessment of Unbalanced Surface Stresses as the Mechanical Origin of Twisting and Scrolling of Polymer Crystals. *Polymer (Guildf).* **2005**, *46* (3), 577–610. https://doi.org/10.1016/j.polymer.2004.07.042.
(50) Keith, H. D.; F. J. Padden, J.; Russell, T. . Blending with Small Concentrations of Polymer Diluents. *Macromolecules* **1989**, *22*, 666–675.
(51) Li, J.; Li, Y.; Zhou, J.; Yang, J.; Jiang, Z.; Chen, P.; Wang, Y.; Gu, Q.; Wang, Z. Increasing Lamellar Twisting Frequency with Poly(Lactic Acid) Segments Incorporation in Poly(Trimethylene Terephthalate) Ring-Banded Spherulites. *Macromolecules* **2011**, *44* (8), 2918–2925. https://doi.org/10.1021/ma1025434.

7. Conclusions

7. CONCLUSIONS

The conclusions of the four main chapters of this thesis are the following:

Crystallization study of P4HB

The melting behavior of P4HB resulted to be strongly dependent on the processing conditions, observing a complex melting peak associated with different lamellar populations of P4HB. Additionally, SAXS experiments demonstrated clear differences in the lamellar supramolecular order between annealed and melt crystallized samples. Annealed samples presented not only higher lamellar thickness and contrast between amorphous and crystalline regions, but also higher macroscopic crystallinity.

An equilibrium melting temperature (79.9 °C) of P4HB was deduced from the typical Hoffman-Weeks analysis.

An average Avrami exponent (n=2.56) and a single secondary nucleation constant (1.69×10^5 K^2) of the isothermal crystallized P4HB from the melt state were determined through DSC. A decrease of the exponent (n=1.93) was observed for the cold crystallization process from the glassy state that occurred under high geometrical constrictions.

A similar secondary nucleation constant (1.58×10^5 K^2) was deduced from the analysis of crystal growth of spherulite obtained from the melt and observed under optical microscopy, even though primary nucleation was increased during crystallization and when temperature decreased. Thus, the impact of the sporadic nucleation was minimized.

Both, crystal growth rate (G) and overall crystallization rate (k) were dependent on the temperature and were defined by bell-shaped curves, with 14-15 °C being the values of the temperatures corresponding to the maximum rates.

The secondary nucleation constant was also determined under non-isothermal conditions by using both, Avrami and isoconversional analysis. The

latter methodology provided the activation energy value and the temperature values related to the maximum growth/overall crystallization rate.

The measurement of the crystal growth rate of spherulites under non-isothermal conditions was in relatively good agreement with calorimetric results and also with those data obtained from isothermal crystallization.

Optical microscopy observations indicated that P4HB crystallized from the melt giving rise to negative and ringed spherulites with clear differences between the widths of black and white rings and an interring spacing. A deep study under infrared microspectroscopy analysis indicated that chemical bonds had the same orientation in the dark and bright rings supporting a model based on rhythmic growth.

SAXS studies demonstrated two different types of lamellar stacks on P4HB samples originating from the different shear stress that experimented with the shell and the core of the fibers during processing. As a result of the slippage of molecular chains the thickness of the lamellae stacks located in the shell was higher than the ones placed in the inner part, where they were constituted by more imperfect lamellae having surfaces perpendicularly oriented to the fiber axis.

The twisting and thickness of the constitutive lamellae of the spherulites were different depending on the cooling rate. Synchrotron data indicated a lower crystallization when the cooling rate increased and a lamellar insertion mechanism that led to a decrease of the crystalline layer thickness, especially when the cooling rate decreased.

Degradation study of P4HB

The hydrolytic study concluded that modification of pH, temperature, and time resulted in different degrees of degradation of P4HB sutures by exposure to hydrolytic media. GPC measurements demonstrated significant chain breakages, but weight losses were practically depreciable even under the most aggressive conditions. Depending on the degradation progress, microstructural changes were found which distinctly affected the lamellar stacks. A higher

increase of both crystalline and amorphous lamellar thicknesses was observed for the inner lamellar.

Thus, the chain breakages occurred in the amorphous regions of a more disordered surface which increased the crystalline region due to a certain reorganization of the chains. On the contrary, enzymatic degradation only caused a surface erosion with loss of surface material and had a scarce influence on the microstructure.

Differences according to the degrees of degradation were also observed during the heating of the stretched sutures of P4HB, where a slight thickening was detected for both types of lamellae as a consequence of the typical temperature reordering process, but with the melting of lamellae placed in the fiber core being faster.

However, in the case of films of P4HB crystallized for melt both hydrolytic and enzymatic degradation proceeds by following different mechanisms. Samples exposed to hydrolytic media underwent bulk degradation and random chain scission, in comparison to samples exposed to enzymatic media that undergo depolymerization. The hydrolytic degradation rate depended on the pH and the temperature, being more enhanced in acidic pH and higher temperature. The enzymatic degradation affected mainly the amorphous regions, causing an increase in the degree of crystallinity as determined by DSC. Additionally, as the amorphous folds on the lamellar surface were more susceptible to degradation, that led to a slight change in the lamellar morphology. In this case, the microstructure was characterized by spherulites constituted by thinner lamellae with a relatively narrow distribution. The degradation progress caused a substantial thickening that affected the thermal properties according to DSC data and SAXS correlation functions.

Cropping out the morphologies of constitutive spherulites is possible by selecting enzymes with adequate activity. Thus, the structure of P4HB banded spherulites could be successfully demonstrated when the amorphous regions were selectively removed during the enzymatic degradation study. Moreover,

SEM micrographs pointed out an alternate disposition of edge-on and flat-of lamellae and supported the theories based on a lamellar twisting.

Continuous, uniform, and smooth microfibers of P4HB with diameters around 7 μm without drops or agglomerations were obtained by using a horizontal set-up configuration in electrospinning equipment.

Due to extensive annealing treatments of P4HB scaffolds the lamellar thickness and melting point were lower compared to the sample coming from the commercial suture. Electrospun scaffolds showed excellent mechanical properties with Young modulus, maximum strength, and elongation values of 4 MPa, 28 MPa, and 360%, respectively, and surfaces with higher hydrophobic character than initial sutures due to an increase in the roughness.

Modification of the electrospinning solvent, by adding a small amount of DMSO percentage, allowed the successful incorporation of the FGF-P peptide growth factor which whatsoever led to a slight decrease of the fiber diameter and a change in the scaffold properties. Specifically, the maximum strength decreased and the elongation at break (i.e., from 360% to 730%) increased. Loaded samples showed good biocompatibility, a slight hydrophobicity, and a clear wound closure effect when the amount of incorporated FGF-P was 0.01 wt-%. Finally, by reducing the wound closure time the new fiber scaffold may have promising biomedical applications in tissue engineering and reparative medicine.

Polymer blends

The production of blends with improved properties was achieved by using reinforced polymeric matrices such as electrospun PGA/PCL nanofibers and PLA/PA610 blends.

Specifically, electrospun scaffolds constituted by different mixtures of hydrophilic PGA and hydrophobic PCL were produced. The PGA/PCL ratio affected not only the crystallinity of the new scaffolds but also the thermal properties. Homogeneous and continuous PGA/PCL-*x* fibers with diameters in the nano/micrometric range have been loaded with pharmacological agents

CUR and PHMB, the incorporation of which had a remarkable effect on the thermal stability of the loaded scaffolds, with the addition of the cationic PHMB being more problematic. Furthermore, the evaluation of the release behavior of the loaded scaffolds in a hydrophilic and hydrophobic media was well-differentiated and dependent on the PGA/PCL ratio, the swell capability of the medium to the polymer matrix, and the diffusion of the selected solvent into the electrospun fibers. Moreover, independently of the hydrophilic or the hydrophobic culture medium, all samples demonstrated a bactericide effect, with the CUR loaded samples being the ones with the lower activity.

Co-continuous morphology even at lower PA content as compared to unmodified PLA/PA blends was achieved by mixing PA610 and prior modified PLA with a chain extender. WAXD studies on PLA/ PA610 blends revealed that the confinement of PA610 domains inside the PLA phase hindered the crystallization of the polyamide, due to the formation of pseudohexagonal γ-form rendered at a high supercooling degree that differs from the characteristic layered structure of PA.

Additionally, SAXS data revealed that crystalline lamellae have differentiated morphological parameters at both immiscible polymer phases. Moreover, enhancement of the lamellar twisting and the crystal growth rate was achieved by the interaction of the amorphous PA chains with the crystalline PLA interfaces but harmed the nucleation process.

Department of Chemical Engineering
Polytechnic University of Catalonia

Barcelona 2021